NANO-MATERIAL-BASED BIOSENSORS FOR THE DETECTION OF ANTIBIOTICS

THESIS SUBMITTED TO DELHI TECHNOLOGICAL UNIVERSITY
FOR THE AWARD OF THE DEGREE OF

DOCTOR OF PHILOSOPHY

IN

BIOTECHNOLOGY

NAVNEET CHAUDHARY
(2K18/PH.D./BT/09)

DEPARTMENT OF BIOTECHNOLOGY
DELHI TECHNOLOGICAL UNIVERSITY
DELHI-110041, INDIA

JULY 2023

Dedicated to
My Beloved Father

CERTIFICATE

This is to certify that the Ph.D. thesis entitled "**Nanomaterial based biosensor for the detection of antibiotic**" submitted to Delhi Technological University, Delhi, for the award of Doctor of Philosophy is based on the original research work carried out by me under the supervision of **Prof. Jai Gopal Sharma**, Department of Biotechnology, Delhi Technological University, Delhi, India, and **Dr.Partima Solanki**, Special Centre For Nanoscience, Jawaharlal Nehru University New Delhi, India. It is further certified that the work embodied in this thesis has neither partially nor fully been submitted to any other university or institution for the award of any degree or diploma.

Navneet Chaudhary
(Enrolment No.2K18/PHD/BT09)

This is to certify that the above statement made by the candidate is correct to the best of our knowledge.

Prof. Jai Gopal Sharma
Supervisor
Department of Biotechnology
Delhi Technological University
Delhi-110042

Dr. Partima Solanki
Co-supervisor
Special Centre for Nanoscience
Jawaharlal Nehru University
New Delhi-110067

Prof. Pravir Kumar
Head of the Department
Department of Biotechnology
Delhi Technological University
Delhi-110042

DECLARATION

I, Navneet Chaudhary, certify that the work embodied in this Ph.D. thesis is my bonafide work carried out under the supervision of **Prof. Jai Gopal Sharma**, Department of Biotechnology, Delhi Technological University, Delhi, and **Dr. Partima Solanki**, Special Centre For Nanoscience, Jawaharlal Nehru University New Delhi, India for a period of July 2018 to July 2023 at the Department of Biotechnology, Delhi Technological University, Delhi and Special Centre For Nanoscience, Jawaharlal Nehru University New Delhi, India. The matter embodied in this Ph.D. thesis has not been submitted for the award of any other degree/diploma. I declare that I have devotedly acknowledged, given credit, and refereed to the research workers wherever their work has been cited in the text and the body of the thesis. I further certify that I have not willfully lifted some other's work, paragraph, text, data, results, etc. reported in the journal, books, reports, dissertations, thesis, etc., or available at websites and included them in Ph.D. thesis and cited as own my work.

Date:

Place:

Navneet Chaudhary

(Enrolment No. 2K18/PHD/BT/09)

ACKNOWLEDGEMENT

The journey to the attainment of ambition is full of ups and downs. During this roller coaster ride, you may come across someone who will consistently guide you on the right path, you may discover some individuals who will help you in shaping up your skills, and you may have some colleagues who will encourage you and help you in your difficult times, and finally, you may come across a bunch of indispensable friends who will play the pivotal role of your family members when you are away from the family. This work somewhere or at some stages of the whole journey reflects the contribution of all of those described below.

First and foremost I am forever indebted to my supervisor **Prof. Jai Gopal Sharma,** Professor at Delhi Technological University, Delhi for offering me the opportunity to carry out my Ph.D. I am thankful for his guidance and fruitful discussions, for his patience, motivation, and immense knowledge. I highly acknowledge his valuable advice that has helped guide and define my thesis. I want to thank him, who managed to shape me from a raw lump of clay into a nicely-formed vessel throughout my Ph.D. duration. Her amicable and positive personality has tremendously encouraged me to grow as a researcher and enabled me to understand the subject each day. Her scientific knowledge, dedication to research, and professional behavior always motivate me.

I extremely extend my heartfelt appreciation to my co-supervisor **Dr. Pratima Solanki**, Assistant Professor for allowing me to work in Special Centre for Nanoscience (SCNS), Jawaharlal Nehru University (JNU) New Delhi, under his co-mentorship. Without her support, I would not have made it this far, and I am indebted to her in ways that cannot be repaid. Throughout this work, she had unflagging faith in me and provided significant moral support. Each time I slowed down due to exhaustion, she encouraged me to push the boundary a little more. I thank her for his patience, good humor, and sincere devotion to helping me succeed. She has provided an excellent example, not just as a successful mentor, but also as a great leader. She made herself available for help whenever I asked for it and rescued my sinking ship in difficult times. Hence, I am very thankful to her, and words would not be enough to express my gratitude towards her. Moreover, her Lab has provided me with equipment and chemicals, without which this research would have been impossible to complete.

I am highly grateful to **Prof. Pravir Kumar**, Head of the Institute of the department of biotechnology, Delhi Technological University to give me space in our shell and providing resources for her department. He has been constantly supportive, cooperative, encouraging, and providing motivation for the research. He is an optimistic person who works as a leader and not a boss as well as believe in progressive thinking

I would like to acknowledge the Indian Council Medical Research (ICMR) Ministry of Science & Technology, New Delhi for financial support to carry out this study.

I must extend thank to the office staff of the Department of Biotechnology (CB Singh, Jitendra Kumar) who were always ready to give their timely support whenever required throughout my research tenure. Furthermore, every endeavor in life is a story about colleagues and collaborators. I would like to thank all the collaborators who provided me with opportunities and assisted me in my research. It has been my pleasure to work with people in the Delhi Technological University and Nano-Bio Laboratory group, SCNS, Jawaharlal Nehru University. I greatly acknowledge the entire Lab members past and present, for their support and friendship. I especially want to acknowledge my seniors for constantly guiding me and valuable suggestions.

Thanks to my co-authors and colleagues particularly those with whom I worked closely: **Dr. Anil Kumar**, **Dr. G.B.V.S Lakshmi**, **Dr. Pramod Kumar Gupta**, **Dr. Payal Gulati**, **Dr. Deepika Thakur**, **Dr. Avinash Singh**, **Reena Sajwan**, **Dr. Rahul Kumar**, **Dr. Smriti Sri**, **Dr**.**Manvi**, **Tarun K Dhiman**, **Amit Ahlawat**, **Zimad, Himanshu, Archana**, **Mrinal, Vimal Kumar, Abhishek Kumar, Vishal Anand, Sheetal Yadav**. I am highly thankful to my research mate **Mr. Amit K. Yadav and Dr. Damini Verma**, who has constantly assisted and supported me throughout the Ph.D. work. Lastly, my deep and sincere gratitude to my family for their continuous and unparalleled love, help, and support. I would like to thank my parents and my Bhaiya- bhabhi, and my sisters, far away from here, who always stood by me and bailed me out in many difficult situations. They taught me to work hard and always reach for my goals, no matter how difficult it may seem. My family had instilled in me the belief that whatever I wanted to achieve, I could. I am forever

indebted to my parents for giving me the opportunities and experiences to make me who I am. They selflessly encouraged me to explore new directions in life and seek my destiny. This journey would not have been possible without them, and I dedicate this milestone to them.

I might have missed acknowledging a few people who have contributed to my journey toward my Ph.D. Nevertheless, I owe them special thanks. At last, I want to thank God for bestowing in me; the perseverance to keep going; despite all odds, the strength to stand up after every fall, and the unfaltering faith in my abilities, without them this entire journey would not be possible.

Navneet Chaudhary

ABSTRACT

Biosensor development is gaining a lot of attention in the healthcare and biomedical industries. Because of the wide range of biosensor applications such as drug delivery, human health management, patient health monitoring, water, and food quality monitoring, environmental monitoring, disease diagnosis, and, the design and development of biosensors have become a priority for scientists and researchers in the last decade. Electrochemical biosensors and optical biosensors are the most prevalent among the various types of biosensors because of their inexpensive cost, quick response time, mobility, selectivity, and high sensitivity. Nanomaterials have made significant progress in sensing applications in recent years. Nanomaterial-based biosensors have attracted researchers to experiment with new concepts to increase analytical performance. These nanomaterials are widely known for their superior mechanical, catalytic, thermal, optical, and electrical properties, opening many possibilities for nanomaterial-based biosensors and systems. Many different forms of nanomaterials, such as carbon quantum dots (CQDs), nanoparticles (Nps), and their composite, have been used to fabricate nanostructured biosensors for the detection of ciprofloxacin antibiotics. Diverse nanomaterial-based biosensing approaches have recently been established for simple and small analytical instruments for on-site investigation of multiple analytes such as environmental contaminants, disease, toxins, etc. In the present thesis, we have detected Ciprofloxacin antibiotic. Ciprofloxacin belongs to the fluoroquinolones (FQs) class of antibiotics. It is a very stable antibiotic that does not go through complete metabolism in the body, and 30–90% of Ciprofloxacin (CPX) constantly remains. The growing public concern about the accumulation of drug residues in the food supply chain and livestock has led to the general administration of this antibiotic. However, CPX residues have been found to jeopardize people's health by influencing mammalian cell replication and adverse drug reactions. There is a strong probability that it reaches the environment through patient urine samples and wastewater due to inadequate metabolization of CPX in the body, which induces antibiotic resistance. In the coming future, the phenomenon of antibiotic resistance will be more complex. The primary stumbling block is the failure to detect pathogenic bacteria, resulting in inadequate antibiotic use and a lower survival rate in septic

situations. As a result, there is an urgent requirement to closely track the use and discharge of these medications in the atmosphere via the human body As a result, sensitive, inexpensive, portable, quick, and selective antibiotic detection is needed and is of great concern. Different analytical methods for determining antibiotics have been developed and used in the past; however, Optical and electrochemical detection approaches have benefits over these techniques in terms of strong selectivity, simple operation, high sensitivity, low cost, speed, and real-time detection with *in situ* analysis. This thesis is devoted to providing electrochemical and optical biosensing systems for ciprofloxacin detection in milk samples. In this context, we have synthesized two different nanomaterials. First is carbon quantum dots (CQDs) and another one is nanoparticles and their composite. In the CQDs category, two types of CQDs are synthesized from different materials such as C.Tmala (tej patta) leaf extract and *Ziziphus mauritiana* (ber) by the green route. In the nanomaterial category, we synthesized lanthanum oxide nanoparticles (La_2O_3)& lanthanum oxide nanoparticles with reduced graphene oxide(La_2O_3-Rgo).The synthesis of nanoparticles and their nanocomposite was confirmed using different techniques like UltraViolet-Visible spectroscopy (UV- Vis), X-ray diffraction (XRD), Fourier transform infrared spectroscopy (FT-IR), Raman, Atomic force microscopy (AFM), Contact Angle, Scanning electron microscopy (SEM), High resolution-transmission electron microscopy (HR-TEM), etc. along with other electrochemical characterization techniques such as cyclic voltammetry (CV), differential pulse voltammetry (DPV) and electrochemical impedance spectroscopy (EIS). The various nano platform developed in this thesis was fabricated using the electrophoretic deposition technique (EPD) on indium tin oxide (ITO) like BSA/anti-CPX/APTES/nLa_2O_3Nps/ITO and BSA/anti-CPXATPES/nLa_2O_3-rGONps/ITO substrate. Though BSA/anti-CPX/ATPES/nLa_2O_3 Nps/ITO showed good electrochemical results, BSA/anti-CPX/ATPES/nLa_2O_3 rGONps/ITO nano platform displayed excellent performance in terms of a broad linear range from (0.001 ng/mL-1000 ng/mL), having a higher sensitivity of 11.44 μA ng^{-1}m Lcm^{-2} and a low limit of detection of 0.001 ng/mL. and linear range from 10^{-6} –600 μg/ mL and sensitivity of 6.52 μA μg^{-1} mL cm^{-2} low limit of detection 0.055 μgmL^{-1} respectively. It also displayed better results in the case of excellent selectivity, repeatability, reproducibility stability, and diffusion coefficient. Moreover, the

electrochemical nano platform was productively helpful in analyzing the real samples to detect ciprofloxacin with acceptable results. CQDs from *Ziziphus mauritiana* (ber) have a good linear range and LOD compares to *C. tmala* (tej patta) CQDs. The linear range from 10 to 100 µM with a low limit of detection is 0.56 µM and the linear range from 1 to 100 µM with a low limit of detection is 6.06 µM respectively.

At last, this thesis also emphasizes the future perspectives for developing biosensors to detect other analytes

CONTENTS

Page No.

LIST OF SYMBOLS

Symbols	Name
θ	Scattering angle
λ	W wavelength of X-ray
d	Average crystallite size
Ipa	Anodic peak current
Ipc	Cathodic peak current
ΔI	Change in current
β	The full width at half maximum of diffraction peaks
D	Inter-planner distance
C	The concentration of redox species
V	Potential
N	Number of electrons involved in the redox process
R_{ct}	Charge-transfer resistance
T	Temperature
A	Electrode area
D	Diffusion coefficient
v	Scan rate
σ	Standard deviation
m	The slope of the calibration plot

LIST OF ABBREVIATIONS

Abbreviations	Full Name
CPX/CIP	Ciprofloxacin
HP-LC	High performance-liquid chromatography
CQDs/CDs	Carbon Quantum Dots
LC-MS	Liquid chromatography-mass spectrometry
0D	Zero dimensional
1D	One dimensional
2D	Two dimensional
3D	Three dimensional
UV-Vis	Ultra Violet-Visible spectroscopy
FT-IR	Fourier transform-infrared spectroscopy
HR-TEM	High-resolution-transmission electron microscopy
SAED	Selected area electron diffraction
EDS	Energy dispersive X-ray spectroscopy
SEM	Scanning electron microscopy
ACN	Acetonitrile
DI	Distilled water
DPV	Differential pulse voltammetry
EIS	Electrochemical impedance spectroscopy
ITO	Indium tin oxide
PBS	Phosphate buffer saline
LOD	Limit of detection
RSD	Relative standard deviation
GO	Graphene oxide
rGO	Reduced graphene oxide

Abbreviations	**Full Name**
-COOH	Carboxylic groups
FCC	Face-centered cubic plane
-OH	Hydroxyl group
Amp	Amperometry
Au	Gold
La_2O_3	Lanthum oxide
La_2O_3 NPs	Lanthanum oxide nanoparticles
ZM	*Ziziphus mauritiana*
C. tamala	*Cinnamomu tamala*

LIST OF FIGURES

Figure No.	*Titles*

LIST OF TABLES

LIST OF SCHEMES

Chapter 1

Introduction and Literature Survey

CHAPTER 1

INTRODUCTION AND LITERATURE SURVEY

1.1 Research Motivation

The emergence of antibiotic resistance has been acknowledged as a pressing concern for the well-being of humans and animals in the foreseeable future. The proliferation of antibiotics and the presence of antibiotic-resistant bacteria in the environment are anticipated to contribute to a rise in the incidence of drug-resistant infections in both populations. In the current scenario, various gram-positive and gram-negative species of bacteria have become resistant to several antibiotics, such as tetracycline, amoxicillin, gentamycin, ciprofloxacin, and norfloxacin. Among all these antibiotics, Ciprofloxacin (CPX) is wildly consumed through food by humans, and this is a leading cause of increased cases of antibiotic resistance in India. As there is a growing interest in the possible health threat posed by antibiotic-resistant so, the detection of antibiotics CPX is essential in food and milk samples. For this purpose, many analytical methods for sensitive detection of CPX in the literature have been devised, including spectrophotometry[1], liquid chromatography-mass spectrophotometry[2], high-pressure liquid chromatography[3], immunoassay[4], chemiluminescence[5], capillary electrophoresis[6], and electrochemical techniques [7],[8]. Though all these procedures provide excellent sensitivity and precision, they also have some disadvantages, such as the need for complex instruments, the fact that they are time-consuming, require pre-treatment stages, use hazardous organic solvents, and require well-trained, skilled operators. As a result, all these approaches are inadequate for on-the-spot investigations. Compared to these traditional techniques, an electrochemical biosensor and optical sensor deliver many benefits, including a powerful sensing approach,extremely sensitive, moderate cost, portability, and instrumental ease. Researchers from all around the world are working to develop new advancements in electrochemical and optical sensors to detect CPX in a straightforward, selective, sensitive, and cost-effective manner. Though nonmaterial-based electrochemical

biosensors and optical sensors have gained significant success in recent decades, still some issues in selectivity, sensitivity, and response rate need to beaddressed.

1.2 Objectives of Thesis

The present thesis aims to synthesize, characterize, and develop different nonmaterial for detecting antibiotics CPX with two different biosensing techniques. In this scenario, various nanomaterials are synthesized to detect CPX antibiotics with the help of electrochemical biosensors and optical sensors to address low detection limits and sensitivity issues. Lanthanum oxide (La_2O_3) nanoparticles & La_2O_3@rGO nanocomposite were used to detect CPX using the electrochemical immune sensor. The effect of pH, incubation time, and scan rate were analyzed with different sensing platforms. Also, the sensing characteristics like selectivity, reproducibility, repeatability, and shelf-life were explored using the sensor electrodes in electrochemical biosensing. Finally, the developed platforms were utilized for CPX detection in spiked real samples. In addition, carbon-based quantum dots, specifically carbon quantum dots (CQDs), derived from the extract of Cinnamomum tamala (C.Tamala) leaves and Ziziphus mauritania (ZM), were synthesized by green route without using any surface passivation, organic salt, and oxidizing agent in optical sensing for detection of trace amount of CPX antibiotic. The research objectives are outlined below:

- Synthesis of nanomaterials, their nanocomposites, and CQDs.
- Structural, morphological, and functional studies of synthesized nanomaterials, their nanocomposites, and CQDs.
- Fabrication of immune-electrode.
- Detection of CPX antibiotic using an electrochemical biosensor
- Detection of CPX antibiotic using an optical sensor
- Studies of spike and real samples of CPX detection.

1.3 Plan of Thesis

This thesis is mainly focused on CPX antibiotic detection based on bio(sensors), which is constructed in different chapters as follows:

Chapter 1

This chapter presents an overview of the research work documented in this thesis, along with the underlying motivation and the specific objectives pursued. The brief introduction of antibiotics, antibiotic resistance, cause of resistance, mechanism of resistance, an overview of CPX and their various detection methods, and also covers the basics of detection techniques, such as electrochemical and optical, which are used for biosensing in this thesis.

Chapter 2

This chapter discusses the materials and experimental techniques and their principles that are used to carry out the characterization of nanomaterials.

Chapter 3

This chapter is related to electrochemical biosensing and is divided into two parts- Part A describes the fabrication of an immunosensor using La_2O_3 nanoparticles, immobilization of antibodies, and bovine serum albumin (BSA), which is used for the detection of CPX using electrochemical measurement technique. Moreover, the efficiency of this electrode is monitored by measuring various parameters such as the sensitivity of the electrode, the limit of detection (LOD), and recovery using a spiked sample. Part B describes the fabrication of an immunosensor using a composite of lanthanum oxide with reduced graphene oxide nanoparticles to determine CPX using the same electrochemical measurement technique.

Chapter 4

This chapter explores the optical sensing models, which are also divided into two parts. Part-A includes the optical sensing method using CQDs for the detection of CPX in the absence of any biomolecules (such as antibodies). Part B describes the detection of CPX using ZM quantum dots in real spike samples in milk.

Chapter 5

This chapter contains the conclusion and future perspective of the thesis.

1.4 Overview of Antibiotics

Antimicrobial substances that are effective against bacteria are known as antibiotics. At present, these drugs play a very crucial role in treating various types of infections caused by bacteria, which is why they are used in very large amounts [https://www.nhs.Uk/conditions/antibiotics]. They can inhibit the growth of bacteria or directly kill them, and a few antibiotics also have antiprotozoal effects[9]. Antibiotics are ineffective against viruses such as the flu or common cold[10]. With the invention of penicillin in 1941, antibiotics gained popularity on a global scale. The general rule for using these drugs is to make sure the patient gets one that the target bacterium is sensitive to, at a dosage high enough to be successful but low enough not to have adverse side effects, and for long enough to assure that the infection is eliminated. The action of antibiotics is different against different types of bacteria. Certain antibiotics are very precise for bacteria, and others have the quality to target more than one bacterial species, such as the tetracyclines. Some antibiotics, such as quinolones and semi-synthetic penicillins, can be taken orally, whereas others must be administered intravenously or intramuscularly. Based on their spectrum of activity, antibiotics are classified into various categories. In which narrow-spectrum and broad-spectrum categories of antibiotics are considered the main ones. Penicillin G is an example of a narrow-spectrum antibiotic that targets gram-positive bacteria. Tetracyclines and chloramphenicol, which are classified as antibiotics, exhibit a wide range of effectiveness against both gram-positive and select gram-negative bacterial species. The names “gram-positive” and “gram-negative” are used to describe different types of bacteria based on their cell wall thickness, whether they are made up of a dense peptidoglycan mesh or only a thin covering of it[11].

1.4.1 Types of Antibiotics

Although various antibiotics are present, most of them are categorized into six main classes.

Penicillins (penicillin, amoxicillin, and phenoxymethyl penicillin) belong to this group and are frequently used to treat UTIs, chest infections, and many other infections as well.

Cephalosporins (like cefalexin) are a group of antibiotics used to treat several infections, and many of those can be effective against more severe conditions like septicemia and meningitis.

Aminoglycosides (like gentamicin and tobramycin) are a class of antibiotics generally used in hospitals to treat significant illnesses such as septicemia. These antibiotics are usually given through injection or sometimes given drops in the ear and eye infections. They also have some side effects, such as kidney damage and hearing loss.

Tetracyclines (like tetracycline and lymecycline) are a group of drugs that can treat many kinds of infections, but they're most frequently used to treat rosacea (skin infections) and acne.

Macrolides (such as azithromycin and clarithromycin) this group of antibiotics can be highly beneficial in the treatment of pulmonary and chest infections and can also be used for those who are allergic to penicillin.

Fluoroquinolones (such as **CPX** and levofloxacin) are a large group of antibiotics that used to be employed to treat a range of illnesses, including UTIs, breathing problems, and other infections. These antibiotics are no longer widely used because they may have serious side effects. Other antibiotics include nitrofurantoin and trimethoprim, which are used to treat UTIs; fusidic acid, which is used to treat skin and eye infections; and chloramphenicol, which is used to treat eye and ear infections [https://www.nhs.uk/ using-the-NHS/about-the-nhs].

1.4.2 Mechanisms of Action

The effects of antibiotics are produced by several different modes of action, of which inhibiting the synthesis of bacterial cell walls is among the most common. Beta-lactam antibiotics generally fall into this category. Antibiotics that block the formation of cell walls have a particular impact on the synthesis process during one or more stages of the process. As an outcome, the bacteria's shape and cell wall are changed, and they finally die.

Some other antibiotics, such as erythromycin, aminoglycosides, and chloramphenicol, inhibit protein synthesis in bacteria. The synthesis process of protein in mammalian and

bacterial cells is almost the same, but the protein is different. The drugs that are toxic against such proteins use these differences to bind and suppress the activity of such proteins in the bacteria, resulting in the prevention of new protein synthesis in the bacterial cell. Some drugs, like sulfonamides, inhibit the synthesis of folic acid in some microbes. Folic acid plays a crucial role in nucleic acid synthesis. Sulfonamide possesses an identical molecular structure to para-aminobenzoic acid, which serves as an intermediary compound undergoing enzymatic conversion into folic acid. Due to the same structure, sulfonamide binds and reacts with enzymes instead of para-aminobenzoic acid, inhibiting the process of folic acid synthesis.

Another antibiotic, rifampin, binds to a subunit of the bacterial enzyme that plays a crucial role in RNA(ribonucleic acid) synthesis in bacteria[11].

1.4.3 Antibiotic-Resistance

Antibiotic resistance develops as microbes adapt to the use of antibiotics. Bacteria became resistant to antibiotics rather than humans or other animals. Such microbes are capable of infecting both humans and animals, and their infections are more challenging to treat than those brought on by non-resistant. Even so, the misuse of these drugs is responsible for antimicrobial resistance (AMR), severe environmental degradation, and harm to human and animal health. Several types of antibiotic resistance are developed in strains with multidrug-resistant (MDR) phenotypes, which reduces the number of treatments available for those infections. The rapid spread of epidemic diffusion can occur as a result of cross-infection and propagation by high-risk multidrug-resistant (MDR) clones [12]. The emergence of highly drug-resistant phenotypes, known as extremely drug-resistant (XDR) or totally drug-resistant (TDR), occurs when the majority of available antibiotics demonstrate ineffectiveness against Gram-negative bacteria [13]. *Staphylococcus aureus and Enterococcus spp. are the two predominant gram-negative bacterial species that have developed resistance to antimicrobial drugs.* A major contributor to the global epidemic of Gram-positive drug resistance is methicillin-resistant *Staphylococcus aureus* (MRSA)[14]. Currently, antibiotic resistance is the biggest challenge to global health, food safety, and the environment, according to the WHO [15]. The WHO warned that the antibiotic resistance scenario

would get more severe by 2014, while the Centers for Disease Control and Prevention (CDC) declared that the "post-antibiotic era" had already begun in 2013. A concerted international campaign to address the antibiotic-resistant dilemma because the causes of antibiotic resistance are complex, and their consequences will have a significant impact on the world in the future[16]. Therefore, it is essential to have rigorous regulations on the use of these substances as well as constant surveillance.

1.4.4 Mechanism for the Development of Antibiotic-Resistant

Antibiotics trigger cellular reactions in the bacteria that enable them to survive if they are present in quantities too low to inhibit bacterial growth. Then, they multiply and pass their resistance gene to future generations; such bacteria can become more prevalent and cause diseases that cannot be treated with antibiotics[17].

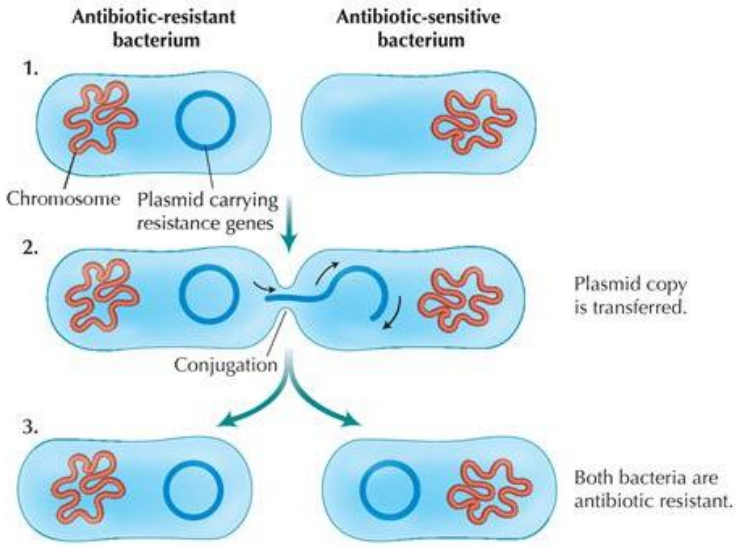

Source: https://www.huvepharma.com

Figure 1.1: Mechanism for the development of antibiotic-resistant by conjugation method in bacteria.

Bacteria may modify their genetic inheritance in two ways: first, by modifying their genetic material, and second, by getting additional genetic material from other bacteria. Bacteria can acquire new genes through a process referred to as conjugation, which involves plasmid-based gene transfer. These conjugative plasmids contain several genes that can be put together and rearranged, allowing bacteria to share beneficial genes with

one another, ensuring their survival against antibiotics and making them inefficient for curing dangerous illnesses in humans, leading to multidrug-resistant organisms[18].

1.4.5 Sources of Antibiotic Resistance

Although the primary cause of antibiotic-resistant illnesses in humans is the use of antibiotics for medical purposes[19], antibiotic-resistance genes can be transferred to humans from a range of animals, including agricultural animals, pets, and wildlife[20]. There are three possible ways that agricultural antibiotic use could result in human illness. The first mechanism involves the direct transmission of resistant bacteria from animals to humans. The second mechanism involves breaches in the species barrier, which allows for the transmission of resistant strains from one species to another, particularly in the case of prolonged transmission within the human population. Lastly, the spread of resistance genes from agriculture to human pathogens represents the third mechanism [21]. As mentioned before, agricultural antibiotics have seriously endangered human health. Although there is cause for alarm, the problem's scope might be overstated.

1.4.6 Causes of the Antibiotic Resistance

Overuse

Antibiotic misuse, sometimes referred to as antibiotic abuse or overuse, is the term for the excessive use of antibiotics that could result in adverse health implications for humans. Worldwide, antibiotics are overprescribed despite warnings against overuse. In numerous other countries, the sale of antibiotics without a prescription is permitted over the counter [21]. Because there is no regulation, antibiotics are widely available, affordable, and plentiful, which encourages the overuse of these medicines[22].

Inappropriate Prescribing

The development of antibiotic-resistant bacteria is also aided by inappropriately given antibiotics[23]. According to several studies, treatment indications, drug selections for that treatment, and timing for medication are incorrect about 30% to 50% of the time[24]. Inappropriate administration of antibiotics exposes patients to the possibility of adverse effects from antibiotic therapy[25].

Extensive Livestock and Agricultural Use

Antibiotics are commonly used in both developed and developing nations as growth promoters for cattle[26]. It is estimated that 80% of these drugs sold in the US were used on animals, primarily to promote growth and prevent illness[27]. Antimicrobial treatments for cattle are thought to increase their general health, resulting in higher yields and better-quality products[28]. Humans consume food, ingesting the antibiotics used on livestock[29]. Recent evidence from molecular detection techniques shows that consumers can contract resistant bacteria from farm animals through meat products. Around 90% of antibiotics employed by animals are excreted through their urine and feces, subsequently disseminating extensively through the means of fertilizers, groundwater, and surface runoff [30].

Regulatory Barriers

In the present scenario, getting regulatory approval can often be a challenge, even for companies that are confident about the search for new antibiotics. There was a substantial decline observed in the quantity of newly approved antibiotics from 1983 to 2007[31]. There exist numerous challenges associated with the acquisition of regulatory approval, as evidenced by factors such as bureaucratic processes, limited transparency, disparities in clinical trial requirements across different countries, fluctuations in regulatory and licensing standards, and insufficient communication channels.

1.5 Ciprofloxacin Antibiotic

Though there are many antibiotics of the fluoroquinolone class here for the present thesis work, the CPX antibiotic was selected for detection purposes. CPX was developed in 1987. Numerous infections caused by bacteria have been effectively treated by using this drug. CPX, an antibiotic belonging to the fluoroquinolone class, has been included in the World Health Organization's list of essential medications. It remains a paramount antibiotic in the management of Pseudomonas aeruginosa infections and is among the most commonly employed antibiotics for addressing this bacterial pathogen[32]. Due to the affordable price, this antibiotic is produced and used in large quantities. Improper usage of CPX can lead to unwanted infections, and side

effects include toxic and allergic reactions, intestinal flora abnormalities in people, as well as an increase in zoonotic CPX-resistant bacteria in animals.

An extremely stable antibiotic, CPX [1-cyclopropyl-6-fluoro-1,4-dihydro-4-oxo-7-(1-piperazinyl)3-quinolone carboxylic acid], is consistently present in the body at concentrations between 30 - 90% [33]. The widespread administration of this antibiotic is a response to the public's rising concern over the excessive collection of drug metabolites in animals and within the agricultural distribution network. Nevertheless, recent findings have revealed that the presence of CPX residues can have detrimental effects on human health, specifically by impeding the replication of mammalian cells and eliciting unfavorable reactions to medication. CPX is absorbed into the environment via patient urine samples and contaminated water because of its poor metabolism, which is also a concern for creating resistance in our environment[34].

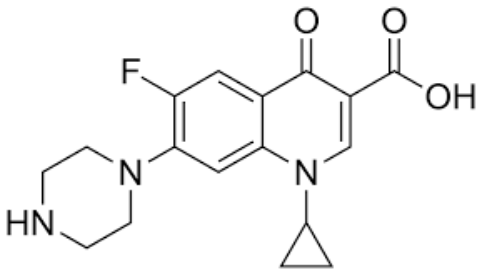

Source: https://en.wikipedia.org/wiki/CPX

Figure 1.2: Chemical structure of CPX

1.6 Need to detect Antibiotic

The growing level of antibiotics and bacteria that have become resistant to these drugs spreads in the environment, which increases the number of infections that are produced by these drug-resistant bacteria in humans as well as animals. So this is a severe threat to our environment, humans, and livestock in the future regarding this resistance[35]. Therefore, strict legislation on the usage of these compounds, along with continuous monitoring, is crucial. Various analytical techniques, including chromatographic methods, capillary electrophoresis, and enzyme-linked immunosorbent assay (ELISA), have been effectively developed for the quantification of antibiotics in water samples

[36]. However, these methods are labor-intensive, expensive, and time-consuming. Therefore, nowadays, the main focus of the scientific community is the development of prompt, sensitive, and selective sensing systems. A variety of sensing platforms for various antibiotics, including electrochemical, fluorometric, colorimetric, and optical sensors, etc., have been developed based on different inorganic and organic materials, viz. CQDs, carbon derivatives, metal oxide nanoparticles, and MIPs[37]. However, Researchers are continuously making efforts to explore different strategies to improve the limit of detection, stability, and reproducibility of prepared biosensors and sensors. In this regard, has emerged as promising candidates, and consequently, these are considered favorable platforms for the detection of different antibiotics because of their specific features[38],[39].

1.7 Conventional Diagnostic Techniques for Antibiotic Detection

1.7.1 High-performance Liquid Chromatography

High-performance liquid chromatography (HPLC) is a conventional technique and has been widely used in terms of selectivity, sensitivity, and time analysis. HPLC is considered a standard tool for the separation of complex mixtures and can detect substances at very low concentrations. HPLC is commonly used in today's time for the detection, separation, and quantification of samples and is also used in biochemistry to separate, identify and quantify active compounds.

1.7.2 Liquid Chromatography Mass Spectroscopy

Liquid chromatography-mass spectrometry (LC-MS) is a conventional analytical technique that combines mass spectrometry (MS) and liquid chromatography (LC). LC is not efficient in separating the components alone, but the association with MS can identify the unknown, known compounds or complex mixtures altogether. LC-MS is the quantitative and qualitative analysis technique. It is extensively used in pharmaceuticals, the food industry, the agrochemical industry, and environmental and forensic applications. It is also used in drug research and quality control analysis.

1.7.3 Enzyme-Linked Immunosorbent Assay

Enzyme-linked immunosorbent assay (ELISA) is a conventional bioanalytical tool used as a biochemistry assay. The principle of ELISA is based on the antibody-antigen reactions where immunoreactions take place between antibodies (produced by cells) and antigens. It is a highly sensitive, selective tool that permits the quantitative and qualitative analysis of antigens, proteins, hormones, nucleic acid, herbicides, and other secondary metabolites, etc. During measurement, the molecules are labeled with enzymes using horseradish peroxidase (HRP) and β-galactosidase, called enzyme immunoassay.

1.8 Limitations of Conventional Techniques

Conventional techniques have been usually applied concerning various detection of analytes, such as foodborne pathogens and clinical applications. However, these are sensitive and specific toward their analytes but also have certain limitations due to their characteristics. These are very tedious, expensive, time-consuming, and complicated and require a trained technician to operate these setups. Several techniques, including ELISA, HPLC, LC-MS, and others, are heavily used to detect various analytes. However, ELISA has certain limitations, such as being laborious, requiring sophisticated laboratory equipment, and high sample volume, which sometimes produce typical errors in the assay. Similarly, HPLC and LC-MS are very costly, require large amounts of samples for analysis, and are also challenging to handle. Analysis of samples using these methods takes longer time and sometimes weeks. Therefore, quick responsive techniques are required from a detection point of view.

Sensing platforms overcome these difficulties and provide a fast, responsive way to analyze varieties of analytes. It is comparatively cost-effective, portable, rapid, requires a very low amount of samples, and easy to handle, etc. The sensing platform comprises a variety of biosensors, including electrochemical, optical, thermal, piezoelectric, and others.

1.9 Biosensors

Biochemical interactions have great importance in biomedical applications. However, it is not easy to transform biochemical data into measurable signals. The biosensor is an analytical device containing bio-recognizing elements immobilized onto the transducing

platform, which interacts with an analyte and produces measurable physical, chemical, or electrical signals proportional to the analyte concentration[40],[41].

Background

The history of biosensors started with the development of an oxygen probe in 1956 by Professor Leland C. Clark, who is also known as the "Father of biosensors"[42]. In 1962 at the New York Academy of Sciences symposium, Clark explained how to fabricate electrochemical biosensors and how to detect a range of analytes. In the same year, Clark fabricated the first biosensor by immobilizing the enzyme "Glucose Oxidase" over an oxygen probe for glucose detection[43]. The estimated oxygen concentration was directly proportional to the concentration of glucose. Updike and Hicks further explored this work and fabricated the first practical enzyme electrode by immobilizing glucose oxidase on the oxygen sensor in the year 1967. After this invention, a range of biosensors were reported based on different detection principles[44]. Guilbault and Montalvo published an article in 1970 on the potentiometric urea sensor based on enzyme urease immobilized ammonia selective liquid membrane electrode[45]. In the year 1974, Klaus Mosbach[46] fabricated a heat-sensitive enzyme sensor. Yellow Springs Instruments Company developed the first amperometric biosensor for the detection of glucose, which was commercialized in 1975.

Further, a new path in the field of biosensors was added in the year 1975 when Divis found that bacteria could also be immobilized on the microbial electrode for the detection of alcohol[47]. In the same year, Lubbers and Opitz described an alcohol oxidase immobilized fiber-optic oxygen sensor for developing an optical biosensor for alcohol detection. In the year 1976, Clemens et al. [48] designed an advanced artificial bedside pancreas named "Biostator" by attaching an electrochemical glucose biosensor to it. Around the same time, La Roche presented Lactate Analyser (LA 640), in which hexacyanoferrate was utilized as a water-dissolvable mediator to flow electrons between lactate dehydrogenase and the electrode. Liedberg*et al.* (1983) published an article concerned with the commercial realization of immunosensors[49]. However, the mechanism of antibody immobilization on the sensing platform was discovered in the 1970s. MediSense, Cambridge, USA, developed a pen-sized meter for monitoring blood glucose in the year 1987. After these discoveries, many research groups belonging to different fields such as material science, physics, chemistry, biology, and

electronics focused attention on the development of advanced biosensing devices. More than 100 research articles on biosensors were published till the year 1985, and in 2011 alone 4500 research papers were published. This rising trend was also seen in the global market share for biosensors which was 2 billion USD in the year 2000[50].In the year 2013, it expanded to 11.39 billion USD and is expected to reach up to 22 billion USD in 2020 [51]. The increased concern of the common person on health care is the basic reason for this increase in global expenditure on healthcare. Currently, the production and development of biosensors are expanding because of the involvement of various new and advanced techniques derived from different branches of sciences and technologies. With time, biosensors will be part of our daily life because of their importance in various fields including healthcare, industries, environment monitoring, food and drink,anddefense.

1.9.1 Components of Biosensors

In the last decades, various nanomaterials have been used in the development of biosensors. A typical biosensor comprises bio-recognizers, a transducer, a signal processor, a signal detector, and displays to detect an analyte of interest [Figure1.3]

- **Analyte:** Analysis of a substance or sample provides its physical and chemical information, such as characteristics or concentration. A substance that needs to be analyzed/detected using a biosensor is known as an analyte, for example, antigens, ligands, nucleic acids, etc.

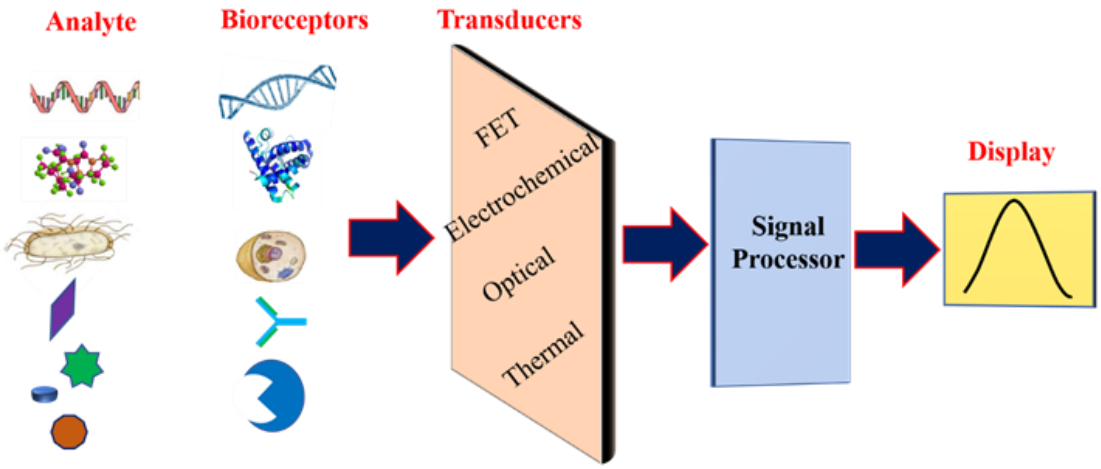

Figure 1.3: Schematic diagram of a biosensor

- **Bioreceptor:** The biomolecules such as antibodies, enzymes, and DNA are particular towards the antigen, ligands, and nucleic acids, respectively. The interaction between antibody-antigen, enzyme-ligand, DNA-nucleic acids produces biochemical signals which are converted into measurable signals using a transducer. The generated signals can be in the form of charge, color, heat, mass, etc.
- **Transducer:** A transducer converts one form of the signal into another one; it can be optical, electrical, mechanical, magnetic, chemical, acoustic, or a combination of any two or more. The biochemical interaction between bio-recognizing elements and the analyte of interest should take place in contact with the transducer to make sure that signals can be detected efficiently.
- **Signal Processor:** The signal(electrical)produced from the transducer is often low and needs to be amplified by superimposing on a high baseline signal. However, the signal may be noisy due to electrical interference or noise signal induced within the transducer. The best way to avoid interference or noise in the signal is the conversion of the analog signal into digital. The signal processor involves complex electronic circuitries, which amplify transduced signals and convert them into digital from analog.
- **Display:** The converted digital signal is passed to the signal detector, where the data is converted into an analog signal and displayed in a quantifiable form.

1.9.2 Characteristics of Biosensors

There are some characteristic parameters, such as selectivity, sensitivity, limit of detection, reproducibility, stability, and linearity, which define the efficiency of a biosensor. The optimization of these parameters is considered an improved performance of biosensors. Above mentioned characteristics of a biosensor are briefly described below.

- **Selectivity:** The most essential characteristic of a biosensor is selectivity, which expresses the ability of a bioreceptor to sense a particular analyte from a solution containing contaminants and other analytes. The interaction between the antibody (bioreceptor) and antigen (analyte) is the best example of selectivity.

- **Sensitivity:** The sensitivity of a biosensor defines a relationship between the analyte concentrations and corresponding output signals, which quantifies the strength of the output signal observed per unit analyte concentration. For an efficient biosensor, sensitivity should be high.
- **Limit of Detection (LOD):** The LOD for a biosensor expresses the minimum detectable analyte concentration. For efficient biosensors, it is required to detect the analyte of interest with a low value of LOD.
- **Linearity:** Linearity is the characteristic of the biosensor that displays the accuracy of the response for a range of analyte concentrations. Besides this, the wide linear detection range of the analyte is also required for a biosensor. For the response or concentration-signal plot, the equation for a straight line is expressed as $y = mx + c$, where x is the concentration of the analyte, y is the output signal, and m is the slope of the line.

1.9.3 Classification of Biosensors

The biosensors can be classified based on the used bio-recognizing element and type of transducing element. The transducing technique relies upon the kind of physicochemical change coming about because of the sensing event. Depending on the type of transducer, a biosensor can be broadly classified into acoustic, optical, Thermal, ion-selective, and electrochemical biosensors[52]. These biosensors are briefly described below.

1.9.3.1 Acoustic Wave Biosensors

Acoustic wave biosensors are also known as piezoelectric biosensors, in which bio-recognizing elements are immobilized on the surface of an acoustic wave transducer. At the point when the analyte of interest binds with the bio-recognizing elements at the surface of the transducer, the mass of the transducer film change. The subsequent change in the mass, along with analyte concentration, changes the resonant frequency of the transducer. The concentration of analyte binds on the transducer surface is directly proportional to the variation in the resonant frequency of the transducer.

1.9.3.2 Thermal Biosensors

Numerous enzyme-catalyzed reactions are exothermic means they produce heat during chemical reactions. The thermal biosensors measure the heat produced by biochemical reactions at the transducer surface that change the temperature of the medium. In this kind of biosensor, the surface of the temperature transducer is used as an immobilizing platform for bio-recognizing elements. At the point when the analyte of interest chemically interacts with the enzyme, an exothermic reaction takes place that produces an amount of heat proportional to the analyte concentration. Usually, the thermostat is used to measure the temperature due to its high-temperature sensitivity. Compared to the other type of biosensors, thermal biosensors are not required repetitive calibration and are free from the optical properties of the sample. Thermal biosensors are often used for the detection of pesticides and pathogenic microscopic organisms. However, such biosensors have revealed low sensitivity and can't be applied to detect a large range of analytes.

1.9.3.3 Ion-Sensitive Biosensors

The ion-selective biosensors are semiconductor electrodes having an ion-sensitive surface. At a point when the surface of the semiconductor interacts with the ion, the surface electrical potential changes that can be measured easily. The ion-selective biosensors are made-up by placing a polymer layer on the surface of the sensing probe. This polymer coating is specifically penetrable to analyte ions. Thus, the selective ions quickly move through the polymer, diffuse at the electrode surface, and result in a change in electrode surface potential. A range of analytes, including proteins, bacteria, drugs, and toxins, can be detected using a different membrane.

1.9.3.4 Optical Biosensors

This type of biosensor is capable of detecting the catalytic as well as affinity reactions. The optical biosensors measure the detection events in the form of light signals. In principle, optical biosensors can be made because of electroluminescence or optical diffraction. The biosensors based on optical diffraction consist of bio-recognizing elements (as antibodies) immobilized on the silicon wafer. A specific area on the

biofunctionalized wafer is opened to UV light to deactivate the biomolecules (antibodies) present in that area. At the point when the wafer interacts with the analyte (antigen), the immunocomplex is formed only in active regions that result in the diffraction gratings. These diffraction gratings produce optical diffraction signals when struck up with an optical source.

In the case of electroluminescence-based optical biosensors, the catalytic reactions are detected in terms of change in fluorescence or absorbance. The binding of biomolecules on the surface of transducer material induces a change in optical properties (absorbance or fluorescence) that directly corresponds to the concentration of the analyte.

1.9.3.5 Electrochemical Biosensors

An electrochemical sensor is a subclass of a chemical sensor, which is much better because of excellent detectability, simple design, and cost-effectiveness. This type of sensor responds to the electrochemical reactions occurring at the electrolyte/electrode interface. In contrast, electrochemical biosensors are comprised of biomolecules as a recognizing component that makes them distinctive from other chemical sensors[53]. Electrochemical biosensors convert biochemical or biological reactions directly into measurable electrical signals related to the analyte concentration.

In designing an efficient electrochemical biosensor, there are some requirements or conditions, which are given below:

- Immobilized bio-recognizer must be specific to the analyte of intrigued.
- The biochemical response should be free of different natural conditions, including pH, temperature, and stirring.
- Electrochemical signals ought to be free from electrical noise signals initiated by the transducer.
- Biosensor strips must be simple to handle, compact, and have no harmful impacts.
- The electrochemical reaction must be precise, reproducible, exact, and straight over a run of analyte concentrations.

- Biosensors ought to be able to make a quick and real-time response for human samples.
- From a commercialization point of view, biosensors must be simple, cost-efficient, compact, and simple to function.

Advantages of Electrochemical Biosensors

- Non-destructive strategy to detect analyte
- Straightforward to use
- Specific detection of analyte
- Rapid and precise response
- Cost-effective

Limitations of Electrochemical Biosensors

- Biomolecules can be denatured in a warm environment; thus, heat sterilization is not possible.
- Biosensor's response can vary with environmental conditions (such as pH and temperature) and structural changes in transducing material.

Among the various types of biosensors, electrochemical sensors and optical sensors are much smart because of excellent delectability, simple design, cost-effectiveness, and flexibility to miniaturization. In the present thesis work, nanomaterials-based electrochemical and optical sensors have been fabricated and utilized for the detection of CPX antibiotics.

1.9.3.5.1 Classification of Electrochemical Biosensors

Electrochemical biosensors are broadly categorized into potentiometric sensors, conductometric sensors, and amperometric sensors depending on the type of electrical signals (potential, conductivity, or current) generated from bioelectrochemical reactions.

Potentiometric Biosensors

In this kind of biosensor, oxidation and reduction potentials of an electrochemical reaction are the deliberate parameters. The biochemical reactions generate a potential

difference between the working and reference electrode due to charge accumulation. The magnitude of potential is directly proportional to the amount of analyte in the electrolyte.

Conductometric Biosensors

The conductometric biosensor measures the electrical conductance or resistance of the solution between the two metal electrodes and calibrates it with analyte concentration. The change in the conductance or solution resistance arrives due to produced electrons or ions by electrochemical or biochemical reactions. However, conductance biosensors have relatively low sensitivity.

Amperometric Biosensors

Amperometric biosensors respond to the current change due to electron transfer originating from biochemical reactions on applying a controlled potential. The measured current must be associated with the concentration of the analyte.

Among the electrochemical biosensors, the amperometric biosensor has a high sensitivity to detect analyte concentration in the electrolyte solution. Thus, in the present research work, amperometric biosensors have been designed to achieve improved biosensing performance.

1.9.4 Electrochemical Nano-biosensors

During the last few years, the applications of advanced analytical techniques and nanotechnology have provided rapid advancement to the field of electrochemical biosensors. The biosensors based on nanomaterials are known as nano-biosensors. The fabrication of nano biosensors involves the use of chemistry, physics, biology, and material science. It is an interdisciplinary field where the biosensing parameters of sensors are studied for the detection of an analyte of interest. Compared to the traditional methods of modern biosensors, electrochemical nano biosensors provide numerous advantages, including rapid, real-time, and specific detection, simple, easy to handle, and low cost. Recently, electrochemical nano biosensors have been much more progressive by utilizing novel nanomaterials and their properties with analytical

techniques. The performance of a biosensor is experimentally evaluated in terms of characteristic parameters such as sensitivity, LOD, linear detection range, the reproducibility or precision of the response, selectivity, assay time, and stability. At present, some of the biosensors have been commercialized and are regularly used in biomedical, agricultural, industrial, and environmental applications.

1.9.5 Electrochemical Immunosensor

An electrochemical biosensor based on the antibody-antigen interaction on the transducer surface is known as an "electrochemical immunosensor." These types of biosensors explore the electrochemical signals produced by the transducer due to antibody-antigen interaction. The electrochemical signals can be potentiometric, voltammetric, impedimetric, or conductometric. A typical electrochemical immunosensor contains a layer of antibodies attached to the transducer surface. When a solution-containing antigen (analyte) is exposed to the transducer antigen interacts with the antibody and produces electrochemical signals, which are sensed using an electroanalytical technique(s). The electrochemical immunosensors are applied in different applications (environmental matrices, industry, food analysis, defense, and medical diagnosis) because of their selectivity, portability, and ease of usability.

Principles

Immunosensors work on the principle of antibody-antigen interaction. The immunochemical reactions between antigen and specific antibodies on the surface of the transducer produce a stable immunocomplex layer. This immunocomplex layer on the electrode surface influences the electron transfer at the electrode/electrolyte interface, which can be detected using the electroanalytical technique.

Antibody and Antigen

Antibodies, also known as immunoglobulins, are protective protein produced by the immune system that responds to the foreign substance (antigen)[54]. When a foreign antigen comes in contact with our body, the immune system senses them by molecules present on their surface and starts to produce specific antibodies. These antibodies bind or attach themselves to the antigen to inactivate them and remove them from our

bodies. There are several antibodies in the human body, and each of them is specific to detect one antigen. In other words, antigens and antibodies are specific to each other like lock and key. Usually, the antibody has a Y-shaped structure and two identical binding sites on each arm of Y. The binding site has a specific shape, and it links with an antigen that matches to fit into a shape. There are several isotypes of antibodies, including IgA, IgD, IgE, IgG, and IgM, and each exhibits different biological properties[55],[56]. In the case of toxins, antibodies attack to bind them to neutralize the poison by changing their chemical composition, and antibodies are known as antitoxins. In the case of microbes, antibodies attach to make them immovable and prevent them from penetrating the body cells. The antibody does not recognize the entire antigen, but it binds with a portion of the antigen surface. An antigen can be microscopic organisms, infections, or growths that reason contamination and ailment. They can likewise be substances called allergens that expedite a hypersensitive response. Regular allergens incorporate dust, creature dander, honeybee stings, and certain foods. The immune system must have the capacity to perceive fungi, microbes, bacterial items, parasites, and infections as immunogens to secure against infectious diseases.

In the present work, the immunoglobulin G (IgG) class of antibodies is used in the fabrication of immunosensors. This configuration protects against bacteria, viruses, and toxins.

1.10 Biomolecules Immobilization Methods

As discussed, an electrochemical biosensor comprises a bio-receptor immobilized on the surface of the transducer material. The immobilization of biomolecules is very important in the development of an efficient biosensor with high sensitivity, high selectivity, high storage ability, high reproducibility, short response time, and low LOD. It is essential that after immobilization, biomolecules must retain their functioning, structure, and biological activity. Moreover, biomolecules attached to the surface of the electrode are not to be detached during storage or utilization of biosensors. The adopted immobilization method also affects the stability and activity of fabricated biosensors. Thus, different strategies are developed for the successful immobilization of biomolecules onto the electrode (transducer) surface to develop an efficient biosensor.

The selection of immobilization method(s) is made based on the nature of the biomolecule, the used transducer, environmental conditions, the analyte of interest, and applications of biosensors[57]. The immobilization methods are majorly divided into two categories: physical immobilization and chemical immobilization[58].

1.10.1 Physical Immobilization

In the physical immobilization method, the binding of biomolecules on the transducer surface does not involve any chemical reactions. This category of immobilization includes adsorption, microencapsulation, and physical entrapment, which are briefly discussed below:

Adsorption

The adsorption method is the simplest one and negligibly affects the activity of immobilized biomolecules. However, this method suffers from very weak bonding, non-specific adsorption, and a small lifetime. The adsorption method is subdivided into physical adsorption (physisorption) and chemical adsorption (chemisorption). The chemical adsorption process is stronger than physical adsorption.

Electrostatic

Electrostatic immobilization of biomolecules on the surface of the transducer material occurs due to electrostatic interaction between biomolecules and the material surface. The electrostatic interaction is non-covalent interaction between two opposite charges, which does not involve sharing of electrons. The strength of electrostatically immobilized biomolecules on the electrode surface depends on the potential difference between them. Example: Antibodies immobilization on the metal oxide nanostructures.

Microencapsulation

The microencapsulation immobilization strategy is more consistent as compared to adsorption. In this method, an inactive layer of polymer on the working electrode traps the biomolecules. Usually, chitosan (CS), Nafion (Nf), and cellulose acetate are used for the microencapsulation of biomolecules on the electrode surface.

Entrapment

In this method, biomolecules to be immobilized are incorporated in the polymeric solution, followed by their entrapment on the surface of the working electrode. The entrapment method does not involve any chemical reaction between the biomolecules and monomers of the polymer solution. Thus, more than one type of biomolecule can be incorporated without loss of their activity. Generally, gelatin, alginate, or conducting polymers like polyaniline and Nf are utilized in the entrapment method. The surface coating of the electrode can be done using various methods, including dip coating, spin coating, drop-cast, etc. However, this method leads to biomolecule leakage and diffusion barrier.

1.10.2 Chemical Immobilization

In this category, biomolecules are immobilized on the transducer surface because of the chemical bonding between the functional groups present on biomolecules and the transducer surface. Covalent attachment and cross-linking methods belong to this category, which is briefly described here:

Covalent Attachment

The covalent attachment is the chemical bonding between the functional groups on electrode material and immobilized biomolecules. Immobilization through covalent attachment is considered reliable and stable compared to other methods. Covalent attachment does not create any diffusion barrier and prevents antibodies from detaching from the electrode surface during measurements. However, this method does not prompt re- generable network.

Cross-linking

Crosslinking holds at least two molecules by covalent bonds. In the cross-linking method, a functional agent like glutaraldehyde or ethylenediamine is used to bind biomolecules on the surface of the transducer.

1.11 EDC-NHS Crosslinking Chemistry

EDC [1-ethyl-3-(-3-dimethyl aminopropyl) carbodiimide] is a water-soluble crosslinking agent, which is used to link carboxyl groups with primary amines *via* forming an amide

bond. No chemical portion of EDC is involved in the final (amide) bond. Thus, EDC is deliberated as a zero-length crosslinker. Figure 4 shows the EDC reaction mechanism to form amide bonds and the importance of N- Hydroxysuccinimide (NHS) in EDC-NHS chemistry. As shown in Figure 4, EDC reacts with the carboxylic acid groups and forms functioning O-acylisourea intermediates, as denoted by (A). These intermediates are removed in the form of by-products on introducing nucleophilic of primary amino groups (B).

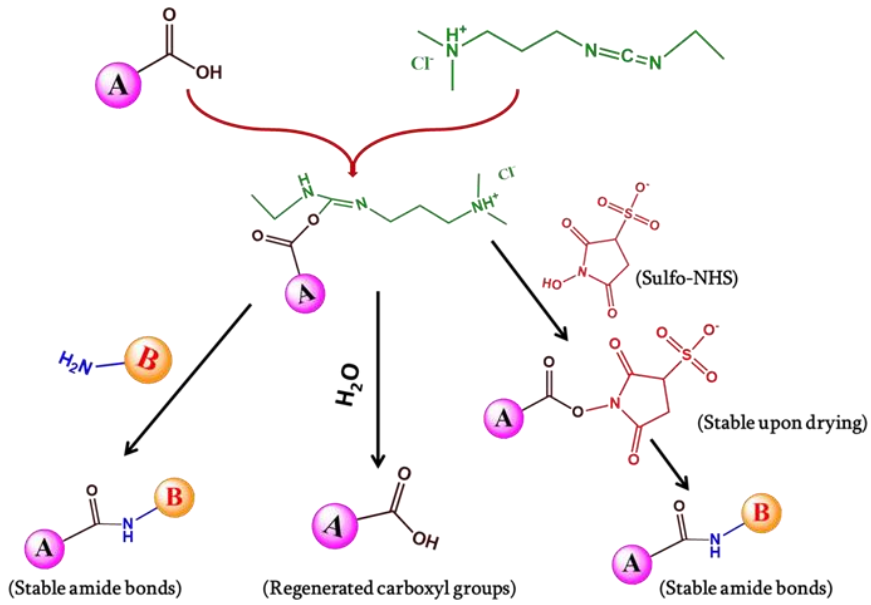

Source: https://www.google.com/EDC+-NHS+crossed+link+chemistry

Figure 1.4: EDC-NHS crosslinking chemistry to couple carboxyl groups to primary amines

In this way, primary amines are linked with the original carboxyl group *via* a covalent bonding (amide bond), and the by-product EDC is extracted as a soluble urea derivative. The as-formed *O-acylisourea* intermediates are unstable in an aqueous medium and hydrolyzed if failed to link with amines. The hydrolysis of intermediates results in the regeneration of the carboxyl group, as shown in Figure 4. To improve the stability and efficiency of EDC crosslinking chemistry, water-soluble NHS is incorporated with it. In EDC-NHS chemistry, EDC links with NHS to the carboxyl group and forms an NHS ester that is highly stable compared to the *O-acylisourea* intermediate. The EDC-NHS chemistry allowed an efficient binding between carboxyl and amine groups at physiologic pH. Moreover, EDC-NHS-activated carboxyl

compounds can be stored and can be used further. In the present thesis, an EDC-NHS crosslinker has been used for the covalent immobilization of antibodies on the electrode surface containing amine or carboxyl groups. When the electrode surface material contains carboxyl groups, then the electrode is treated with EDC-EHS to activate groups on the electrode surface. Whereas fragment crystallizable (Fc) regions of antibodies are activated using EDC-NHS chemistry if the electrode surface material contains amine groups.

1.12 Nanomaterials Used

New methods have been employed for biosensor and sensor technology to fulfill the rising demands of distinct areas. The biosensor technology can be further extended with advancements in nanoscience and nanotechnology. Nanotechnology is a fast-developing discipline of science with applications in vast areas that include environmental remediation[59], Nanomedicine[60], energy storage, and sensing[61]. The "nanomaterials" are the fundamental and essential components of nanotechnology. Nanomaterials have got attention as an interesting new class of materials with broad practical applications. They are materials having a size of <100 nm in at least one dimension. The physical and chemical properties of a substance change dramatically when it is reduced in size from bulk to nano. Nanomaterials have recently achieved significant popularity due to their excellent structural, optical, magnetic, and electrical properties[62]. They are categorized based on nanoscale dimensions (less than 100 nm), as shown in Figure 1.5

- **Zero-dimensional Nanomaterials (0D):** It covers all the nanomaterials whose three dimensions are in the nanoscale range. For example, nanoparticles fall under this category.
- **One-dimensional Nanomaterial (1D):** In this type, the two dimensions are outside the nano range, while only one dimension falls under the nano range. Nanowires or nanotubes, or nanorods are included in this category.
- **Two-dimensional Nanomaterials (2D):** In this, any two dimensions fall in the nano range, whereas the one remaining dimension is outside its range. Nanosheets, nanocoating, nanolayers, and nanofilms are involved in this class.

- **Three-dimensional/Bulk Nanomaterials (3D):** In these materials, all the dimensions are out of an orange, which means the three arbitrary dimensions are found to be more than the 100 nm range. These materials involve nanotube bundles, core shells, multi-nanolayers, nanowires, and nanocomposites[63].

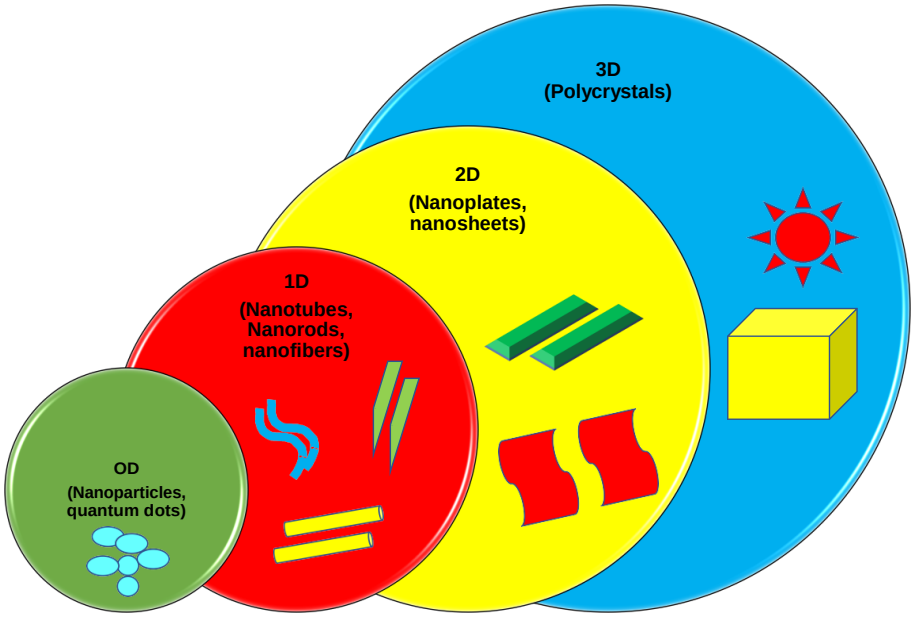

Figure 1.5: Classification of nanomaterials based on dimensions

The electrochemical and optical performance of a biosensor and sensor for detecting an analyte is primarily dependent on the type of electrode material, size, and shape. The application of nanoscience and nanotechnology offers great potential for improving material properties by adopting different strategies to design nanomaterials with the desired shape, size, surface properties, and other characteristics[64]. The improvement in properties of nanomaterials, such as faster rate of electron transfer and large surface area, compared to bulk materials, is being applied to design efficient and novel electrochemical biosensors. Moreover, functional nanomaterials show a synergic effect that improves catalytic activity, electronic conductivity, biocompatibility, efficiency to link with recognition events, and transduction of signals in electronic devices[65]. In this context, various nanomaterials based on inorganic (metals & semiconductor oxides) and composites have been utilized to develop efficient electrochemical biosensors and optical sensors.

1.12.1 Carbon-based Nanomaterials

The family of carbon-based nanomaterials comprises materials that are widely explored for several applications due to their remarkable properties. CQDs, carbon nanotubes, fullerenes, graphene, and many more novel compounds belong to the family of carbon. These materials provide unique benefits extending to several fields, such as high mechanical strength, biocompatibility, chemical stability, high electrical conductivity, and a surface-to-volume ratio[66]. Therefore, they are frequently included as sensing materials.

1.12.1.1 Quantum Dots

Quantum dots (QDs) is generally referred to as semiconductor nanocrystals which are tiny form of nanomaterials with extremely smaller size, below 10 nm, and having a high surface-to-volume ratio.QDs are of new interest in nanotechnology due to their optoelectrical properties[67],[68].

It was first discovered by *Alexie Ekimov*and*Louis E Brus* in the 1980s during their research work on glass matrix and the colloidal solution, respectively[69]. Although QDs are not new, it has been used by Greeks and Romans for several years the cosmetics purposes. In another study, it is reported that early 20^{th} century, Cadmium sulfide (CdS) and Cadmium selenide.

(CdSe) quantum dots has been utilized as a precipitate for colorful silicate glasses[70]. Unlike nanomaterials (bulk), QDs are zero-dimensional nanostructures, and a limited number of electrons are present in their quantized discrete energies in the density of states (DOS)[71]. Staircase and DOS formation result due to the repulsion of the electronic charge on the quantum dots with the addition of another charge. The step size of the staircase is formed, which is inversely proportional to the radius of the QDs.The shape and size of the QDs are significant and play an important role, such as affecting the conductive properties and band gap (the larger the QDs size smaller the band gap)[72]. A greater band gap in QDs results in a higher energy difference between the lowest conduction band and highest valence band, which means higher energy is required to excite the QDs, resulting in emission with lesser energy when dots comes down to the ground state. As mentioned above, the higher the band gap lower the particle size, which

is also responsible for the shifting of wavelength of the absorption/emission spectra from blue to red and vice-versa. It is also reported that QDs present different emission colors for different sizes.

For the idealized cubic dot, the energy separation (ΔE) between the conduction band and valence bond is given below:

$$\Delta E = E_g + \sum_{i=x,y,z} \frac{\hbar^2 \pi^2 n_i^2}{2d_i^2} \left(\frac{1}{m_e} + \frac{1}{m_h}\right)$$

Where, E_g Represent band gap energy of host material, Coordinate (x,y,z) shows the energy confined dimension for conduction and valence band, d_i is the z size of the quantum dot, m_h and I are the effective masses of the conduction band of electron and valence band of hole respectively. The term 'quantum confinement' is related to the charge carrier capability of QDs in their smaller physical dimension size[73].

Advantages of QDs against Organic Dyes

1. QDs show a broad absorption profile and allow efficient excitation in the presence of a limited number of excitation photons[74].
2. QDs consist of a larger number of molar extinction coefficients (~100 000 000 M^{-1} cm^{-1})compared to organic dyes (~250 000 M^{-1} cm^{-1})at excitation peak[75].
3. One of the essential properties of QDs is observed at the tuneable emission peak, which often changes with the size of particles, while in the case of organic dyes, it is impossible.
4. QDs show a high quantum yield, especially in the NIR region over organic dyes.
5. A major difference is the long fluorescent lifetime of QDs, around 10 ns in the visible region, while only a 5 ns lifetime was observed for organic dyes[76].
6. QDs are more photostable as compared to conventional organic dyes.

Disadvantages of QDs

Surface defect in quantum dots is a disadvantage; it arises due to the temporary trapping of electrons, holes, or excitons which causes several factors, such as quenching of radiative emission and reduction of quantum yields.

Carbon Quantum Dots

CDs are carbon-based nanomaterials and are considered carbon nanodots or carbon quantum dots. CDs are below 10 nm in size and have unique fluorescent and chemical properties. Due to this, CDs possess tremendous attention towards recent research. These CDs were unintentionally discovered in 2004 while single-walled carbon nanotubes were being purified[77],[78]. It is also a good alternative to heavy metal or inorganic quantum dots and has several properties, such as stable photoluminescence, aqueous solubility, low cytotoxicity, good biocompatibility, tuneable wavelength emission, chemical inertness, etc.[79].Having distinct properties, CDs have attracted several areas and wide applications, such as light-emitting diode (LED), photovoltaic cells, photocatalysis, cell imaging, and medical diagnosis[80]. Chemical sensors, biosensors, drug delivery, and fluorescence resonance energy transfer (FRET) based sensor act as analytical probes for inorganic molecules detection, etc. [81],[82]. The CDs can be chemically synthesized by using chemical precursors, which are conjugated or non-conjugated molecules. Non-conjugated aliphatic molecules such as citric acid with ammonia, alkyl amine, ethanolamine, ethylenediamine, L-cysteine, urea, or thiourea, etc. On the hand, conjugated precursors usually relate to aromatic's molecules such as phenylenediamines, phenol, and their derivatives[83]. Other than these, the green synthesis route is the attractive way for synthesizing the CDs using natural precursors such as orange peel[84], rise husk[85], lychee seeds[86], orange juice[87], peanut skin[88], watermelon peel[89], grape peels[90], tomato juice[91], rose flower[92], grape juice[93], lime juice[94], milk[95], potato[96], plant leaves[97], cherry tomatoes[98], vegetables and waste biomass product[99], etc. The advantages of green synthesis carbon dots are inexpensive, clean, non-toxic, and easily accessible.

Graphene Quantum Dots

Similar to CQDs, graphene quantum dots (GQDs) are also carbon-based nanomaterials with zero-dimensional (0-D) scale and having lateral dimensions smaller than 10 nm, exhibit excellent physical and chemical properties that allow them various biological applications[100],[101]. GQDs possess essential features due to graphene lattice and show high crystallinity with a large sp^2 hybridized carbon structure; on the contrary, CDs manifest quasi-spherical particles with a lesser number of sp^2 hybridized carbon

atoms, smaller than 10 nm in size[102]. The structural characteristic of GQDs is distinct, having anisotropic properties and layered structure. In contrast, CDs have nanoparticle features and colloidal behavior. However, the structural properties of GQDs are dependent on the synthesizing conditions and have a honeycomb crystal lattice where six carbon atoms are arranged in the rings, and each atom is covalently bonded with adjacent three atoms and shows sp^2 hybridized property and delocalization of electrons in the π orbitals. These structural properties are responsible for enhancing electrical and optical properties[103]. Carbon-based GQDs endow several properties such as less toxicity, biocompatibility, photostability, semiconducting, electrical conductivity, dispersibility, and luminescence properties [104],[105]. GQDs have been employed in several characteristics such as nanofibers, composite molecularly imprinted polymers, aerogels, and others, etc. Applications of GQDs have explored remarkable areas, including sensors, bioimaging, antibacterial, photothermal therapy, and drug delivery [106],[107],[108].

1.12.1.2 Graphene and its Derivatives

Graphene is recognized as one of the thinnest materials that possess remarkable mechanical strength[109]. It has revolutionized different fields like membrane technology, sensors, catalysis, field-effect transistors, solar cells, supercapacitors, and batteries due to its striking characteristics[110]. It comprises 2D sp^2-hybridized carbon atom planar sheets that are tightly packed into a honeycomb-like structure[111]. In the literature survey, many graphene-related, as well as its derivatives, are reported, like reduced graphene oxide (rGO) and graphene oxide (GO) [112]. The surface area of graphene is much higher than fullerenes, graphite, and CNTs. Thus, graphene displays high sensitivity compared to its counterparts like MWCNTs[113]. Also, graphene exhibits two significant benefits over CNTs for electrochemical sensor development. Firstly, it is synthesized from graphite which is the economical route, and secondly, it does ‟tcarryanymetallicimpuritieslikeCNTs.It also delivers several benefits in developing the biosensors and sensors, such as p–p stacking interactions with molecules and biocompatibility. Numerous graphene-based nanomaterials are used to construct nanostructured bio-sensors.

Graphene Oxide and Reduced Graphene Oxide

Among the graphenes, graphene oxide (GO) is the most common and explored graphene-based material, which is used as a precursor for chemically modified graphene. The route for its synthesis is straightforward and cost-effective, as graphite powder is required for its facile synthesis, which is easily accessible[114]. The oxidized graphene, i.e., GO, consists of numerous oxygen-containing functional groups like carboxyl, hydroxyl, and epoxy groups. Due to these active functional groups, its functionalization with other nanostructured materials becomes easy for understanding many applications[115]. However, these oxygen-containing functional group slower their conductivity, leading to poor electrochemical performance.

This is because the inclusion of the oxygen functionalities in the case of GO breaks the conjugation present in graphene and restricts the p-electron system, ensuing reduced carrier concentration and mobility[116]. But, the electrochemical performance of a biosensor electrode can be improved considerably after removing oxygenated functional groups that are reduced through chemical, electrochemical, and thermal means[117]. The product form after reducing the functional moieties is recognized as rGO. TherGOis being employed for improving the performances of different electrochemical devices [118]. The incorporation of reduced graphene layers to the surface of the electrode can significantly enhance the surface sensitivity as well as electrocatalytic activity against the numerous analytes[119]. Due to these characteristic properties of rGO, it is being utilized in Chapter Third as one of the nanomaterials. Figure 1.6 depicts the structural difference between graphene, GO, and rGO.

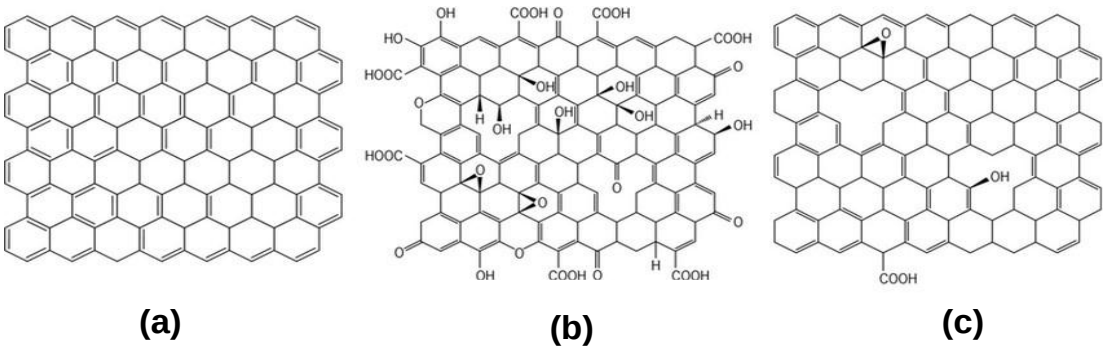

Figure 1.6: Structure of graphene, GO, and rGO. Reproduced from Ref. [120].

1.12.2 Metal Oxides

Metal oxide-based nanomaterials (MONMs) exhibit interesting properties such as catalytic efficiency, high surface-to-volume ratio, surface activity, higher isoelectric point (IEP), and strong adsorption ability. The MONMs such as Lanthanum oxide(La_2O_3), Zirconium oxide(ZnO), Manganese oxide (MnO_2), Titanium oxide(TiO_2), Cerium oxide(CeO_2), and Iron oxide(Fe_3O_4)are commonly used as a matrix for immobilizing biomolecules to fabricate electrochemical biosensors [121],[122]. The high surface-to-volume ratio of MONMs, due to nano-sized, provides a large surface area for interaction as a result of enhanced electrochemical properties of the material. MONMs consisting of high isoelectric points facilitate strong electrostatic interaction with biomolecules (antibodies and enzymes) of lower IEP [123],[124]. The chemical inertness and pH stability of MONMs ensure the reproducibility and stability of the electrochemical reaction. The presence of oxygen moieties on MONMs delivers a suitable microenvironment for the immobilization of biomolecules and encourages electron transport between the electrode surface and the active site of biomolecules [125],[126]. Such properties of MONMs facilitated higher adsorption capability, enhanced electron transfer kinetics, and enhanced biosensing properties of an electrochemical nanosensor. However, while developing highly sensitive, stable, and efficient electrochemical biosensors, transducer material must have high electrochemical activity, conductivity, functional groups, and structural and chemical stability. The physicochemical properties of metal oxides can be improved by chemical doping of appropriate elements or forming nanocomposites with a material having relatively high electrochemical behavior, electronic conductivity, and desired functional groups.

1.12.2.1 Metal and Metal Oxide Nanoparticles

As discussed, MONMs have attracted much interest and have been widely utilized as the platform for immobilizing biomolecules to develop electrochemical biosensors due to their interesting morphological, catalytic, biocompatible, and functional properties[127]. The electrochemical activity of the metal oxide depends on its electronic or ionic conductivity, which can be enhanced by the chemical doping of suitable elements[128]. The type of dopant also influences the structural properties like

phase, crystallite size, and crystallinity of synthesized oxide nanomaterials[129]. The chemical doping of elements such as rare earth metals magnesium, calcium, yttrium, and lanthanum or transitional metals is extensively considered an effective approach to enhance the surface properties, electron transport performance, and electrical and electrochemical properties of metal oxides [130],[131].

1.12.2.2 Metal Oxides-Carbon based Nanocomposites

The MONMs usually encounter the problem of aggregation and limited functional groups, which limit their biosensing properties. These issues associated with MONMs can be easily avoided by fabricating nanocomposites with a substrate material having higher conductivity and functional groups. It is found that the use of relatively high conductive substrate material with adequate available functional groups improves the electrochemical performance of the nanocomposite as well as the biosensing performance of the electrochemical nanobiosensor[132],[133]. In the past years, various MONMs-based nanocomposites have been engineered to improve the performance of MONMs for different applications, including photovoltaic devices, energy harvesting, photocatalysis and storage devices, electrochemical sensors, etc.[134]. The unique properties of carbon-based nanomaterials, such as high electrical conductivity, low toxicity, environmental-friendly, large surface area, excellent biocompatibility, and high mechanical strength, are considered the preferred material for the augmentation as well as functionalization of metal oxide in the nanocomposite[135],[136]. The metal oxides–carbon hybrid nanocomposites have been utilized to improve the mechanical stability of metal oxide by the process of reinforcing with carbon nanostructures[137], minimization of NPs aggregation [138], and functionalization of materials withimprovedconductivity[139]. Moreover, the hybrid interface of nanocomposite provides a higher electron transfer rate as compared to individual materials [140]. These advancements of MONMs- carbon nanocomposites provide a turning point for the improvement in the performance of MONMs-based electrochemical nano biosensors.

Keeping these in view, La_2O_3-based nanocomposites with carbon nanomaterials, such as reduced graphene oxide, have been synthesized through the hydrothermal method. These nanocomposites have been used to improve the biosensing performance of electrochemical immunosensors for CPX detection.

1.13 Synthesis of Nanomaterials

For synthesizing the nanomaterials, two main approaches are utilized: the bottom-up and top-down approaches (Figure 1.7)[141]. In the top-down approach, the bulk materials are broken down to form nanomaterials. This approach comprises electro-explosion, sputtering, etching, laser ablation, and mechanical milling. But this method suffers from a disadvantage in preparing nanomaterials with the desired particle shape and size[142]. On the other hand, the constructive or bottom-up approach comprises building material from an atom to clusters and finally to nanomaterial. Green synthesis, chemical reduction, pyrolysis, chemical vapor deposition, spinning, and sol-gel are the various methods included in this category for nanomaterials synthesis[143]. In this thesis work, a bottom-up approach has been used, especially green synthesis and chemical reduction, which are described below in detail.

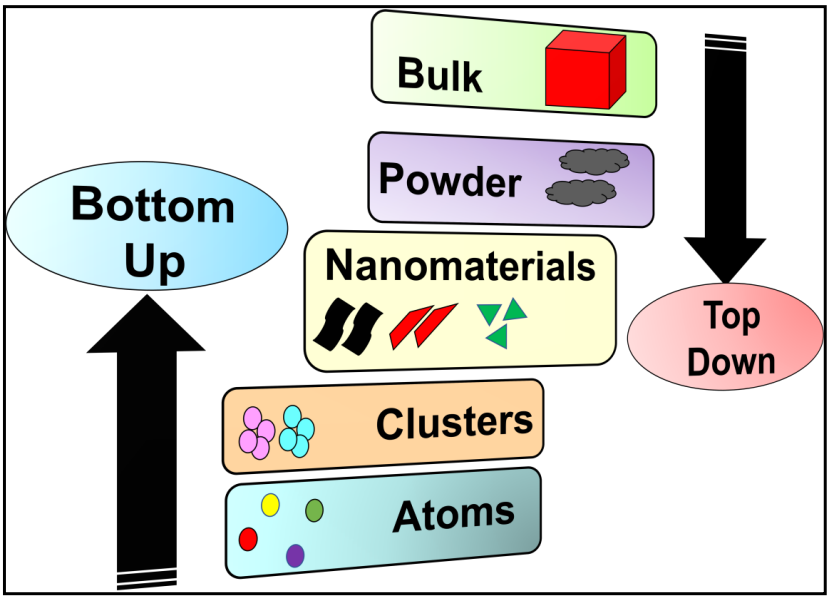

Figure 1.7: Types of approaches to synthesizing nanomaterials

1.13.1 Synthesis Route

Chemical Route

The synthesis of nanomaterials is of much interest to the scientific community because of their wide applications. Different reducing agents like Tollen's reagent, ascorbate, elemental hydrogen, sodium citrate, and sodium borohydride ($NaBH_4$) are employed for

reducing the metal ions in non-aqueous or aqueous solutions[144]. Also, stabilizing agents are utilized for preventing agglomeration and stabilizing the nanoparticles. However, nanomaterials synthesized by this method are costly and potentially hazardous to the environment involving perilous and toxic chemicals, which are accountable for numerous biological risks. Therefore, some alternative route must be selected, i.e., a green approach for synthesizing nanoparticles to overcome its challenges.

Green Route

Green synthesis is a chemical-free, environmentally friendly approach for preparing non-toxic and biodegradable nanoparticles and uses bacteria, plant extracts, fungi, etc.[145]. The progress of green synthesis in comparison to the chemical methods includes facile large-scale production, cost-effective, and environment-friendly benefits. Moreover, there is no requirement to use toxic chemicals, energy, pressure, and high temperature. The plant extracts, and other parts of plants are employed for synthesizing the different nanoparticles. The nanoparticles are reduced due to the phytochemicals existing in the plant extract or other parts of plants, such as quinones, alkaloids, organic acids, flavones, and more, which are naturally occurring reducing agents for nanoparticle synthesis. They not only act as reducing agents but also act as natural capping agents for the stabilization of nanoparticles.

1.13.2 Synthesis Methods

The development of a reproducible and easy synthesis method for the nanomaterial's preparation is of great significance. Exploring an appropriate synthesis method to produce nanomaterials with controlled particle size and morphology is important and necessary. In this research work, co-precipitation and hydrothermal were employed to synthesize nanomaterials for electrochemical and optical sensing applications. For synthesizing nanoparticles, majorly two methods were used, i.e., hydrothermal and co-precipitation, which are explained in brief.

Hydrothermal Method

A hydrothermal method is a technique to synthesize crystalline nanomaterials from a precursor's solution at vapor pressure and temperature $\leq$ 200°C. It works on the

phenomenon of solubility of insoluble materials under high temperature and high-pressure conditions, which cannot be attained under ambient conditions[146]. The hydrothermal apparatus contains a stainless-steel pressure vessel (autoclave) and a Teflon pot to keep the precursor solution inside the autoclave. The hydrothermal method has many advantages compared to other synthesis methods: facile, environmentally friendly, and one-step process to prepare nanomaterials, as well as having an early control on grain size and shape. This method has been employed in chapters third and fourth to synthesize the nanocomposite and carbon quantum dots.

Co-precipitation Method

Co-precipitation is a straightforward and cost-effective method for synthesizing nanomaterials with higher purity and better stoichiometric control[147]. In brief, it is a method comprising two or more soluble salts mixture of trivalent and divalent metal ions. To synthesize different nanoparticles using the co-precipitation method, water-soluble metal precursors (salts such as nitrates and chlorides) are usually co-precipitated from a basic precipitating agent as hydroxide. The water-soluble metal precursors make an acidic aqueous solution, and the introduction of a precipitating agent makes the solution pH neutral. Washing of the resulting precipitant is needed to eliminate unwanted side products that can be done using centrifugation or filtration to separate the solvent and further kept for drying. This method is advantageous as it enables the direct synthesis of homogeneous nanomaterials of small sizes having uniform size distribution. In the current thesis work, this method is being adopted for synthesizing nanoparticles and nanocomposite in chapter third.

1.14 Literature Review

In the upcoming decades, antibiotic resistance will become a potential threat to the world. This is occurring worldwide, and globalization is catalyzing this process. At this time, biosensors are the best method that is used most frequently to detect these drugs. To detect antibiotics in the food items such as milk samples, there are various researchers have developed several nanomaterials-based electrochemical biosensors and optical sensors to detect antibiotics. In the present thesis work, CPX antibiotics were selected for making electrochemical biosensors and optical sensors. To detect CPX in

various samples, researchers have developed several nanomaterials-based electrochemical biosensors. Gill et al.achieved a one-pot synthesis of silver nanoparticles modified with beta-cyclodextrin for very sensitive CPX detection in water from runoff and sheep serum. The fabricated immunosensors showed a detection range from 0.1–50 nM with a LOD of 0.028 nM[148].In another study, Chauhan et al. developed a very specific electrochemical identification method for CPX in human serum utilizing reduced graphene oxide and poly(phenol red) modified glassy carbon electrodes. The fabricated electrode exhibits two linear ranges of 0.002-0.05 μM and 0.05-400 μM, as well as sensitivities of 516.41 μA μM^{-1} cm^{-2} and 0.239μ A M1 cm^{-2}, respectively, and the limit of detection is 2 nM[149]. N.R. Jalal et al.designed Polyethylenimine@Fe_3O_4@carbon nanotubes nanocomposite as a modification in glassy carbon electrodes for efficient detection of CPX antibiotics in clinical samples. The designed electrode has a low limit of detection (LOD) of 3.0 nM and a linear range of 0.03-70.0 mM.[150]. X. Fang et al. developed nanocomposites that are used for electrochemical sensing of CPX detection in water samples with reduced graphene oxide and Zr(IV)-based metal-organic frameworks. The developed NH_2-UiO-66/RGO sensor has a linear detection range of 0.02 to 1μM and sensitivity of 10.86μA μM^{-1}, which allows it to detect very small quantities of CPX with a 6.67 nM LOD[151].M. Mahmoudpouret al., developed Using nanogold-functionalized poly(amidoamine) dendrimer and reduced graphene oxide, efficient sensing of CPX antibiotic traces in unprocessed milk samples: An novel APTA-platform for antimicrobial electroanalysis. The developed electrode shows a very low limit of detection is 1 mM with a 1 mM to 1 nM linear range[152]. Q. Zhu et al. developed a highly sophisticated electrochemical apta sensor that improved the detection performance of apta sensors based on gold nanoparticle/COF composites, with very low detection of limit (LOD) 2.34 fM with a linear range from 1.0×10^{-5} to 0.5 ng mL^{-1} [153].Giroudetal.established Impedimetric Immunosensor for Label-Free CPX detection in the picomolar range based on a polypyrrole antibiotic model film. The developed electrode shows a good limit of detection (LOD) of 3.0 pM with a linear range of 1×10^{-12} to 1×10^{-6} g mL^{-1}[154]. Xu et al. developed Graphitic carbon nitride/BiOCl composites for sensitive photoelectrochemical detection of CPX. The developed electrode shows a good range of linearity is 0.5–1840 nMandaverylow limit of detection (LOD) is 0.2 nM[155].To detect CPX, researchers have developed several

carbon quantum-based optical sensors. Yuphintharakun et al. developed an optical sensor for highly precise and sensitive determination of CPX in chicken samples, milk samples, and standard buffer with the help of nanocomposite that is synthesized by carboxylic functionalized multiwall carbon nanotubes and quantum dots. This optical sensor shows a very low limit of detection of 0.066 $\mu g\,L^{-1}$ with two different linear ranges of 0.10–1.0 $\mu g\,L^{-1}$ and 1.0–100.0 μg^{L-1}[156]. Q.-D. Huang et al. developed a novel luminescent optical fiber sensor based on a replaceable molecularly imprinted nanomaterial composite hydrogel detector has been developed for the highly specific identification of CPXantibiotics.The developed optical sensor shows a very good linear range of 1mM10–500 μM and a very low limit of detection (LOD) of 6.86 μM[157]. Lu et al. developed an optical sensor determination of CPX at ppm level in urine by Eu3+ functionalized Ga-MOF integrated with logic gate operation. The developed optical sensor shows a low detection limit (LOD) of 0.301 μM with a goodlinear range of 0.009–1.508 mM[158]. Pawar, et al., developed Selective CPX antibiotic detection by fluorescent siderophore pyoverdin. The developed optical sensor shows a linear range of 0–5 μM with a very low limit of detection (LOD) of 7.13 μM[159].A. Segundo et al. developed fully-Programmable Synthesis of Sucrose-Mediated Gold Nanoparticles for the Detection of CPX. The developed optical sensor shows a linear range of 50−150 μM with a low detection limit (LOD) of 12 μM[160].

1.15 References

[1] S. Mostafa, M. El-Sadek, and E. A. Alla, "Spectrophotometric determination of CPX, enrofloxacin, and pefloxacin through charge transfer complex formation," *J. Pharm. Biomed. Anal.*, vol. 27, no. 1–2, pp. 133–142, 2002.

[2] H. Y. Ji, D. W. Jeong, Y. H. Kim, H.-H. Kim, D.-R. Sohn, and H. S. Lee, "Hydrophilic interaction liquid chromatography–tandem mass spectrometry for the determination of levofloxacin in human plasma," *J. Pharm. Biomed. Anal.*, vol. 41, no. 2, pp. 622–627, 2006.

[3] G. Carlucci, "Analysis of fluoroquinolones in biological fluids by high-performance liquid chromatography," *J. Chromatogr. A*, vol. 812, no. 1–2, pp. 343–367, 1998.

[4] G. G. Snitkoff, D. W. Grabe, R. Holt, and G. R. Bailie, "Development of an Immunoassay for Monitoring the Levels of CPX Patient Samples," *J. Immunoass. Immunochem.*, vol. 19, no. 4, pp. 227–238, 1998.

[5] H.-W. Sun, L.-Q. Li, and X.-Y. Chen, "Flow-injection enhanced chemiluminescence method for determination of CPX in pharmaceutical preparations and biological fluids," *Anal. Bioanal. Chem.*, vol. 384, pp. 1314–1319, 2006.

[6] R. H. O. Montes, M. C. Marra, M. M. Rodrigues, E. M. Richter, and R. A. A. Muñoz, "Fast determination of CPX by batch injection analysis with amperometric detection and capillary electrophoresis with capacitively coupled contactless conductivity detection," *Electroanalysis*, vol. 26, no. 2, pp. 432–438, 2014.

[7] A. Radi, M. A. El Ries, and S. Kandil, "Electrochemical study of the interaction of levofloxacin with DNA," *Anal. Chim. Acta*, vol. 495, no. 1–2, pp. 61–67, 2003.

[8] A. A. Ensafi, A. R. Allafchian, and R. Mohammadzadeh, "Characterization of MgFe2O4 nanoparticles as a novel electrochemical sensor: application for the voltammetric determination of CPX," *Anal. Sci.*, vol. 28, no. 7, pp. 705–710, 2012.

[9] M. Kumar and J. Bharti, "Isolation and Characterization of Multi Drug Resistant Escherichia coli Isolated from Urinary Tract Infected Patients".

[10] M. K. Sudhakar, S. T. Nakhate, and M. L. D. Hingane, "ANTI BIOTIC RESISTANNE," 2021.

[11] T. Britannica, "Editors of encyclopaedia," *Argon. Encycl. Br.*, 2020.

[12] N. Woodford, J. F. Turton, and D. M. Livermore, "Multiresistant Gram-negative bacteria: the role of high-risk clones in the dissemination of antibiotic resistance," *FEMS Microbiol. Rev.*, vol. 35, no. 5, pp. 736–755, 2011.

[13] A.-P. Magiorakos *et al.*, "Multidrug-resistant, extensively drug-resistant and pandrug-resistant bacteria: an international expert proposal for interim standard definitions for acquired resistance," *Clin. Microbiol. Infect.*, vol. 18, no. 3, pp. 268–281, 2012.

[14] H. Hanberger *et al.*, "Increased mortality associated with meticillin-resistant Staphylococcus aureus (MRSA) infection in the Intensive Care Unit: results from the EPIC II study," *Int. J. Antimicrob. Agents*, vol. 38, no. 4, pp. 331–335, 2011.

[15] A. Talebi Bezmin Abadi, A. A. Rizvanov, T. Haertlé, and N. L. Blatt, "World Health Organization report: current crisis of antibiotic resistance," *Bionanoscience*, vol. 9, pp. 778–788, 2019.

[16] C. L. Ventola, "The antibiotic resistance crisis: part 1: causes and threats," *Pharm. Ther.*, vol. 40, no. 4, p. 277, 2015.

[17] Y. Ben, C. Fu, M. Hu, L. Liu, M. H. Wong, and C. Zheng, "Human health risk assessment of antibiotic resistance associated with antibiotic residues in the environment: A review," *Environ. Res.*, vol. 169, pp. 483–493, 2019.

[18] P. M. Bennett, "Plasmid encoded antibiotic resistance: acquisition and transfer of antibiotic resistance genes in bacteria," *Br. J. Pharmacol.*, vol. 153, no. S1, pp. S347–S357, 2008.

[19] H. S. Hurd and S. Malladi, "A stochastic assessment of the public health risks of the use of macrolide antibiotics in food animals," *Risk Anal. An Int. J.*, vol. 28, no. 3, pp. 695–710, 2008.

[20] K. M. Shea, "Antibiotic resistance: what is the impact of agricultural uses of antibiotics on children's health?," *Pediatrics*, vol. 112, no. Supplement_1, pp. 253–258, 2003.

[21] A. Cassini *et al.*, "Attributable deaths and disability-adjusted life-years caused by infections with antibiotic-resistant bacteria in the EU and the European Economic Area in 2015: a population-level modelling analysis," *Lancet Infect. Dis.*, vol. 19, no. 1, pp. 56–66, 2019.

[22] E. Nature, "The antibiotic alarm," *Nature*, vol. 495, no. 7440, p. 141, 2013.

[23] S. L. Solomon and K. B. Oliver, "Antibiotic resistance threats in the United States: stepping back from the brink," *Am. Fam. Physician*, vol. 89, no. 12, pp. 938–941, 2014.

[24] C.-E. Luyt, N. Bréchot, J.-L. Trouillet, and J. Chastre, "Antibiotic stewardship in the intensive care unit," *Crit. care*, vol. 18, pp. 1–12, 2014.

[25] B. D. Lushniak, "Antibiotic resistance: a public health crisis," *Public Health Rep.*, vol. 129, no. 4, pp. 314–316, 2014.

[26] L. M. Weiner *et al.*, "Antimicrobial-resistant pathogens associated with healthcare-associated infections: summary of data reported to the National Healthcare Safety Network at the Centers for Disease Control and Prevention, 2011–2014," *Infect. Control Hosp. Epidemiol.*, vol. 37, no. 11, pp. 1288–1301, 2016.

[27] B. Spellberg and D. N. Gilbert, "The future of antibiotics and resistance: a tribute to a career of leadership by John Bartlett," *Clin. Infect. Dis.*, vol. 59, no. suppl_2, pp. S71–S75, 2014.

[28] C. A. Michael, D. Dominey-Howes, and M. Labbate, "The antimicrobial resistance crisis: causes, consequences, and management," *Front. public Heal.*, vol. 2, p. 145, 2014.

[29] Z. Golkar, O. Bagasra, and D. G. Pace, "Bacteriophage therapy: a potential solution for the antibiotic resistance crisis," *J. Infect. Dev. Ctries.*, vol. 8, no. 02, pp. 129–136, 2014.

[30] J. G. Bartlett, D. N. Gilbert, and B. Spellberg, "Seven ways to preserve the miracle of antibiotics," *Clin. Infect. Dis.*, vol. 56, no. 10, pp. 1445–1450, 2013.

[31] I. M. Gould and A. M. Bal, "New antibiotic agents in the pipeline and how they can help overcome microbial resistance," *Virulence*, vol. 4, no. 2, pp. 185–191, 2013.

[32] S. M. AMIN and F. K. IBRAHIM, "TOXIC KINETICS OF CPX IN MICE," *ةيجولونكتلاو ةيقيبيطتلاو ةفرصلا موعلل سماخلا يلودلا يملعلا رمتؤملا*, p. 117.

[33] M. C. Dodd, A. D. Shah, U. von Gunten, and C.-H. Huang, "Interactions of fluoroquinolone antibacterial agents with aqueous chlorine: reaction kinetics, mechanisms, and transformation pathways," *Environ. Sci. Technol.*, vol. 39, no. 18, pp. 7065–7076, 2005.

[34] F. Toldrá and M. Reig, "Methods for rapid detection of chemical and veterinary drug residues in animal foods," *Trends Food Sci. Technol.*, vol. 17, no. 9, pp. 482–489, 2006.

[35] K. Bush *et al.*, "Tackling antibiotic resistance," *Nat. Rev. Microbiol.*, vol. 9, no. 12, pp. 894–896, 2011.

[36] C. Blasco, A. Di Corcia, and Y. Picó, "Determination of tetracyclines in multi-specie animal tissues by pressurized liquid extraction and liquid chromatography–tandem mass spectrometry," *Food Chem.*, vol. 116, no. 4, pp. 1005–1012, 2009.

[37] X. Guo *et al.*, "Fluorescent carbon dots based sensing system for detection of enrofloxacin in water solutions," *Spectrochim. Acta Part A Mol. Biomol. Spectrosc.*, vol. 219, pp. 15–22, 2019.

[38] J. Calbo, M. J. Golomb, and A. Walsh, "Redox-active metal–organic frameworks for energy conversion and storage," *J. Mater. Chem. A*, vol. 7, no. 28, pp. 16571–16597, 2019.

[39] Ü. Kökçam-Demir *et al.*, "Coordinatively unsaturated metal sites (open metal sites) in metal–organic frameworks: design and applications," *Chem. Soc. Rev.*, vol. 49, no. 9, pp. 2751–2798, 2020.

[40] P. Bhalla and N. Singh, "Generalized Drude scattering rate from the memory function formalism: an independent verification of the Sharapov-Carbotte result," *Eur. Phys. J. B*, vol. 89, pp. 1–8, 2016.

[41] C. Zhu, G. Yang, H. Li, D. Du, and Y. Lin, "Electrochemical sensors and biosensors based on nanomaterials and nanostructures," *Anal. Chem.*, vol. 87, no. 1, pp. 230–249, 2015.

[42] L. C. Clark, "The control and monitoring of blood and tissue oxygen," *Trans. Amer. Soc. Anat. Int. Org*, vol. 2, pp. 41–48, 1956.

[43] L. C. Clark Jr and C. Lyons, "Electrode systems for continuous monitoring in cardiovascular surgery," *Ann. N. Y. Acad. Sci.*, vol. 102, no. 1, pp. 29–45, 1962.

[44] E.-H. Yoo and S.-Y. Lee, "Glucose biosensors: an overview of use in clinical practice," *Sensors*, vol. 10, no. 5, pp. 4558–4576, 2010.

[45] M. T. Giardi, E. V Piletska, and M. Mascini, "A brief story of biosensor technology," *Biotechnol. Appl. Photosynth. Proteins Biochips, Biosens. Biodevices*, pp. 4–10, 2006.

[46] M. S. Thakur and K. V Ragavan, "Biosensors in food processing," *J. Food Sci. Technol.*, vol. 50, pp. 625–641, 2013.

[47] D. Barceló, *Emerging organic pollutants in waste waters and sludge*. Springer Science & Business Media, 2004.

[48] A. H. Clemens, P. H. Chang, and R. W. Myers, "De Diabetologie de L'Hotel-Dieu," *Proc Journees Ann, Paris*, 1976.

[49] B. Liedberg, C. Nylander, and I. Lunström, "Surface plasmon resonance for gas detection and biosensing," *Sensors and actuators*, vol. 4, pp. 299–304, 1983.

[50] A. P. F. Turner, "Biosensors: sense and sensibility," *Chem. Soc. Rev.*, vol. 42, no. 8, pp. 3184–3196, 2013.

[51] S. Neethirajan, S. K. Tuteja, S.-T. Huang, and D. Kelton, "Recent advancement in biosensors technology for animal and livestock health management," *Biosens. Bioelectron.*, vol. 98, pp. 398–407, 2017.

[52] B. Srinivasan and S. Tung, "Development and applications of portable biosensors," *J. Lab. Autom.*, vol. 20, no. 4, pp. 365–389, 2015.

[53] Y. Shao, J. Wang, H. Wu, J. Liu, I. A. Aksay, and Y. Lin, "Graphene based electrochemical sensors and biosensors: a review," *Electroanal. An Int. J. Devoted to Fundam. Pract. Asp. Electroanal.*, vol. 22, no. 10, pp. 1027–1036, 2010.

[54] M. Schaechter, N. C. Engleberg, V. J. DiRita, and T. S. Dermody, *Schaechter's mechanisms of microbial disease*. Lippincott Williams & Wilkins, 2012.

[55] H. W. Schroeder Jr and L. Cavacini, "Structure and function of immunoglobulins," *J. Allergy Clin. Immunol.*, vol. 125, no. 2, pp. S41–S52, 2010.

[56] P. J. Delves and I. M. Roitt, *Encyclopedia of immunology*. Academic Press, 1998.

[57] W. Putzbach and N. J. Ronkainen, "Immobilization techniques in the fabrication of nanomaterial-based electrochemical biosensors: A review," *Sensors*, vol. 13, no. 4, pp. 4811–4840, 2013.

[58] L. Barthelmebs, R. Carpentier, and R. Rouillon, "Physical and chemical immobilization methods of photosynthetic materials," *Photosynth. Res. Protoc.*, pp. 247–256, 2011.

[59] Y. Zhang *et al.*, "Electrochemical sensor for bisphenol A based on magnetic nanoparticles decorated reduced graphene oxide," *Talanta*, vol. 107, pp. 211–218, 2013.

[60] D. Patiño-Ruiz, L. Sánchez-Botero, L. Tejeda-Benitez, J. Hinestroza, and A. Herrera, "Green synthesis of iron oxide nanoparticles using Cymbopogon citratus extract and sodium carbonate salt: Nanotoxicological considerations for potential environmental applications," *Environ. Nanotechnology, Monit. Manag.*, vol. 14, p. 100377, 2020.

[61] K. P. O. Mahesh, I. Shown, L.-C. Chen, K.-H. Chen, and Y. Tai, "Flexible sensor for dopamine detection fabricated by the direct growth of α-Fe2O3 nanoparticles on carbon cloth," *Appl. Surf. Sci.*, vol. 427, pp. 387–395, 2018.

[62] J. Su, M. Cao, L. Ren, and C. Hu, "Fe3O4–graphene nanocomposites with improved lithium storage and magnetism properties," *J. Phys. Chem. C*, vol. 115, no. 30, pp. 14469–14477, 2011.

[63] P. J. Sephra, P. Baraneedharan, M. Sivakumar, T. D. Thangadurai, and K. Nehru, "In situ growth of hexagonal-shaped α-Fe 2 O 3 nanostructures over few layered graphene by hydrothermal method and their electrochemical performance," *J. Mater. Sci. Mater. Electron.*, vol. 29, pp. 6898–6908, 2018.

[64] S. Nag, A. Roychowdhury, D. Das, and S. Mukherjee, "Synthesis of α-Fe2O3-functionalised graphene oxide nanocomposite by a facile low temperature method and study of its magnetic and hyperfine properties," *Mater. Res. Bull.*, vol. 74, pp. 109–116, 2016.

[65] A. K. Yadav, T. K. Dhiman, G. Lakshmi, A. N. Berlina, and P. R. Solanki, "A highly sensitive label-free amperometric biosensor for norfloxacin detection based on chitosan-yttria nanocomposite," *Int. J. Biol. Macromol.*, vol. 151, pp. 566–575, 2020.

[66] G. Lakshmi, A. K. Yadav, N. Mehlawat, R. Jalandra, P. R. Solanki, and A. Kumar, "Gut microbiota derived trimethylamine N-oxide (TMAO) detection through molecularly imprinted polymer based sensor," *Sci. Rep.*, vol. 11, no. 1, pp. 1–14, 2021.

[67] X. Cheng, S. B. Lowe, P. J. Reece, and J. J. Gooding, "Colloidal silicon quantum dots: from preparation to the modification of self-assembled monolayers (SAMs) for bio-applications," *Chem. Soc. Rev.*, vol. 43, no. 8, pp. 2680–2700, 2014.

[68] W. Zhou, D. T. Schwartz, and F. Baneyx, "Single-pot biofabrication of zinc sulfide immuno-quantum dots," *J. Am. Chem. Soc.*, vol. 132, no. 13, pp. 4731–4738, 2010.

[69] Z.-B. Li, W. Cai, and X. Chen, "Semiconductor quantum dots for in vivo imaging," *J. Nanosci. Nanotechnol.*, vol. 7, no. 8, pp. 2567–2581, 2007.

[70] P. Walter *et al.*, "Early use of PbS nanotechnology for an ancient hair dyeing formula," *Nano Lett.*, vol. 6, no. 10, pp. 2215–2219, 2006.

[71] A. P. Alivisatos, "Perspectives on the physical chemistry of semiconductor nanocrystals," *J. Phys. Chem.*, vol. 100, no. 31, pp. 13226–13239, 1996.

[72] D. M. Kroupa *et al.*, "Synthesis and spectroscopy of silver-doped PbSe quantum dots," *J. Am. Chem. Soc.*, vol. 139, no. 30, pp. 10382–10394, 2017.

[73] L. Brus, "Electronic wave functions in semiconductor clusters: experiment and theory," *J. Phys. Chem.*, vol. 90, no. 12, pp. 2555–2560, 1986.

[74] W. W. Yu, L. Qu, W. Guo, and X. Peng, "Experimental determination of the extinction coefficient of CdTe, CdSe, and CdS nanocrystals," *Chem. Mater.*, vol. 15, no. 14, pp. 2854–2860, 2003.

[75] D. Rueda and N. G. Walter, "Fluorescent energy transfer readout of an aptazyme-based biosensor," *Fluoresc. Energy Transf. Nucleic Acid Probes Des. Protoc.*, pp. 289–310, 2006.

[76] M. Dahan *et al.*, "Time-gated biological imaging by use of colloidal quantum dots," *Opt. Lett.*, vol. 26, no. 11, pp. 825–827, 2001.

[77] S. N. Baker and G. A. Baker, "Luminescent carbon nanodots: emergent nanolights," *Angew. Chemie Int. Ed.*, vol. 49, no. 38, pp. 6726–6744, 2010.

[78] N. Murugan and A. K. Sundramoorthy, "Green synthesis of fluorescent carbon dots from Borassus flabellifer flowers for label-free highly selective and sensitive detection of Fe 3+ ions," *New J. Chem.*, vol. 42, no. 16, pp. 13297–13307, 2018.

[79] A. Sachdev and P. Gopinath, "Green synthesis of multifunctional carbon dots from coriander leaves and their potential application as antioxidants, sensors and bioimaging agents," *Analyst*, vol. 140, no. 12, pp. 4260–4269, 2015.

[80] J. Shen, Y. Zhu, X. Yang, and C. Li, "Graphene quantum dots: emergent nanolights for bioimaging, sensors, catalysis and photovoltaic devices," *Chem. Commun.*, vol. 48, no. 31, pp. 3686–3699, 2012.

[81] L. Shi *et al.*, "Naked oats-derived dual-emission carbon nanodots for ratiometric sensing and cellular imaging," *Sensors Actuators B Chem.*, vol. 210, pp. 533–541, 2015.

[82] Z. Fan, S. Li, F. Yuan, and L. Fan, "Fluorescent graphene quantum dots for biosensing and bioimaging," *RSC Adv.*, vol. 5, no. 25, pp. 19773–19789, 2015.

[83] D. Qu and Z. Sun, "The formation mechanism and fluorophores of carbon dots synthesized via a bottom-up route," *Mater. Chem. Front.*, vol. 4, no. 2, pp. 400–420, 2020.

[84] A. Prasannan and T. Imae, "One-pot synthesis of fluorescent carbon dots from orange waste peels," *Ind. Eng. Chem. Res.*, vol. 52, no. 44, pp. 15673–15678, 2013.

[85] S. Pandey *et al.*, "Synthesis of mesoporous silica oxide/C-dot complex (meso-SiO 2/C-dots) using pyrolysed rice husk and its application in bioimaging," *RSC Adv.*, vol. 4, no. 3, pp. 1174–1179, 2014.

[86] M. Xue, M. Zou, J. Zhao, Z. Zhan, and S. Zhao, "Green preparation of fluorescent carbon dots from lychee seeds and their application for the selective detection of methylene blue and imaging in living cells," *J. Mater. Chem. B*, vol. 3, no. 33, pp. 6783–6789, 2015.

[87] S. Sahu, B. Behera, T. K. Maiti, and S. Mohapatra, "Simple one-step synthesis of highly luminescent carbon dots from orange juice: application as excellent bio-imaging agents," *Chem. Commun.*, vol. 48, no. 70, pp. 8835–8837, 2012.

[88] M. Saxena and S. Sarkar, "Synthesis of carbogenic nanosphere from peanut skin," *Diam. Relat. Mater.*, vol. 24, pp. 11–14, 2012.

[89] J. Zhou, Z. Sheng, H. Han, M. Zou, and C. Li, "Facile synthesis of fluorescent carbon dots using watermelon peel as a carbon source," *Mater. Lett.*, vol. 66, no. 1, pp. 222–224, 2012.

[90] J. Xu, T. Lai, Z. Feng, X. Weng, and C. Huang, "Formation of fluorescent carbon nanodots from kitchen wastes and their application for detection of Fe3+," *Luminescence*, vol. 30, no. 4, pp. 420–424, 2015.

[91] H. Miao, L. Wang, Y. Zhuo, Z. Zhou, and X. Yang, "Label-free fluorimetric detection of CEA using carbon dots derived from tomato juice," *Biosens. Bioelectron.*, vol. 86, pp. 83–89, 2016.

[92] Y. Feng, D. Zhong, H. Miao, and X. Yang, "Carbon dots derived from rose flowers for tetracycline sensing," *Talanta*, vol. 140, pp. 128–133, 2015.

[93] H. Huang, Y. Xu, C.-J. Tang, J.-R. Chen, A.-J. Wang, and J.-J. Feng, "Facile and green synthesis of photoluminescent carbon nanoparticles for cellular imaging," *New J. Chem.*, vol. 38, no. 2, pp. 784–789, 2014.

[94] A. Barati, M. Shamsipur, E. Arkan, L. Hosseinzadeh, and H. Abdollahi, "Synthesis of biocompatible and highly photoluminescent nitrogen doped carbon dots from lime: analytical applications and optimization using response surface methodology," *Mater. Sci. Eng. C*, vol. 47, pp. 325–332, 2015.

[95] L. Wang and H. S. Zhou, "Green synthesis of luminescent nitrogen-doped carbon dots from milk and its imaging application," *Anal. Chem.*, vol. 86, no. 18, pp. 8902–8905, 2014.

[96] V. N. Mehta, S. Jha, R. K. Singhal, and S. K. Kailasa, "Preparation of multicolor emitting carbon dots for HeLa cell imaging," *New J. Chem.*, vol. 38, no. 12, pp. 6152–6160, 2014.

[97] L. Zhu, Y. Yin, C.-F. Wang, and S. Chen, "Plant leaf-derived fluorescent carbon dots for sensing, patterning and coding," *J. Mater. Chem. C*, vol. 1, no. 32, pp. 4925–4932, 2013.

[98] P. Wang, R.-B. Zhong, M. Yuan, P. Gong, X.-M. Zhao, and F. Zhang, "Mercury (II) detection by water-soluble photoluminescent ultra-small carbon dots synthesized from cherry tomatoes," *Nucl. Sci. Tech.*, vol. 27, pp. 1–5, 2016.

[99] S. Y. Park *et al.*, "Photoluminescent green carbon nanodots from food-waste-derived sources: large-scale synthesis, properties, and biomedical applications," *ACS Appl. Mater. Interfaces*, vol. 6, no. 5, pp. 3365–3370, 2014.

[100] M. H. M. Facure, R. Schneider, L. A. Mercante, and D. S. Correa, "A review on graphene quantum dots and their nanocomposites: from laboratory synthesis towards agricultural and environmental applications," *Environ. Sci. Nano*, vol. 7, no. 12, pp. 3710–3734, 2020.

[101] H. Sun, L. Wu, W. Wei, and X. Qu, "Recent advances in graphene quantum dots for sensing," *Mater. today*, vol. 16, no. 11, pp. 433–442, 2013.

[102] E. Haque *et al.*, "Recent advances in graphene quantum dots: synthesis, properties, and applications," *Small Methods*, vol. 2, no. 10, p. 1800050, 2018.

[103] T. Ohta, A. Bostwick, T. Seyller, K. Horn, and E. Rotenberg, "Controlling the electronic structure of bilayer graphene," *Science (80-.).*, vol. 313, no. 5789, pp. 951–954, 2006.

[104] Y. Chong *et al.*, "The in vitro and in vivo toxicity of graphene quantum dots," *Biomaterials*, vol. 35, no. 19, pp. 5041–5048, 2014.

[105] D. Pan *et al.*, "Cutting sp 2 clusters in graphene sheets into colloidal graphene quantum dots with strong green fluorescence," *J. Mater. Chem.*, vol. 22, no. 8, pp. 3314–3318, 2012.

[106] C. Zhao *et al.*, "Synthesis of graphene quantum dots and their applications in drug delivery," *J. Nanobiotechnology*, vol. 18, pp. 1–32, 2020.

[107] J. Ju and W. Chen, "Graphene quantum dots as fluorescence probes for sensing metal ions: synthesis and applications," *Curr. Org. Chem.*, vol. 19, no. 12, pp. 1150–1162, 2015.

[108] W.-S. Kuo *et al.*, "Graphene quantum dots with nitrogen-doped content dependence for highly efficient dual-modality photodynamic antimicrobial therapy and bioimaging," *Biomaterials*, vol. 120, pp. 185–194, 2017.

[109] A. K. Geim, "Graphene: status and prospects," *Science (80-.).*, vol. 324, no. 5934, pp. 1530–1534, 2009.

[110] G. K. Dalapati *et al.*, "Nanoengineered advanced materials for enabling hydrogen economy: functionalized graphene–incorporated cupric oxide catalyst for efficient solar hydrogen production," *Glob. Challenges*, vol. 4, no. 3, p. 1900087, 2020.

[111] A. K. Geim, "KS Novoselov The rise of graphene," *Nat. Mater.*, vol. 6, no. 3, pp. 183–191, 2007.

[112] N. Baig, A.-N. Kawde, and M. Ibrahim, "Efficient ionic medium supported reduced graphene oxide-based sensor for selective sensing of dopamine," *Mater. Adv.*, vol. 1, no. 4, pp. 783–793, 2020.

[113] A. M. Youssef, M. E. El-Naggar, F. M. Malhat, and H. M. El Sharkawi, "Efficient removal of pesticides and heavy metals from wastewater and the antimicrobial activity of f-MWCNTs/PVA nanocomposite film," *J. Clean. Prod.*, vol. 206, pp. 315–325, 2019.

[114] D. Konios, M. M. Stylianakis, E. Stratakis, and E. Kymakis, "Dispersion behaviour of graphene oxide and reduced graphene oxide," *J. Colloid Interface Sci.*, vol. 430, pp. 108–112, 2014.

[115] J. Chen *et al.*, "Water-enhanced oxidation of graphite to graphene oxide with controlled species of oxygenated groups," *Chem. Sci.*, vol. 7, no. 3, pp. 1874–1881, 2016.

[116] S. Pei and H.-M. Cheng, "The reduction of graphene oxide," *Carbon N. Y.*, vol. 50, no. 9, pp. 3210–3228, 2012.

[117] K. K. H. De Silva, H.-H. Huang, R. K. Joshi, and M. Yoshimura, "Chemical reduction of graphene oxide using green reductants," *Carbon N. Y.*, vol. 119, pp. 190–199, 2017.

[118] N. Baig, A. Kawde, and M. Ibrahim, "A new approach of controlled single step in situ fabrication of graphene composite sensor for simultaneous sensing of small biomolecules in human urine," *ChemistrySelect*, vol. 4, no. 5, pp. 1640–1649, 2019.

[119] N. Baig and A.-N. Kawde, "A novel, fast and cost effective graphene-modified graphite pencil electrode for trace quantification of l-tyrosine," *Anal. Methods*, vol. 7, no. 22, pp. 9535–9541, 2015.

[120] K. Tadyszak, J. K. Wychowaniec, and J. Litowczenko, "Biomedical applications of graphene-based structures," *Nanomaterials*, vol. 8, no. 11, p. 944, 2018.

[121] P. R. Solanki, A. Kaushik, V. V Agrawal, and B. D. Malhotra, "Nanostructured metal oxide-based biosensors," *NPG Asia Mater.*, vol. 3, no. 1, pp. 17–24, 2011.

[122] P. F. Manicone, P. R. Iommetti, and L. Raffaelli, "An overview of zirconia ceramics: basic properties and clinical applications," *J. Dent.*, vol. 35, no. 11, pp. 819–826, 2007.

[123] F. Zhang *et al.*, "Immobilization of uricase on ZnO nanorods for a reagentless uric acid biosensor," *Anal. Chim. Acta*, vol. 519, no. 2, pp. 155–160, 2004.

[124] S. A. Kumar and S. Chen, "Nanostructured zinc oxide particles in chemically modified electrodes for biosensor applications," *Anal. Lett.*, vol. 41, no. 2, pp. 141–158, 2008.

[125] M. M. Rahman, A. J. Saleh Ahammad, J.-H. Jin, S. J. Ahn, and J.-J. Lee, "A comprehensive review of glucose biosensors based on nanostructured metal-oxides," *Sensors*, vol. 10, no. 5, pp. 4855–4886, 2010.

[126] Y.-B. Hahn, R. Ahmad, and N. Tripathy, "Chemical and biological sensors based on metal oxide nanostructures," *Chem. Commun.*, vol. 48, no. 84, pp. 10369–10385, 2012.

[127] H. Karimi-Maleh, S. Rostami, V. K. Gupta, and M. Fouladgar, "Evaluation of ZnO nanoparticle ionic liquid composite as a voltammetric sensing of isoprenaline in the presence of aspirin for liquid phase determination," *J. Mol. Liq.*, vol. 201, pp. 102–107, 2015.

[128] S. Azad *et al.*, "Nanoscale effects on ion conductance of layer-by-layer structures of gadolinia-doped ceria and zirconia," *Appl. Phys. Lett.*, vol. 86, no. 13, p. 131906, 2005.

[129] P. Li, I. Chen, and J. E. Penner-Hahn, "Effect of dopants on zirconia stabilization—an X-ray absorption study: I, trivalent dopants," *J. Am. Ceram. Soc.*, vol. 77, no. 1, pp. 118–128, 1994.

[130] N. Lavanya, S. Radhakrishnan, C. Sekar, M. Navaneethan, and Y. Hayakawa, "Fabrication of Cr doped SnO 2 nanoparticles based biosensor for the selective determination of riboflavin in pharmaceuticals," *Analyst*, vol. 138, no. 7, pp. 2061–2067, 2013.

[131] S. D. Bukkitgar, N. P. Shetti, R. M. Kulkarni, and M. R. Doddamani, "Electro-oxidation of nimesulide at 5% barium-doped zinc oxide nanoparticle modified glassy carbon electrode," *J. Electroanal. Chem.*, vol. 762, pp. 37–42, 2016.

[132] S. N. A. Mohd Yazid, I. Md Isa, S. Abu Bakar, N. Hashim, and S. Ab Ghani, "A review of glucose biosensors based on graphene/metal oxide nanomaterials," *Anal. Lett.*, vol. 47, no. 11, pp. 1821–1834, 2014.

[133] B. D. Malhotra and M. A. Ali, "Nanomaterials in biosensors: Fundamentals and applications," *Nanomater. Biosens.*, p. 1, 2018.

[134] C. Hu, T. Lu, F. Chen, and R. Zhang, "A brief review of graphene–metal oxide composites synthesis and applications in photocatalysis," *J. Chinese Adv. Mater. Soc.*, vol. 1, no. 1, pp. 21–39, 2013.

[135] X. Jia, J. Li, and E. Wang, "One-pot green synthesis of optically pH-sensitive carbon dots with upconversion luminescence," *Nanoscale*, vol. 4, no. 18, pp. 5572–5575, 2012.

[136] S. C. Ray, A. Saha, N. R. Jana, and R. Sarkar, "Fluorescent carbon nanoparticles: synthesis, characterization, and bioimaging application," *J. Phys. Chem. C*, vol. 113, no. 43, pp. 18546–18551, 2009.

[137] K. Duan, L. Li, Y. Hu, and X. Wang, "Interface mechanical properties of graphene reinforced copper nanocomposites," *Mater. Res. Express*, vol. 4, no. 11, p. 115020, 2017.

[138] A. Duszová, J. Dusza, K. Tomášek, J. Morgiel, G. Blugan, and J. Kuebler, "Zirconia/carbon nanofiber composite," *Scr. Mater.*, vol. 58, no. 6, pp. 520–523, 2008.

[139] M. Khan *et al.*, "Graphene based metal and metal oxide nanocomposites: synthesis, properties and their applications," *J. Mater. Chem. A*, vol. 3, no. 37, pp. 18753–18808, 2015.

[140] C. B. Jacobs, M. J. Peairs, and B. J. Venton, "Carbon nanotube based electrochemical sensors for biomolecules," *Anal. Chim. Acta*, vol. 662, no. 2, pp. 105–127, 2010.

[141] A. Tuantranont, "Applications of nanomaterials in sensors and diagnostics," *Springer Ser. Chem. sensors Biosens.*, vol. 14, 2013.

[142] S. Thakore, P. S. Rathore, R. N. Jadeja, M. Thounaojam, and R. V Devkar, "Sunflower oil mediated biomimetic synthesis and cytotoxicity of monodisperse hexagonal silver nanoparticles," *Mater. Sci. Eng. C*, vol. 44, pp. 209–215, 2014.

[143] L. A. Kolahalam, I. V. K. Viswanath, B. S. Diwakar, B. Govindh, V. Reddy, and Y. L. N. Murthy, "Review on nanomaterials: Synthesis and applications," *Mater. Today Proc.*, vol. 18, pp. 2182–2190, 2019.

[144] S. Iravani, H. Korbekandi, S. V. Mirmohammadi, and B. Zolfaghari, "Synthesis of silver nanoparticles: chemical, physical and biological methods," *Res. Pharm. Sci.*, vol. 9, no. 6, p. 385, 2014.

[145] P. Mohanpuria, N. K. Rana, and S. K. Yadav, "Biosynthesis of nanoparticles: technological concepts and future applications," *J. nanoparticle Res.*, vol. 10, pp. 507–517, 2008.

[146] S.-H. Feng and G.-H. Li, "Hydrothermal and solvothermal syntheses," in *Modern inorganic synthetic chemistry*, Elsevier, 2017, pp. 73–104.

[147] M. Das and S. Chatterjee, "Green synthesis of metal/metal oxide nanoparticles toward biomedical applications: Boon or bane," in *Green synthesis, characterization and applications of nanoparticles*, Elsevier, 2019, pp. 265–301.

[148] A. A. S. Gill *et al.*, "One-pot synthesis of β-cyclodextrin modified silver nanoparticles for highly sensitive detection of CPX," *J. Pharm. Biomed. Anal.*, vol. 203, p. 114219, 2021.

[149] R. Chauhan, A. A. S. Gill, Z. Nate, and R. Karpoormath, "Highly selective electrochemical detection of CPX using reduced graphene oxide/poly (phenol red) modified glassy carbon electrode," *J. Electroanal. Chem.*, vol. 871, p. 114254, 2020.

[150] N. R. Jalal, T. Madrakian, A. Afkhami, and M. Ghamsari, "Polyethylenimine@ Fe3O4@ carbon nanotubes nanocomposite as a modifier in glassy carbon electrode for sensitive determination of CPX in biological samples," *J. Electroanal. Chem.*, vol. 833, pp. 281–289, 2019.

[151] X. Fang *et al.*, "Nanocomposites of Zr (IV)-based metal–organic frameworks and reduced graphene oxide for electrochemically sensing CPX in water," *ACS Appl. Nano Mater.*, vol. 2, no. 4, pp. 2367–2376, 2019.

[152] M. Mahmoudpour, H. Kholafazad-Kordasht, J. E. N. Dolatabadi, M. Hasanzadeh, A. H. Rad, and M. Torbati, "Sensitive aptasensing of CPX residues in raw milk samples using reduced graphene oxide and nanogold-functionalized poly (amidoamine) dendrimer: An innovative apta-platform towards electroanalysis of antibiotics," *Anal. Chim. Acta*, vol. 1174, p. 338736, 2021.

[153] Q.-Q. Zhu, W.-W. Zhang, H.-W. Zhang, R. Yuan, and H. He, "Elaborately manufacturing an electrochemical aptasensor based on gold nanoparticle/COF composites for amplified detection performance," *J. Mater. Chem. C*, vol. 8, no. 47, pp. 16984–16991, 2020.

[154] F. Giroud *et al.*, "Impedimetric immunosensor based on a polypyrrole−antibiotic model film for the label-free picomolar detection of CPX," *Anal. Chem.*, vol. 81, no. 20, pp. 8405–8409, 2009.

[155] L. Xu *et al.*, "Graphitic carbon nitride/BiOCl composites for sensitive photoelectrochemical detection of CPX," *J. Colloid Interface Sci.*, vol. 483, pp. 241–248, 2016.

[156] N. Yuphintharakun *et al.*, "A nanocomposite optosensor containing carboxylic functionalized multiwall carbon nanotubes and quantum dots incorporated into a molecularly imprinted polymer for highly selective and sensitive detection of CPX," *Spectrochim. Acta Part A Mol. Biomol. Spectrosc.*, vol. 201, pp. 382–391, 2018.

[157] Q.-D. Huang, C.-H. Lv, X.-L. Yuan, M. He, J.-P. Lai, and H. Sun, "A novel fluorescent optical fiber sensor for highly selective detection of antibiotic CPX based on replaceable molecularly imprinted nanoparticles composite hydrogel detector," *Sensors Actuators B Chem.*, vol. 328, p. 129000, 2021.

[158] X. Li *et al.*, "Dynamic adsorption of CPX on carbon nanofibers: quantitative measurement by in situ fluorescence. J Water Process Eng 9: e14–e20." 2016.

[159] M. K. Pawar, K. C. Tayade, S. K. Sahoo, P. P. Mahulikar, A. S. Kuwar, and B. L. Chaudhari, "Selective CPX antibiotic detection by fluorescent siderophore pyoverdin," *Biosens. Bioelectron.*, vol. 81, pp. 274–279, 2016.

[160] V. Springer, M. A. Segundo, M. E. Centurion, and M. Avena, "Fully-programmable synthesis of sucrose-mediated gold nanoparticles for detection of CPX," *Mater. Chem. Phys.*, vol. 238, p. 121917, 2019.

Chapter 2

Material and Characterization

CHAPTER 2

MATERIAL AND CHARACTERIZATION

The present chapter will describe the information of various characterization techniques that are used to confirm the synthesis of various nanomaterials and nanocomposites that are utilized for the detection of ciprofloxacin antibiotic with different sensing techniques and materials that are also used in all experiments that are concluded in this thesis work.

2.1 Materials

The description of the materials utilized in this thesis work is provided below:

Ciprofloxacin antibiotic, other antibiotics such as (norfloxacin, amoxicillin, levofloxacin, moxifloxacin, tetracycline, ampicillin, and gentamycin were procured from SRL), Lanthanum nitrate tetrahydrate (99.99%)($LaNO_3.4H_2O$), C. tamala (tej patta), the fruit of*Ziziphusmauritiana* (was bought from the market of Delhi., Quinine sulfate and absolute ethanol were brought from Sigma-Aldrich (3-aminopropyl) tri methoxy silane (APTES), 1-(3-(dimethylamino)-propyl)−3-ethyl carbodiimide hydrochloride (EDC), was bought at Sigma Aldrich, sodium nitrate ($NaNO_3$) (CAS: 7631-99-4), sulphuric acid (H_2SO_4, hydrogen peroxide (H_2O_2), potassium permanganate ($KMnO_4$) potassium persulfate ($K_2S_2O_8$) and phosphorus pentoxide (P_2O_5) (CAS: 1314-56-3) were procured from Merck (Sigma-Aldrich), India. While ferric nitrate nonahydrate [Fe $(NO_3)_3.9H_2O$] (CAS: 7782-61-8) was brought from Thomas Baker, India. Graphite flakes, concentrated nitric acid (HNO_3, 69%), concentrated sulphuric acid (H_2SO_4), acetonitrile (ACN), sodium chloride extra pure (NaCl), sodium carbonate anhydrous (Na_2CO_3), sodium phosphate dibasic dihydrate (Na_2HPO_4), potassium ferricyanide ($K_3[Fe(CN)_6]$), sodium monophosphate (NaH_2PO_4), and potassium ferrocyanide ($K_4[Fe(CN)_6]$) (CAS: 14459-95-1), sodium molybdenum oxide dihydrate ($Na_2MoO_4.2H_2O$) were procured from Fisher Scientific, India, ITO-coated glass from Blazers (UK) with a transmittance of 90%, a resistance of 25 sq^{-1}, and a thickness of 1.1 mm. All of the electrochemical studies employed phosphate buffer saline (PBS) as the working buffer and Ferro-Ferri $[Fe(CN)_6]^{3-/4-}$ as the redox species. The PBS was prepared freshly from NaH_2PO_4(0.2 M) and $Na_2HPO_4.2H_2O$ (0.2 M) for pH 7.0, followed by NaCl (0.9%) addition into it. The preparation of diverse concentrations of ciprofloxacin was done using the stock solution

(5 mM) prepared in DIof 0.2 M, from which further concentrations were made by serial dilutions of anti-CPX (ciprofloxacin) monoclonal antibodies were purchased from MyBioSource in the United States, milk, All the other chemicals were of analytical grade and used without any further treatment. Distilled water was used for all the experiments.

2.2 Characterization Techniques

2.2.1 X-ray Diffraction [XRD]

X-ray diffraction (XRD) [Rigaku Miniflex 600 diffractometer, Japan] is an advanced non-destructive technique used for characterizing the crystalline properties of nanomaterials. It is a rapid analytical technique that is used for the investigation of grain size, phase, crystallinity structure, strain, and crystal defects. XRD is a very reliable and common equipment for the identification of the crystal structure and interplanar atomic d-spacing. This XRD system is mainly based on X-ray generation and its monochromatic diffraction. The XRD has three main components in its structure: a sample holder, a cathode ray tube, and a detector[1]. X-rays are produced by an x-ray tube or cathode ray tube due to applied voltage on the filament (as copper material), electrons accelerating towards the target material and bombarding with the electrons at the angle θ[2]. The incident beam is diffracted by the constructing interference of monochromatic X-rays due to multiple layers and crystalline samples. When the sample interacts with the incident rays, it produces monochromatic X-rays due to constructive interference., it follows Bragg's law which is given below:

$$n\lambda = 2d\sin\theta \qquad \text{Eq:2.1}$$

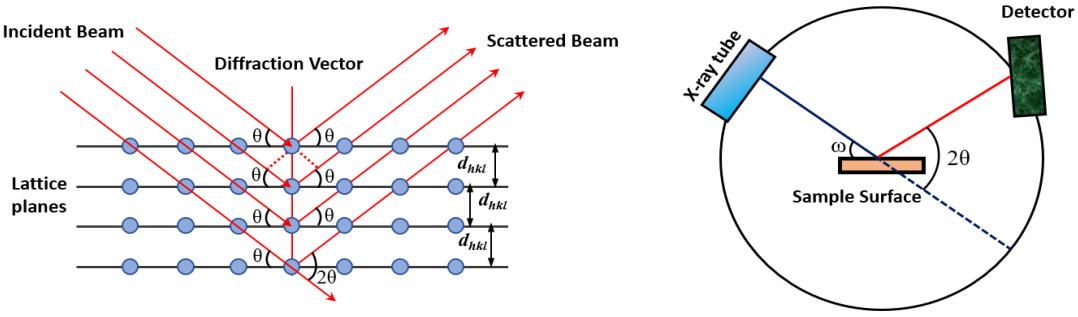

Figure 2.1: Schematic representation of x-ray diffraction.

Where n is an integer, λ is the wavelength of the x-ray, d is the interplanar spacing between multiple layers of the sample, and θ is the diffraction angle.

Using the Debye-Scherrer formula, the average crystalline size of a nanomaterial will be estimated as follows:

$$D = \frac{k\lambda}{\beta cos(\theta)} \qquad \text{Eq:2.2}$$

Where D represents the crystalline size of nanomaterial, K is a dimensionless factor (~0.9), λ is the wavelength (1.5406 Å), β represents FWHM (full width at half maximum) of the diffraction peaks, and last θ is for Bragg's angle.

2.2.2 Fourier Transform Infrared Spectroscopy [FTIR]

FT-IR [Perkin Elmer, US] is also known as vibrational spectroscopy, but instead of scattering, it is based on absorbance, transmittance, or reflectance of incident infrared light[3]. The amount of absorbed incident light at different frequencies corresponds to the vibrational frequencies of different types of binding in the sample[4],[5]. However, FT-IR measurement depends on sample parameters like thickness, uniformity, and dilution. In a typical FT-IR operation, the IR light originates from the source strikes on the beamsplitter. In this way, half a portion of the light is transmitted toward the scanning mirror, and the rest half portion is refracted towards the fixed mirror. Light reflected from both mirrors strikes back to the beam splitter, and a fraction of light moves towards the detector through the sample to be analyzed. A schematic of the FT-IR setup is displayed in Figure 2.2 for the present work. FT-IR measurements of thin films and powder samples were recorded using Varian 600UMA.

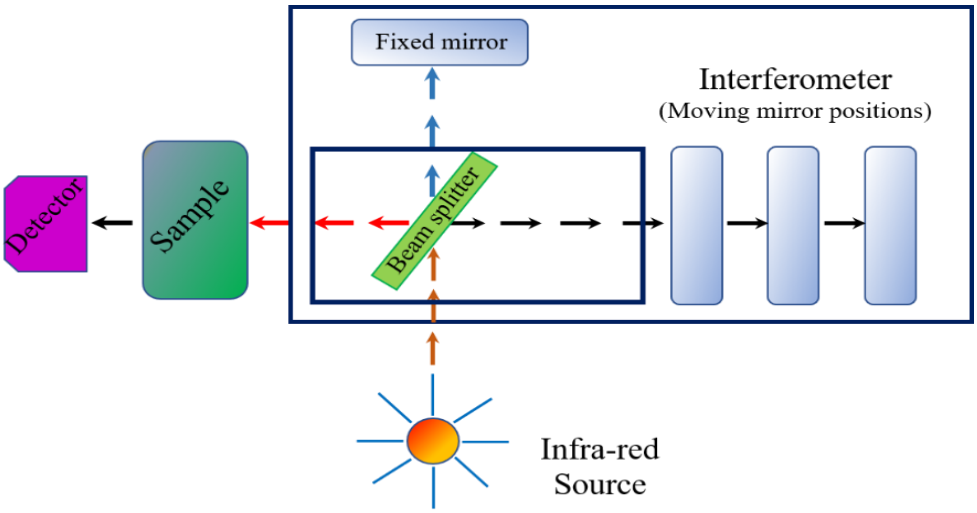

Figure 2.2: Schematic representation of FTIR setup.

2.2.3 Scanning Electron Microscopy [SEM]

Scanning Electron Microscopy is considered a non-destructive technique, and the surface of the sample can be viewed multi-times. Moreover, quantitative and qualitative elemental analysis can be performed using EDX spectroscopy attached with SEM. Figure 2.3 shows a simplified schematic of scanning electron microscopy and EDX.

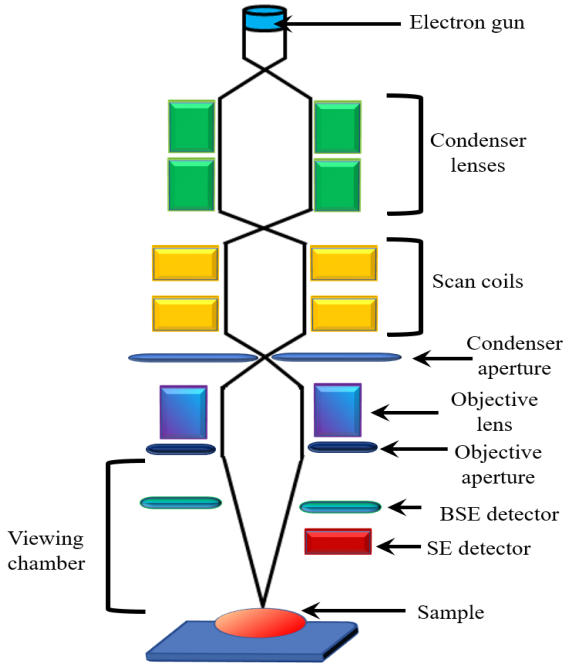

Figure 2.3: Schematic representation of SEM.

The interaction between high-energy electrons and the sample surface produces a variety of signals, including backscattered electrons, secondary electrons, and photons, which reveal the surface morphology and chemical composition of the sample[6].[7]. Among these signals, both secondary electrons and backscattered electrons are used to produce 2-D images and generated photons for elemental analysis. During SEM image production, secondary electrons are most important for revealing the topography and morphology of the sample, whereas backscattered electrons assist in illustrating contrasts in the composition of multiphase samples[8]. Energy-dispersive X-ray (EDX) spectroscopy uses photons or X-rays, which are produced due to the inextensible clash of high-energy photoelectrons with electrons present in distinct atomic frames in the sample[9]. The high-energy electrons emit recognizable X-rays with a specific wavelength as they return to lower energy states. Since the elemental analysis is limited

to a tiny area of the sample, thus it is required to make multiple analyses on different portions of the sample to extract correct information about elemental composition. The measuring sample should be electrically conducting; if it is non-conducting, then it should be coated with conducting material like gold. SEM images shown in this thesis were captured using SEM, JEOL, Japan. Samples for SEM were prepared in the form of thin film on an ITO substrate and then coated with gold for good quality of the image.

2.2.4 Transmission Electron Microscopy [TEM]

Transmission electron microscopy (TEM)[HR-TEM, JEM-2200 FS, Jeol, Japan] is an electron microscopy that uses an electron source for imaging. TEM is a highly advanced imaging technology that provides the morphological, topographic, compositional, and crystalline information of several varieties of nanomaterials, including nanoparticles, nanorods, and nanocubes, and also can determine the size of CQDs (lowest nanomaterials). Unlike SEM, TEM is based on the transmission process. TEM has limitless applications and is also useful in the biological field to determine the cellular function and structure of cells and tissue. Ernst Ruska and Max Knoll constructed the first TEM in the 1930s, and a decade later, Keith Porter recorded the first electron microscopic picture of eukaryotic cells[10],[11]. Thus, TEM was considered an efficient instrument for studying the functioning of cells and tissues at the nanoscale.

In TEM, an electron beam passes through the extremely thin specimen. During transmission, specimens interact with electron beams which lead to the formation of images. A visualization device, which might be a fluorescent screen, magnifies and focuses this image, and a CCD camera detects this image as a detector. However, the interference of an electron beam is extremely reliant on the nature of materials because less dense or porous materials are transmitted easily by electron beam, while dense material allows less transmittance. As a result, a material having non-uniform properties can easily be detected using TEM.

TEM comprises several components in the imaging, such as an electron gun, magnetic condenser lens, specimen, magnetic objective lens, aperture, projector lens, fluorescent screen, and CCD camera (detector). The working function of TEM is as follows: the

electrical potential is applied, the filament is heated, a stream of electrons is produced by an electron gun which passes through the condenser lens, then the condenser aperture filter out the unwanted scattered electrons that strikes the specimen (sample). Following the angle of incidence, the beam is partially transmitted or diffracted. The objective lens plays an important role in focusing the transmittance of electrons from a specimen into an image. Objective aperture enhances the contrast of the image and eliminates the high-angled diffracted electrons. The transmitted beam passes through the projector lens, and the final image is obtained. The magnified image is obtained on a fluorescent screen by a CCD camera. TEM produces high-resolution black-and-white images in vacuum chambers during interaction with specimens and energetic electrons. A vacuum chamber pumps out the air and creates a space where electrons can move[12].

The high-resolution image of the sample obtains at a high voltage of ~ 100 - 200 kV. TEM can imagine particle size up to 0.1 nm rather than SEM. TEM has several advantages, such as powerful magnification, having potential more than one million times, producing high-quality images, and having the capability to insight into the surface feature, shape, size, and structure of the material.

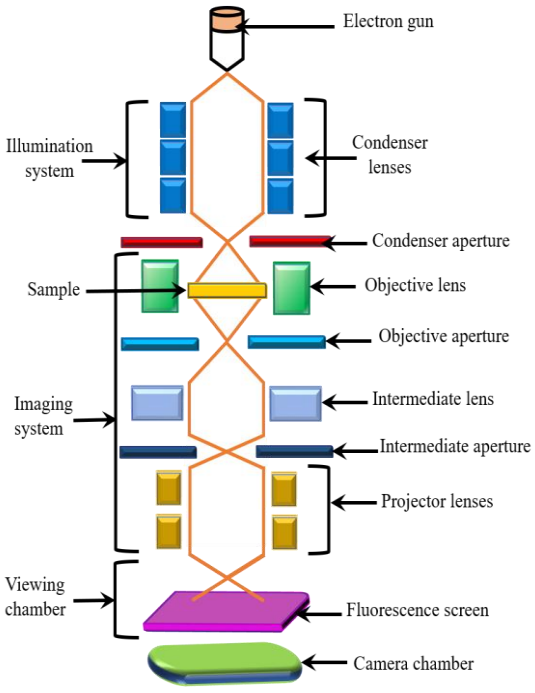

Figure 2.4: Schematic representation of TEM.

2.2.5 Raman Spectroscopy

Raman spectroscopy is considered a sensitive and non-destructive technique that provides details about chemical species present in the sample in the form of molecular vibrations[13],[14]. Raman scattering originates due to the interaction of incident monochromatic light with vibrations of a molecule[15]. A typical Raman spectroscopy is comprised of four major modules: a laser source, an optics system to collect light, a wavelength selector, and a detector [Figure 2.5]. The chemical compound in the sample absorbs the incident light (electromagnetic waves) and remits electromagnetic waves of a frequency different from the incident. The scattered light signals are collected using the lens, which is sent through a wavelength filter to the detector. At this point, a filter (notch or bandpass or edge pass filter) is used to filter out the scattered light of wavelength similar to incident light (Rayleigh scattering). This frequency shift is called as "Raman shift"[16], which provides rotational, vibrational, and transitional information about molecules. In the present work, Raman analyzer EnSpectr R532 with 30 mW single mode laser emitting at 532 nm was used to record Raman spectra for reduced graphene oxide nanocomposite La_2O_3@rGO.

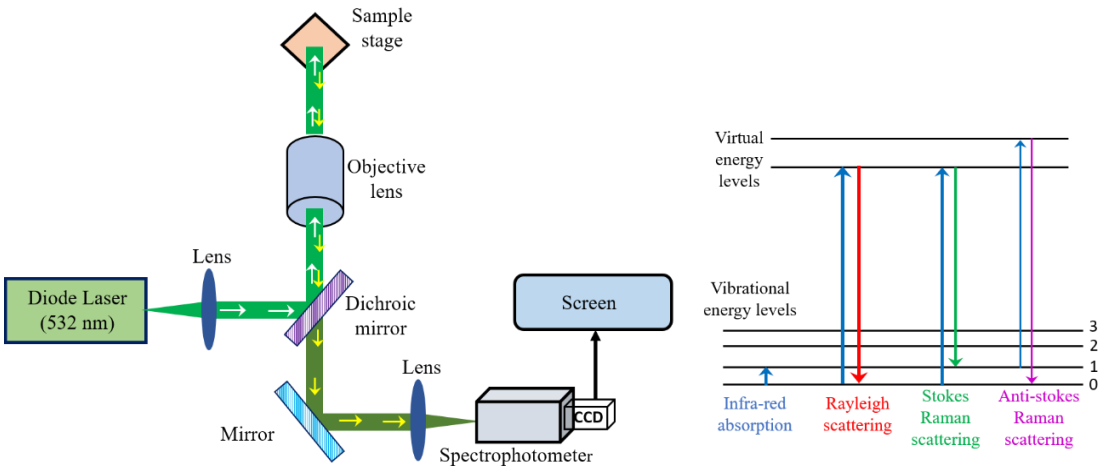

Figure 2.5: Schematic representation of Raman spectroscopy.

2.2.6 UV-Visible Spectroscopy [UV-Vis]

UV-visible spectroscopy[T90 + UV/vis spectrometer]is used to study the interaction of UV or visible light with molecules or ions[17]. It is a non-destructive tool that capable of providing qualitative and quantitative information about the sample understudying.

UV and visible light have sufficient energy to make the electronic transition from the highest occupied molecular orbital to the lowest occupied molecular orbital, and every material has a specific value of band gap[18]. Thus, the absorption of light (with appropriate wavelength) by molecule results in the transition of electrons to a high-energy orbital or excited state. In this way, the wavelength of the absorbed light will correspond to the energy band gap of the material which is related to the functional groups[19].

Sample absorption depends on the principle of Lambert-Beer law. According to this law, absorption depends on the concentration of the sample, the path length of the cuvette (used for measurement of the sample), and the molar extinction coefficient. The relation of these components is given in the equation.

$$A = \varepsilon c l \qquad \text{Eq:2.3}$$

Where A represents the absorption, ε is the molar extinction coefficient (liter mol^{-1} cm^{-1}), c indicates concentration (mol $liter^{-1}$), and *l* shows the path length of the cuvette.

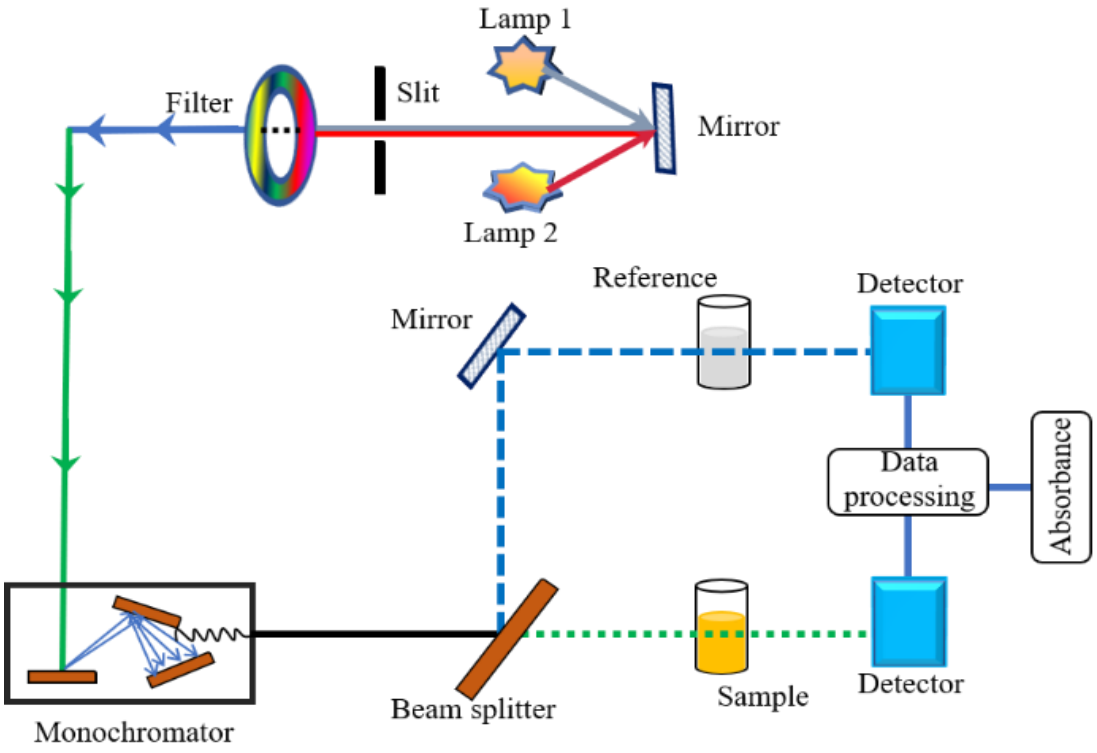

Figure 2.6: Schematic representation of UV-visible spectroscopy.

2.2.7 Fluorescence spectroscopy

The term "Fluorescence" can be defined as the emission of light from a substance within its emission band that absorbs light within its absorption band[20]. Compared to the absorbed light, which has a higher energy, the light that is released has a longer wavelength. Fluorescence spectrometry works on the fluorescence phenomenon and is used to measure and detect chemical activity[21],[22]. This method is relatively fast, easy, inexpensive, and sensitive to analyzing the analyte concentration in liquid samples. The changing of some factors, such as the solvent concentration, cuvette path length, and excitation wavelength, will also alter the emission curve's intensity and shape[23],[24]. In a typical fluorescence spectroscopy measurement, Fluorescence spectroscopy comprises several components such as a light source, excitation monochromator, emission monochromator, polarizer filter, polarizer analyzer, sample, and detector. In the typical functioning of fluorescence spectroscopy, a source of light falls on the sample through an excitation monochromator where the polarizer filter eliminates the unwanted light source, allowing it to pass the polarizer which polarizes the signal and sends it to the emission monochromator. Emission signals reach the detector and obtain fluorescence spectra. In the present work, fluorescence spectra were recorded using the Cary Eclipse Fluorescence spectrometer for the sample.

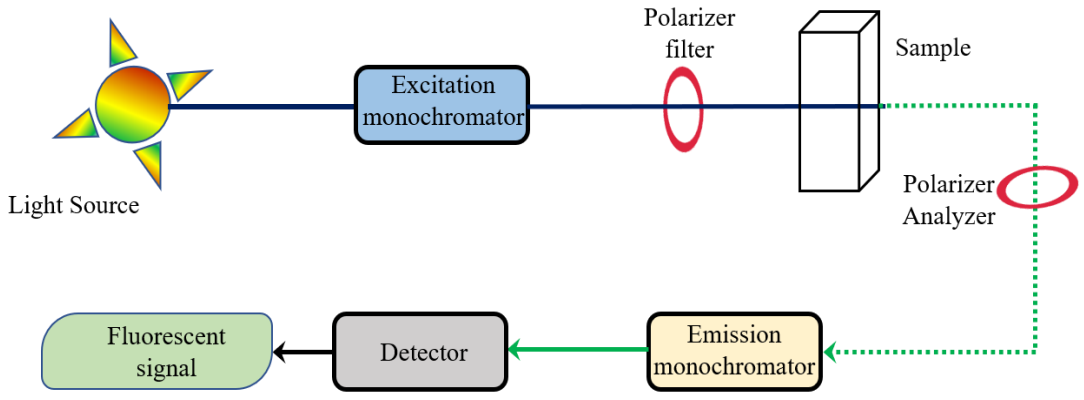

Figure 2.7: Schematic representation of fluorescence spectroscopy.

2.2.8 Zeta Potential Measurement

Zeta Potential is defined as the charge developed on the surface of the solid material when it comes in contact with the water. Zeta potential is measured in the range of mV,

which may arise by different mechanisms, including adsorption of solution ions on the material surface or dissociation of the solution, or protonation of functional groups[25]. In a liquid medium, an electrical double layer develops in the region of the solid-liquidinterfaceduetothesurfacechargeonthematerial'ssurfacesasshowninFigure 2.8. This double layer consists of a stern layer (inner layer) and a diffused layer (outer layer). The stern layer contains ions, which are tightly bonded to the material surface. In the diffused layer, the equilibrium of random thermal motion and electrostatic forces defines the ion distribution. The potential in the double-layer region decreases with the increase in distance from the solid-liquid interface, and after a certain distance, it approaches zero [Figure 2.8]. From the figure, it can be seen that the value of zeta potential is equal to the surface charge of the share. In a typical measurement, under an applied electric potential, particles and their associated ions move towards the electrode having opposite polarity *via* solution. This process is known as electrophoresis, and the potential at the surface of the share is known as zeta potential. The presence of a layer of the macromolecule on the material surface can shift the shear plane and thus the value of zeta potential. In the present work, an electrophoresis instrument (ZC-2000, Microtec, Japan) was used to measure the surface charge of nanomaterials.

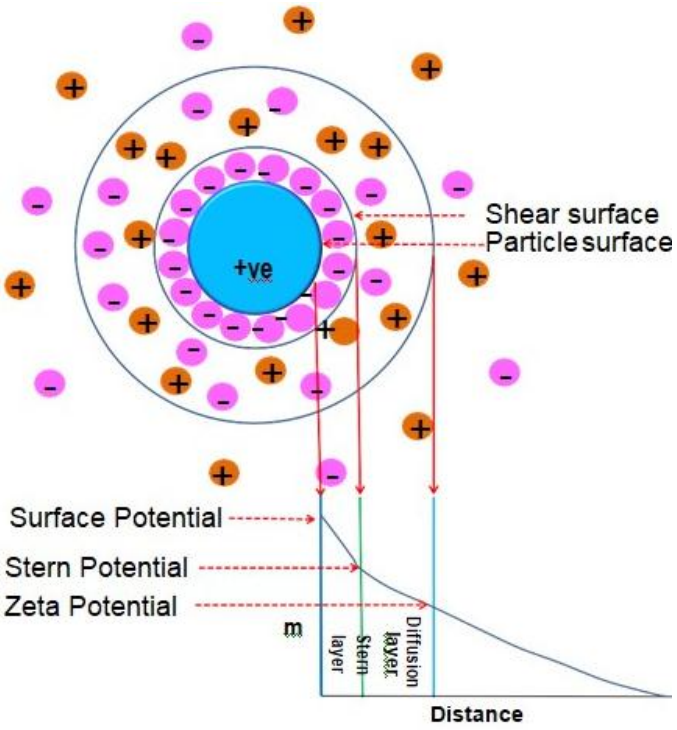

Figure 2.8: Schematic representation of the electrical double layer and the zeta potential

2.2.9 Contact Angle Measurement

The angle formed between a liquid and a solid surface is known as the contact angle. The material's wettability correlates precisely with the contact angle's value[26]. There are four cases of wettability exist depending on the value of contact angle: 0 - complete wetting (spreading), 0-90°- wettable (hydrophilic), above 90° - the surface is not wettable (hydrophobic) and near to theoretical limit 180° - superhydrophobic as shown in Figure 2.9[27]. In a typical measurement, a deionized water droplet is released on the surface of the fabricated electrode, and the contact angle is monitored using the Laplace–Young calculation method in static mode. The young equation relates contact angle with the surface tension of the liquid (σ_l), surface free energy (σ_S), and interfacial tension at the liquid-solid interface (σ_{Sl}) by the following relation[28].

$$\sigma S = \sigma SL + \sigma L \cos \theta \qquad \text{Eq:2.4}$$

The wetting property of the material depends on the chemical composition, surface morphology, and free energy. In our research work, contact angle measurements of modified electrodes were conducted by A.KRUSS Optronics GmbH instrument.

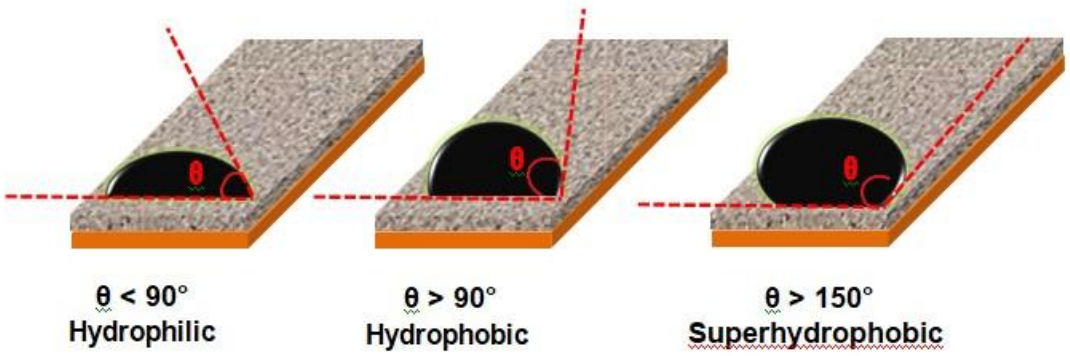

Figure 2.9: Categorization of the material surface by their contact angles

2.3 Electrophoretic Deposition [EPD]

Electrophoretic deposition is a thin film formation technique where stable colloidal suspended charge particles migrate under the effect of an electric field and deposit onto the oppositely charged conductive surface. It is a cost-effective two-step process. The first step involves the movement of particles having an electric charge in the colloidal

suspended liquid solution towards the electrode by applying the electric field. At the same time, the second step allows the coherent deposition of particles on the electrode. EPD enables the fabrication of various desired structures using traditional to advanced materials. It can be used in the fabrication of nanometric thin film to 1 mm thick film. EPD is heavily used in the fabrication of electrodes for biosensing platforms.

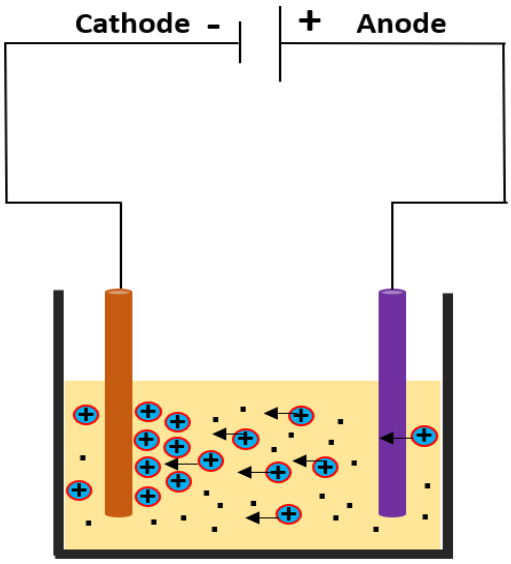

Figure 2.10: Schematic representation of EPD.

2.4 Electrochemical Measurement Techniques

An electroanalytical approach, referred to as electrochemistry, is dependent on changes in current, voltage, or impedance. There are numerous benefits to using electrochemical techniques as a tool for analysis, including accuracy, high sensitivity, precision, and a wide linear dynamic range with inexpensive instrumentation. This technique is significant in a wide and interdisciplinary area of research, which can analyze a smaller number of biological samples such as blood, serum, urine, vitamins, and cancerous cells. Besides these, it is also explored in different phenomena like electrophoresis, electrochemical sensors or biosensors, battery and fuel cells. These techniques improve the applicability of detection and determination limits of the samples.

The electrochemical technique is employed in kinetics study using the electron transfer process in the system. It is a very sensitive technique and is employed for the detection

of analytes in the electrolytic solution in the electrochemical cell. The response of the analyte is measured in terms of change in electrical current. This electrochemical technique recognizes the different concentrations of analyte at the electrode surface and leads to a change in current or voltage in the electrolyte solution. This technique is divided into various groups: potentiometry, voltammetry, coulometry, impedance spectroscopy, etc. Among these, voltammetry and impedance-based techniques are often used in the detection of analytes. The present work of the thesis is related to the study of analytes using three electrode systems in the electrochemical cell. In a three-electrode system, the first electrode is known as the working electrode, the second is known as the reference electrode, and the last one is called the counter electrode.

(i) Working Electrode

Working electrode accomplishes the electrochemical events for the system. Working electrodes provide a surface where chemical reactions take place in terms of current or voltage change. It is composed of redox-inert material (ITO glass or glassy electrode). The variety of working electrodes varies from experiment to experiment and can act as an anode or cathode depending upon the redox reaction. Different electrode materials can also change the electrochemical response during the electron transfer process.

(ii) Reference Electrode

Although this kind of electrode exhibits a distinct and stable equilibrium potential, that is why it serves as a reference electrode for measurements of the potential of other electrodes in the electrochemical cells. There are a variety of electrodes, like standard hydrogen electrodes, Ag/AgCl electrodes, and saturated calomel electrodes (SCE), that are used in electrochemical cells.

(iii) Counter Electrode

Counter electrode helps in the flow of current at a working electrode when the potential is applied to the electrode and oxidation or reduction of the analyte takes place. Generally, electron flow between the working electrode (WE) and counter electrode (CE) is recorded. CE also completed the electrical circuit. CE shows inertness as much as possible when a reduction is recorded at WE; in turn, an oxidation occurs at CE. Platinum (Pt) wire or carbon-based disk electrode is used as a counter electrode.

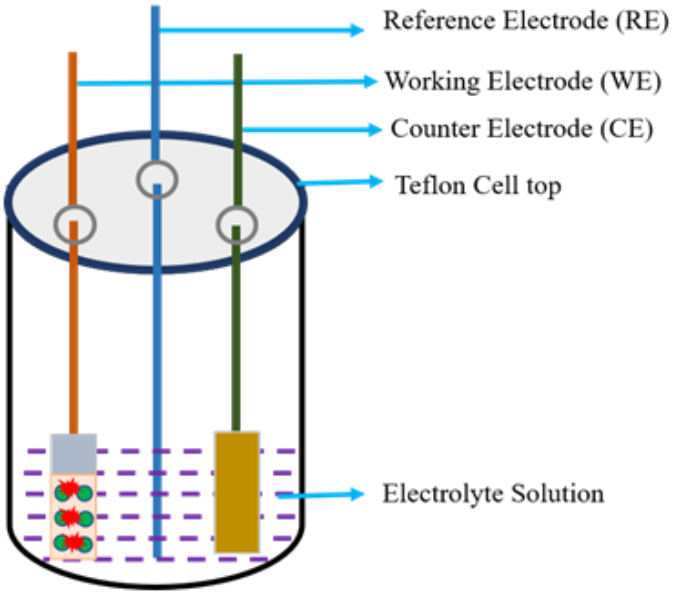

Figure 2.11: Schematic representation of electrochemical cells.

2.5 Voltammetry

Voltammetry is a term used to describe an electroanalytical technique that measures current as a function of time and a specific applied potential or voltage. Current flows as a result of electrode response at the working electrode to the reference electrode, where the applied potential occurs. Voltammetry is widely employed in inorganic, physical, and biological studies for nonanalytical reasons, including basic investigations of the oxidation and reduction of different media and the mechanisms of electron transfer at the transformed electrode surface. Voltammetry involves various categories: cyclic, square wave, pulse voltammetry, linear sweep, stripping, alternative current, steady-state microelectrode, and hydrodynamic voltammetry. This thesis is mainly focused on cyclic voltammetry (CV) and differential pulse voltammetry (DPV) techniques which are employed for kinetic and sensing studies.

2.5.1 Cyclic Voltammetry

Cyclic voltammetry is an advanced and powerful electrochemical tool used to study the electron transfer process initiated by chemical reactions that take place at the electrode surface. It is based on the principle of oxidation and reduction of molecular species. A CV

consists of two types of voltage sweep profiles: forward and reverse or backward. In the forward sweep, Fe^{+2} ions in the ferry/ferrocyanide buffer are oxidized into the Fe^{+3} ions, while in the backward, Fe^{+3} ions are reduced into the Fe^{+2} ions. This process results in the anodic current (Ipa) in the forward scan and the cathodic current (Ipc) in the backward scan. Thus, these oxidation and reduction processes show an equilibrium profile of cyclic voltammetry. CV is a reversible process and provides several characteristics such as (a) voltage separation among current peaks obtained in forward and reverse mode, (b) The relationship between the current peak and the scan rate is directly proportional to each other; (c) the peak voltage positioning is independent of the voltage scan rate; and (d) the ratio of the current peaks Ipa and Ipc is almost equal to 1.

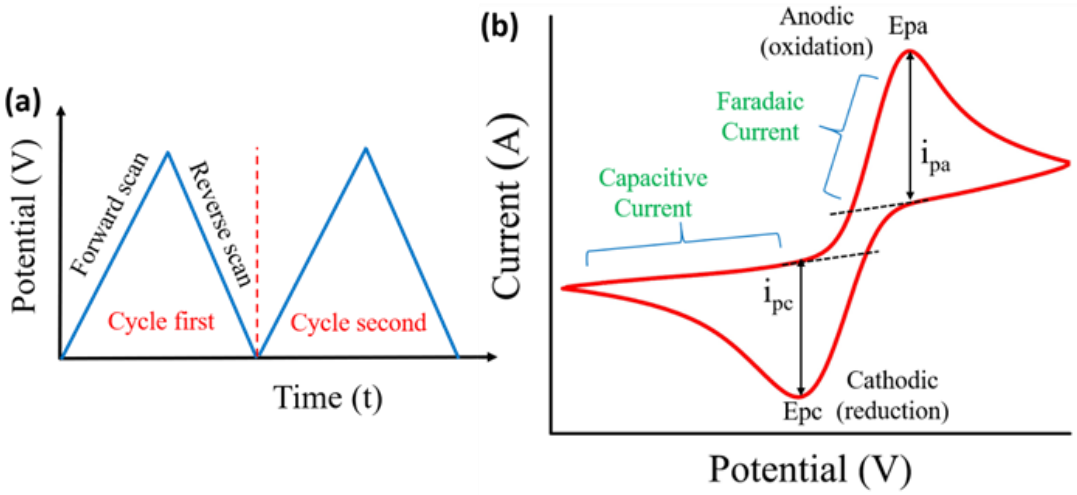

Figure 2.12: Cyclic voltammetry (a) applied ramp potential and (b) a typical voltagramm.

In the typical CV, the variable voltage is applied to the electrode that is used as a working electrode (WE) parallel to the electrode that is used as the reference electrode (like Ag or AgCl), and electron flow between the counter electrode and working electrode results in the electrode reaction. In the CV, the applied voltage can range from 10 mV/s to 100 mV/s. With increasing of the potential of the solution, the current is proportionally increasing. The CV measures various electrokinetics parameters for biologically modified immunoelectrode at the electrode/electrolyte interface. Mainly three electrokinetic parameters are measured by CV, such as diffusion constant (D_f), the surface concentration of redox species (I*), and effective electroactive area (Ae).

Using the Randles-Sevcik equation, which is explained below, one may determine the D_f and Ae of the redox species:

$$I_p = (2.69 \times 10^5) n^{3/2} A D_f^{1/2} v^{1/2} \quad 2.5$$

Where I_p represents the peak current, n is the number of participating electrons, A is the electrode surface area, *v* is the scan rate, and lastly, C indicates the redox species $[Fe(CN)_6]^{3-/4-}$ concentration in the solution electrolyte. And the expression for Ae:

$$Ae = \frac{S}{(2.99\times10^5) n^{3/2} A D_f^{1/2} C} \quad \text{Eq:2.6}$$

Where S represents the value of the linear curve's slope as determined by the Ipa vs. $v^{1/2}$.

The Brown-Anson model calculates the surface concentration of redox species (I*), which is as follows:

$$I_p = \frac{n^2 F^2 I^* A v}{4RT} \quad \text{Eq:2.7}$$

Where F represents the Faraday constant (96485 C mol^{-1}) and other symbols have the same meaning.

2.5.2 Differential Pulse Voltammetry

Differential pulse voltammetry (DPV) is the most sensitive voltammetry analytical tool, often allowing analyses at PPB (part per billion) level. Because the charging currents are strongly differentiated and the ratio of faradaic to charging current is high, DPV is intended to reduce the background charging current. Barker and Gardner proposed this DPV method for DME (dropping mercury electrodes) in 1960 to increase the detection threshold. In the DPV approach, the working electrode is repeatedly exposed to a constant pulse amplitude overlaid on the linear potential ramp right before the drop. The value of the current is measured two times for each pulse; one just starts the pulse, and another ending of the pulse. This technique measured the current in the electrochemical cell at the electrode/electrolyte interface. In the typical DPV measurement, the curve is plotted against ΔI (current) *vs.* V (potential).

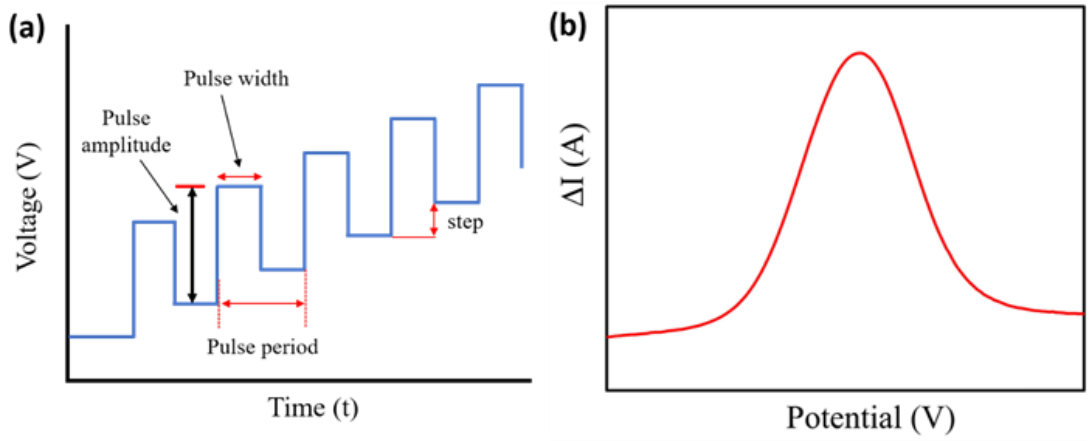

Figure 2.13: (a) Formation of staircase potential for DPV and (b) a typical DPV plot.

2.5.3 Electrochemical Impedance Spectroscopy

Electrochemical impedance spectroscopy (EIS) is an effective and non-destructive technique utilized for studying the surface of the modified electrode, diffusion of an electron at the interface of electrolyte/electrode, the kinetics of electron transfer, and electrochemical reactions[29]. The current passes to the circuit comprising an inductor, a capacitor (C), or/and resistance (R) that finally results in impedance or complex resistance, which is a fusion of imaginary and real impedance. In an EIS graph, the relation between the imaginary (Z‟‟‟‟) and real (Z‟) impedance versus frequency is called a “Nyquist plot” [30]. The Nyquist plot depicts many significant parameters, such as capacitance of double layer (C_{dl}), Warburg impedance (W), charge transfer resistance (R_{ct}), and electrolyte resistance (R_s). The Nyquist curve consists of a semi-circle portion and a straight line corresponding to electron transfer at high frequency and diffusion-limited processes at low frequency, respectively. The R_{ct}valueisgiven by the diameter of the semi-circle, revealing that modification of electrode surface has taken place. In the current thesis work, the Nyquist plots for various electrodes were conducted in the frequency range at zero potential from 0.1 to 10^5Hz for examining the relative variations in the R_{ct}. The EIS is associated with many benefits compared to amperometricdetection, such as faster assay, low cost, easy detection of an analyte, and high signal-to-noise ratio. The diagram of an equivalent circuit of EIS is shown in Fig. 2.14.

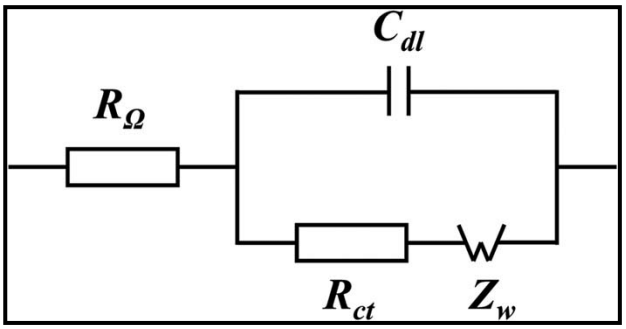

Figure 2.14: Equivalent circuit of EIS

2.6 General Calculations

pH Effect

For observing the maximum activity of electrodes, different PBS of various pH having redox species were taken for the electrochemical analysis. Hence, pH optimization is regarded as a vital parameter for sensing study. The electrode activity was examined in a pH range between 6.0 and 8.0 to determine a suitable pH.

Estimation of Incubation Time

While taking the electrode's response, its surface interaction with the analyte is essential. The time required for the adsorption of the analyte on the surface of the electrode is described as incubation time. Thus, the current values are observed for a particular electrode at regular time intervals in the presence of the analyte. The time at which no further change in current occurs and a saturated value comes is known as the incubation time for that electrode.

Determining Selectivity, Repeatability, Reproducibility, and Shelf-life (stability) of the Sensing Platform

Selectivity is a vital parameter for the sensor as the attachment of interferents could interfere, resulting in the false detection of analytes. The selectivity of an electrode was assessed using the DPV technique and introducing interferents at many high concentrations than the detecting analyte for studying the performance of the sensor. Furthermore, reproducibility and repeatability were also studied to evaluate sensor performance. RSD, which stands for relative standard deviation, was estimated for selectivity, repeatability, and reproducibility, which is calculated using the formula given by Eq: 2.8

$$(\%) = \text{Standard Deviation Average} \times 100 \qquad \text{Eq:2.8}$$

The stability of the sensor is determined by shelf-life or storage stability, i.e., the time interval for which a particular sensor electrode has maximum activity or is considered for further utilization. The number of weeks/days up to which the current gets saturated is recognized as the shelf-life of the sensor. All these parameters are studied in chapters third to six to depict the performance of sensor electrodes.

Sensitivity and Linear Detection Range

The efficacy of the sensor electrode is determined by numerous parameters such as sensitivity (variations in sensing response per unit analyte concentration), linear detection range (the range of concentrations for which an electrode linearly detects the analyte), the limit of detection (LOD) and regression coefficient (R^2) of linearity. These parameters are estimated using the DPV technique. The linear curve is plotted between peak currents taken during sensing and logarithm concentrations of the analyte. The sensitivity and LOD were calculated using the formula given by Eq.(2.9) and (2.10), respectively:

$$\text{Sensitivity} = \frac{slopoflinearplot}{areaofsensingelectrode} \qquad \text{Eq:2.9}$$

$$\text{LOD} = 3\sigma/m \qquad \text{Eq:2.10}$$

where σ indicates the standard deviation of the intercept and m denotes the linear plot slope.

2.7 References

[1] J. R. Connolly, "Elementary crystallography for X-ray diffraction," *EPS400-001, Introd. to X-Ray Powder Diffraction, Spring*, 2007.

[2] A. A. Bunaciu, E. G. UdriŞTioiu, and H. Y. Aboul-Enein, "X-ray diffraction: instrumentation and applications," *Crit. Rev. Anal. Chem.*, vol. 45, no. 4, pp. 289–299, 2015.

[3] J. A. N. T. Soares, "Introduction to optical characterization of materials," *Pract. Mater. Charact.*, pp. 43–92, 2014.

[4] A. A. Ismail, F. R. van de Voort, and J. Sedman, "Fourier transform infrared spectroscopy: principles and applications," in *Techniques and instrumentation in analytical chemistry*, vol. 18, Elsevier, 1997, pp. 93–139.

[5] U. Dembereldorj, E.-O. Ganbold, J.-H. Seo, S. Y. Lee, S. I. Yang, and S.-W. Joo, "Conformational changes of proteins adsorbed onto ZnO nanoparticle surfaces investigated by concentration-dependent infrared spectroscopy," *Vib. Spectrosc.*, vol. 59, pp. 23–28, 2012.

[6] T. L. Hayes and R. F. W. Pease, "The scanning electron microscope: principles and applications in biology and medicine," *Adv. Biol. Med. Phys.*, vol. 12, pp. 85–137, 1968.

[7] J. I. Goldstein, D. E. Newbury, J. R. Michael, N. W. M. Ritchie, J. H. J. Scott, and D. C. Joy, *Scanning electron microscopy and X-ray microanalysis*. Springer, 2017.

[8] M. A. Saghiri *et al.*, "Back-scattered and secondary electron images of scanning electron microscopy in dentistry: a new method for surface analysis," *Acta Odontol. Scand.*, vol. 70, no. 6, pp. 603–609, 2012.

[9] S. Tavernier and S. Tavernier, "Interactions of particles in matter," *Exp. Tech. Nucl. Part. Phys.*, pp. 23–53, 2010.

[10] M. Knoll and E. Ruska, "Das elektronenmikroskop," *Zeitschrift für Phys.*, vol. 78, pp. 318–339, 1932.

[11] K. R. Porter, A. Claude, and E. F. Fullam, "A study of tissue culture cells by electron microscopy: methods and preliminary observations," *J. Exp. Med.*, vol. 81, no. 3, p. 233, 1945.

[12] P. Anka, "Uses of transmission electron microscope in microscopy and its advantages and disadvantages," *Int. J. Curr. Microbiol. Appl. Sci*, vol. 7, pp. 743–747, 2018.

[13] N. Sheppard, "IR spectroscopy, surface studies," 2017.

[14] G. S. Bumbrah and R. M. Sharma, "Raman spectroscopy–Basic principle, instrumentation and selected applications for the characterization of drugs of abuse," *Egypt. J. Forensic Sci.*, vol. 6, no. 3, pp. 209–215, 2016.

[15] Z. Li, M. J. Deen, S. Kumar, and P. R. Selvaganapathy, "Raman spectroscopy for in-line water quality monitoring—Instrumentation and potential," *Sensors*, vol. 14, no. 9, pp. 17275–17303, 2014.

[16] F. J. Colas *et al.*, "Red-shift effects in surface enhanced Raman spectroscopy: spectral or intensity dependence of the near-field?," *J. Phys. Chem. C*, vol. 120, no. 25, pp. 13675–13683, 2016.

[17] P. Misra and M. A. Dubinskii, *Ultraviolet spectroscopy and UV lasers*. CRC Press, 2002.

[18] D. Klimm, "Electronic materials with a wide band gap: recent developments," *IUCrJ*, vol. 1, no. 5, pp. 281–290, 2014.

[19] W. S. Choi, S. S. A. Seo, and H. N. Lee, "Optoelectronics: Optical properties and electronic structures of complex metal oxides," in *Epitaxial growth of complex metal oxides*, Elsevier, 2015, pp. 331–363.

[20] W. T. Godbey, *An introduction to biotechnology: the science, technology and medical applications*. Elsevier, 2014.

[21] A. Bhambhani, S. Thakkar, S. B. Joshi, and C. R. Middaugh, "A formulation method to improve the physical stability of macromolecular-based drug products," in *Therapeutic Protein Drug Products*, Elsevier, 2012, pp. 13–45.

[22] R. Karoui and C. Blecker, "Fluorescence spectroscopy measurement for quality assessment of food systems—a review," *Food Bioprocess Technol.*, vol. 4, pp. 364–386, 2011.

[23] Q. Gu and J. E. Kenny, "Improvement of inner filter effect correction based on determination of effective geometric parameters using a conventional fluorimeter," *Anal. Chem.*, vol. 81, no. 1, pp. 420–426, 2009.

[24] J. R. Lakowicz, *Principles of fluorescence spectroscopy*. Springer, 2006.

[25] R. Schweiss, P. B. Welzel, C. Werner, and W. Knoll, "Dissociation of surface functional groups and preferential adsorption of ions on self-assembled monolayers assessed by streaming potential and streaming current measurements," *Langmuir*, vol. 17, no. 14, pp. 4304–4311, 2001.

[26] Y. Yuan and T. R. Lee, "Contact angle and wetting properties," *Surf. Sci. Tech.*, pp. 3–34, 2013.

[27] D. J. C. Gomes, N. C. de Souza, and J. R. Silva, "Using a monocular optical microscope to assemble a wetting contact angle analyser," *Measurement*, vol. 46, no. 9, pp. 3623–3627, 2013.

[28] S. Hidaka, A. Yamashita, and Y. Takata, "Effect of contact angle on wetting limit temperature," *Heat Transf. Res. Co-sponsored by Soc. Chem. Eng. Japan Heat Transf. Div. ASME*, vol. 35, no. 7, pp. 513–526, 2006.

[29] S. Vogt, Q. Su, C. Gutiérrez-Sánchez, and G. Nöll, "Critical view on electrochemical impedance spectroscopy using the ferri/ferrocyanide redox couple at gold electrodes," *Anal. Chem.*, vol. 88, no. 8, pp. 4383–4390, 2016.

[30] A. I. Zia, S. C. Mukhopadhyay, A. I. Zia, and S. C. Mukhopadhyay, "Impedance spectroscopy and experimental setup," *Electrochem. Sens. Carcinog. Beverages*, pp. 21–37, 2016.

Chapter 3

Electrochemical Biosensors for Ciprofloxacin Detection

CHAPTER 3

ELECTROCHEMICAL BIOSENSORS FOR CIPROFLOXACIN DETECTION

This chapter exhibits the synthesis of lanthanum oxide nanoparticles(La_2O_3 NPs) and the composite of lanthanum oxide nanoparticles with reduced graphene oxide (La_2O_3@rGONPs) using the co-precipitation route and in-situ synthesis of nanocomposite and their characterization using various techniques. Thereafter, utilization of these nanoparticles and nanocomposite in developing the electrochemical-based biosensor for the detection of CPX antibiotic.La_2O_3 NPsandLa_2O_3@rGONPs are the first time explored in the detection of CPX. The novel electrochemical sensor is fabricated using ITO glass substrate, coated with lanthanum oxide nanomaterials, nanocomposite, and immobilization of receptors to design an efficient biosensing platform for selective analyte detection.

Part A: Designing and characterization of a highly sensitive and selective biosensing platform for ciprofloxacin detection utilizing lanthanum oxide nanoparticles

3.A1 Introduction

Antibiotics are being used widely in veterinary practices to manage livestock and inhibit microbial infections[1, 2]. Over-use and possibly fraudulent misuse of these antibiotics as dietary growth promoters necessitate the development of surveillance and monitoring technologies. After China and the USA, India is in third place in the consumption of antibiotics[3]. The over-usage of drugs has led to antibiotic resistance in bacteria, creating challenges for many societies, hospitals, and health centers due to increased patient numbers and costly treatment[4-6]. Quinolones, specifically fluoroquinolones (FQs), are highly significant antibiotic classes that effectively impede DNA synthesis. These compounds find extensive application in veterinary and aquatic

medicine [7, 8]. Ciprofloxacin (CPX), which is classified as a fluoroquinolone (FQ) antibiotic, exhibits remarkable stability within the human body and undergoes incomplete metabolism. Consequently, a significant portion, ranging from 30% to 90%, of ciprofloxacin remains unchanged [9, 10]. The increasing public apprehension regarding the buildup of drug residues in the food supply chain and livestock has prompted the widespread administration of this antibiotic. Nevertheless, it has been observed that CPX residues can pose a threat to human health by impacting the replication of mammalian cells and causing adverse reactions to drugs. There is a strong probability that it reaches the environment through patients' urine samples and wastewater due to inadequate metabolization of CPX in the body, which induces antibiotic resistance [4-6]. In the coming future, the phenomenon of antibiotic resistance will be more complex. The primary stumbling block is the failure to detect pathogenic bacteria, resulting in inadequate antibiotic use and a lower survival rate in septic situations. As a result, there is an urgent requirement to closely track the use and discharge of these medications in the atmosphere *via* the human body.

Several techniques for the detection of CPX have been used so far, including spectrophotometry [11], liquid chromatography-mass spectrophotometry [12], high-pressure liquid chromatography [13], immunoassay [14], chemiluminescence [15], capillary electrophoresis [16] and electrochemical techniques [17, 18]. The only disadvantage of these approaches is that they are all time-consuming, costly, complex methods, and they all necessitate advanced automation and the assistance of skilled users. Various efforts have been made to develop simple, rapid, inexpensive, and sensitive sensors for CPX detection electrochemically, as given in Table(3.3)[18-28]. Ganta et al. developed a disposable and cost-effective sensor for rapid detection of CPX in water with a linear range of 13.75-135 μM, a sensitivity of 0.031 μA μM^{-1}, with a limit of detection of 0.33 μM [25]. Gayen et al. fabricated an electrochemical sensor for CPX detection using multi-walled carbon nanotubes (MWCNTs) and boron-doped diamond electrodes. They got dynamic detection range from 0.005-0.05 μM and 0.05-10 μM and sensitivities of 41 μA μM^{-1} and 2.1 μA μM^{-1} in natural water and wastewater effluents, respectively [28]. Cinkovaet al. designed an electrochemical

method based on the boron-doped diamond electrode as a point of care detection (POC) for CPX within a concentration range from 0.74 to 20.0 $\times 10^{-6}$ M with a limit of detection (LOD) of 6.0×10^{-7} M [29]. Also, Yan et al. developed a simple and reliable molecularly imprinted polymer-based electrochemical sensor to determine CPX hydrochloride (HCl) with a linear range from 1×10^{9}-1×10^{-3}M with a detection limit of 7.58×10^{-11} M [30].

The establishment of an immobilization matrix for biosensing constitutes a crucial stage in the fabrication process of biosensors. The use of an immobilization matrix is crucial in achieving a biosensor with extended lifespan and dependable performance. Specifically, the biosensing element must be securely affixed to the electrode surface, safeguarding the integrity of the bioreceptor structure throughout the analysis process, thereby enabling the detection and tracking of the resulting electrical signal [31]. In recent times, researchers have shown considerable interest in rare earth metal oxides due to their lack of toxicity and remarkable electrocatalytic and electrochemical properties [32]. Among various rare earth metal oxides, nanostructured lanthanum oxide (nLa_2O_3) comes under the category of p-type semiconductors, having unique chemical and physical properties like electrochemical inertia, dielectric constant, high stability, and surface area to volume ratio, environmental friendliness, large bandgap (4.3 eV) and chemical co-ordination capability [33]. The electrochemical properties of nLa_2O_3 are primarily due to the transfer of electrons inside the 4f shell. Also, nLa_2O_3 offers more free binding or adsorption sites, resulting in increased bioactive molecule loading (antibodies) with improved biosensing electrode stability, making them an effective material for the application of biosensing. Cubic La_2O_3 is stable at low temperatures, whereas hexagonal La_2O_3 is more stable at high temperatures [34]. These kinds of metal oxides are explored in optical coatings, biomedicine, biosensors, magnetic resonance imaging, magnetic storage, optical devices, catalysts, Li-ion batteries, photoelectrochemical cells, supercapacitors, gas sensors, etc. [35]. Further, nLa_2O_3 is also not much explored as a sensing material for the fabrication of biosensors and, thus, was selected for electrochemical detection of CPX for the first time.

The present study involved the synthesis of n La_2O_3 nanoparticles (NPs) using the co-precipitation method, which is widely recognized as a straightforward and efficient process for NP synthesis. The nanoparticles of n La_2O_3, as they are synthesized, exhibit noteworthy physio-electrochemical characteristics. This leads to the creation of an electrochemical biosensor that is highly effective in detecting CPX. The biosensor demonstrates exceptional sensitivity, repeatability, stability, and selectivity. To the best of our current understanding, this study represents the initial effort in the development of an electrochemical-based immunosensor for the detection of CPX utilizing n La_2O_3 nanoparticles. The biofunctional substrate used for sensitive detection of target CPX from milk samples consisted of indium tin oxide (ITO) coated glass electrodes that were modified with n La_2O_3 NPs. Monoclonal antibodies against CPX (anti-CPX) were applied on this substrate. As a result of their outstanding properties, like better surface adhesion, wide electrochemical working area, good electrical conductivity, improved optical visibility, low cost, and robust physical and electrochemical features of ITO materials have attracted a lot of attention in recent years [36], several experiments using ITO materials as the working electrode have been conducted to develop optical and electrochemical sensors [32, 33, 37]. The developed immunosensor has shown outstanding biosensing parameters in two broad linear ranges from 0.001 - 0.5 ng/mL and 1 - 1000 ng/mL with two superior sensitivities of 11.44 μA ng^{-1} mL cm^{-2} (R^2=0.968) and 7.88 μA ng^{-1} mL cm^{-2} (R^2=0.972), and LOD of 1 pg/mL. The practical application of the developed CPX biosensor was also examined in the real milk sample. Consequently, this innovative immunosensor is appropriate for the amperometric detection of CPX in milk samples.

3.A2 Experimental Section

3.A2.1 Synthesis and Functionalization La_2O_3 NPs

Nanostructured La_2O_3 NPs were synthesized *via* the wet chemical co-precipitation method. For this, 0.1 M solution of $La(NO_3).4H_2O$ and 0.3 M NaOH solution were made in distilled water (DI). The addition of NaOH to the solution of $La(NO_3).4H_2O$ was done drop-wise till the pH of the solution became 14. It was observed that a white-

colored precipitate was formed at the end of the reaction that was filtered and washed with DI and ethanol using centrifugation for 20 min at 6000 rpm to neutralize the pH and remove the impurities. Finally, the resultant precipitate was dried at 80 °C for 12 h to obtain $La(OH)_3$ NPs. Then the product was crushed using a mortar pestle to obtain a fine powder of $La(OH)_3$ NPs. Further, the sample was calcined for 2 h at 800 °C to convert $La(OH)_3$NPs to nanostructured lanthanum oxide (nLa_2O_3 NPs). The biochemical reaction for the synthesis of nLa_2O_3 NPs was given in Scheme 3.1(a).

Moreover, the functionalization of nLa_2O_3NPs was achieved using (3-aminopropyl) tri methoxy silane (APTES). For this, 100 mg of nLa_2O_3 NPs was dissolved in 40 mL of isopropanol at the constant stirring of 250 rpm at 60 ˚C. When a highly dispersed solution of nLa_2O_3NPs was obtained, 200 µL of APTES (98%) was further added to with constant stirring at 300 rpm for 48 h at room temperature. Finally, washing the APTES/nLa_2O_3 NPs was done with DI to eliminate the unbound APTES, followed by drying and storing the sample in a dry place [38-40].

(a)

$$La(NO_3)_3.4H_2O + NaOH \xrightarrow{\text{1-1.5 Hour, 500 rpm, pH 14}} La(OH)_3 + NaNO_3$$

$$La(OH)_3\ (\text{Impure}) \xrightarrow{\text{Calcination at 800°C for 2 Hours}} La_2O_3(\text{Pure})$$

Scheme 3.1(a): Synthesis process of nLa_2O_3 nanoparticles.

3.A2.2 Deposition of Functionalized nLa_2O_3 NPs via Electrophoretic on ITO Electrode (APTES/nLa_2O_3/ITO)

A similar size, i.e., 1.5 x 0.5 cm of ITO-coated glass substrates, was taken, and its hydrolyzation was carried out with the mixture of H_2O: NH_4OH: H_2O_2 having a 5:1:1 ratio for 1 h at 80˚C followed by washing with DI and ethanol and dried in an oven at 60˚C. The smooth films of nLa_2O_3NPs were made on ITO-coated glass surface *via*theEPD technique as this method provides reproducible and uniform films. Before deposition, a stock colloidal solution of nLa_2O_3NPs (5 mg/mL) in ACN and isopropyl alcohol (1:1) was prepared, followed by ultra-sonication. In this, the platinum wire was utilized as the reference electrode, while indium tin oxide (ITO) was employed as the

working electrode, with the electrodes positioned 1 cm apart from each other. The surface area of APTES/nLa_2O_3NPs/ITO electrodes was determined as 0.25 cm^2. Further, 4 mL of ACN was taken in a cell carrying a two-electrode system along with 200 µL of stock APTES/nLa_2O_3 NPs solution, and 20 µL of magnesium ions [0.1 M] were added. After optimizing the parameters, the EPD of APTES/La_2O_3 NPs was achieved at 80 V for 2 min on ITO coated glass surface. The fabricated electrode was given a wash with ultrapure water, and dried at 25 ^oC overnight, and further used for FTIR, contact angle, and electrochemical studies such as DPV and CV.

3.A2.3 Fabrication of Biosensing Platform (BSA/anti-CPX/APTES/nLa_2O_3 NPs/ITO)

To fabricate the immunoelectrode, an anti-CPX (50 µg/mL) solution was freshly made in PBS of pH 7.0. Next, the anti-CPX solution was mixed with the EDC activator (0.4 M) and NHS coupling agent (0.2 M) in a ratio of 2:1:1 and stored at 4 ºC for 1 h. Subsequently, 30 µL of this solution was drop cast on the APTES/nLa_2O_3Nps/ITO electrode to form a uniform layer. This electrode was further retained for 6 h in a humid chamber at room temperature, after which washing was done with PBS to remove the unbound anti-CPX particles. To prevent the leaching-out of antibodies from the electrode surface, the carboxylic group (–COOH) present upon the Fc fragment of anti-CPX antibodies was involved in covalent bond formation with the amine group (-NH_2) of APTES silane molecules. EDC activated -COOH groups of anti-CPX antibodies, resulting in the generation of unstable O-acylisourea ester, which upon further reaction with the NHS, was converted to an amine-reactive NHS ester (a stable intermediate product). The anti-CPX antibody activation by NHS promotes the connection of –NH_2 groups of silane molecules (APTES), resulting in amide bond formation. Furthermore, 10 µL of BSA (2 %) was utilized as a blocking agent to cover non-specific areas on the surface of the anti-CPX/APTES/nLa_2O_3/ITO electrode by keeping it at 25 ºC in a humid chamber for 4 h. Finally, BSA/anti-CPX/APTES/nLa_2O_3Nps/ITO immunoelectrode was washed using PBS buffer and kept at 25 ºC when not in use. A step-wise fabrication process of the BSA/anti-CPX/APTES/nLa_2O_3Nps/ITO immunoelectrode was shown in Scheme 3.1(b).

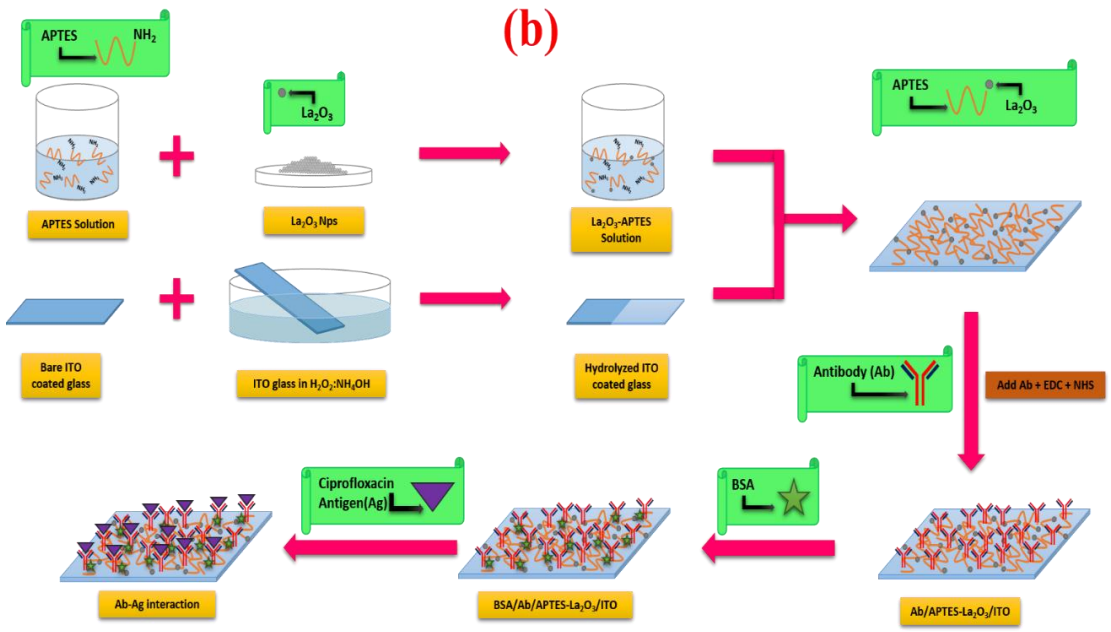

Scheme 3.1(b): The fabrication process of BSA/anti-CPX/ATPES/nLa_2O_3/ITO immunoelectrode for CPX detection.

3.A3 Results and Discussion

3.A3.1 X-ray Diffraction (XRD) Analysis

Figure 3.1 shows the X-ray diffraction (XRD) pattern of the synthesized product nLa_2O_3 after calcination at 800 °C that confirmed the crystalline structure and phase purity of nLa_2O_3 NPs. The XRD spectrum analysis was conducted in a 2θ angle range from 20° to 80° at room temperature. The peaks observed at 2θ=25.7°, 28.8°, 29.6°, 39.2°, 45.7°, 51.8°, 53.4°, 55.0°, 55.5°, 60.0°, 61.9°, 66.6°, 71.8°, 73.2°, 74.9°, and 78.8° correspond to hexagonal planes of nLa_2O_3 as (100), (002), (011), (012), (110), (103), (200), (112), (201), (004), (202), (014), (023), (210), (121) and (114), respectively. These data show good co-relation with JCPDS card no. 83-1344 for the hexagonal phase of nLa_2O_3. The sharp, strong, and well-defined peaks prove the high crystallinity of nLa_2O_3 NPs [41, 42]. After optimizing the calcination temperature (400 °C, 600 °C and 800 °C), the best results were seen at 800 °C, showing an increment in peaks intensity along with a reduction in FWHM as compared to the lower calcined temperature. Hence, XRD characterization confirms the formation of

the hexagonal phase of nLa_2O_3, and no additional impurity peaks were obtained in its XRD. The crystallite size (D) of as-synthesized nLa_2O_3 NPs was estimated using the Scherrer formula and was obtained as 30.9 nm relates to 2θ =29.6 (grain), as given below:

$$D = K\lambda/\beta \cos\theta \qquad \text{Eq.(3.1)}$$

Where β shows the full width at half maximum (FWHM) of the diffraction peak, θ shows the Bragg's diffraction angle, λ depicts the wavelength of the target Cu-Kα (1.540 Å), and K depicts the dimensionless shape factor (0.9).

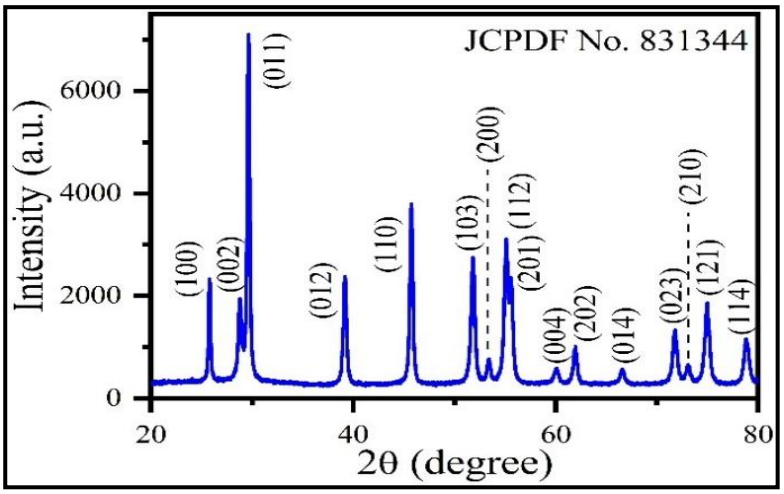

Figure 3.1: XRD spectra of nLa_2O_3 NPs

3.A3.2 Raman Analysis

Raman spectroscopy is a useful tool to observe phonon vibration modes of chemical bonds, especially in crystalline samples. This method is well-known for detecting the existence of secondary phases. This characterization technique is quite sensitive to microcrystals and could detect various defects in elaborated layers. Figure 3.2 shows the Raman active modes of nLa_2O_3 NPs at 190 cm^{-1}, 404 cm^{-1}, 452 cm^{-1}, and 557 cm^{-1}. Out of these peaks, 196 cm^{-1} is associated with hexagonal structure [43], while peaks at 404 and 452 cm^{-1} are associated with La–O stretching vibration and Eg^1 mode[44, 45]. However, due to the non-polarization effect in nLa_2O_3 NPs, some of the peaks are absent. Further, the XRD analysis also agrees with this finding.

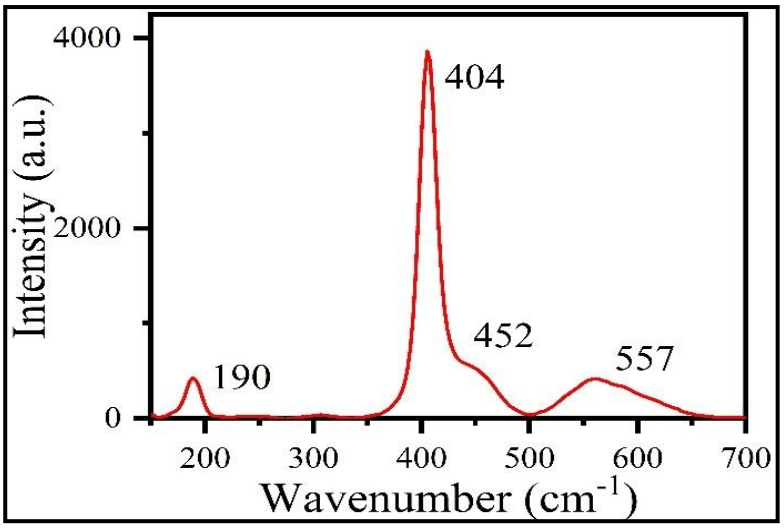

Figure 3.2: Raman spectra of La_2O_3 NPs

3.A3.3 Transmission Electron Microscopy (TEM) Study

The morphology, shape, and size of as-synthesized nLa_2O_3 NPs were investigated *via* transmission electron microscopy (TEM) [Figure 3.3 (A-D)]. The TEM image of nLa_2O_3 NPs at lower and higher magnification revealed that nLa_2O_3 NPs have irregular shapes that are highly agglomerated, as shown in Figure 3.3 (A and B). This is due to high surface energy and smaller sizes of nLa_2O_3 NPs, and they have a general tendency to clump together. Figure 3.3 (C and D) notably showed high-resolution TEM image (HR-TEM) and selected area electron diffraction (SAED) patterns of nLa_2O_3 NPs, respectively. The value of d-spacing is calculated to be 5.39 Å, which relates to the (011) plane of the hexagonal nLa_2O_3 NPs. Moreover, the highly crystalline nature of nLa_2O_3 NPs was confirmed by the SAED ring pattern, which is well indexed to (011), (012), (110), (103), and (112) planes of hexagonal nLa_2O_3 NPs (JCPDS NO. – 83-1344) as it is a known fact that polycrystalline materials show a ring pattern, whereas single-crystal materials show a spotty diffraction pattern in SAED [46]. Thus, the rings obtained are well-defined, which indicates the high crystallinity of nLa_2O_3 NPs that show polycrystalline nature. Further, these results are also found to be in good agreement with the XRD data.

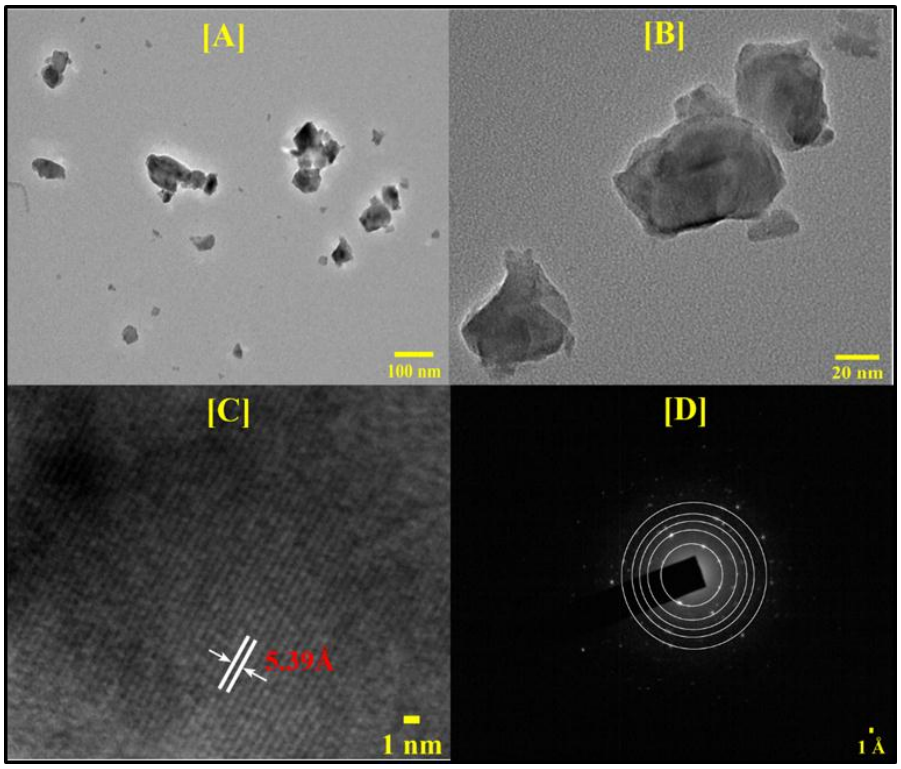

Figure 3.3: [A and B] TEM image.[C] HR-TEM image, and [D] SAED pattern of nLa_2O_3 NPs.

3.A3.4 Fourier Transform Infrared (FT-IR) Spectroscopy Study

Figure 3.4 [A] shows the FTIR spectra of the nLa_2O_3 NPs calcined at 800 °C in the wavenumber range (4000–400 cm^{-1}). The existence of O–H stretching, consistent with absorbed moisture on the sample surface, is confirmed by the strong bands found at 3574 cm^{-1}, 3557 cm^{-1}, and 3453 cm^{-1} [41]. The asymmetric and symmetric stretching of -COO functional groups were responsible for the peaks at 1638 and 1329 cm^{-1} and the sharp bands at 1487 and 1428 cm^{-1} [42]. The intense bands at 858 cm^{-1} are connected to C–O bending vibrations, while another band at 1074 cm^{-1} is linked to C–O stretching vibrations. The large bands at 696 and 636 cm^{-1} are caused by La–O stretching, while the small bands at 552 cm^{-1} are caused by La–O bending vibrations. As a result, the inclusion of these La–O stretching and bending vibration bands supports nLa_2O_3 phases in NPs samples [47]. The -OH and -NH stretching vibrations of water molecules are also represented by the peak present at 3340 cm^{-1} in Figure 3.4 [B]. The –C=O stretching and amide II peak formed between the -COOH group of the anti-CPX and -NH_2 present on the APTES/nLa_2O_3/ITO were seen at 1071 and 991 cm^{-1}, supporting the

antibodies attachment on the functionalized nano-hybrid [40]. As shown in Figure 3.4 [C], the peak at 1487 and 1428 cm^{-1} disappeared, and peak intensities of 1071 and 991 cm^{-1} got shrunk, which confirmed the blocking of immunoelectrode with BSA molecules.

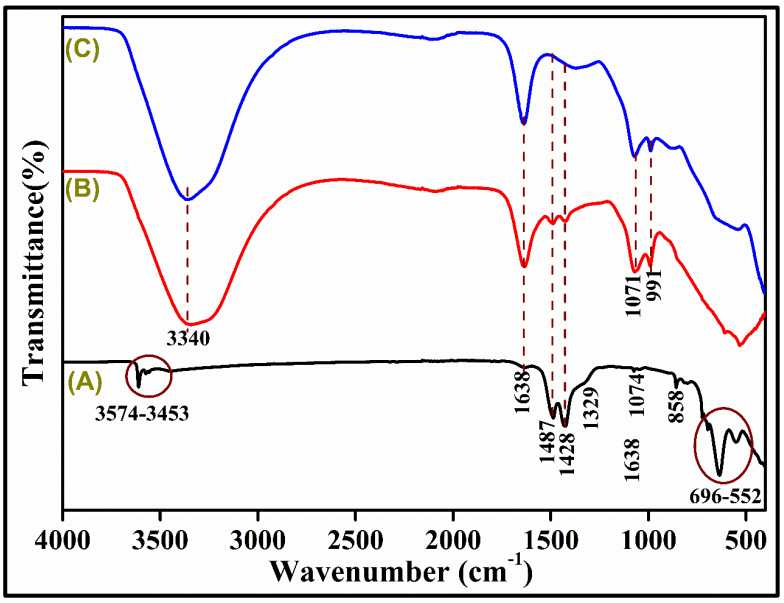

Figure 3.4: FTIR spectra of (A) APTES/nLa_2O_3/ITO; (B) anti-CPX/nLa_2O_3/ITO; and (C) BSA/anti-CPX/nLa_2O_3/ITO electrode.

3.A3.5 Contact Angle

The wettability and hydrophilicity of the electrode's surface were strongly influenced by its chemistry. The wettability calculation is necessary as the operative charges stay on the surface of the electrode. For this, the water contact angle (CA) of ITO, nLa_2O_3/ITO, anti-CPX/nLa_2O_3/ITO, and BSA/anti-CPX/nLa_2O_3/ITO immunoelectrode are calculated in a static state [Figure 3.5]. Using a syringe, a drop of water was kept on each electrode surface, and a measurement of the contact angle at the electrode surface's interface was done. The ITO touch angle was estimated at 73.4°, showing that it is hydrophobic [Figure 3.5 (A)]. The CA of the nLa_2O_3/ITO electrode was 25.6° [Figure 3.5 (b)], indicating more hydrophilic than ITO. The enhanced hydrophilic activity of the nLa_2O_3/ITO electrode creates ideal conditions for monoclonal anti-CPX adsorption. The interface angle value was decreased to 0° after immobilization of bioactive molecules such as anti-CPX and BSA on the nLa_2O_3/ITO electrode [Figure

3.5 (C and D)], indicating a significant rise in hydrophilic properties of anti-CPX/nLa_2O_3/ITO; and BSA/anti-CPX/nLa_2O_3/ITO immunoelectrodes owing to the covalent association between anti-CPX and nLa_2O_3/ITO electrode [38, 48].

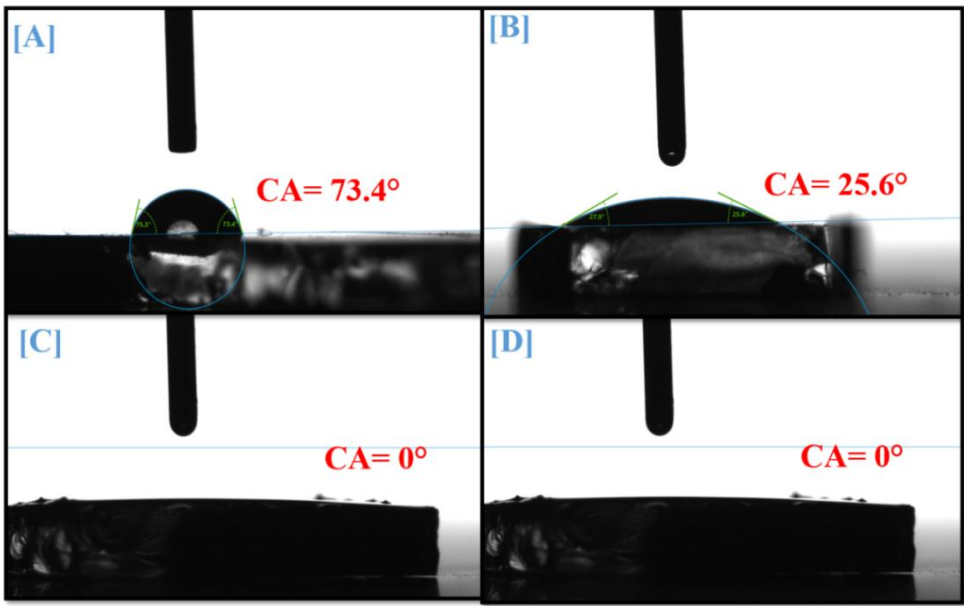

Figure 3.5: Contact angle of (A) ITO; (B) APTES/nLa_2O_3/ITO; (C) anti-CPX/nLa_2O_3/ITO; and (D) BSA/anti-CPX/nLa_2O_3/ITO electrode.

3.A3.6 Atomic Force Microscopy (AFM) Study

The utilization of Atomic Force Microscopy (AFM) enables the acquisition of high-resolution images in the tapping mode, facilitating the examination of surface morphology, thickness, uniformity, and roughness of nLa_2O_3/ITO and anti-CPX/nLa_2O_3/ITO electrodes. Figure 3.6 (a) shows the AFM images of the nLa_2O_3/ITO electrode obtained from the co-precipitation method at room temperature and calcination at 800 °C. The findings indicated that the ITO surface exhibited a smooth texture and granular topography, with a dense composite material evenly distributed across its surface. The Ra value of nLa_2O_3 was found as -4.98×10^{-9} nm. Further,3.6 (b) displayed the AFM images of anti-CPX/nLa_2O_3/ITO electrode that showed globular structures due to the covalent attachment of anti-CPX with increased Ra value of -4.60×10^{-9} nm.

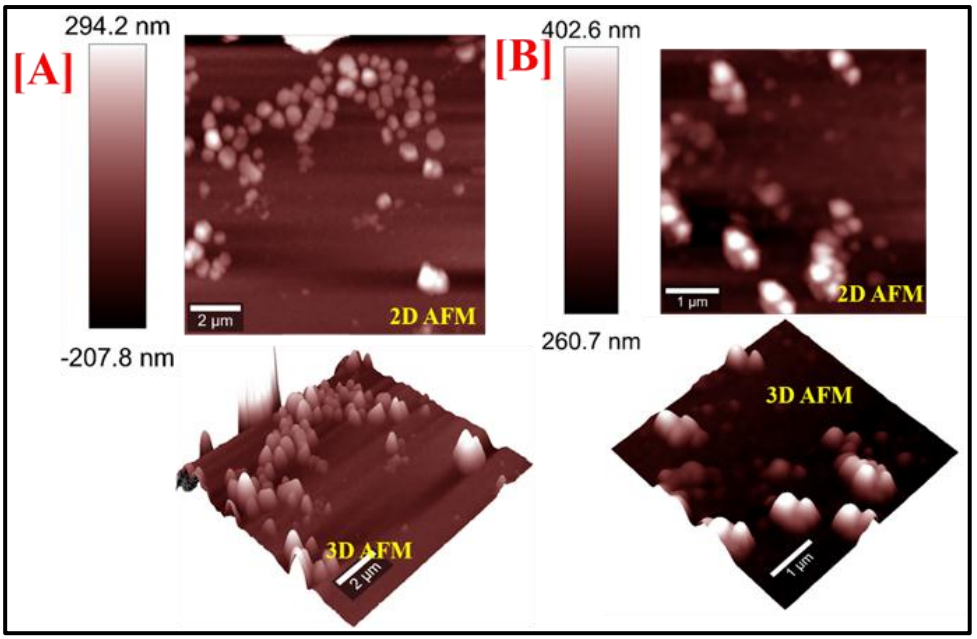

Figure 3.6: Atomic force microscopy of 2D and 3D images of [A] nLa_2O_3/ITO electrode; and [B] anti-CPX/nLa_2O_3/ITO immunoelectrode.

3.A4 Electrochemical Studies

3.A4.1 Optimization Study

Optimizing the different experimental conditions is vital for constructing a reproducible, repeatable, and sensitive biosensor. The effect of pH, the concentration of anti-CPX and BSA molecules, and the interaction period between anti-CPX and CPX were examined before the characterization to obtain the optimal experimental conditions. The concentration of bioactive molecules like antibodies and BSA had an impact on the immunosensor response. As a result, anti-CPX concentrations ranging from 10 to 70 g/mL were measured; the outcomes are depicted in Figure 3.7(a). The optimum anti-CPX concentration associated with the nLa2O3/ITO electrode was determined using the DPV approach. As shown in Figure 3.7(a), peak currents increased when anti-CPX concentration increased from 10 to 50 g/mL; however, peak currents then decreased at anti-CPX concentrations of 60 and 70 g/mL. The anti-CPX dilution was chosen to further immobilize the nLa2O3/ITO electrode at a concentration of 50 g/mL. Furthermore, by changing the BSA concentration from 0.5 to 4%, the change in peak current is shown in Figure 3.7 (b). The increase in the peak current was

observed from 0.1 to 2%; before reaching stability, which is why 2% BSA was chosen to block the non-specific electrode sites.

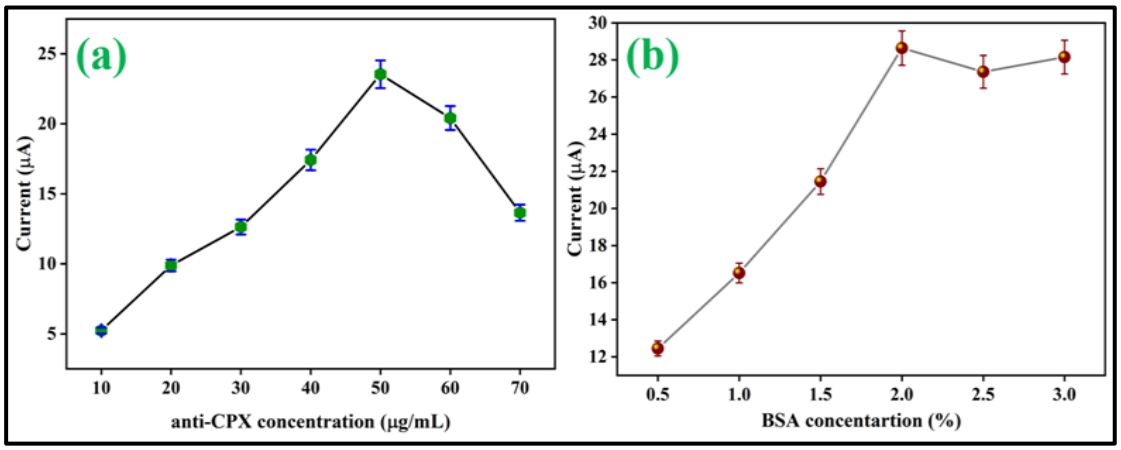

Figure 3.7: Effect of the immobilization of anti-GEN concentration (a) and the BSA concentration (b).

3.A4.2 pH Study

Structural conformations of biomolecules are dependent on the pH of the buffer, which affects the antibody-antigen interaction. Thus, the pH effect has been evaluated before electrochemical studies. The pH study has been done using the DPV technique at 50 mVs^{-1} scan rate and using 5 mV step potential at 0.5 ms intervals in the potential range of -0.4 to 0.8 V in PBS of different pH (6.0-8.0) having Ferro-Ferri to investigate the electro-kinetics of anti-CPX present on the designed immunoelectrode. At pH 7.0, maximum peak current is observed for BSA/anti-CPX/ ATPES/nLa_2O_3/ITO immunoelectrode [Figure 3.8 (a)], as the biomolecules show powerful activity at pH 7.0, i.e., in their pure form while at basic or acidic pH, the polypeptides of antibodies are deactivated due to excessive OH^- or H^+ ions [49]. Based on the results, all the further electrochemical studies were carried out at pH 7.0.

3.A4.3 Electrode Study

Moreover, the steps included in the synthesis of the BSA/anti-CPX/ATPES/nLa_2O_3/ ITO immunoelectrode over the surface of bare ITO were electrochemically inspected by using DPV plots of the ITO (curve i), APTES/nLa_2O_3/ITO (curve ii), anti-

CPX/ATPES/nLa_2O_3/ITO (curve iii) and BSA/anti-CPX/ATPES/nLa_2O_3/ITO (curve iv) immunoelectrode as illustrated in Figure 3.8 (c). The DPV curves were employed at 50 mVs^{-1} scan rate and employing a 5 mV step potential at 0.5 ms interval in the -0.4 to 0.8 V potential range. The DPV plots of all the electrodes displayed symmetry, with bare ITO exhibiting the lowest peak current among all the electrodes (i.e., curve i; 22.67 μA). Among the modified electrodes, the deposition of APTES/nLa_2O_3 on the ITO electrode enhanced this current to 25.15 μA because of the rise in the transfer of electrons between the APTES/nLa_2O_3/ITO electrode and medium (curve ii). A significant decrease was seen after immobilizing the anti-CPX monoclonal antibodies, i.e., anti-CPX/APTES/nLa_2O_3/ITO immunoelectrode (curve iii; 22.98 μA), which might be due to the bulky size and insulating nature of anti-CPX antibodies where Ferro-Ferri species were captured into macrostructure of antibodies [50]. Furthermore, the blocking of non-specific areas at anti-CPX/APTES/nLa_2O_3/ITO immunoelectrode surface was carried out by immobilization of BSA, which resulted in an apparent rise in peak current of BSA/anti-CPX/APTES/nLa_2O_3/ITO immunoelectrode (curve iv; 28.71 μA). This is due to the metal oxide associated with the zwitterionic nature of BSA and thus alters the isoelectric point at the interface of the electrolyte and electrode, which can lead to an increase in the current [51, 52]. The connection between BSA and metal ions can also help establish an electron transfer route between electrolyte-rich electrons and electrodes, increasing current [48]. The same conclusion is given by CV studies, as shown in Figure 3.8 (b).

The electrochemical impedance spectroscopic studies of ITO, APTES/nLa_2O_3/ITO, anti-CPX/APTES/nLa_2O_3/ITO, and BSA/anti-CPX/APTES/nLa_2O_3/ITOhave been done in PBS (pH 7.0) solution containing $[Fe(CN)_6]^{3-/4-}$ in the frequency range of 100 kHz to 10 Hz [Figure 3. 8 (d)]. The charge transfer resistance (Rct) of various electrodes is displayed in the semicircle of the Nyquist plot and depends on the dielectric properties of the electrolyte and the electrode surface. In Figure 3.8(d), curve (i) Represents the Nyquist plot of ITO, curve (ii) represents the APTES/nLa_2O_3/ITO, curve (iii) anti-CPX/APTES/nLa_2O_3/ITO and curve (iv) represent BSA/anti-CPX/APTES/nLa_2O_3/ITO

immunoelectrode. For the ITO glass substrate, the value of R_{ct} was 2.70kΩ, which is the highest. After the APTES functionalized nLa2O3 NPs were deposited onto the ITO surface, the value of R_{ct}as 925Ω, however, decreased, showing the strong conductivity for APTES functionalized nLa2O3 NPs with high dissemination of $Fe(CN)_6]^{3-/4-}$to the electrode.

However, the value of R_{ct} slightly increases to 1.36kΩ for the anti-CPX/APTES/ nLa_2O_3/ITO immunoelectrode after the covalent immobilization of anti-CPX to the free NH_2 sites of APTES functionalized nLa_2O_3 NPs. The spatial orientation of the anti-CPX molecule on the electrode surface, which promotes a decreased charge transfer between $[Fe(CN)_6]^{3-/4-}$. The functional group (NH_2) of anti-CPX, is responsible for this increase in the value of Rct. After immobilizing BSA on the anti-CPX/APTES/ nLa_2O_3/ITO immunoelectrode, Rct increases (2.44kΩ) due to an increase in the transfer of charge between the electrode surface and $[Fe(CN)_6]^{3-/4-}$.

The K_{ct} for all corresponding electrodes was given in Table 3.1andwas calculated using Eq. (3.2):

$$\text{Kct} = \frac{RT}{n^2F^2\text{ARct[S]}} \qquad \text{Eq.(3.2)}$$

Where [S] is the redox probe's concentration (mol cm-3), F is the Faraday constant, A is the electrode's surface area (cm^2), and n is the number of electrons transferred per $[Fe(CN)_6]$3-/4-, molecule.T (absolute temperature), and R (gas constant).

Table 3.1: Characteristics of different Electrodes' ElS Study

Electrode	**R_{ct}**	**K_{ct}**
ITO	2700 Ω	7.88×10^{-9} cms^{-1}
APTES/nLa_2O_3/ITO	1360 Ω	1.56×10^{-7} cms^{-1}
anti-CPX/APTES/nLa_2O_3/ITO	2440 Ω	8.72×10^{-8} cms^{-1}
BSA/anti-CPX/APTES/nLa_2O_3/ITO	925 Ω	2.30×10^{-7} cms^{-1}

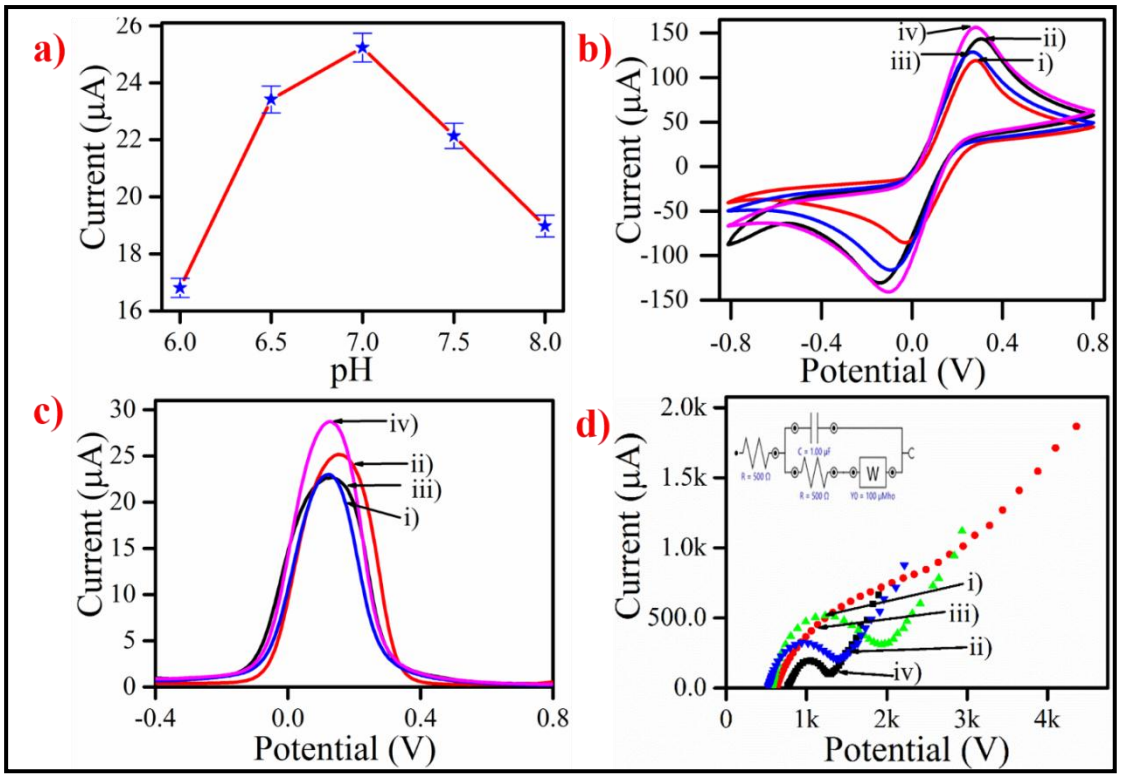

Figure 3.8: (a) Shows the effect of various pH concentration on BSA/anti-CPX/APTES/ nLa_2O_3/ITO immunoelectrode; (b) CV, (c) DPV, and (d) FRA of (i) ITO; (ii) nLa_2O_3/ITO, (iii) anti-CPX/APTES/nLa_2O_3/ITO, and (iv) BSA/anti-CPX/APTES/nLa_2O_3/ITO immunoelectrode.

3.A4.4 Scan Rate Studies

The cyclic voltammetric (CV) techniques were accompanied to explore the response of the nLa_2O_3/ITO electrode and BSA/anti-CPX/ATPES/nLa_2O_3/ITO immunoelectrode at the interface of the electrode surface and electrolyte with increasing scan rate from 10 mV/sto 100 mV/s and the observed results are shown in Figure 3.9 (a)and (b), respectively. Figure 3.9 (a) and (b), upper inset, shows a linear relationship between the peak currents (Ipc and Ipa) and the square root of scan rate (v1/2), indicating that diffusion controls the redox reaction primarily as the redox species move to and from the redox centers at the BSA/anti-CPX/ATPES/nLa_2O_3/ITO immunoelectrode surface. The Ipa/Ipc value is 1.1 for BSA/anti-CPX/ATPES/nLa_2O_3/ITO immunoelectrode, which is nearly 1, indicating electron transfer is quasi-reversible, approaching reversible kinetics. Although Ipa/Ipc value is 1.05 for the nLa_2O_3/ITO electrode, it demonstrates the occurrence of an irreversible allocation

movement of electrons. As displayed in the upper inset of Figure 3.9 (a)and (b), the slopes and intercepts can be examined from Eqs. (3.3-3.6).

$Ipc_{(APTES/La2O3/ITO)}$ = -[16.365μA (s/mV)×(scan rate [mV/s])$^{1/2}$] – 30.97μA, R^2 = 0.992 (Eq. 3.3)

$Ipa_{(APTES/La2O3/ITO)}$ = [20.177μA (s/mV)×(scan rate [mV/s])$^{1/2}$] + 22.679μA, R^2 = 0.992 (Eq. 3.4)

$Ipc_{(BSA/anti-CPX/APTES/La2O3/ITO)}$ = -[16.059μA(s/mV)×(scan rate [mV/s])$^{1/2}$] – 45.64μA, R^2 = 0.992 (Eq. 3.5)

$Ipa_{(BSA/anti-CPX/APTES/La2O3/ITO)}$ = [19.631μA (s/mV)×(scan rate [mV/s])$^{1/2}$] + 37.09μA, R^2 = 0.996 (Eq. 3.6)

With an increased scan rate, a minor shift in the peak potential was seen, showing the quasi-reversibility of the redox reaction occurring at the electrode surface. In addition, the potential peak shift among the cathodic peak potential (EPC) and the anodic peak potential (Epa) (ΔEp = Epa– Epc) was found to vary linearly (R^2 = 0.99) in case of nLa_2O_3/ITO electrode (0.17 V) and BSA/anti-CPX/ATPES/nLa_2O_3/ITO immunoelectrode (1.22 V), with square root of scan rate as per Eqs.3.7-3.10 (Figure 3.9 (a) and (b), lower inset), indicating enhanced electro-catalytic behavior of the fabricated electrode.

$\Delta Ep(V_a)_{(APTES/La2O3/ITO)}$= [0.0162V(s/mV)×(scan rate [mV/s])$^{1/2}$] + 0.1520 V, R^2=0.992 (Eq. 3.7)

$\Delta Ep(V_c)_{(APTES/La2O3/ITO)}$= [0.0143V(s/mV)×(scan rate [mV/s])$^{1/2}$] + 0.0217 V, R^2=0.992 (Eq. 3.8)

$\Delta Ep(V_a)_{(BSA/anti-CPX/APTES/La2O3/ITO)}$= [0.016V(s/mV)×(scan rate [mV/s])$^{1/2}$]+ 0.160V, R^2= 0.994 (Eq. 3.9)

$\Delta Ep(V_c)_{(BSA/anti-CPX/APTES/La2O3/ITO)}$= -[0.017V(s/mV)×(scan rate [mV/s])$^{1/2}$]+ 0.032V, R^2= 0.941 (Eq. 3.10)

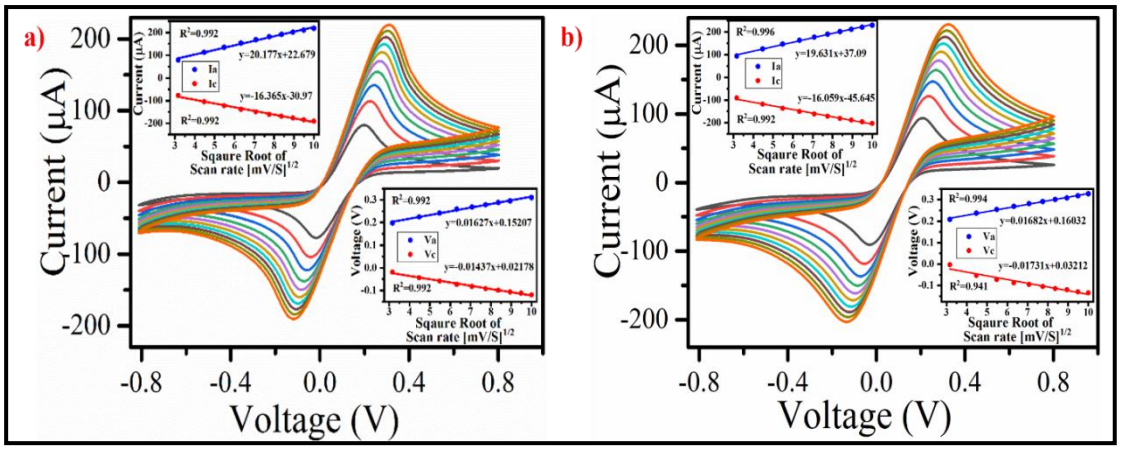

Figure 3.9: (a) Represent the CV plot at different scan rates (10-100 mV/s) for (a) nLa_2O_3/ITO; and (b)BSA/anti-CPX/ATPES/nLa_2O_3/ITOimmunoelectrode in PBS with $[Fe(CN)_6]^{3-/4-}$. Peak current (Ipa and Ipc) vs. scan rate (upper) and peak potentials (Epa and Epc) vs. scan rate (lower) for the corresponding electrodes were shown in the corresponding insets.

For ATPES/nLa_2O_3/ITO electrode and BSA/anti-CPX/ATPES/nLa_2O_3/ITO immunoelectrode, the values of kinetic interface factor as diffusion constant (D), surface concentration of redox probe of the electrode (I^*), effective electroactive surface area (A_e), and standard heterogeneous electron transfer rate constant (K_s) were measured to look at the movement of electrons. Table 3.2 lists the electrode-corresponding interface kinetic parameters. Using the Randles-Sevcik equation 3.11, the diffusion coefficient (D) at the immunoelectrode surface and electrolyte interface with redox species $[Fe(CN)_6]^{3-/4-}$ was calculated;

$$Ip = (2.69\times10^5)\, C\, n^{3/2}\, D^{1/2}\, v^{1/2}\, A \qquad \text{Eq.3.11}$$

The symbol Ip (Ipa or Ipc) represents the peak current of the electrodes. In this context, 'n' denotes the number of electrons involved in the redox process, which is equal to 1. The variable A represents the surface area of the immunoelectrode, specifically 0.25 cm^2. D represents the coefficient of diffusion, measured in cm^2s^{-1}. C represents the concentration of electrolytes, and v represents the scan rate, measured in volts (V). When compared to ATPES/nLa_2O_3/ITO (5.0510-4 cm^2s^{-1}), BSA/anti-CPX/ATPES/nLa_2O_3/ITO ((5.0510-4 cm^2s^{-1}) immunoelectrode's higher value of D shows a higher rate of electron transfer at the electrolyte/electrode interface.

The obtained value of D by the Randles-Sevcikh equation has been applied to the following equation 3.12 to determine the value of the efficient and effective electroactive surface area (Ae) of the unmodified electrode ATPES/nLa2O3/ITO and BSA/anti-CPX/ATPES/nLa_2O_3/ITO immunoelectrode:

$$Ae = \frac{S}{(2.69\times10^5)n^3\ CD^{1/2}} \qquad \text{Eq.3.12}$$

Where Ipa is plotted against the square root of the scan rate ($v^{1/2}$) [in $(mV/s)^{1/2}$], and S is the slope of the linear curve resulting from that analysis. Table 3.2 provides the calculated values. The electroactive area (A_e) of the BSA/anti-CPX/ATPES/nLa_2O_3/ITO immunoelectrode is 62.10×10^3 mm^2, which is higher than that of the ATPES/nLa_2O_3/ITO electrode (29.70×10^3 mm^2) and indicates that it is more suitable for having more reaction sites/unit volume due to the immobilization of biomolecules (i.e., BSA and antibody).

The linear relationship between I_{pa}value of the scan rate for ATPES/nLa_2O_3/ITO electrode and BSA/anti-CPX/ATPES/nLa_2O_3/ITO immunoelectrode exhibited a consistent phase of electroactive species on the electrodes. In addition, the determination of the surface concentration of the absorbed electroactive ionic species (I* in $molcm^2$) for the respective electrodes has been performed through the utilization of the Brown-Anson equation 3.13, as stated below;

$$I_p = \frac{n^2F^2I^*\ A\ V}{4\ R\ T} \qquad \text{Eq.3.13}$$

The F represents the Faraday constant is equal to 96485 C mol^{-1}. T denotes the ambient temperature is approximately 300 K, and last R denotes the gas constant is about(8.314 mol^{-1} K^{-1}). In comparison to ATPES/nLa_2O_3/ITO electrode 1.45×10^{-8}mol cm^2, the surface concentration (I*) for BSA/anti-CPX/ATPES/nLa_2O_3/ITOimmunoelectrode(1.52×10^{-8}mol cm^2)is approximately higher, indicating that the presence of BSA and biomolecules at the surface has an enhanced electro-catalytic behavior.

Both the scan rate and the heterogeneous electron transfer rate constant (K_s) affect the reversibility of the electron transfer kinetics. According to Laviron Equation 3.14, the K_s values for the ATPES/nLa_2O_3/ITO electrode and the BSA/anti-CPX/ATPES/nLa_2O_3/ITO immunoelectrode are 0.690 s^{-1} and 0.733 s^{-1}, respectively. The immunoelectrode (shown in

Table 3.2) exhibited a higher Ks value, demonstrating that the electron exchange between the electrode surface and electrolyte redox species is fast.

$$K_s = \frac{mn\,Fv}{RT} \qquad \text{Eq.3.14}$$

Where m- is the potentials' peak-to-peak separating (V). The immunoelecrode BSA/anti-CPX/ATPES/nLa_2O_3/ITO has higher interface kinetic parameters than the ATPES/nLa_2O_3/ITO electrode, indicating that biomolecules like Ab and BSA have a significant impact on the enhancement of electron transfer at the interface of electrolyte and immunoelectrode.

Table 3.2: Projected values of interface kinetic parameters corresponding to both electrodes.

Electrode	**D** ($cm^2\,s^{-1}$)	**A_e** (mm^2)	**I^*** (mol cm^2)	**K_s** (s^{-1})	**I_{pa}** (A)	**I_{pc}** (A)
ATPES/nLa_2O_3/ITO	5.05×10^{-4}	29.70×10^{3}	1.52×10^{-8}	0.733	$1.69E^{-4}$	$1.49E^{-4}$
BSA/anti-CPX/ATPES/ nLa_2O_3/ITO	5.54×10^{-4}	62.10×10^{3}	1.45×10^{-8}	0.690	$1.77E^{-4}$	$1.61E^{-4}$

3.A4.5 Electrochemical Response Study

Initially, the duration needed to stabilize the current response of the synthesized BSA/anti-CPX/ATPES/nLa_2O_3/ITO immunoelectrode towards CPX (10 ng/mL) was adjusted and achieved results are summarized in Figure 3.10 (a). Results exhibited erratic behavior till 12 min followed by constant value suggesting that the optimal time needed for complete attachment of CPX molecule to anti-CPX is 12 min and was selected as the ideal incubation time for further experiments.

The DPV response was applied to examine the variation in the electrochemical response of BSA/anti-CPX/ATPES/nLa_2O_3/ITO immunoelectrode with increasing concentration of CPX from 1 pM to 1 μM (1 pM, 100 pM, 500 pM, 1 nM, 10 nM, 100 nM, 500 nM, and 1μM), recorded in the −0.2 V to +0.6 V potential range with 12 min as incubation time. The current response was increased linearly with the addition of each CPX concentration as illustrated in [Figure 3.10 (b)] within the concentration range 1 pM to 1μM due to interaction that occurred between CPX molecules and anti-CPX on the electrode surface and became constant after 1μM. On the addition of CPX

concentration, there is a rise in the peak current mainly due to the CPX and anti-CPX complex formation over the BSA/anti-CPX/ATPES/nLa_2O_3/ITO immunoelectrode surface, further resulting in the development of an electron transfer accelerating layer at the surface of biosensor [53]. The development of an electron transfer accelerating layer on the surface of the BSA/anti-CPX/APTES/nLa_2O_3/ITO immunoelectrode by the interaction between the CPX and anti-CPX might explain the increase in anodic peak current with regard to increasing CPX concentration. The positively charged immune complex attracted the negatively charged redox probe $[Fe(CN)_6]^{3-/4-}$, enhancing the redox reaction at the electrode surface and resulting in an increase in current when CPX is added.

Linear calibration curves were observed at two distinct concentration ranges, as depicted in Figure 3.10 (c). Two distinct linear behavior were obtained one in the range of 0.001-0.5 ng/mL(slope =2.86 μA ng/mL, R^2 = 0.968) and another in 1-1000 ng/mL (slope = 1.97 μA ng/mL, R^2 = 0.972). The initial sharp rise in current value could be credited to prompt interaction between CPX and anti-CPX on BSA/anti-CPX/ATPES/nLa_2O_3/ITO immunoelectrode surface. A slower increase in peak current is due to a decrease in the concentration of freely available anti-CPX on the surface of the electrode with Ag-CPX. The equations (3.15) and (3.16) obtained from linear plots between peak current and CPX concentration are:

$$IP = [(2.86\ \mu A\ ng^{-1}) * log(conc.of\ CPX\left(\frac{ng}{mL}\right))] + 33.07; R^2 = 0.96 \quad \text{Eq. (3.15)}$$

$$IP = [(1.97\ \mu A\ ng^{-1}) * log(conc.of\ CPX\left(\frac{ng}{mL}\right))] + 37.48; R^2 = 0.972 \quad \text{Eq. (3.16)}$$

The sensitivity of BSA/anti-CPX/ATPES/nLa_2O_3/ITO immunoelectrode was assessed from the calibration curve' slope/surface area of the electrode, i.e., 0.25 cm^2, as 11.44 μA ng^{-1} mL cm^{-2} (R^2=0.968) and 7.88 μA ng^{-1} mL cm^{-2} (R^2 = 0.972) of the linear plots [54]. Further, formula 3σ/k has been used to calculate the lower detection limit of the immunoelectrode, where 'k' denotes the slope of linear calibration and 'σ' denotes the standard deviation of the intercept. The obtained lower detection limit of BSA/anti-CPX/ATPES/nLa_2O_3/ITO immunoelectrode is 0.001 ng/mL. The obtained linear range of BSA/anti-CPX/ATPES/nLa_2O_3/ITO immunoelectrode is from 1 pM to 1 μM. From

obtained results; it could be inferred that the immunoelectrode exhibited high sensitivity, wide linear range, low detection limit, and faster response time for CPX. The results were also compared with earlier published research articles in Table 3.3. Moreover, the reproducibility and repeatability of sensing studies were evaluated three times.

Compared to previous studies (Table 3.3), the optimized BSA/anti-CPX/APTES/nLa_2O_3/ITO immunosensor had a higher sensitivity, lower LOD, and a broader detection range than other sensors. This was due to the modified antibodies, which expanded the amount of reactive functional groups on the ITO electrode, resulting in more effective CPX binding. Furthermore, the procedure was soft, causing no harm to the electrode surface, which was beneficial for responsive CPX identification. This study presents the inaugural report on the development of an electrochemical immunosensor for the detection of CPX, based on nLa_2O_3 NPs in 12 minutes at low concentration (1 pg/mL) and high sensitivity (11.44 μA ng^{-1} mL cm^{-2})as evidenced by our comprehensive literature review.

Figure 3.10 (d) displays the Hanes-wolf plot [(CPX concentration) versus (CPX conc/ΔI)] of BSA/anti-CPX/ATPES/nLa_2O_3/ITO immunoelectrode. The K_d value is estimated by dividing the intercept of the linear curve by the slope. The decreased K_d value of immunoelectrode (1.7 ng/mL) demonstrates a stronger binding affinity towards CPX.

Table 3.3: Comparison of BSA/anti-CPX/ATPES/nLa_2O_3/ITO biosensor to previously reported bio-sensor for CPX detection.

Sensor/Biosensor	**Technique**	**Sensitivity [μA $μM^{-1}$]**	**LOD (μM)**	**Linear Range (μM)**	**Sample**	**Ref.**
$MgFe_2O_4$-MWCNT/GCE	CV	-	0.01	0.1−1000	Tablet, plasma, and urine	[18]
PAR/EGR/GCE	DPV	-	0.01	0.04–10 and 10–120	Pharmaceutical preparation and biological media	[19]
P-β-CD-L-arg/CPE	DPV	-	0.05	0.05-100	Pharmaceutical formulations and human serum	[20]
DNA biosensor	DPV	-	9	40–80	-	[21]
NiONPs-GO-CTS: EPH/GCE	SWV	9.87	6.0×10^{-3}	0.040–0.97	Urine, serum	[22]
MWCNT/GCE	CA	-	6	40–1000	Urine and serum	[23]

Sensor/Biosensor	**Technique**	**Sensitivity [μA μM^{-1}]**	**LOD (μM)**	**Linear Range (μM)**	**Sample**	**Ref.**
CZF/CPE	ASV	0.657	2.58× 10^{-3}	0.909 - 4.70×10^{3}	Urine, serum, pharmaceutical preparations	[24]
SPE	CA	0.031	0.33	13.75–135	DI water	[25]
TiO_2/PB/AuNPs/ CMK-3/Nafion/GE	CV	15.93	1.08× 10^{-1}	1–10	Environmental water	[26]
NP-GCE	DPV	-	0.008	0.25–100	Groundwater and tap water	[27]
Porous-Nafion-MWCNT/BDD	DPV	41 ± 5.2 and 2.1 ± 0.22	0.005	0.005−0.05, 0.05−10	Natural waters and wastewater effluents	[28]
BSA/anti-CPX/ APTES/nLa_2O_3/ ITO	**DPV**	**11.44 and 7.88**	**0.000001**	**0.000001-0.0005 and 0.001-1**	**Milk**	**This work**

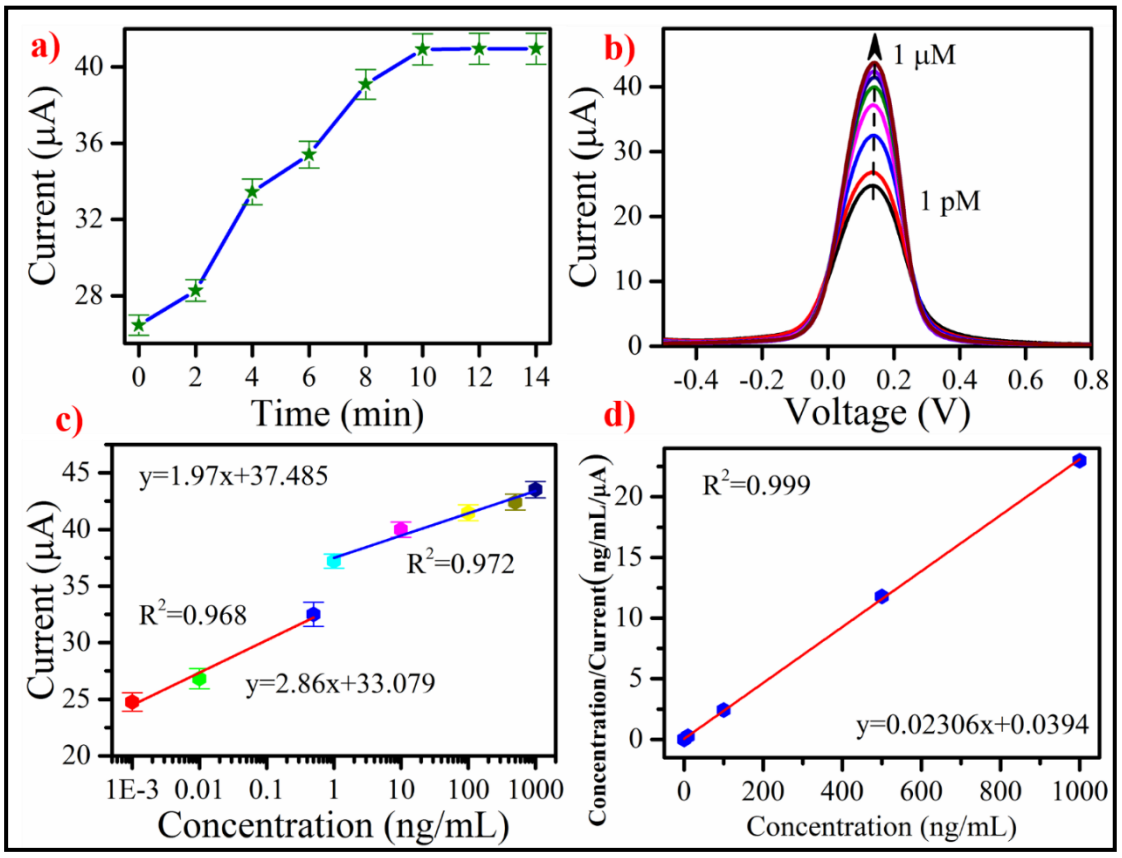

Figure 3.10: (a) Incubation study; (b) DPV response studies of BSA/anti-CPX/ATPES/nLa_2O_3/ITO immunoelectrode with different CPX concentrations in 0.2 M PBS (pH 7.0) containing $[Fe(CN)_6]^{3-/4-}$; (c) Calibration curve of BSA/anti-CPX/ATPES/nLa_2O_3/ITO immunoelectrode between peak current and concentration of CPX; and (d) Hanes-wolf Graph plot for BSA/anti-CPX/ATPES/nLa_2O_3/ITO immunoelectrode.

3.A4.6 Control, Interference, Spiked, Reproducibility, Repeatability, and Stability Studies

Furthermore, a controlled experiment was carried out to validate that CPX- anti-CPX interaction is the sole reason behind electrochemical responses displayed by BSA/anti-CPX/ATPES/nLa_2O_3/ ITO immunoelectrode upon exposure to CPX [Figure 3.11 (a)]. For this, the ATPES/nLa_2O_3/ITO electrode response was recorded at varying CPX concentrations. Even at higher concentrations, no substantial variation was observed in electrode responses. Thus, these results can verify the importance of CPX- anti-CPX interactions towards the response of immunosensors. Moreover, from obtained results, it could be stated that the surface of the ATPES/nLa_2O_3/ITO electrode is inert towards the CPX molecule. Specificity plays an essential role in the examination of the sensing performance of a biosensor. To evaluate specificity, changes in the electrochemical responses of the designed BSA/anti-CPX /ATPES/nLa_2O_3/ITO immunoelectrode were investigated by DPV studies in the presence of interfering agents [Figure 3.11 (b)]. Initially, the biosensor response was obtained in the presence of CPX (10 ng/mL), which showed an increased current value due to CPX and anti-CPX interaction. Further, different interferents (generally present in milk) were added sequentially, including BSA [100 μM], Glucose [100 μM], Norfloxacin [5 mM], Levofloxacin [5 mM], and Calcium ions (Ca^{2+}) [0.015 g/100 mL]. Negligible changes (0-1 %) were noticed in the peak response after the addition of various interferents. Therefore, it can be concluded that the designed BSA/anti-CPX/ATPES/nLa_2O_3/ITO immunoelectrode is not affected by the presence of different interferents, and it is a great candidate to detect CPX for practical usage.

Further, the workability of developed BSA/anti-CPX/ATPES/nLa_2O_3/ITO immunoelectrode in actual sample was evaluated using a spiked sample of milk. CPX recovery percentage and the obtained RSD from spiked milk samples (summarized in Table 3.4) are 95.9 – 101.3 % and 0.91–2.89 %, respectively, illustrated in Figure 3.11 (c). The estimated values demonstrate improved accuracy and reliability of the sensor, thereby confirming its suitability for analyzing real milk samples.

Table 3.4: Recovery of CPX from milk samples using BSA/anti-CPX/ATPES/nLa_2O_3/ITO immunoelectrode.

CPX Added to the milk sample	DPV peak current for CPX (µA)	DPV peak current of spike-sample (µA)	Relative Standard Deviation (%)	Recovery (%)
1 pM	26.824	27.163	0.89	101.263
100 pM	32.501	31.324	2.69	96.378
500 pM	37.200	35.810	2.69	96.263
1 nM	39.978	38.601	2.45	96.588
10 nM	41.473	42.013	0.91	101.302
100 nM	42.419	42.968	0.91	101.294
500 nM	43.518	43.863	2.74	96.196
1 µM	43.762	44.011	2.89	95.998

Repeatability and reproducibility results are vital parameters in immunosensor fabrication. To examine the reproducibility of the fabricated biosensor, six immunoelectrodes were developed in the same set of conditions and studied using the DPV. The obtained RSD value for reproducibility was 2.73 % of the BSA/anti-CPX/ATPES/nLa_2O_3/ITO immunoelectrode, as illustrated in Figure 3.11 (d). The reproducibility of immunoelectrode was within a reasonable range. The repeatability of the BSA/anti-CPX/ATPES/nLa_2O_3/ITO immunoelectrode was monitored by studying DPV response at the particular concentration (100 ng/mL) of CPX [Figure 3.11 (e)]. RSD for consecutive measurements (6 times) was found at 1.51 %. The repeatability experiment of BSA/anti-CPX/ATPES/nLa_2O_3/ITO immunoelectrode was satisfactory.

The shelf-life of BSA/anti-CPX/ATPES/nLa_2O_3/ITO immunoelectrode was assessed over a period of 40 days, with measurements taken every 5 days using the differential pulse voltammetry (DPV) technique. According to Figure 3.11 (f), the immunoelectrode demonstrates a retention of 90% of the peak current up to the 20th day. Subsequently, a notable decline in electrical current was observed, indicating that the immunosensor exhibits favorable stability for a duration of 20 days. The fabricated BSA/anti-CPX/ATPES/nLa_2O_3/ITO biosensor was kept in the refrigerator when not in utilization.

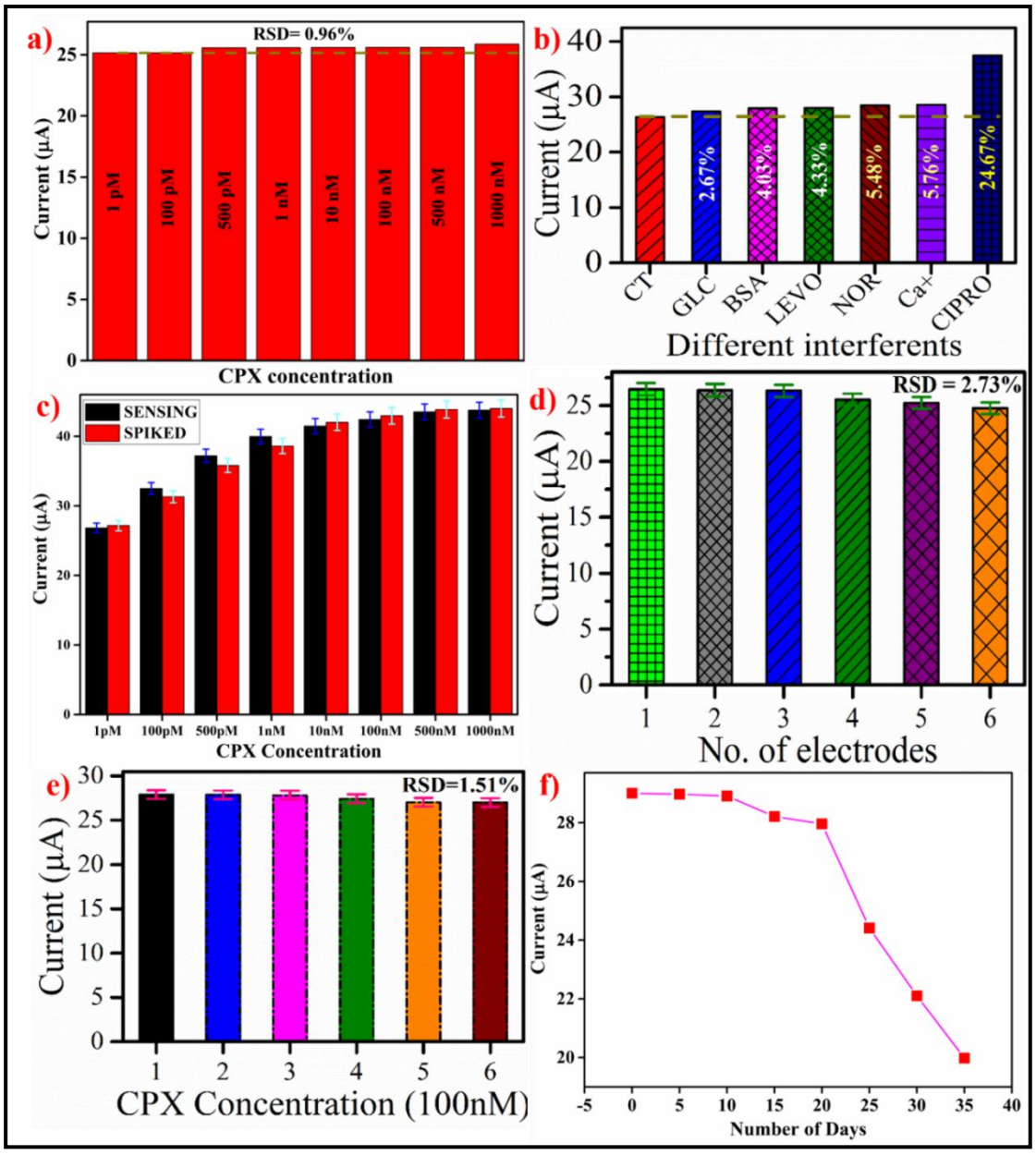

Figure 3.11: (a) Control study; (b) Interferent study; (c) Spiked sample study in milk; (d) Reproducibility study; (e) Repeatability study; and (f) Stability study.

As nanomaterials have a large surface area, they could be used for loading a large number of bio-recognition molecules like enzymes, antibodies, and DNA. for amplifying the electrochemical response. Thus, it is essential to synthesize nanomaterials having good biocompatibility and electrochemical properties using a simple and cost-effective technique. Keeping this in mind, in the present study, nLa_2O_3 NPs were synthesized using a facile, easy, economical, and rapid technique called the

co-precipitation method without using any harsh conditions (temperature, pressure, etc.). This method was adopted to obtain water-soluble nanoparticles directly with much higher yields. Further, this method offers several advantages, including control over the shape, morphology, and properties of the prepared nanomaterials [19]. The nanoparticles of nLa_2O_3, in their original form, have demonstrated notable physio-electrochemical characteristics, leading to the creation of an electrochemical biosensor with exceptional efficiency for detecting CPX. This biosensor exhibits excellent sensitivity, repeatability, stability, and selectivity.Moreover, it is believed that the fabricated biosensing platform could be used for detecting other various antibiotics or other analytes by substituting the specific bio-recognition molecules against the target analyte. However, the key challenge for developing the biosensor using nLa_2O_3 NPs was the sensitivity, as the antibiotics are found to be highly diluted in milk samples. Therefore, it is highly required to improve the sensitivity of the biosensor by utilizing other nanomaterials (graphene, carbon nanotubes, etc.) in combination with the existing one.

3.A5 References

[1] R. M. Kalunke, G. Grasso, R. D'Ovidio, R. Dragone, and C. Frazzoli, "Detection of ciprofloxacin residues in cow milk: a novel and rapid optical β-galactosidase-based screening assay," *Microchemical Journal,* vol. 136, pp. 128-132, 2018.

[2] A. Yadav, D. Verma, and P. Solanki, "Electrophoretically deposited L-cysteine functionalized MoS2@ MWCNT nanocomposite platform: a smart approach toward highly sensitive and label-free detection of gentamicin," *Materials Today Chemistry,* vol. 22, p. 100567, 2021.

[3] R. Laxminarayan and R. R. Chaudhury, "Antibiotic resistance in India: drivers and opportunities for action," *PLoS medicine,* vol. 13, p. e1001974, 2016.

[4] F. Toldrá and M. Reig, "Methods for rapid detection of chemical and veterinary drug residues in animal foods," *Trends in Food Science & Technology,* vol. 17, pp. 482-489, 2006.

[5] L. Chen, Z. Wang, M. Ferreri, J. Su, and B. Han, "Cephalexin residue detection in milk and beef by ELISA and colloidal gold based one-step strip assay," *Journal of agricultural and food chemistry,* vol. 57, pp. 4674-4679, 2009.

[6] G. R. Marchesini, W. Haasnoot, P. Delahaut, H. Gerçek, and M. W. Nielen, "Dual biosensor immunoassay-directed identification of fluoroquinolones in chicken muscle by liquid chromatography electrospray time-of-flight mass spectrometry," *Analytica chimica acta,* vol. 586, pp. 259-268, 2007.

[7] Y. Zhu, L. Li, Z. Wang, Y. Chen, Z. Zhao, L. Zhu, *et al.*, "Development of an immunochromatography strip for the rapid detection of 12 fluoroquinolones in chicken muscle and liver," *Journal of agricultural and food chemistry,* vol. 56, pp. 5469-5474, 2008.

[8] P. Higgins, A. Fluit, and F. Schmitz, "Fluoroquinolones: structure and target sites," *Current drug targets,* vol. 4, pp. 181-190, 2003.

[9] M. C. Dodd, A. D. Shah, U. von Gunten, and C.-H. Huang, "Interactions of fluoroquinolone antibacterial agents with aqueous chlorine: reaction kinetics, mechanisms, and transformation pathways," *Environmental science & technology*, vol. 39, pp. 7065-7076, 2005.

[10] G. Carlsson, S. Örn, and D. J. Larsson, "Effluent from bulk drug production is toxic to aquatic vertebrates," *Environmental Toxicology and Chemistry*, vol. 28, pp. 2656-2662, 2009.

[11] S. Mostafa, M. El-Sadek, and E. A. Alla, "Spectrophotometric determination of ciprofloxacin, enrofloxacin and pefloxacin through charge transfer complex formation," *Journal of pharmaceutical and biomedical analysis*, vol. 27, pp. 133-142, 2002.

[12] H. Y. Ji, D. W. Jeong, Y. H. Kim, H.-H. Kim, D.-R. Sohn, and H. S. Lee, "Hydrophilic interaction liquid chromatography–tandem mass spectrometry for the determination of levofloxacin in human plasma," *Journal of pharmaceutical and biomedical analysis*, vol. 41, pp. 622-627, 2006.

[13] G. Carlucci, "Analysis of fluoroquinolones in biological fluids by high-performance liquid chromatography," *Journal of Chromatography A*, vol. 812, pp. 343-367, 1998.

[14] G. G. Snitkoff, D. W. Grabe, R. Holt, and G. R. Bailie, "Development of an Immunoassay for Monitoring the Levels of Ciprofloxacin Patient Samples," *Journal of Immunoassay and Immunochemistry*, vol. 19, pp. 227-238, 1998.

[15] H.-W. Sun, L.-Q. Li, and X.-Y. Chen, "Flow-injection enhanced chemiluminescence method for determination of ciprofloxacin in pharmaceutical preparations and biological fluids," *Analytical and bioanalytical chemistry*, vol. 384, pp. 1314-1319, 2006.

[16] R. H. Montes, M. C. Marra, M. M. Rodrigues, E. M. Richter, and R. A. Muñoz, "Fast determination of ciprofloxacin by batch injection analysis with amperometric detection and capillary electrophoresis with capacitively coupled contactless conductivity detection," *Electroanalysis*, vol. 26, pp. 432-438, 2014.

[17] A. Radi, M. El Ries, and S. Kandil, "Electrochemical study of the interaction of levofloxacin with DNA," *Analytica chimica acta,* vol. 495, pp. 61-67, 2003.

[18] A. A. Ensafi, A. R. Allafchian, and R. Mohammadzadeh, "Characterization of MgFe2O4 nanoparticles as a novel electrochemical sensor: application for the voltammetric determination of ciprofloxacin," *Analytical Sciences,* vol. 28, pp. 705-710, 2012.

[19] X. Zhang, Y. Wei, and Y. Ding, "Electrocatalytic oxidation and voltammetric determination of ciprofloxacin employing poly (alizarin red)/graphene composite film in the presence of ascorbic acid, uric acid and dopamine," *Analytica chimica acta,* vol. 835, pp. 29-36, 2014.

[20] F. Zhang, S. Gu, Y. Ding, Z. Zhang, and L. Li, "A novel sensor based on electropolymerization of β-cyclodextrin and l-arginine on carbon paste electrode for determination of fluoroquinolones," *Analytica chimica acta,* vol. 770, pp. 53-61, 2013.

[21] H. Nawaz, S. Rauf, K. Akhtar, and A. M. Khalid, "Electrochemical DNA biosensor for the study of ciprofloxacin–DNA interaction," *Analytical biochemistry,* vol. 354, pp. 28-34, 2006.

[22] A. M. Santos, A. Wong, A. A. Almeida, and O. Fatibello-Filho, "Simultaneous determination of paracetamol and ciprofloxacin in biological fluid samples using a glassy carbon electrode modified with graphene oxide and nickel oxide nanoparticles," *Talanta,* vol. 174, pp. 610-618, 2017.

[23] L. Fotouhi and M. Alahyari, "Electrochemical behavior and analytical application of ciprofloxacin using a multi-walled nanotube composite film-glassy carbon electrode," *Colloids and Surfaces B: Biointerfaces,* vol. 81, pp. 110-114, 2010.

[24] M. P. Kingsley, P. K. Kalambate, and A. K. Srivastava, "Simultaneous determination of ciprofloxacin and paracetamol by adsorptive stripping voltammetry using copper zinc ferrite nanoparticles modified carbon paste electrode," *RSC advances,* vol. 6, pp. 15101-15111, 2016.

[25] D. Ganta, N. Trevino, and W. Montes, "Disposable chronoamperometric sensor for detecting ciprofloxacin," *Engineering Research Express*, vol. 1, p. 015031, 2019.

[26] A. Pollap, K. Baran, N. Kuszewska, and J. Kochana, "Electrochemical sensing of ciprofloxacin and paracetamol in environmental water using titanium sol based sensor," *Journal of Electroanalytical Chemistry*, vol. 878, p. 114574, 2020.

[27] T. Chen, Y. Liu, J. Lu, J. Xing, J. Li, T. Liu, *et al.*, "Highly efficient detection of ciprofloxacin in water using a nitrogen-doped carbon electrode fabricated through plasma modification," *New Journal of Chemistry*, vol. 43, pp. 15169-15176, 2019.

[28] P. Gayen and B. P. Chaplin, "Selective electrochemical detection of ciprofloxacin with a porous nafion/multiwalled carbon nanotube composite film electrode," *ACS applied materials & interfaces*, vol. 8, pp. 1615-1626, 2016.

[29] K. Cinková, D. Andrejcakova, and L. Svorc, "Electrochemical method for point-of-care determination of ciprofloxacin using boron-doped diamond electrode," *Acta Chimica Slovaca*, vol. 9, pp. 146-151, 2016.

[30] C. Yan, J. Li, T. Meng, X. Liu, R. Zhang, Y. Chen, *et al.*, "Selective recognition of ciprofloxacin hydrochloride based on molecular imprinted sensor via electrochemical copolymerization of pyrrole and o-phenylenediamine," *International Journal of Electrochemical Science*, vol. 11, pp. 6466-6476, 2016.

[31] S. Soylemez, Y. A. Udum, M. Kesik, C. G. Hızlıateş, Y. Ergun, and L. Toppare, "Electrochemical and optical properties of a conducting polymer and its use in a novel biosensor for the detection of cholesterol," *Sensors and Actuators B: Chemical*, vol. 212, pp. 425-433, 2015.

[32] P.-p. Wang, B. Bai, S. Hu, J. Zhuang, and X. Wang, "Family of multifunctional layered-lanthanum crystalline nanowires with hierarchical pores: hydrothermal synthesis and applications," *Journal of the American Chemical Society*, vol. 131, pp. 16953-16960, 2009.

[33] M. R. Sovizi and S. Mirzakhani, "A chemiresistor sensor modified with lanthanum oxide nanoparticles as a highly sensitive and selective sensor for dimethylamine at room temperature," *New Journal of Chemistry,* vol. 44, pp. 4927-4934, 2020.

[34] A. Weidenkaff, R. Robert, M. Aguirre, L. Bocher, T. Lippert, and S. Canulescu, "Development of thermoelectric oxides for renewable energy conversion technologies," *Renewable Energy,* vol. 33, pp. 342-347, 2008.

[35] H. Kabir, S. H. Nandyala, M. M. Rahman, M. A. Kabir, Z. Pikramenou, M. Laver, *et al.*, "Polyethylene glycol assisted facile sol-gel synthesis of lanthanum oxide nanoparticles: Structural characterizations and photoluminescence studies," *Ceramics International,* vol. 45, pp. 424-431, 2019.

[36] H. Tang, W. Zhang, P. Geng, Q. Wang, L. Jin, Z. Wu, *et al.*, "A new amperometric method for rapid detection of Escherichia coli density using a self-assembled monolayer-based bienzyme biosensor," *Analytica Chimica Acta,* vol. 562, pp. 190-196, 2006.

[37] S. Tiwari, P. K. Gupta, Y. Bagbi, T. Sarkar, and P. R. Solanki, "L-cysteine capped lanthanum hydroxide nanostructures for non-invasive detection of oral cancer biomarker," *Biosensors and Bioelectronics,* vol. 89, pp. 1042-1052, 2017.

[38] A. K. Yadav, D. Verma, G. Lakshmi, S. Eremin, and P. R. Solanki, "Fabrication of label-free and ultrasensitive electrochemical immunosensor based on molybdenum disulfide nanoparticles modified disposable ITO: An analytical platform for antibiotic detection in food samples," *Food Chemistry,* vol. 363, p. 130245, 2021.

[39] C. Chaudhary, S. Kumar, and R. Chandra, "Monophasic molybdenum selenide-reduced graphene oxide nanocomposite sheets based immunosensing platform for ultrasensitive serotonin detection," *Microchemical Journal,* vol. 159, p. 105344, 2020.

[40] S. Kumar, J. G. Sharma, S. Maji, and B. D. Malhotra, "Nanostructured zirconia decorated reduced graphene oxide based efficient biosensing platform for non-invasive oral cancer detection," *Biosensors and Bioelectronics,* vol. 78, pp. 497-504, 2016.

[41] X. Wang, M. Wang, H. Song, and B. Ding, "A simple sol–gel technique for preparing lanthanum oxide nanopowders," *Materials Letters,* vol. 60, pp. 2261-2265, 2006.

[42] M. Salavati-Niasari, G. Hosseinzadeh, and F. Davar, "Synthesis of lanthanum carbonate nanoparticles via sonochemical method for preparation of lanthanum hydroxide and lanthanum oxide nanoparticles," *Journal of alloys and compounds,* vol. 509, pp. 134-140, 2011.

[43] A. Orera, G. Larraz, and M. Sanjuán, "Spectroscopic study of the competition between dehydration and carbonation effects in La2O3-based materials," *Journal of the European Ceramic Society,* vol. 33, pp. 2103-2110, 2013.

[44] J. Denning and S. Ross, "The vibrational spectra and structures of rare earth oxides in the A modification," *Journal of Physics C: Solid State Physics,* vol. 5, p. 1123, 1972.

[45] J. Cui and G. A. Hope, "Raman and Fluorescence Spectroscopy of CeO_2, Er_2O_3, Nd_2O_3, Tm_2O_3, Yb_2O_3, La_2O_3, and Tb_4O_7," *Journal of Spectroscopy,* vol. 2015, 2015.

[46] R. B. Borade, S. E. Shirsath, G. Vats, A. S. Gaikwad, S. M. Patange, S. Kadam, *et al.*, "Polycrystalline to preferred-(100) single crystal texture phase transformation of yttrium iron garnet nanoparticles," *Nanoscale Advances,* vol. 1, pp. 403-413, 2019.

[47] Q. Zhou, H. Zhang, F. Chang, H. Li, H. Pan, W. Xue, *et al.*, "Nano La2O3 as a heterogeneous catalyst for biodiesel synthesis by transesterification of Jatropha curcas L. oil," *Journal of Industrial and Engineering Chemistry,* vol. 31, pp. 385-392, 2015.

[48] A. K. Yadav, T. K. Dhiman, G. Lakshmi, A. N. Berlina, and P. R. Solanki, "A highly sensitive label-free amperometric biosensor for norfloxacin detection based on chitosan-yttria nanocomposite," *International journal of biological macromolecules,* vol. 151, pp. 566-575, 2020.

[49] D. Chauhan, A. K. Yadav, and P. R. Solanki, "Carbon cloth-based immunosensor for detection of 25-hydroxy vitamin D 3," *Microchimica Acta,* vol. 188, pp. 1-11, 2021.

[50] M. Garg, M. Chatterjee, A. L. Sharma, and S. Singh, "Label-free approach for electrochemical ferritin sensing using biosurfactant stabilized tungsten disulfide quantum dots," *Biosensors and Bioelectronics,* vol. 151, p. 111979, 2020.

[51] A. V. Singh, B. M. Bandgar, M. Kasture, B. Prasad, and M. Sastry, "Synthesis of gold, silver and their alloy nanoparticles using bovine serum albumin as foaming and stabilizing agent," *Journal of Materials Chemistry,* vol. 15, pp. 5115-5121, 2005.

[52] A. Singh, R. Patil, M. Kasture, W. Gade, and B. Prasad, "Synthesis of Ag–Pt alloy nanoparticles in aqueous bovine serum albumin foam and their cytocompatibility against human gingival fibroblasts," *Colloids and Surfaces B: Biointerfaces,* vol. 69, pp. 239-245, 2009.

[53] S. Kumar, S. Kumar, S. Augustine, and B. D. Malhotra, "Protein functionalized nanostructured zirconia based electrochemical immunosensor for cardiac troponin I detection," *Journal of Materials Research,* vol. 32, pp. 2966-2972, 2017.

[54] G. Lakshmi, A. K. Yadav, N. Mehlawat, R. Jalandra, P. R. Solanki, and A. Kumar, "Gut microbiota derived trimethylamine N-oxide (TMAO) detection through molecularly imprinted polymer based sensor," *Scientific reports,* vol. 11, pp. 1-14, 2021.

Part B:Electrochemical immunosensor based on nanostructured lanthanum oxide substituted reduced graphene oxide interface for ultralow ciprofloxacin detection in spiked milk samples

3.B1 Introduction

CPX is a 2^{nd-}generation fluoroquinolone utilized as an antibiotic against Gram-negative and Gram-positive aerobic pathogens and is broadly applied to livestock and humans[1]–[5]. CPX has been discovered in surface waters that are strongly affected by domestic wastewater and agricultural runoff effluents because the medicine is not fully metabolized [6]. Additional investigations have found CPX in cow's milk at concentrations greater than 0.1-100 ng mL^{-1}. The presence of CPX and other antibiotics in the environment is a matter of great concern due to the potential growth of antibiotic-resistant bacteria [7],[8]. The presence of antibiotics in various environmental matrices, including milk, surface water, and wastewater, has prompted ongoing research efforts towards the development of selective and sensitive sensors.

Many analytical techniques are being employed to determine CPX indifferent matrices, which include electrochemical[9][10], immunoassay[11], Spectro fluorimetric[12], capillaryelectrophoresis[13], chemiluminescence[14], spectrophotometry[15], [16], high-performance liquid chromatography[17] and liquid chromatography−mass spectroscopy[18] techniques. However, these analysis methods require expensive instrumentation, complex sample pre-treatment, and preparation, which cannot meet actual large-scale testing [19][20]. Moreover, some of them require the separation of the analytes before detecting them, which were expensive and not simple detection methods. To overcome these disadvantages, a more cost-effective, simple, authentic, and rapid approach to CPX determination is needed. The electrochemical techniques, such as impedance spectroscopy and voltammetry, have garnered significant research interest for the detection of antibiotics. This is primarily due to their ability to enhance the signal power to noise power ratio, their simplicity, excellent sensitivity, low energy consumption, rapid output time, user-friendly nature, short processing time, and cost-effectiveness. [21][22][23].

The immobilization matrix's role in the fabrication of nano-immunosensing platforms is inevitable. Different metal oxides, for example, ZnO, TiO_2, MgO, Fe_3O_4, etc., have occupied a profound position as an efficient matrix support[24], [25]. Among the metal oxides, nanostructured lanthanum oxide nanoparticles (nLa_2O_3 NPs) have gained more scientific curiosity among the research community, as they have a large surface area to volume ratio, excellent electrochemical properties, biocompatibility, and high adsorption ability[26]–[28]; thus, could be efficiently employed for high biomolecules loading with desired alignment. Moreover, nLa_2O_3 NPs also allow covalent bonding between the hydroxyl of ITO and silane groups of organosilanes (like APTES). Though many studies have described nLa_2O_3 NPs to form massive clusters owing to aggregation, functionalizing different metal oxides could deliver high surface area and high sensitivity for homogeneous dispersion of metal oxides and analyte detection [29], [30].

Two-dimensional materials have gained consideration as promising candidates that could increase surface area for metal oxide dispersion. Several studies in the past have shown that graphene and its derivatives, such as reduced graphene oxide (rGO), graphene oxide, etc., have been used as sensing materials[31]. Among the derivatives, rGO containing different oxygen functional groups has displayed immense potential in the fabrication of nano-immunosensing platforms owing to its distinct properties, likeability for facilitating electron transfer directly from biomolecules, high catalytic activity, good mechanical flexibility, remarkable conductivity, and excellent heterogeneous electron transfer[32]–[34]. The high surface area to volume ratio of rGO may help in the dispersion of metal oxides, thus preventing the NPs agglomeration. The attachment of metal oxide on the surface of the rGO sheet will help decrease the steric hindrance occurring between the biomolecules[35]. In addition, the electrochemical performance is also reported to increase the large surface area and conductivity support for metal oxides[36]. AnrGO sheet decorated with nLa_2O_3 NPs-based biosensors has been effectively used for immobilization of enzyme and chlorpyrifos pesticide detection. Gupta and co-workers displayed the electrochemical characteristics improvement and ZrO_2 NPs low-agglomeration by using ZrO_2-rGOcomposite for Ochratoxin determination A[37]. Also, in another research, homogenized zirconia-

supported rGO has been employed as an efficient immobilization substrate for oral cancer detection [38]. In addition, 2D materials are being consistently used for point-of-care (POC) device development, ascribed to their outstanding mechanical strength, favorable flexibility, tailor-made chemical, and physical properties, etc. Several reports have employed these 2D material-based biosensors to determine various environmental and metabolic imperfections risk factors comprising toxins and pathogens [39][40]. Withthese contemplations in mind, nLa_2O_3NPs@rGO composite appears to be highly effective immobilization substrate for nano-immunosensing platform development in which both thecomponents synergistically pay off each other's limitations.

Most research on sensor development is focused on CPX detection in tablets, water, urine, and human serum, but the application of its sensor to determine CPX in milk matrices has not been performed. Therefore, this work devised a fast, selective, and sensitive method for detecting CPX in milk by indium tin oxide (ITO) electrode modification with a conductive, nLa_2O_3NPs@rGO film. Various modified electrodes were fabricated and set for testing to obtain selectivity and sensitivity toward CPX determination. The determination of CPX was conducted through the utilization of electrochemical techniques, specifically cyclic voltammetry (CV) and differential pulse voltammetry (DPV), on various modified electrodes. The immunoelectrodes that were created underwent various characterization techniques including X-ray diffraction (XRD), Raman spectroscopy, Fourier-transform infrared spectroscopy (FT-IR), energy-dispersive X-ray spectroscopy (EDS), elemental mapping, scanning electron microscopy (SEM), transmission electron microscopy (TEM), contact angle measurement, differential pulse voltammetry (DPV), and cyclic voltammetry (CV) using common redox couples. The optimized immunosensor was utilized to detect CPX in processed milk and other interfering agents. The fabricated immunosensor has displayed remarkable biosensing parameters having linear ranges of 10^{-6} - 600μgmL^{-1} with a sensitivity of 6.52μA mL $\mu g^{-1} cm^{-2}$ with regression coefficient (R^2) of 0.992 and LOD and LOQ of 0.055μgmL^{-1} and 0.18 μg mL^{-1}, respectively. To the best of our knowledge, this is the first report on an antibiotic (CPX) detection using nLa_2O_3NPs@rGOcomposite.

3.B2 Experimental Section

3.B2.1 Graphene Oxide (GO) synthesis

The modified Hummer method was employed for the synthesis of graphene oxide (GO) using graphite flakes as the starting material. Firstly, 8 g of $K_2S_2O_8$ and 8 g of P_2O_5 were made into a solution with 24 mL of H_2SO_4. The solution was further heated at 80 °C, and finally,3 g of graphite flakes were added. The solution was left to stir for 6 hours after being diluted with 350 mL of distilled water. After that, the solution is left to dry in the air for the whole night. Further, oxidized graphite was added to 92 mL of H_2SO_4 solution that was cooled to 0 °C in the ice bath. Briefly, 12 g of $KMnO_4$ was added slowly to this mixture while maintaining the temperature below 10 °C.

Furthermore, after 15 minutes, 1 gram of $NaNO_3$ was added to the above solution for 2 hours at 35 °C, and to maintain the temperature below 50 °C, 300 mL of distilled water was added. After some time, 8 mL of H_2O_2 and 800 mL of distilled water were added to the solution with continuous steering for approximately two hours until the solution color changed to brown suspension. The suspension was left for 12 hours without any disturbance to settle the supernatant. The remaining solution was centrifuged with HCL (10%) and distilled water. Finally, the obtained residue was kept in the oven for drying for approximately 12 hours at 60 °C to get dried GO.

3.B2.2 Synthesis and Functionalization of nLa_2O_3NPs@rGO Composite

The nLa2O3 NPs@rGO composite was fabricated in situ by a hydrothermal process. A one-pot, low-temperature, facile protocol was followed for forming nLa_2O_3NPs on a 2D graphene derivative, i.e., reduced graphene oxide (rGO). For this, 150 mg GO was weighed in 50 mL DI and 3 h sonication was provided for obtaining the homogenous solution and stacked GO sheets exfoliation. Next, the other solution was made by the addition of 0.7 g of $La(NO_3).4H_2O$in 15 mL DI. This solution was added to the GO solution and stirred at 300 rpm for 15 min till a mixture solution was obtained. Afterward, a dropwise addition of HCl (8 M) was done to make the above solution's pH acidic. At last, the mixture solution was transferred to a 100mL autoclaved Teflon vessel and placed in a muffle furnace at 160 °C for 6 h. The resulting solution was then centrifuged for 20 min at 9000 rpm and washed with DI several times. The greyish-yellow-colored residue was collected and dried in the oven overnight at 60 °Cas well as stored at RT for further use.

For functionalizing the prepared nLa_2O_3NPs@rGOcomposite, a homogeneous solution was formed by mixing nLa_2O_3NPs@rGO (50 mg) in1 mg mL^{-1} isopropanol and stirring it at 300 rpm at 60 °C. Thus, the addition of 200 μLof APTES was done slowly with succeeding 5 mL milli-Q water addition followed by stirring the solution for subsequent 48 h. Finally, the filtration of the achieved product,i.e., APTES/nLa_2O_3NPs@rGO, was performed using Whatman filter paper, followed by drying the sample for 4h at 70 °C and then kept at a dry location for further utilization.

3.B2.3 Fabrication of BSA/anti-CPX/APTES/nLa_2O_3NPs@rGO/ITO Nano-immunosensing Platform

The first step was to hydrolyze ITO-coated substrates made from glass employing a 5:1:1 solution of water, H_2O_2, and NH_4OH for 1h at 80°C. The APTES/nLa_2O-NPs@rGOcomposite was disseminated in 0.4 $mgmL^{-1}$ ACN using ultrasonication for electrophoretic deposition (EPD) to increase surface charge through $Mg(NO_3)2.6H_2O$. The thin layer of APTES/nLa_2O_3NPs@rGOwas deposited onto a pre-hydrolyzed ITO surface for 120s at DC of 60V using a traditional 2-electrode setup with Pt and ITO serving as the cathode and anode, respectively with a 1 cm distance between them. To immobilize anti-CPX antibodies, a 30 μL solution comprising NHS of 0.4 M, anti-CPX of 50 μg mL^{-1}, as well as EDC of 0.2 M are mixed in a 1:2:1 ratio and allowed to pre-incubate for 45 min before being applied to the surface of APTES/nLa_2O_3NPs@rGO/ITO electrode. Here EDC served as a coupling agent for binding the amine group of APTES functionalized electrode and antibody's carboxyl group, whereas NHS acts as activating agent for anti-CPX. To lessen CPX's non-specific attachment, 20 μL of BSA was used after washing with PBS. The developed BSA/anti-CPX/APTES/nLa_2O_3NPs@rGO/ITO immunosensor was subsequently rinsed with PBS and kept at 4°C until further usage. The carboxylic (–COOH) group that is found on the anti-CPX antibodies (F_c fragment) formed a covalent link with the APTES silane molecules' amine ($-NH_2$) group to stop antibodies from leaching from the surface of the electrode. anti-CPX antibodies' -COOH groups that were activated by EDC, resulting in the creation of an unstable O-acylisourea ester, which was then changed into a stable intermediate product, i.e., an amine-reactive NHS ester, by interaction with the NHS molecule. As a result of NHS triggering the anti-CPX antibody, silane molecules' $-NH_2$ groups (APTES) are encouraged to join, forming an amide bond[42][43]. In Scheme 3.2, the developing processes for the BSA/anti-CPX/APTES/nLa_2O_3NPs@rGO/ITO immunosensor are schematically depicted.

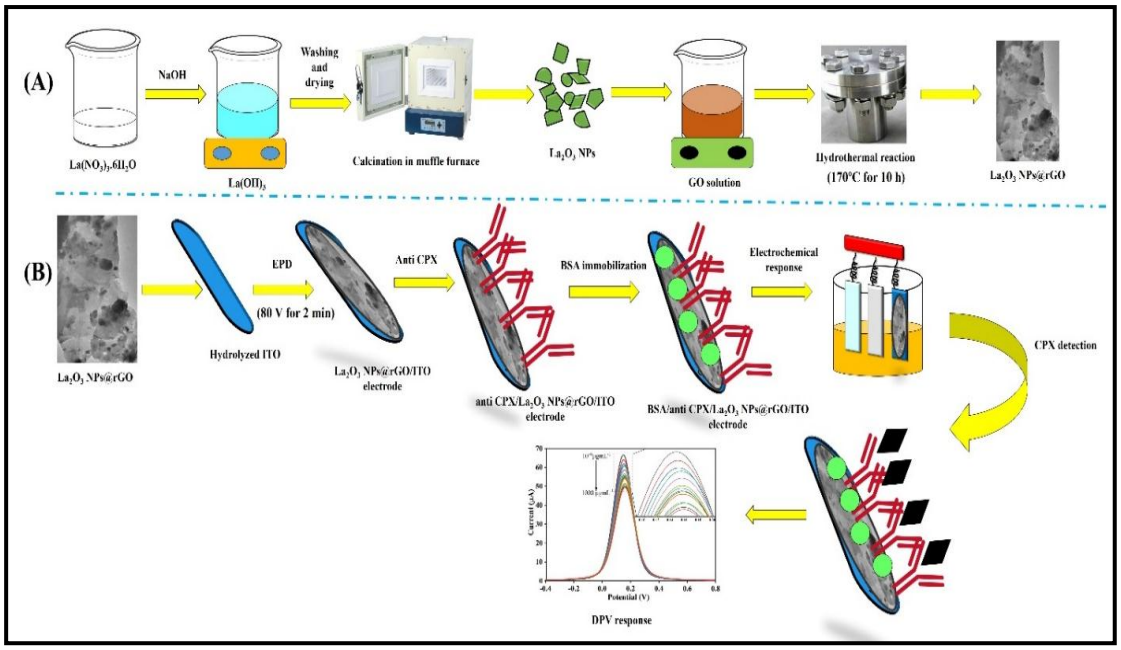

Scheme 3.2: (a) Chemically synthesized nLa_2O_3NPs@rGOnanocomposite. (b) The developmental stages of BSA/anti-CPX/ATPES/ nLa_2O_3NPs@rGO/ITO immunoelectrode for the determination of CPX.

3.B2.4 Determination of CPX in the Milk Sample

The stock solutions of various concentrations of CPX that range from 10^{-6} μgmL^{-1} to 1000 μgmL^{-1} were made in PBS (pH 7.0) to characterize the constructed immunosensor. In order to do this, the modified BSA/anti-CPX/APTES/nLa_2O_3NPs@rGO/ITO was subjected to the stock solution of CPX for 10 min. The whole set of electrochemical tests for the immunosensor was completed utilizing the DPV in PBS with redox species. Additionally, a control analysis was carried out without using CPX.

By spiking samples of milk, the designed immunosensor was put to testing employing the real samples. To investigate the actual spiked samples, milk samples were collected from the JNU campus's surrounding market. The pre-treatment of the 50 mL milk involved the addition of 0.5 mL of 20 mM trichloroacetic acid and 3 mL of 5 mM ethanol. The mixture was then combined and centrifuged at RT for 15 min at 10,000 revolutions per min, and its leftover liquid was used to prepare the test sample. First, these real samples were examined for the presence of CPX. However, the sample was spiked because there was no current change to indicate the existence of CPX in them. For real sample analysis, the analyte quantity used was 20 μL, as well as the different concentrations varied from 10^{-6}μg mL^{-1} to 1000 μg mL^{-1} of CPX were used for spiking

the milk sample. The sensing measurement for the immunosensor was conducted using these real spiked samples. The BSA/anti-CPX/APTES/APTES/nLa_2O_3NPs@rGO/ITO immunosensor was then applied to milk samples to find CPX antibiotics for 10 min. At RT (25 °C ± 2 °C), whole experiments were carried out thrice.

3.B3 Results and Discussion

The present study employed an electrochemical nano-immunosensing approach to detect CPX, utilizing the DPV technique for the first time. The electrochemical biosensing mechanism relies on the specific interaction between CPX and anti-CPX immobilized on an ITO electrode, as depicted in Scheme 3.2. In this scheme, the anti-CPX molecules are covalently attached to the APTES/APTES/nLa2O3 NPs@rGO/ITO surface, enabling high selectivity by capturing the CPX.

3.B3.1 X-ray Diffraction (XRD) Analysis

The synthesized nLa_2O_3NPs@rGOcomposite's XRD spectrum was displayed in Figure 3.12(a), which indicates its phase purity and crystalline structure. At ambient temperature, a 2θ angle ranging from 10° to 80° was used for the XRD pattern investigation. The fact that the (002) plane is prominent at 23.6° shows that the reduction process results in the formation of crystalline rGO nanosheets [44]. The XRD structure exhibits peaks at 2θ = 24.1°, 26.9°, 27.7°, 30.0°, 39.1°, 43.3°, 46.6°,48.3°, 49.1°, 54.9°, 63.6°, 69.4°, and 77.1°, that correspond to the nLa_2O_3 NPs alignments in accordance to (200), (222), (222), (321), (422), (611), (125), (433), (611), (136), (156), (822) and (655) cubic planes, respectively. These findings demonstrate a strong correlation for nLa_2O_3NPs@rGOthe cubic phase with the JCPDS card no. 65-3185. The nLa_2O_3NPs@rGO composite samples show excellent insertion of nLa_2O_3 NPs into rGO due to the existence of (002) planes and nLa_2O_3NPs peaks. The remarkable crystallinity of nLa_2O_3NPs@rGO is demonstrated by the well-defined, sharp, and strong peaks [45], [46]. Therefore, nLa_2O_3NPs@rGO's body-centered lattice with cubic phase formation is confirmed by its XRD characterization, and no other impurity peaks were found. The Scherrer formula was used to calculate the crystallite size (D) of the nLa_2O_3NPs@rGONPs, and the D value was calculated as 30.9 nm corresponding to 2θ = 29.6 (grain) as provided below:

$$D = K\lambda/\beta \cos\theta \qquad (3.17)$$

where K stands for the dimensionless shape factor (0.9),λisthe target's wavelength Cu-Kα: 1.540 Å),θ is the Bragg's diffraction angle, andβ is the full width at half maximum (FWHM) of the diffraction peak.

3.B3.2 Raman Analysis

For investigating the phonon vibrational patterns of chemical bonds, particularly in crystalline samples, Raman spectroscopy is a valuable instrument. This technique is widely known for identifying secondary phases. This characterization method may identify various flaws in complex layers and is highly sensitive to microcrystals. Therefore, Raman analysis was performed on our synthetic material to verify that rGO had successfully hybridized with nLa_2O_3 NPs. nLa_2O_3NPs@rGO composite's Raman active modes are depicted in Figure 3.12(b). The Raman spectra of reduced graphene oxide (rGO) exhibit two prominent peaks at 1591 cm^{-1} (G band) and 1339 cm^{-1} (D band). Two distinct peaks were observed in the sample containing pure nLa2O3 nanoparticles. The Eg band at 410 cm^{-1} is associated with the La-O stretching vibration, whereas the A1g band at 208 cm^{-1} is assigned to the La-O bending vibration.[47]. The degree of defect or disorder in graphene-based derivatives is assessed using the intensities of the D band (ID) to G band (IG), i.e., by ID/IG ratio. IN THIS CASE, the ID/IG ratio similarly falls to 0.92 from 1.23. These were caused by the oxygen-rich rGO being reduced during the nLa_2O_3 NPs formation. Additionally, this conclusion is supported by the XRD study.

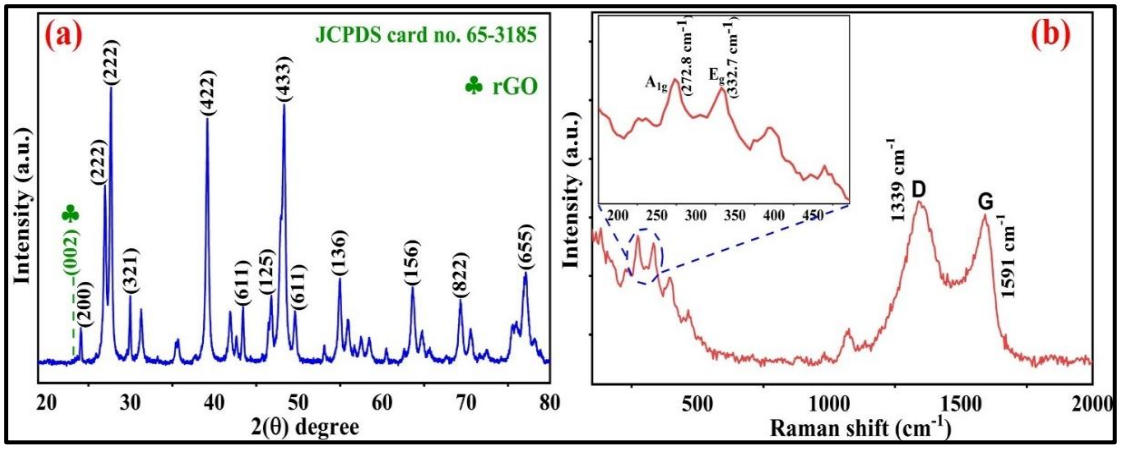

Figure 3.12: (a) XRD spectrum of nLa_2O_3NPs@rGOcomposite; and (b) Raman curve of nLa_2O_3NPs@rGOcomposite.

3.B3.3 Transmission Electron Microscopy (TEM) Study

TEM was employed to examine the size, shape, and morphology of the as-prepared nLa_2O_3NPs@rGO composite [Figure 3.13 (a-d)]. The apparent, sheet-like structure of the rGO is depicted in Figure 3.13(a-b), with wrinkled and folded structures suggesting a minimal number of layers.

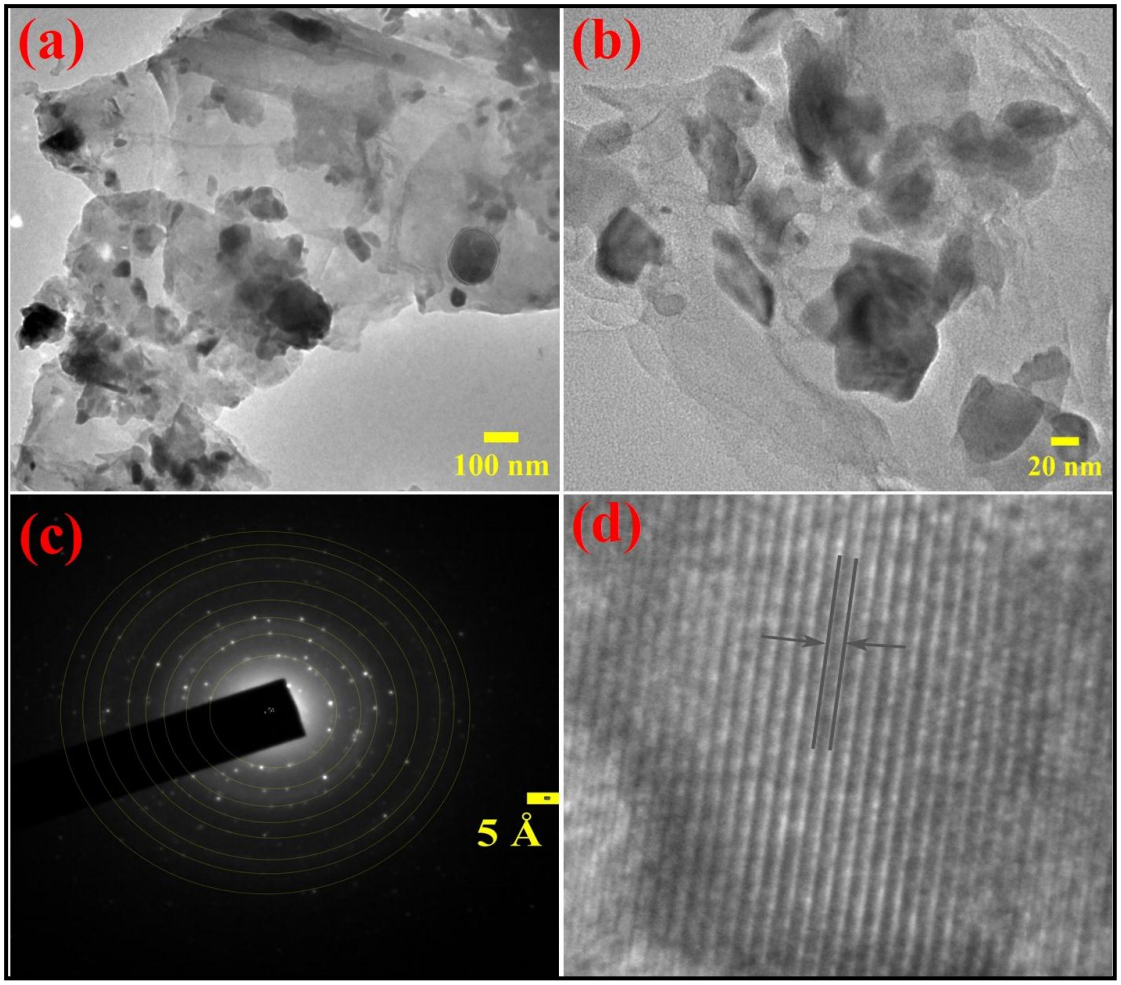

Figure 3.13: (a and b) TEM pictures ofnLa_2O_3NPs@rGO composite depicting rGO sheet-like structure in high and low magnification; (c) SAED pattern; and (d) HR-TEM picture of nLa_2O_3NPs@rGO nanocomposite depicting (222) crystal plane of nLa_2O_3NPs.

In Figure 3.13(a-b), nLa_2O_3 NPs adhere to the wrinkly rGO surface. A more evenly distributed nLa_2O_3 NPs implies more significant nanoparticle-electrolyte connections and hence higher utilization of the nanoparticles for capacitance generation. Additionally, the selected area electron diffraction (SAED) ring trends [Figure 3.13(c)], which shows the nLa_2O_3 NPs diffraction rings in the nLa_2O_3NPs@rGOcomposite are in

accordance to nLa_2O_3 NPs planes, represents a highly crystalline nature of nLa_2O_3 NPs. As is widely recognized, single-crystal solids exhibit a patchy diffraction pattern in SAED, while polycrystalline substances exhibit a ring distribution [48]. As a result, the resulting rings are clearly defined, indicating strong crystallinity and a polycrystalline character. Additionally, it is discovered that these results and the XRD data are in good agreement. As shown in Figure 3.13(c), the HRTEM picture of rGO and nLa_2O_3 NPs in nLa_2O_3NPs@rGOcomposite displays a distinct 0.31 nm lattice fringes value that corresponds to (222) plane, which happens to be the nLa_2O_3 NPs largest orientation plane, as well as 0.385 nm ascribing to rGO (002) plane, which is supported by XRD findings.

3.B3.4 SEM Analysis

The utilization of scanning electron microscopy (SEM) characterization provided a valuable technique for visualizing the surface of the nanomaterial. The top-facing SEM images of the nLa_2O_3NPs@rGO composite are shown in Figure 3.14(a). The nLa_2O_3 NPs were dispersed more evenly throughout the rGO sheets, as seen in Figure 3.14(a). The filament composition and structure were investigated using EDS. This technique is utilized for qualitative examination and investigates the energy and wavelength of the material' irritated x-ray and the elemental detection. The EDS picture, which consists of C, O, and La components, displayed in Figure 3.14(b), demonstrates the effective insertion of nLa_2O_3 NPs to the rGO surface. Each peak in this graph corresponds to an atom based on its energy. Prominent peaks reflect that an element's concentration in the sample is increased. The elemental compositions in % are 59.83±1023 wt.% for La, 11.23±0.35 wt.% for C, and28.94±0.79 wt.% for O. The calculated composition is consistent with what has been determined theoretically.

The nLa_2O_3NPs@rGOnanocomposite distribution characteristics and the specific and dominant elements, i.e., C, O, and La, were further investigated using the elemental mapping method. The elemental mapping investigation for the nLa_2O_3NPs@rGO composite [Figure 3.14(c)] revealed a flawless homogeneous distribution of the sample's C, O, and La elements. The EDS findings showing the existence of C, O, and La elements in the sample were also supported by elemental mapping investigation. The

existence of the C, O, and La elements in the corresponding active sample, depicted in Figure 3.14(c), is confirmed by elemental map assessment, which displays each element in a sample's area.

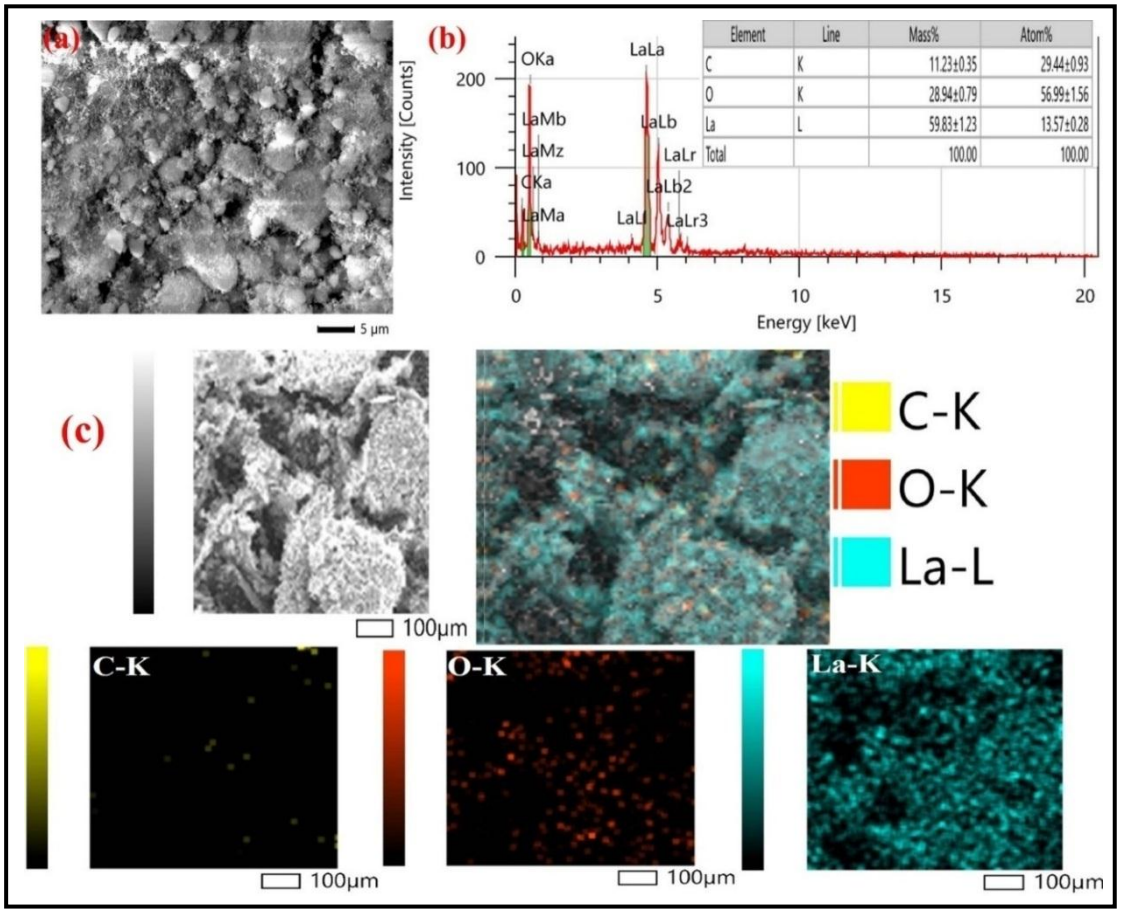

Figure 3.14: (a) SEM pictures; (b) EDS spectrum of nLa_2O_3NPs@rGO composite; and (c) elemental mapping of nLa_2O_3NPs@rGO composite.

3.B3.5 Fourier Transformed Infrared Spectroscopy (FT-IR) Study

The vibrational modes and functional groups present in the synthesized samples were proved by spectral investigation, which was carried out utilizing a Perkin Elmer FTIR spectrometer ranging from 4000–400 cm^{-1}having a 10.4.00 version. Figure 3.15(a) shows the measured spectrum of APTES/nLa_2O_3NPs@rGO /ITO electrode. The FTIR curve of reduced graphene oxide (rGO) exhibits an absorption band at 1589 cm-1, which can be attributed to the stretching vibration of carbon-carbon (C=C) bonds and is indicative of the presence of sp2 hybridization. The stretching vibration modes of the COOH functional group, specifically the C-OH and C=O vibrations, were identified as

the bands located at 1108 cm^{-1} and 1603 cm^{-1}, respectively. The La-O's stretching vibrations can be seen by peaks from 1108 to 852 cm^{-1}, whereas its twisting oscillations are indicated by peaks from 649 to 556 cm^{-1}[49]. The prominent peaks discovered at 3703 cm^{-1}[38] further support the O-H stretching presence, which is compatible with the moisture absorbed on the sample's surface. The FTIR curve of the nLa_2O_3NPs@rGO composite contained all of the characteristic functional groups associated with rGO and La_2O_3 NPs. Additionally, peaks at 1636 and 1949 cm^{-1} were seen that correspond to the amide II peak and -C O stretching, respectively produced between the anti-CPX's -COOH group and the APTES/nLa_2O_3NPs@rGO/ITO amine group, suggesting the antibodies' adherence to the functionalized nanocomposite [50]. [Figure 3.15(b)]. Further, the peak at 1428 and 1487 cm^{-1} vanished, and peak intensities of 1636 and 1949 cm^{-1} decreased, as illustrated in Figure 3.15(c), confirming the immunoelectrode's blockage by BSA particles.

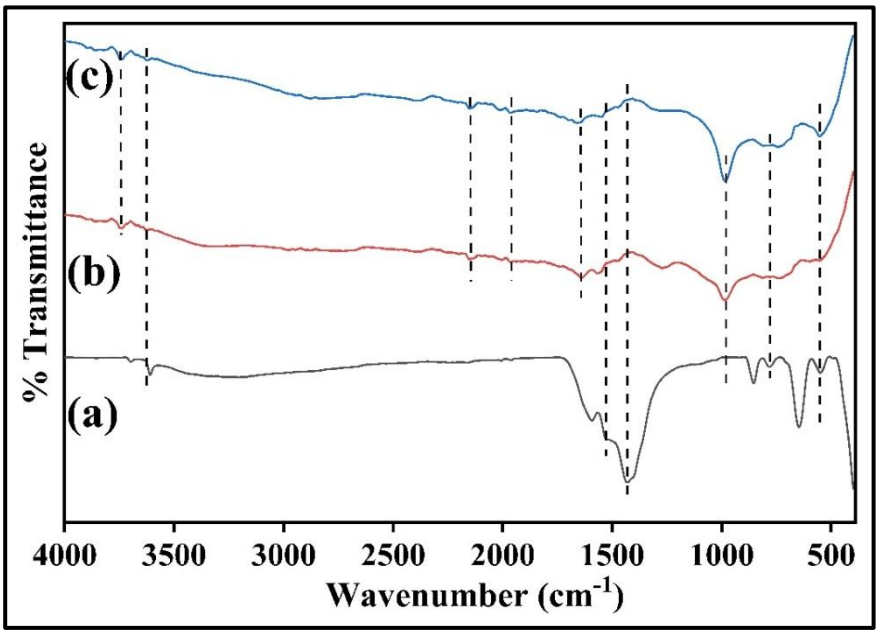

Figure 3.15: FT-IR spectra of (a) APTES/nLa_2O_3NPs@rGO/ITO electrode; (b) anti-CPX/APTES/nLa_2O_3NPs@rGO/ITO electrode; and (c) BSA/anti-CPX/APTES/nLa_2O_3 NPs@rGO/ITO immunoelectrodes.

3.B3.6 Contact Angle Study

For estimating the contact angle, the sessile drop method is employed after modifying every stage of fabrication to assess the hydrophobic or hydrophilic activity of the

developed electrodes [Figure 3.16(a-d)]. The hydrophobic character of the unmodified hydrolyzed ITO electrode has been demonstrated by the CA value (75.7°), which is illustrated in Figure 3.16(a). The CA value grew to 119.5° [Figure 3.16(b)] after the nLa_2O_3NPs@rGOnanocomposite' EPD on the ITO electrode, suggesting the highly hydrophobic property of the APTES/nLa_2O_3NPs@rGO/ITO electrode providing a suitable condition for anti-CPX immobilization. Furthermore, the value of CA was reduced to 21.0° [Figure 3.16(d)] and 40.6° [Figure 3.16(c)] after BSA and anti-CPX immobilization of molecules, respectively on surface of APTES/nLa_2O_3NPs@rGO/ITO electrode, demonstrating a rise in hydrophilic behavior of BSA/anti-CPX/APTES/ nLa_2O_3NPs@rGO/ITO immunoelectrode and anti-CPX/APTES/nLa_2O_3NPs@rGO/ITO electrode due to the covalent relation between the APTES/nLa_2O_3NPs@rGOelectrode and anti-CPX [36]. This hydrophilicity helps to boost sensitivity and improve antigen adhesion in PBS [51][42].

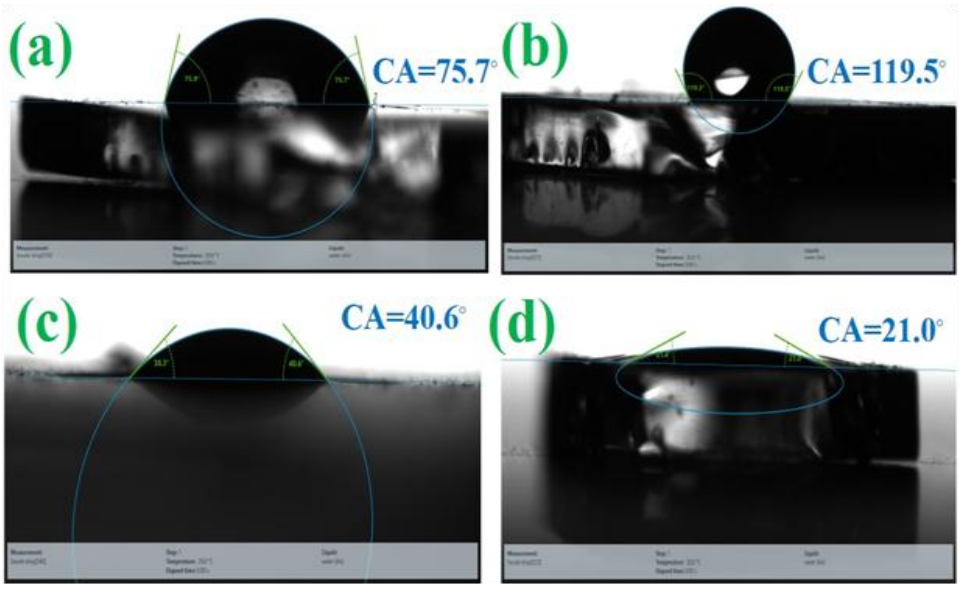

Figure 3.16: Water contact angle of ITO (a), APTES/nLa_2O_3@rGO/ITO (b), anti-CPX/APTES/nLa_2O_3@rGO/ITO (c), and BSA/anti-CPX/APTES/nLa_2O_3@rGO/ITO (d).

3.B4 Electrochemical Characterization Studies

3.B4.1 pH and Electrode Study

At first, optimization of the best experimental parameters for electrochemical characterization was done by employing a variety of PBS solutions with different pH

levels through pH studies. DPV responses were measured in potential ranges that extend from -0.4V to +0.8V to explore the impact of pH (6.0 - 9.0) on the electrochemical characteristics of the constructed nano-biosensor (BSA/anti-CPX/APTES/nLa_2O_3NPs@rGO/ITO). As can be seen from Figure 3.17(a), the highest peak current is seen at pH 7.0, which could be due to the antibodies that are present in their original state at neutral pH and have the most activity therein, while they tend to get destroyed in the basic or acidic environment [52]. Thus, a PBS buffer having pH 7.0 was employed to conduct further electrochemical investigations.

Additionally, in the presence of PBS pH 7.0 comprising 5 mM $[Fe(CN)_6]^{3-/4-}$ as a redox coupler, the electrochemical features of the developed electrodes have been investigated using DPV and CV. To examine the peak current variations at various stages of electrode alterations, the electrochemical behavior of BSA/anti-CPX/APTES/nLa_2O_3NPs@rGO/ITO (curve iv), anti-CPX/APTES/nLa_2O_3NPs@rGO/ITO (curve iii), APTES/nLa_2O_3 NPs@rGO/ITO (curve ii), and ITO (curve i) electrodes were monitored *via* CV having potential window ranging from -0.8 V to +0.8 V), and the outcomes achieved are displayed in Figure 3.17(b). It was discovered that the APTES/nLa_2O_3NPs@rGO/ITO electrode' peak current was improved (251.80 μA) than the ITO electrode (228.17 μA). The high electrical conductivity of reduced graphene oxide (rGO) present in nLa2O3 NPs@rGO has facilitated the rapid kinetics of electron transfer from the electrolyte to the electrode. This, in turn, has resulted in enhanced electrochemical properties and an increase in current. Furthermore, the addition of incorporated nLa_2O_3 on rGO sheets allows for the transfer of different ions across the interface of the electrodes via its permeable pathways, which enhances peak current in a synergistic manner [53]. The peak current jumped to 291.16 μA once the antibody (anti-CPX) was immobilized, indicating a quick electron transport to the electrode's surface. This was possible because nLa_2O_3NPs@rGO acted as a mediator at the surface of ITO and significantly shortened the distance over which electrons could tunnel from the anti-CPX to the electrode. Additionally, non-covalent interaction between the redox species and unbound anti-CPX -NH_2 terminal was the cause of the immunoelectrode's rapid diffusion of electrons [54][54], [55]. This demonstrated that the antibodies were successfully immobilized. The peak current also dropped to 280.36 μA following the attachment of BSA on anti-CPX/APTES/nLa_2O_3NPs@rGO/ITO

immunoelectrode. It could be due to the non-specific active regions on the surface of the immunoelectrode that have been blocked. In addition, DPV was also obtained for BSA/anti-CPX/APTES/nLa_2O_3NPs@rGO/ITO (curve iv), anti-CPX/APTES/nLa_2O_3 NPs@rGO/ITO (curve iii), APTES/nLa_2O_3NPs@rGO/ITO (curve ii), and ITO (curve i) electrodes in the -0.6 V to +0.8 V potential window at a 50 mVs^{-1} scan rate, showing comparable results such as in CV [Figure 3.17 (c)]. These results demonstrate an effective and sequential fabrication process for an immunoelectrode, as shown by the contact angle, FTIR, and SEM analyses.

The electrochemical impedance spectroscopic investigations were conducted on four different samples: ITO (curve i), APTES/nLa_2O_3@rGO/ITO (curve ii), anti-CPX/APTES/nLa_2O_3@rGO/ITO (curve iii), and BSA/anti-CPX/APTES/nLa_2O_3@ rGO/ITO (curve iv). These studies were carried out in a PBS solution containing 5 mM $[Fe(CN)_6]^{3-/4-}$ over a frequency range spanning from 100 kHz to 10 Hz, as shown in Figure 3.17(d). The Nyquist plot's semicircle provides information about the charge transfer resistance (R_{ct}) associated with the electrode. This resistance is influenced by the dielectric properties of both the electrode surface and the electrolyte interface. The highest value of R_{ct}, 249.35 Ω, was obtained for the ITO glass substrate (curve i). Nevertheless, the value of R_{ct}205.2 Ω experiences a notable decline after the deposition of the APTES/nLa_2O_3@rGO nanocomposite onto the ITO surface (curve ii). This decline suggests that the nLa_2O_3@rGO nanocomposite possesses a high level of electrical conductivity and facilitates the rapid diffusion of redox species $[Fe(CN)_6]^{3-/4-}$ towards the electrode surface.Nevertheless, following the covalent immobilization of anti-CPX antibodies onto the unoccupied -NH2 sites of the APTES functionalized nLa_2O_3@rGO nanocomposite, the R_{ct} value experiences a significant reduction to 165.58 Ω for the anti-CPX/APTES/nLa_2O_3@rGO/ITO configuration (curve iii). The observed reduction in the value of R_{ct} can be attributed to the spatial alignment of the anti-CPX molecule on the electrode surface, which promotes enhanced charge transfer between the redox species $[Fe(CN)_6]^{3-/4-}$ and the exposed functional group (NH_2) of the anti-CPX molecule (Kumar et al., 2015). The resistance of the charge transfer process (R_{ct}) exhibits an increase (measured at 176.42 Ω; curve iv) following the immobilization of Bovine Serum Albumin (BSA) on the anti-CPX/APTES/ nLa_2O_3@rGO/ITO immunoelectrode. This can be attributed to the macromolecular nature

and insulating properties of BSA, which impede the efficient transfer of charges between the redox species $[Fe(CN)_6]$ and the surface of the electrode.

The heterogeneous electron transfer rate constant (K_{ct}) for all respective electrodes was calculated using Eq.3.18

$$\text{Kct}\frac{RT}{n^2F^2\text{ARct[S]}} \qquad \text{Eq 3.18}$$

Where R is the gas constant, T is the absolute temperature, n is the no. of transferred electrons per molecule of the redox probe, F is Faraday constant, A is the surface area of the electrode (cm^2), and [S] is the concentration of redox probe. The K_{ct} value of the indium tin oxide (ITO) electrode was determined to be 2.006×10^{-6}. However, in the case of the APTES/nLa_2O_3@rGO/ITO electrode, the Kct value increases to 3.044×10^{-6}, indicating a higher rate of electron transfer between the APTES/nLa_2O_3@rGO/ITO electrode and the redox species. Following the immobilization of anti-CPX, the K_{ct} value experiences a subsequent increase to 4.329×10^{-6}, indicating a rapid exchange of electrons between the immunoelectrode and the redox species. Nevertheless, following the immobilization of Bovine Serum Albumin (BSA) on the immunoelectrode composed of anti-CPX/APTES/nLa_2O_3@rGO/ITO, the Kct value experiences a decrease to 2.160×10^{-6}. This decrease can be attributed to the insulating properties of the immunoelectrode, which hinder the transfer of electrons.

The equation provided below has been utilized to compute the time constant (τ) for each electrode.

$$R_{ct}.C_{dl} = 1 / 2\pi f_{max} = \tau \qquad \text{Eq 3.19}$$

After the EPD of APTES/nLa_2O_3@rGOon ITO substrate, there is an abrupt decrease in the value of the time constant was found as compared to ITO glass substrate (8.938×10^{-4} s). It reveals the fast diffusion of $[Fe(CN)_6]^{3-/4-}$ ions at the interface of the electrolyte and APTES/nLa_2O_3@rGO/ITO electrode. The immobilization of anti-CPX onto the APTES/nLa_2O_3@rGO/ITO results in a decrease of τ value 2.716×10^{-4}s due to the fast diffusion of $[Fe(CN)_6]^{3-/4-}$ ions. After the BSA immobilization, the value of τ again increases (2.724×10^{-4} s) due to the insulating behavior of BSA.

Table 3.5: EIS features of various electrodes

Electrode	**Charge transfer resistance (R_{ct})**	**Heterogeneous electron transfer rate constant [K_{ct} (cms^{-1})]**	**The time constant (τ) s**
ITO	249.35 Ω	2.006×10^{-6}	8.938×10^{-4}
APTES/nLa_2O_3@rGO/ITO	205.2 Ω	3.044×10^{-6}	5.631×10^{-4}
anti-CPX/APTES/nLa_2O_3@rGO/ITO	165.58 Ω	4.329×10^{-6}	2.716×10^{-4}
BSA/anti-CPX/APTES/nLa_2O_3@rGO/ITO	176.42 Ω	2.160×10^{-6}	2.724×10^{-4}

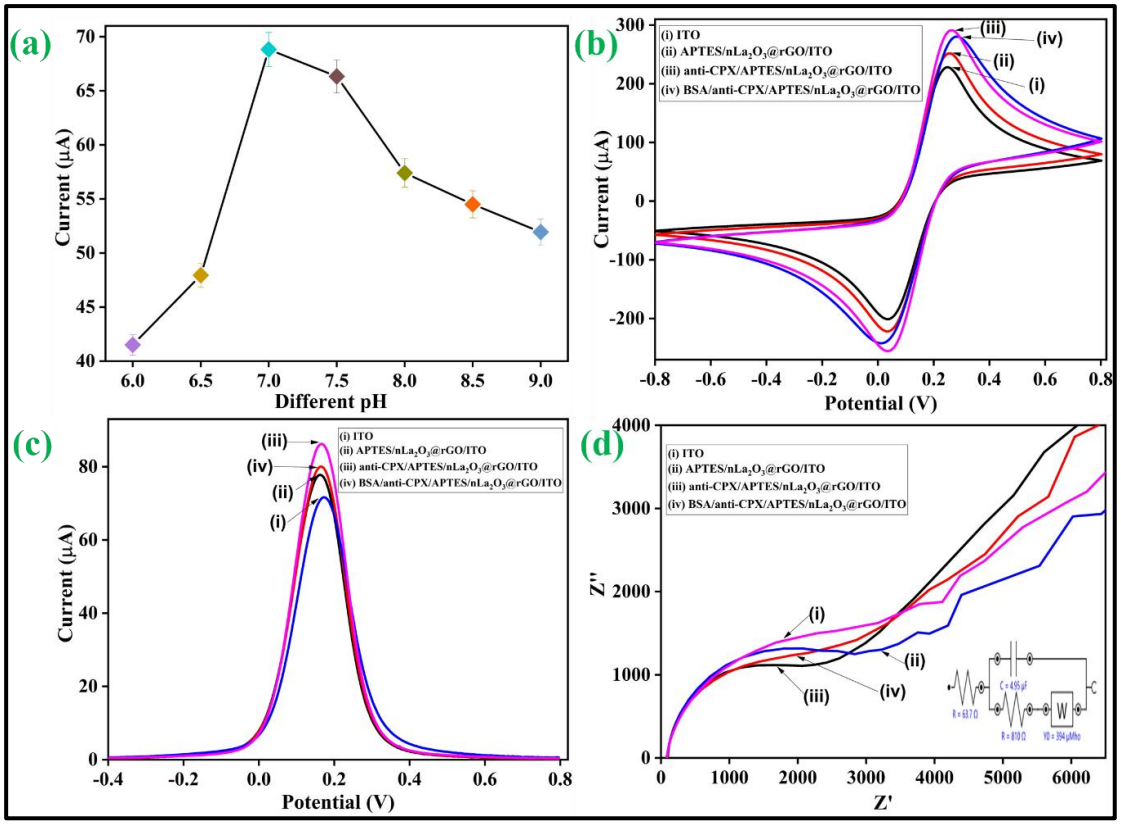

Figure 3.17: (a) pH effect of BSA/anti-CPX/APTES/nLa_2O_3NPs@rGO/ITO immunoelectrode; (b)CV; (d) DPV; and (e) EIS study of ITO (curve i), APTES/nLa_2O_3NPs@rGO/ITO (curve ii), anti-CPX/APTES/nLa_2O_3NPs@rGO/ITO (curve iii) and BSA/anti-CPX/APTES/nLa_2O_3NPs@rGO/ITO (curve iv)electrodes [inset depicts the Nyquist circuit diagram].

3.B4.2 Interfacial Kinetics Studies

By examining changes in peak current versus varying scan rates from 10 to 100 mVs^{-1}, the interfacial kinetics of the BSA/anti-CPX/APTES/nLa_2O_3NPs@rGO/ITO

immunoelectrode and APTES/nLa_2O_3NPs@rGO/ITO electrodes were studied *via* CV in the -0.8 V to +0.8V potential range. The peak currents magnitudes of both anodic (I_{pa}) and cathodic (I_{pc})exhibit a linearly rising pattern against the square root of scan rate, as illustrated in the figures [Figure 3.18A(i) and B(i)], indicating that the electrochemical system is diffusion regulated [9][56] and implies eq. 3.20 to 3.23

$I_{pa(APTES/nLa2O3\ NPs@rGO/ITO)}$ = –[17.63 μA (s/mV)×(scan rate [mV/s])$^{1/2}$] –63.92μA, R^2 = 0.978 Eq 3.20

$I_{pc(APTES/nLa2O3\ NPs@rGO/ITO)}$ = [21.93 μA (s/mV)×(scan rate [mV/s])$^{1/2}$] + 65.94 μA, R^2 = 0.989 Eq 3.21

$I_{pa(BSA/anti\text{-}CPX/APTES/nLa2O3\ NPs@rGO/ITO)}$ = –[21.42 μA (s/mV)×(scan rate [mV/s])$^{1/2}$] –71.63 μA, R^2 = 0.986 Eq 3.22

$I_{pc(BSA/anti\text{-}CPX/APTES/nLa2O3\ NPs@rGO/ITO)}$ = [26.87μA(s/mV)×(scan rate [mV/s])$^{1/2}$] + 67.23 μA, R^2 = 0.992 Eq 3.23

On increasing the sweep rate, the I_{pc} and I_{pa} values change to greater negative and positive potentials, respectively. The E_{pa} and E_{pc} represent anodic and cathodic peak potentials, respectively, and their magnitude difference ($\Delta Ep = E_{pa}\text{-}E_{pc}$) exhibits a linear fluctuation with scan rate squared. The findings, which are reflected by Eq. 3.24 and 3.25, are displayed in [Figure 3.18 A(ii) and B(ii)] and demonstrate the easy charge transfer kinetics between the electrode interface and medium. These outcomes demonstrated the suitability of the fabricated electrodes for electrochemical biosensing purposes.

$\Delta E_p(V)_{(APTES/nLa2O3\ NPs@rG/ITO)}$ = [0.024 V (s/mV) × (scan rate [mV/s])$^{1/2}$] + 0.085 V, R^2 = 0.993 Eq. 3.24

$\Delta E_p(V)_{(BSA/anti\text{-}CPX/APTES/nLa2O3NPs@rGO/ITO)}$= [0.023 V(s/mV) × (scan rate [mV/s]) $^{1/2}$] + 0.093 V, R^2 = 0.994 Eq 3.25

An essential factor that can be used to predict the fabrication electrode's ability for biosensing is the diffusion coefficient (D). The D value at the interface between the BSA/anti-CPX/APTES/nLa_2O_3NPs@rGO/ITO immunoelectrode and redox couple $[Fe(CN)_6]^{3-/4-}$ is calculated using the Randles-Sevcik equation.

$$Ip = (2.69\times10^{5})\ C\ n^{3/2}\ D^{1/2}\ \upsilon^{1/2}\ A \qquad \text{Eq 3.26}$$

Where A depicts the working electrode's surface area i.e., 0.25 cm^2, Ip depicts the electrode's peak current, C stands for the redox species' concentration, D depicts the diffusion coefficient ($cm^2\ s^1$), and v depicts 0.05 Vs^{-1}scan rate. The estimated D value is $9.71\times10^{-4}\ cm^2\ s^{-1}$.

Additionally, the following has been calculated using the Brown-Anson equation [Eq. (3.25)] to represent the anti-CPX surface concentration on the immunoelectrode electrode surface:

$$I_p = \frac{n^2 F^2 \gamma^* A\, \upsilon}{4\ R\ T} \qquad \text{Eq 3.27}$$

Where T depicts 298 K temperature, υ stands for scan rate (50 mV s^{-1}), R depicts the gas constant i.e., 8.314 J mol^{-1} K^{-1}, n depicts number of electron transfers (i.e., 1), F is the Faraday constant (96,584 C mol^{-1}), A is the electrode surface area (0.25 cm^2), v is the scan rate (50 mV s^{-1}), Ip is the immunoelectrode current and γ stands for absorbed electro-active species' surface concentration (mol cm^{-2}). The BSA/anti-CPX/APTES/ nLa_2O_3NPs@rGO/ITO immunoelectrodes surface concentration of anti-CPX was determined as 3.23×10^{-8} mol cm^2, which suggests the immunoelectrode might have effective biosensing attributes.

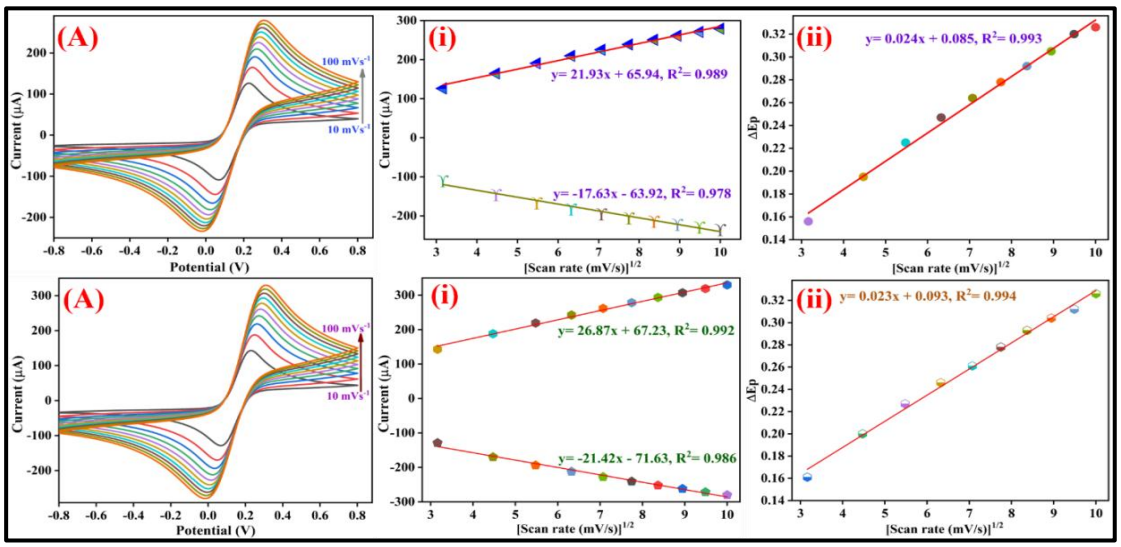

Figure 3.18: CV of the (A) APTES/nLa_2O_3NPs@rGO/ITO electrode; and (B) BSA/anti-CPX/APTES/nLa_2O_3NPs@rGO/ITO immunoelectrode at various scan rates ranging from 10 to 100 mV s^{-1}), (A(i) and B(i)) Calibration curve showing cathodic and anodic current versus square root of scan rate, (A(ii) and B(ii)) Potential difference ($\Delta E_p = E_{pa}–E_{pc}$) versus square root of the scan rate.

3.B4.3 Electrochemical Response Studies

An incubation analysis was conducted before the electrochemical response experiments for the developed immunosensor to determine an approximate time frame for the attachment of antibodies and antigens. In order to investigate the fluctuation in current values when CPX interacts with the proposed BSA/anti-CPX/APTES/nLa_2O_3NPs@rGO/ITO immunoelectrode for various period, i.e., from 0 to 16 min, a DPV study was carried out. An incubation-period study with a decreasing peak current in relation to time is shown in Figure 3.19(a). The peak current has been seen to fall to 14 min, after which the peak current reaches saturation. According to the data, CPX antibiotics must bind to the BSA/anti-CPX/APTES/nLa_2O_3NPs@rGO/ITO immunoelectrode for 15 min. Therefore, 15 min are provided to investigate the various CPX levels of antibiotics to conduct subsequent electrochemical response experiments.

The CPX was analyzed at different concentrations using DPV approaches to assess the analytical characterization of the nLa_2O_3NPs@rGO-derived immunosensor, as illustrated in Figure 3.19 (b). The determination of antigens using a biosensing platform has made extensive use of the versatile and effective electrochemical DPV approach. In this method, a 3-electrode system was used with Ag/AgCl, proposed immunosensor, and platinum electrodes functioning as a reference, working, and counter electrode, respectively. The DPV spectra of the constructed BSA/anti-CPX/APTES/nLa_2O_3 NPs@rGO/ITO immunoelectrode were obtained under the best experimental circumstances following incubation with various CPX antibiotics concentrations ranging from 10^{-6} to 1000 μg mL^{-1} at 50 mVs^{-1} scan rate at 0.4 to +0.8 V potential window. After 15 min of engagement with CPX concentrations that vary from 10^{-6} to 1000 g mL^{-1}, immunoelectrodes are shown to have a DPV response in Figure 3.19(b). The peak current gradually dropped from 10^{-6} to 1000 μg mL^{-1} as the CPX concentration was raised because more immunological complexes between CPX and anti-CPX antibodies were formed, preventing the electron transfer [Figure 3.19(b)], and then became steady after adding 1000 μg mL^{-1}. The development of an electrically insulating immunocomplex, which prevents the transmission of electrons between electrolytic species $[Fe(CN)_6]^{3-/4-}$ and immune electrode, is thought to be the cause of the drop in peak current noticed following the addition of CPX antibiotics [57][58].

This decline also demonstrated that the CPX antibiotics were successfully attached to the immunoelectrode surface following the reaction. In conclusion, the amount of immune complex formed on the immunoelectrode interface was the source of the drop in peak currents. The enlarged area of the DPV plot is shown in the inset.

As observed in Figure 3.19(c), the variation in the current (I) exhibited an excellent linear correlation with the CPX concentration ranging from 10^{-6} to 1000 μg mL^{-1} under the optimal circumstances. The following equation, which has a 0.992 linear regression coefficient, is obtained from the calibration graph involving peak current as well as standard concentrations of CPX.

$$I_p = [-1.63\ (\mu A\ mL\ \mu g^{-1}) \times \text{conc. of CPX}\ (\mu g\ mL^{-1})] + 56.57 \mu A,\ R^2 = 0.992 \qquad \text{Eq3.28}$$

This showed that the immunocomplex formed between the anti-CPX antibody and antigen CPX, particularly on the BSA/anti-CPX/APTES/nLa_2O_3NPs@rGO/ITO immune sensing platform, offered fewer electroactive areas for unstrained transfer of electrons at electrode surface that resulted in thickness broadening of insulating layer development because of which current dropped in proportion to CPX concentration. The sensitivity value for the manufactured BSA/anti-CPX/APTES/nLa_2O_3NPs@rGO/ITO immunosensor electrode was determined as 6.52 μA mL μg^{-1} cm^2 having 0.992 R^2 determined by the slope of the linear plot/surface area of the electrode, i.e., 0.25 cm^{-2}. The limit of quantification (LOQ: 10σ/m) and limit of detection (LOD: 3σ/m), where m stands for linear plot' sensitivity, and σ depicts intercept' standard deviation, were discovered to be 0.18 μg $mL^{-1}$and 0.055 μg mL^{-1}, respectively. The immunosensor also has a broad linear detection range between 10^{-6} and 600 μg mL^{-1}. The distinctive interaction between CPX and anti-CPX and the thin film generation of well-ordered nLa_2O_3NPs@rGO composites may be the source of the immunosensor's high sensitivity. Having an efficient covalent connection with a widely recognized amide bond, APTES functionalized nLa_2O_3NPs@rGO produced an ideal matrix for effective antibody attachment.

The improved BSA/anti-CPX/APTES/nLa_2O_3NPs@rGO/ITO immunosensor outperformed other sensors regarding wide detection range, LOD, and sensitivity compared with earlier investigations (Table 3.6). This occurred due to the antibodies and the modified nanocomposite, which increased the number of reactive functional

sites on the ITO surface electrode and boosted more efficient CPX binding. Additionally, the process was gentle and did not damage the electrode surface, which assisted in recognizing responsive CPX. According to our literature review, this study provides the first account of the development of an electrochemical immunosensor for detecting CPX using a nLa_2O_3NPs@rGOcomposite in just 14 min.

Table 3.6: Comparative table depicting BSA/anti-CPX/ATPES/nLa_2O_3/ITO biosensor' electrochemical parameters to earlier published data against CPX determination.

Sensor/Biosensor	**Technique**	**Sensitivity [μA μM^{-1}]**	**LOD (μM)**	**Linear Range (μM)**	**Sample**	**Ref.**
$MgFe_2O_4$-MWCNT/ GCE	CV	-	0.01	0.1−1000	Tablet, plasma, and urine	[59]
PAR/EGR/GCE	DPV	-	0.01	0.04–10 and10–120	Pharmaceutical preparation and biological media	[60]
P-β-CD-L-arg/CPE	DPV	-	0.05	0.05-100	Pharmaceutical formulations and human serum	[61]
DNA biosensor	DPV	-	9	40–80	-	[62]
NiONPs-GO-CTS: EPH/GCE	SWV	9.87	6.0× 10^{-3}	0.040–0.97	Urine, serum	[63]
MWCNT/GCE	CA	-	6	40–1000	Urine and serum	[64]
CZF/CPE	ASV	0.657	2.58× 10^{-3}	0.909 - 4.70×10^{3}	Urine, serum, pharmaceutical preparations	[65]
SPE	CA	0.031	0.33	13.75–135	DI water	[66]
TiO_2/PB/AuNPs/ CMK-3/Nafion/GE	CV	15.93	1.08× 10^{-1}	1–10	Environmental water	[67]
NP-GCE	DPV	-	0.008	0.25–100	Groundwater and tap water	[68]
Porous-Nafion-MWCNT/BDD	DPV	41 ± 5.2 and 2.1 ± 0.22	0.005	0.005−0.05, 0.05−10	Natural waters and wastewater effluents	[69]
BSA/anti-CPX/ APTES/nLa_2O_3/ITO	DPV	11.44 and 7.88	0.000001	0.000001-0.0005 and 0.001-1	Milk	[9]
BSA/anti-CPX/ APTES/nLa_2O_3 NPs@rGO/ITO	**DPV**	**6.52**	**0.005**	**1×10^{-6} - 600**	**Milk**	**This work**

In addition, the value of association constant (Ka) for the BSA/anti-CPX/APTES/nLa_2O_3NPs@rGO/ITO immunoelectrode shown in Figure 3.19(d) was determined from the Hens-Wolf graph, which consists of a plot relating CPX concentration with CPX conc./current and estimated to be 50 μg mL^{-1}. Ka depends on several aspects of the immunosensor's design, including biomolecule binding sites and the immobilization of antibodies (anti-CPX), which may result in different conformation modifications in the structure of antibodies on the electrode. Here, the increased K_a value shows how the constructive anti-CPX confirmation, as well as more significant loading on the electrode's surface, have increased the BSA/anti-CPX/APTES/nLa_2O_3NPs@rGO/ITO immunoelectrode affinity against CPX. The dissociation constant (K_d) was found at -3.2 μg mL^{-1}, indicating a strong, centered CPX affinity. The linear fitting plot of Hanes-Wolf yielded inverse slope values for the K_a calculations, whereas K_d value is estimated using intercept and K_a product [70][71].

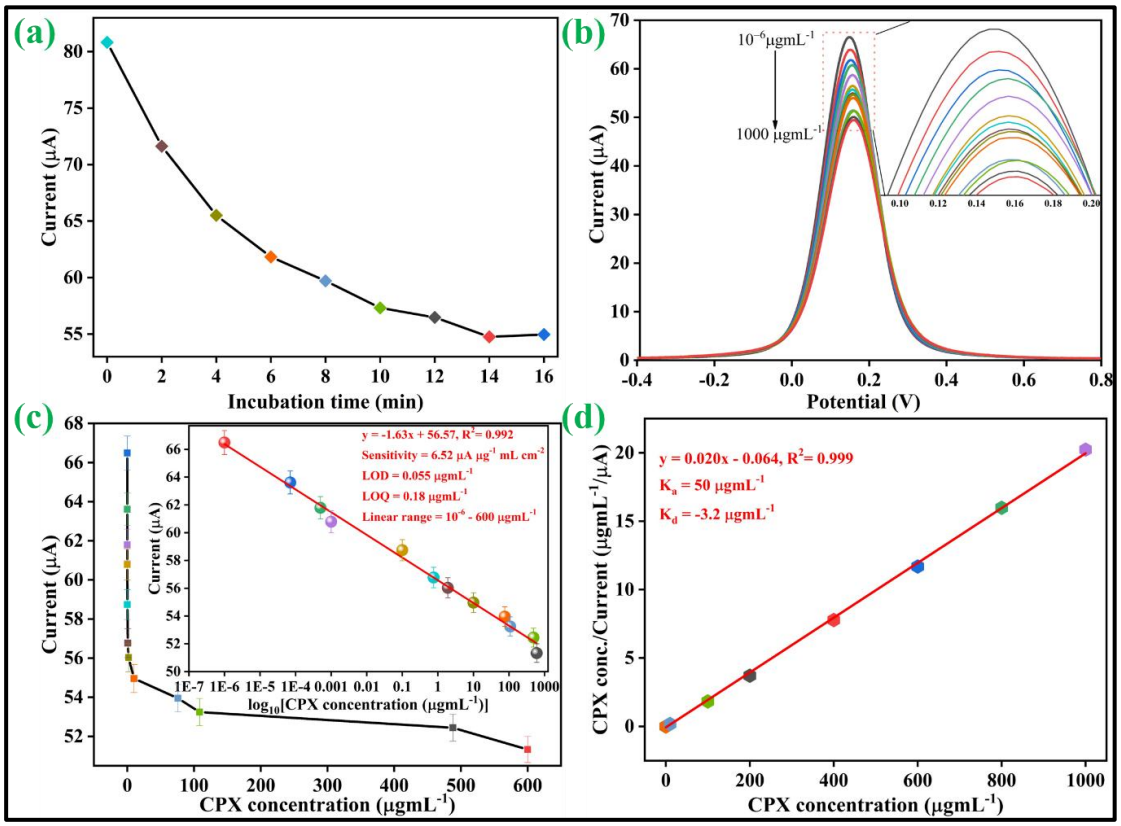

Figure 3.19: (a) BSA/anti-CPX/APTES/nLa_2O_3NPs@rGO/ITOimmunoelectrode's incubation analysis for attaching of CPX to electrode surface, (b) Electrochemical response studies of BSA/anti-CPX/APTES/nLa_2O_3NPs@rGO/ITOimmunoelectrodeas a function of the concentration of CPXi.e., 10^{-6}- 600 μgmL^{-1} using DPV [inset displayed the zoomed magnification]; (c) Linear plot of peak current versus the log of the concentration of CPX (μg mL^{-1}) and; (d)BSA/anti-CPX/APTES/nLa_2O_3NPs@rGO/ITOimmunoelectrode'sHens-Wolf plot.

3.B4.4 Control, Interferent, Repeatability, as well as Reproducibility Studies

Analyzing the APTES/nLa_2O_3NPs@rGO/ITO electrochemical signals at higher CPX levels from 10^{-6} to 600 μg mL^{-1} was carried out as a controlled study to determine the APTES/nLa_2O_3NPs@rGO/ITO electrode' cross-reactivity against CPX antibiotics. As seen in Figure 3.20(a), there were no discernible variations in anodic peak current with higher CPX concentration, proving that antigens have no interaction with the APTES/nLa_2O_3NPs@rGO/ITO electrode substrate. Consequently, the immune reaction between the CPX antigen and BSA/anti-CPX/APTES/nLa_2O_3NPs@rGO/ITO electrode was the main reason for the rising current in response tests.

As is widely understood, foodstuffs are extremely rich in both organic and inorganic analytical substances such as Mg^{++} (0.01 gmL^{-1}), ciprofloxacin (50 mM), Na^{+}(0.6 g/100 mL), ofloxacin (50 mM), norfloxacin (50 mM), cholesterol (100 M), vitamin C (100 M), glucose (100 M), BSA (100 M), and so forth. The interfering agents were prepared in the milk samples following the respective concentration. Additionally, the sensor response to the CPX was evaluated in milk samples in the presence of different potential interfering agents to test BSA/anti-CPX/APTES/nLa_2O_3 NPs@rGO/ITO immunosensor' cross-reactivity [Figure 3.20(b)]. The constructed BSA/anti-CPX/APTES/nLa_2O_3NPs@rGO/ITO immunoelectrode was first tested in the presence of a particular CPX concentration. Then, following a 15-min incubation period, a different analyte was gradually added (20 μL at a time) to the electrolyte that had already been premixed by the CPX analyte, and the current output was measured. The current of whole interferents has been shown to be merely unaltered, demonstrating the biosensor's high specificity for the CPX antigen.

Using the equation 3.26, the selectivity coefficient was determined to be 1 for each interfering agent.

$$SC = Ic + Ic+i \qquad \text{Eq 3.29}$$

Where Ic, as well as Ic+i, are the immunosensor's current values in absence and presence, respectively, exhibiting barely any change in the response.

By using the DPV approach on 7 separate developed electrodes under similar experimental circumstances, the reproducibility of the developed BSA/anti-CPX/APTES/nLa_2O_3NPs@rGO/ITO immunosensor is examined (data displayed in Figure 3.20(c)). Relative standard deviation (%RSD) was determined for every electrode to evaluate the variance of data from various electrodes to standard I_{pa} magnitude. The average %RSD was discovered as 3.43%, demonstrating that the calculated %RSD is below an acceptable limit. The BSA/anti-CPX/APTES/nLa_2O_3NPs@rGO/ITO immunosensor showed good reproducibility as the current response was barely altered. Similar to this, the repeatability of the BSA/anti-CPX/APTES/nLa_2O_3NPs@rGO/ITO immunosensor was assessed by employing the DPV approach to take6 subsequent readings for a specific CPX concentration, i.e., 100 μg mL^{-1} [Figure 3.20(d)]. The repeatability RSD results have been found as 2.43%, which is within the permitted range.

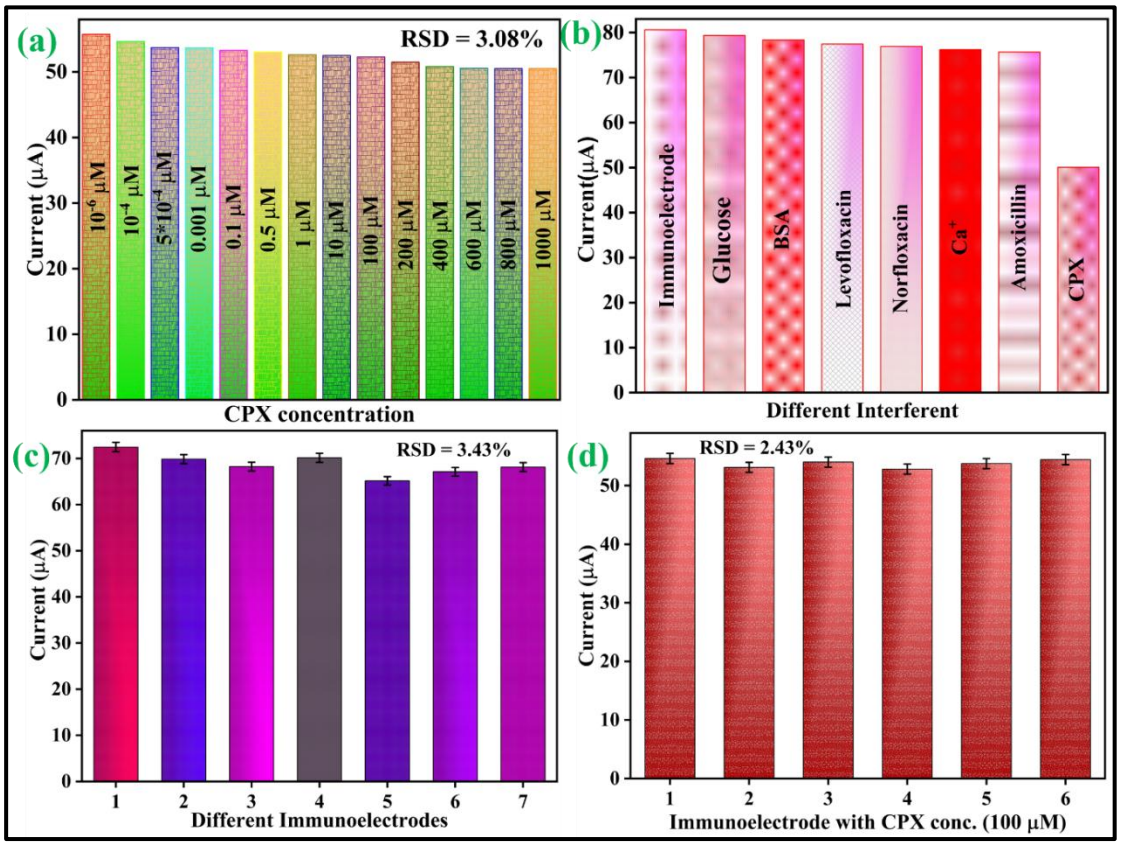

Figure 3.20: (a) APTES/nLa_2O_3NPs@rGO/ITOelectrodeshowing control studies versus concentration of CPX antigen from 10^{-6}- 600 μgmL^{-1}; (b) BSA/anti-CPX/APTES/ nLa_2O_3NPs@rGO/ITOimmunoelectrodedepicting bar graph of different interferents found in the milk sample using DPV technique; (c) and (d) Reproducibility as well as repeatability responses of BSA/anti-CPX/APTES/nLa_2O_3NPs@rGO/ITOimmunoelectrode, respectively.

3.B4.5 Regeneration, Stability, and Spiked Sample Studies

Regeneration is a crucial characteristic in the creation of affordable biosensors, the procedure for reusing the fabricated biosensor multiple times. The immunosensor BSA/anti-CPX/APTES/nLa_2O_3NPs@rGO/ITO was examined following anti-CPX and CPX interactions to assess how well it regenerates. Different kinds of regeneration solutions, including $MgCl_2$ (salt), NaOH (basic), and glycine-HCl buffer or HCl (acidic), were prepared for this study. The Ab-Ag immunological complex was broken in this experiment using 0.010% Tween-20 and 10% (1:1) formamide/DMSO in PBS (pH 7.0) [72][51]. Following that, a specific CPX concentration was once again re-examined using a regenerated immunoelectrode (BSA/anti-CPX/APTES/nLa_2O_3NPs@ rGO/ITO). To evaluate the DPV signal in this investigation, a specific CPX antigen concentration was used [Figure 3.21(a)]. Following each regeneration process, the immunosensor electrochemical changes were recorded. The BSA/anti-CPX/APTES/ nLa_2O_3NPs@rGO/ITO immunosensor could potentially be reused for a minimum of 4 times depicting 95% retention, as well as 5 more times for 84% retention of the first response that was recorded, as shown in Figure 3.21(a). Furthermore, the BSA/anti-CPX/APTES/nLa_2O_3NPs@rGO/ITO immunosensor was put to the test using CV at a 5-day interval to determine its endurance. The findings are displayed in Figure 3.21(b), which depicts that it maintains a current value of 95% for the first 25 days, then slightly declines to 80% after 35 days. As a result, the manufactured immunosensor has 25-day durability.

For investigating the exploitation of CPX in a food sample study, the immunosensor's practical use is crucial. To illustrate the ability of the constructed immunosensor to recognize CPX in milk samples, a spiked sample investigation has been examined. For this, the proposed BSA/anti-CPX/APTES/nLa_2O_3NPs@rGO/ITO immunoelectrode reaction on treated milk was evaluated. However, the milk sample was treated/ spiked with particular concentrations of CPX when no CPX had been identified to evaluate the accuracy of the constructed immunosensor. As shown in Table 3.7, the measured RSD and their recoveries values for CPX identification were determined as 0.67-2.99% and 95.87-102.73%, respectively. The estimated outcomes fell within an acceptable range, further validating the immunosensor's reliability and accuracy in milk samples. Additionally, as shown in Figure 3.21(d), the linear fitting graph was examined in the presence of spiked milk and standard samples. In the standard sample's response, the most suitable linear fitting curve was discovered at 0.992 R^2 value.

Table 3.7: Developed BSA/anti-CPX/APTES/nLa_2O_3NPs@rGO/ITOimmunoelectrode showing RSD and recovery of CPX antibiotic in spiked milk samples.

Sample	Concentrations added (μgmL^{-1})	DPV current for Amp (μA)	DPV current for spike-sample (μA)	RSD (%)	Recovery (%)
Milk	1×10^{-6}	66.49	67.53	1.1	101
	1×10^{-4}	63.6146	62.13	1.67	97
	4×10^{-4}	61.79	62.43	0.72	101
	0.001	60.79	60.12	0.78	98
	0.1	58.74	57.13	1.97	97
	0.5	56.7691	57.53	0.94	101
	1	56.03056	53.22	3.64	94
	10	54.96	53.78	1.53	97
	100	53.95246	55.01	1.37	101
	200	53.24448	52.98	0.35	99
	400	52.44482	51.01	1.96	97
	600	51.33	50.43	1.25	98
	800	50.07	50.12	0.07	100
	1000	49.43	49.32	0.15	99

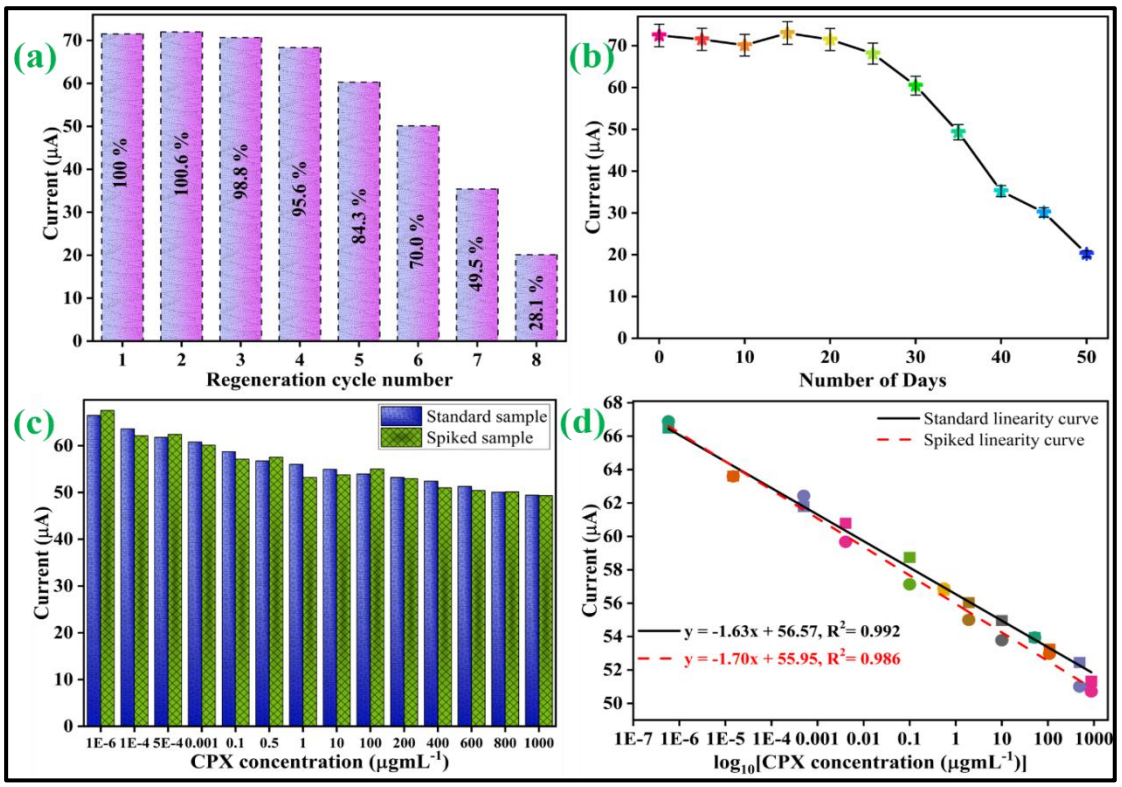

Figure 3.21: (a) Regeneration effect studies of the BSA/anti-CPX/APTES/nLa_2O_3 NPs@rGO/ITO immunosensing platform at a particular concentration of CPX; (b) Stability of developed BSA/anti-CPX/APTES/nLa_2O_3NPs@rGO/ITO immunosensor; (c) Real spiked milk sample studies versus CPX concentration; and (d) Comparative calibration curve in spiked milk and standard samples.

3.B5 References

[1] V. F. Samanidou, C. E. Demetriou, and I. N. Papadoyannis, "Direct determination of four fluoroquinolones, enoxacin, norfloxacin, ofloxacin, and ciprofloxacin, in pharmaceuticals and blood serum by HPLC," *Anal. Bioanal. Chem.*, vol. 375, pp. 623–629, 2003.

[2] J. Bertino Jr and D. Fish, "The safety profile of the fluoroquinolones," *Clin. Ther.*, vol. 22, no. 7, pp. 798–817, 2000.

[3] C. Fierens, S. Hillaert, and W. Van den Bossche, "The qualitative and quantitative determination of quinolones of first and second generation by capillary electrophoresis," *J. Pharm. Biomed. Anal.*, vol. 22, no. 5, pp. 763–772, 2000.

[4] C. B. Inderlied and K. A. Nash, "Antibiotics in laboratory medicine," *Lippincott Williams & Wilkins, Philadelphia*, pp. 127–129, 1996.

[5] A. H. Gilani, S. Bashir, K. H. Janbaz, and A. Khan, "Pharmacological basis for the use of Fumaria indica in constipation and diarrhea," *J. Ethnopharmacol.*, vol. 96, no. 3, pp. 585–589, 2005.

[6] D. G. J. Larsson, C. de Pedro, and N. Paxeus, "Effluent from drug manufactures contain extremely high levels of pharmaceuticals," *J. Hazard. Mater.*, vol. 148, no. 3, pp. 751–755, 2007.

[7] S. Pakpinyo and J. Sasipreeyajan, "Molecular characterization and determination of antimicrobial resistance of Mycoplasma gallisepticum isolated from chickens," *Vet. Microbiol.*, vol. 125, no. 1–2, pp. 59–65, 2007.

[8] S.-C. Chang, Y.-C. Chen, K.-T. Luh, and W.-C. Hsieh, "In vitro activites of antimicrobial agents, alone and in combination, against Acinetobacter baumannii isolated from blood," *Diagn. Microbiol. Infect. Dis.*, vol. 23, no. 3, pp. 105–110, 1995.

[9] N. Chaudhary, A. K. Yadav, J. G. Sharma, and P. R. Solanki, "Designing and characterization of a highly sensitive and selective biosensing platform for ciprofloxacin detection utilizing lanthanum oxide nanoparticles," *J. Environ. Chem. Eng.*, vol. 9, no. 6, p. 106771, 2021.

[10] A. Radi, M. A. El Ries, and S. Kandil, "Electrochemical study of the interaction of levofloxacin with DNA," *Anal. Chim. Acta*, vol. 495, no. 1–2, pp. 61–67, 2003.

[11] G. G. Snitkoff, D. W. Grabe, R. Holt, and G. R. Bailie, "Development of an Immunoassay for Monitoring the Levels of Ciprofloxacin Patient Samples," *J. Immunoass. Immunochem.*, vol. 19, no. 4, pp. 227–238, 1998.

[12] S. Mostafa, M. El-Sadek, and E. A. Alla, "Spectrophotometric determination of ciprofloxacin, enrofloxacin and pefloxacin through charge transfer complex formation," *J. Pharm. Biomed. Anal.*, vol. 27, no. 1–2, pp. 133–142, 2002.

[13] R. H. O. Montes, M. C. Marra, M. M. Rodrigues, E. M. Richter, and R. A. A. Muñoz, "Fast determination of ciprofloxacin by batch injection analysis with amperometric detection and capillary electrophoresis with capacitively coupled contactless conductivity detection," *Electroanalysis*, vol. 26, no. 2, pp. 432–438, 2014.

[14] H.-W. Sun, L.-Q. Li, and X.-Y. Chen, "Flow-injection enhanced chemiluminescence method for determination of ciprofloxacin in pharmaceutical preparations and biological fluids," *Anal. Bioanal. Chem.*, vol. 384, pp. 1314–1319, 2006.

[15] Y. Ni, Y. Wang, and S. Kokot, "Multicomponent kinetic spectrophotometric determination of pefloxacin and norfloxacin in pharmaceutical preparations and human plasma samples with the aid of chemometrics," *Spectrochim. Acta Part A Mol. Biomol. Spectrosc.*, vol. 70, no. 5, pp. 1049–1059, 2008.

[16] Y. Liang, C. Yu, and J. Song, "Cathodic electrochemiluminescence of the peroxydisulphate–ciprofloxacin system and its analytical applications," *Luminescence*, vol. 26, no. 6, pp. 662–669, 2011.

[17] G.-H. Wan, H. Cui, Y.-L. Pan, P. Zheng, and L.-J. Liu, "Determination of quinolones residues in prawn using high-performance liquid chromatography with Ce (IV)–Ru (bpy) 32+–HNO3 chemiluminescence detection," *J. Chromatogr. B*, vol. 843, no. 1, pp. 1–9, 2006.

[18] H. Y. Ji, D. W. Jeong, Y. H. Kim, H.-H. Kim, D.-R. Sohn, and H. S. Lee, "Hydrophilic interaction liquid chromatography–tandem mass spectrometry for the determination of levofloxacin in human plasma," *J. Pharm. Biomed. Anal.*, vol. 41, no. 2, pp. 622–627, 2006.

[19] A. K. Yadav, D. Verma, and P. R. Solanki, "Electrophoretically deposited L-cysteine functionalized MoS2@MWCNT nanocomposite platform: a smart approach toward highly sensitive and label-free detection of gentamicin," *Mater. Today Chem.*, vol. 22, p. 100567, Dec. 2021, doi: 10.1016/J.MTCHEM.2021.100567.

[20] A. K. Yadav, T. K. Dhiman, G. Lakshmi, A. N. Berlina, and P. R. Solanki, "A highly sensitive label-free amperometric biosensor for norfloxacin detection based on chitosan-yttria nanocomposite," *Int. J. Biol. Macromol.*, vol. 151, pp. 566–575, 2020.

[21] J.-M. Moon, D.-M. Kim, M. H. Kim, J.-Y. Han, D.-K. Jung, and Y.-B. Shim, "A disposable amperometric dual-sensor for the detection of hemoglobin and glycated hemoglobin in a finger prick blood sample," *Biosens. Bioelectron.*, vol. 91, pp. 128–135, 2017.

[22] S. Chung, J.-M. Moon, J. Choi, H. Hwang, and Y.-B. Shim, "Magnetic force assisted electrochemical sensor for the detection of thrombin with aptamer-antibody sandwich formation," *Biosens. Bioelectron.*, vol. 117, pp. 480–486, 2018.

[23] A. C. Sun and D. A. Hall, "Point-of-care smartphone-based electrochemical biosensing," *Electroanalysis*, vol. 31, no. 1, pp. 2–16, 2019.

[24] S. Bhattacharya, R. Maiti, M. B. Sen, S. K. Saha, and D. Chakravorty, "Anomalous enhancement in the magnetoconductance of graphene/CoFe2O4 composite due to spin–orbit coupling," *J. Phys. D. Appl. Phys.*, vol. 48, no. 43, p. 435002, 2015.

[25] P. Hota, A. J. Akhtar, S. Bhattacharya, M. Miah, and S. K. Saha, "Ferromagnetism in graphene due to charge transfer from atomic Co to graphene," *Appl. Phys. Lett.*, vol. 111, no. 4, p. 42402, 2017.

[26] X. Zhu *et al.*, "Syntheses, structures and photoluminescence of a series of lanthanide-organic frameworks involving in situ ligand formation," *J. Solid State Chem.*, vol. 182, no. 3, pp. 421–427, 2009.

[27] D. Lin *et al.*, "High ionic conductivity of composite solid polymer electrolyte via in situ synthesis of monodispersed SiO2 nanospheres in poly (ethylene oxide)," *Nano Lett.*, vol. 16, no. 1, pp. 459–465, 2016.

[28] Z. Li, X. Hou, L. Yu, Z. Zhang, and P. Zhang, "Preparation of lanthanum trifluoride nanoparticles surface-capped by tributyl phosphate and evaluation of their tribological properties as lubricant additive in liquid paraffin," *Appl. Surf. Sci.*, vol. 292, pp. 971–977, 2014.

[29] C. Tan, X. Huang, and H. Zhang, "Synthesis and applications of graphene-based noble metal nanostructures," *Mater. Today*, vol. 16, no. 1–2, pp. 29–36, 2013.

[30] R. Kumar, R. K. Singh, P. K. Dubey, D. P. Singh, and R. M. Yadav, "Self-assembled hierarchical formation of conjugated 3D cobalt oxide nanobead–CNT–graphene nanostructure using microwaves for high-performance supercapacitor electrode," *ACS Appl. Mater. Interfaces*, vol. 7, no. 27, pp. 15042–15051, 2015.

[31] R. Kumar, M. M. Abdel-Galeil, K. Z. Ya, K. Fujita, W. K. Tan, and A. Matsuda, "Facile and fast microwave-assisted formation of reduced graphene oxide-wrapped manganese cobaltite ternary hybrids as improved supercapacitor electrode material," *Appl. Surf. Sci.*, vol. 481, pp. 296–306, 2019.

[32] R. Kumar, E. Joanni, R. K. Singh, D. P. Singh, and S. A. Moshkalev, "Recent advances in the synthesis and modification of carbon-based 2D materials for application in energy conversion and storage," *Prog. Energy Combust. Sci.*, vol. 67, pp. 115–157, 2018.

[33] I. S. El-Hallag, M. N. El-Nahass, S. M. Youssry, R. Kumar, M. M. Abdel-Galeil, and A. Matsuda, "Facile in-situ simultaneous electrochemical reduction and deposition of reduced graphene oxide embedded palladium nanoparticles as high performance electrode materials for supercapacitor with excellent rate capability," *Electrochim. Acta*, vol. 314, pp. 124–134, 2019.

[34] R. Kumar, R. K. Singh, D. P. Singh, E. Joanni, R. M. Yadav, and S. A. Moshkalev, "Laser-assisted synthesis, reduction and micro-patterning of graphene: Recent progress and applications," *Coord. Chem. Rev.*, vol. 342, pp. 34–79, 2017.

[35] A. Devadoss *et al.*, "Ultrathin functional polymer modified graphene for enhanced enzymatic electrochemical sensing," *Biosensors*, vol. 9, no. 1, p. 16, 2019.

[36] N. G. Hallfors, S. A. Al Junaibi, K. Liao, M. Ismail, and A. F. Isakovic, "Reduced Graphene oxide for the design of electrocardiogram sensors: Current status and perspectives," *IoT Phys. Layer Des. Implement.*, pp. 3–11, 2019.

[37] P. K. Gupta, Z. H. Khan, and P. R. Solanki, "Improved electrochemical performance of metal doped Zirconia nanoparticles for detection of Ochratoxin-A," *J. Electroanal. Chem.*, vol. 829, pp. 69–80, 2018.

[38] S. Kumar, J. G. Sharma, S. Maji, and B. D. Malhotra, "Nanostructured zirconia decorated reduced graphene oxide based efficient biosensing platform for non-invasive oral cancer detection," *Biosens. Bioelectron.*, vol. 78, pp. 497–504, 2016.

[39] Y. Li *et al.*, "Nitidine chloride-assisted bio-functionalization of reduced graphene oxide by bovine serum albumin for impedimetric immunosensing," *Biosens. Bioelectron.*, vol. 79, pp. 536–542, 2016.

[40] Y. Chen *et al.*, "Effective immobilization of Au nanoparticles on TiO2 loaded graphene for a novel sandwich-type immunosensor," *Biosens. Bioelectron.*, vol. 102, pp. 301–306, 2018.

[41] D. Verma, A. K. Yadav, M. Das Mukherjee, and P. R. Solanki, "Fabrication of a sensitive electrochemical sensor platform using reduced graphene oxide-molybdenum trioxide nanocomposite for BPA detection: An endocrine disruptor," *J. Environ. Chem. Eng.*, vol. 9, no. 4, p. 105504, 2021.

[42] A. K. Yadav, P. Gulati, R. Sharma, A. Thakkar, and P. R. Solanki, "Fabrication of alkoxysilane substituted polymer-modified disposable biosensing platform: Toward sperm protein 17 sensing as a new cancer biomarker," *Talanta*, p. 123376, 2022.

[43] A. K. Yadav, D. Verma, G. Lakshmi, S. Eremin, and P. R. Solanki, "Fabrication of label-free and ultrasensitive electrochemical immunosensor based on molybdenum disulfide nanoparticles modified disposable ITO: An analytical platform for antibiotic detection in food samples," *Food Chem.*, vol. 363, p. 130245, 2021.

[44] R. Rajagopal, A. Ragunathan, S. K. SM, R. Krishnan, and B. A. Kamaludeen, "Synthesis and electrochemical studies of Ta–Graphene nanocomposite film modified platinum electrode," *J. Electroanal. Chem.*, vol. 780, pp. 53–59, 2016.

[45] P. Cui, J. Lee, E. Hwang, and H. Lee, "One-pot reduction of graphene oxide at subzero temperatures," *Chem. Commun.*, vol. 47, no. 45, pp. 12370–12372, 2011.

[46] R. Senthil Kumar and B. Gnanavel, "High performance catalytic activity of pure and silver (Ag) doped TiO 2 nanoparticles by a novel microwave irradiation technique," *J. Mater. Sci. Mater. Electron.*, vol. 28, pp. 4253–4259, 2017.

[47] M. Salavati-Niasari, G. Hosseinzadeh, and F. Davar, "Synthesis of lanthanum carbonate nanoparticles via sonochemical method for preparation of lanthanum hydroxide and lanthanum oxide nanoparticles," *J. Alloys Compd.*, vol. 509, no. 1, pp. 134–140, 2011.

[48] R. B. Borade *et al.*, "Polycrystalline to preferred-(100) single crystal texture phase transformation of yttrium iron garnet nanoparticles," *Nanoscale Adv.*, vol. 1, no. 1, pp. 403–413, 2019.

[49] Q. Zhou *et al.*, "Nano La2O3 as a heterogeneous catalyst for biodiesel synthesis by transesterification of Jatropha curcas L. oil," *J. Ind. Eng. Chem.*, vol. 31, pp. 385–392, 2015.

[50] S. Augustine, P. Kumar, and B. D. Malhotra, "Amine-functionalized MoO3@ RGO nanohybrid-based biosensor for breast cancer detection," *ACS Appl. Bio Mater.*, vol. 2, no. 12, pp. 5366–5378, 2019.

[51] A. K. Yadav, D. Verma, A. Kumar, A. N. Bhatt, and P. R. Solanki, "Biocompatible epoxysilane substituted polymer-based nano biosensing platform for label-free detection of cancer biomarker SP17 in patient serum samples," *Int. J. Biol. Macromol.*, p. 124325, 2023.

[52] S. Kumar, Y. Lei, N. H. Alshareef, M. A. Quevedo-Lopez, and K. N. Salama, "Biofunctionalized two-dimensional Ti3C2 MXenes for ultrasensitive detection of cancer biomarker," *Biosens. Bioelectron.*, vol. 121, pp. 243–249, 2018.

[53] M. Zhou, Y. Zhai, and S. Dong, "Electrochemical sensing and biosensing platform based on chemically reduced graphene oxide," *Anal. Chem.*, vol. 81, no. 14, pp. 5603–5613, 2009.

[54] S. Kumar *et al.*, "Biofunctionalized nanostructured zirconia for biomedical application: a smart approach for oral cancer detection," *Adv. Sci.*, vol. 2, no. 8, p. 1500048, 2015.

[55] S. Tiwari, P. K. Gupta, Y. Bagbi, T. Sarkar, and P. R. Solanki, "L-cysteine capped lanthanum hydroxide nanostructures for non-invasive detection of oral cancer biomarker," *Biosens. Bioelectron.*, vol. 89, pp. 1042–1052, 2017.

[56] D. Verma, D. Chauhan, M. Das Mukherjee, K. R. Ranjan, A. K. Yadav, and P. R. Solanki, "Development of MWCNT decorated with green synthesized AgNps-based electrochemical sensor for highly sensitive detection of BPA," *J. Appl. Electrochem.*, vol. 51, no. 3, pp. 447–462, 2021.

[57] S. Kumar *et al.*, "Highly sensitive protein functionalized nanostructured hafnium oxide based biosensing platform for non-invasive oral cancer detection," *Sensors Actuators B Chem.*, vol. 235, pp. 1–10, 2016.

[58] P. K. Gupta, Z. H. Khan, and P. R. Solanki, "One-step electrodeposited porous ZnO thin film based immunosensor for detection of Vibrio cholerae toxin," *J. Electrochem. Soc.*, vol. 163, no. 7, p. B309, 2016.

[59] A. A. Ensafi, A. R. Allafchian, and R. Mohammadzadeh, "Characterization of $MgFe_2O_4$ nanoparticles as a novel electrochemical sensor: application for the voltammetric determination of ciprofloxacin," *Anal. Sci.*, vol. 28, no. 7, pp. 705–710, 2012.

[60] X. Zhang, Y. Wei, and Y. Ding, "Electrocatalytic oxidation and voltammetric determination of ciprofloxacin employing poly (alizarin red)/graphene composite film in the presence of ascorbic acid, uric acid and dopamine," *Anal. Chim. Acta*, vol. 835, pp. 29–36, 2014.

[61] F. Zhang, S. Gu, Y. Ding, Z. Zhang, and L. Li, "A novel sensor based on electropolymerization of β-cyclodextrin and l-arginine on carbon paste electrode for determination of fluoroquinolones," *Anal. Chim. Acta*, vol. 770, pp. 53–61, 2013.

[62] H. Nawaz, S. Rauf, K. Akhtar, and A. M. Khalid, "Electrochemical DNA biosensor for the study of ciprofloxacin–DNA interaction," *Anal. Biochem.*, vol. 354, no. 1, pp. 28–34, 2006.

[63] A. M. Santos, A. Wong, A. A. Almeida, and O. Fatibello-Filho, "Simultaneous determination of paracetamol and ciprofloxacin in biological fluid samples using a glassy carbon electrode modified with graphene oxide and nickel oxide nanoparticles," *Talanta*, vol. 174, pp. 610–618, 2017.

[64] L. Fotouhi and M. Alahyari, "Electrochemical behavior and analytical application of ciprofloxacin using a multi-walled nanotube composite film-glassy carbon electrode," *Colloids Surfaces B Biointerfaces*, vol. 81, no. 1, pp. 110–114, 2010.

[65] M. P. Kingsley, P. K. Kalambate, and A. K. Srivastava, "Simultaneous determination of ciprofloxacin and paracetamol by adsorptive stripping voltammetry using copper zinc ferrite nanoparticles modified carbon paste electrode," *RSC Adv.*, vol. 6, no. 18, pp. 15101–15111, 2016.

[66] D. Ganta, N. Trevino, and W. Montes, "Disposable chronoamperometric sensor for detecting ciprofloxacin," *Eng. Res. Express*, vol. 1, no. 1, p. 15031, 2019.

[67] A. Pollap and J. Kochana, "Electrochemical immunosensors for antibiotic detection," *Biosensors*, vol. 9, no. 2, p. 61, 2019.

[68] T. Chen *et al.*, "Highly efficient detection of ciprofloxacin in water using a nitrogen-doped carbon electrode fabricated through plasma modification," *New J. Chem.*, vol. 43, no. 38, pp. 15169–15176, 2019.

[69] P. Gayen and B. P. Chaplin, "Selective electrochemical detection of ciprofloxacin with a porous nafion/multiwalled carbon nanotube composite film electrode," *ACS Appl. Mater. Interfaces*, vol. 8, no. 3, pp. 1615–1626, 2016.

[70] D. Chauhan, A. K. Yadav, and P. R. Solanki, "Carbon cloth-based immunosensor for detection of 25-hydroxy vitamin D 3," *Microchim. Acta*, vol. 188, no. 4, pp. 1–11, 2021.

[71] A. K. Yadav, P. Gulati, R. Sharma, A. Thakkar, and P. R. Solanki, "Fabrication of alkoxysilane substituted polymer-modified disposable biosensing platform: Towards sperm protein 17 sensing as a new cancer biomarker," *Talanta*, vol. 243, p. 123376, 2022.

[72] A. Sangili, T. Kalyani, S.-M. Chen, A. Nanda, and S. K. Jana, "Label-free electrochemical immunosensor based on one-step electrochemical deposition of AuNP-RGO nanocomposites for detection of endometriosis marker CA 125," *ACS Appl. Bio Mater.*, vol. 3, no. 11, pp. 7620–7630, 2020.

Chapter 4

Optical Sensors for Ciprofloxacin Detection

CHAPTER 4

OPTICAL SENSORS FOR CIPROFLOXACIN DETECTION

This chapter displays the optical sensing system for selective CPX detection. It has been categorized into two parts. In the first part, CQDs are synthesized using the leaves of C.Tamala (Tejpata) through a simple hydrothermal route. The green synthesized CQDs are fluorescent and showed good stability in terms of fluorescence. The properties of CQDs were characterized using various characterizing tools. On the other hand, a fluorescence-based optical sensing platform has been explored for the detection of CPX through the synthesis of CQDs from *Ziziphus mauritiana (Ber).* These methods provide a promising sensing system that is simple, robustness, easy and cost-effective, etc.

Part A: A novel bio-inspired carbon quantum dots-based optical sensor for ciprofloxacin detection

4.A1 Introduction

Fluoroquinolones are a class of antibiotics extensively used for fighting against numerous Gram-positive and Gram-negative microorganisms as human and veterinary medicines [1]. Among them, CPX is the most explored antibiotic known for its stability that does not go complete metabolism, and 30–90% residue stays in the body [2],[3]. The increasing public apprehension regarding the buildup of pharmaceutical remnants in the food supply chain and livestock has prompted the widespread implementation of this antibiotic. Nevertheless, it has been observed that CPX residues can pose a threat to human health through their impact on the replication of mammalian cells and the occurrence of adverse drug reactions. There is a strong probability that it reaches the environment through patients' urine samples and wastewater due to inadequate metabolization of CPX in the body, which induces antibiotic resistance [4],[5]. In the coming future, the phenomenon of antibiotic resistance will be more complex. Failure to detect pathogenic bacteria is the primary stumbling block, resulting in inadequate antibiotic use and a lower survival rate in septic situations [6]. Therefore, the detection of

antibiotic residues is a serious issue and need of the hour. Numerous techniques are employed for detecting CPX remains, such as spectrophotometry [7], liquid chromatography-mass spectrophotometry [8], high-pressure liquid chromatography [9], and immunoassay [10], etc. But due to several disadvantages associated with it, they are not suitable for onsite food safety and environmental monitoring. On the other hand, the fluorometric detection technique has emerged as an alternate way for detecting CPX in real samples due to their rapid response, cost-efficiency, less interference, selectivity, and high sensitivity [11],[12]. The fluorescent carbon quantum dots (CQDs) exhibit appealing and intelligent characteristics as constituents of the carbon family. These materials have garnered significant interest due to their notable biocompatibility, abundant functional groups, minimal toxicity, exceptional water solubility, and efficient synthesis process [13],[14]. The utilization of natural carbon precursors for the green synthesis of carbon quantum dots (CQDs) has become increasingly important due to its cost-effectiveness, environmental sustainability, reproducibility, and simplicity compared to conventional chemical synthesis methods. The ample availability of carbon from natural sources is another reason for achieving attention to synthesizing green CQDs [15]. Out of the various spices, C. tamala was chosen as a natural precursor to synthesize green CQDs prepared via a hydrothermal process. C. tamala, recognized as tej patta, belongs to the family Lauraceae whose tej patta oil is used as a medicine for treating cardiac disorders diuretic, anti-flatulent, and carminative [16]. This work reports novel bioinspired, fluorescent CQDs derived from C. tamala leaves extract via a one-step, simple hydrothermal approach. The CQDs were characterized using different techniques and gave good quantum yield (QY). The CQDs show excellent solubility in water with blue emission and specific determination of CPX in the range from 1 to 100 µM.

4.A2 Experimental Methods

4.A2.1 Synthesis of CQDs

The CQDs were synthesized from *C.tamala* via a simple, one-step hydrothermal approach. For this, leaves extract was prepared by boiling the chopped leaves in 100 mL distilled water (DI) for 1 h. Then 40 mL of leaves extract was sonicated for 30 min and shifted to a Teflon vessel. The hydrothermal pot carrying the Teflon vessel was kept in the muffle furnace for 12 h at 200°C. The obtained brownish-yellow solution

was centrifuged to remove the bigger particles. Also, the filtrate after centrifugation was dialyzed in 1 L DI through a dialysis membrane having 3.5 KDa for 6 h whose water was changed every 30 min. Finally, the acquired fluorescent, green CQDs were kept at 4 °C for further use. Scheme 4.1 shows the synthesis of CQDs from *C. tamala* leaves extract

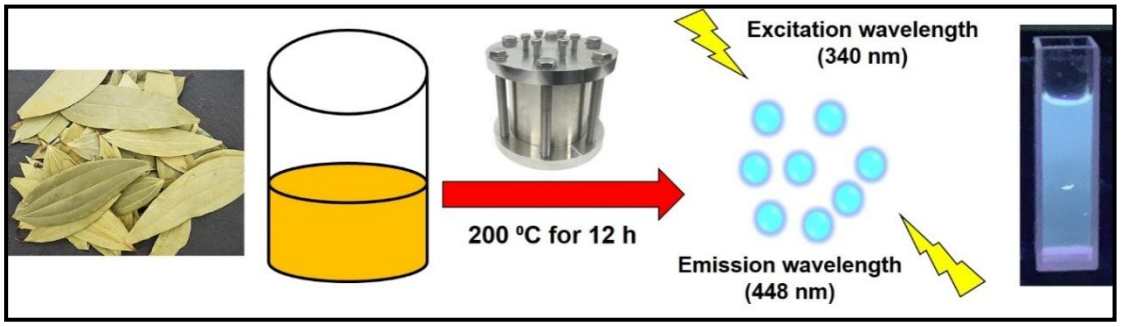

Scheme 4.1: Green synthesis of CQDs from *C. tamala* leaves extract

4.A3 Results and Discussion

4.A3.1 Quantum Yield Estimation

The QY of CQDs was found in an aqueous medium at 340 nm excitation wavelength by utilizing quinine sulfate as a reference. It was observed that hydrothermal synthesis of CQDs from *C. tamala* yielded 31 % of QY, which was highest in comparison to other naturally derived CQDs [17],[18]. This could be due to the high temperature and pressure conditions generated during the hydrothermal reaction owing to the well-organized carbonization of leaf extract.

4.A3.2 X-ray Diffraction (XRD) Analysis

The crystallinity of CQDs was examined through XRD. Figure 4.1 (a) depicts the XRD pattern of CQDs whose broad peak is located at 17.1°, which corresponds to the plane of graphitic material.

4.A3.3 Fourier Transformed Infrared Spectroscopy (FT-IR) Study

Figure 4.1(b) depicts broad peaks at 3443 and 2091cm^{-1} corresponding to O–H/N-H stretching vibrations of hydrogen bond and -C≡C- stretch, respectively. Also, the occurrence of prominent peaks at 1652 cm^{-1} corresponds to the C=O stretch bond, while

weak peaks at 2347,1406, and 1051 cm^{-1} are ascribed to C≡N, C-N, and C-O stretching vibrations, respectively.

4.A3.4 UV-Vis and PL Studies

The UV-Visible spectra of CQDs depict an absorption peak at 280 nm that corresponds to the π–π* transition of the conjugated C=C group [Figure 4.1(c)]. Also, in Figure 4.1 (d), a strong luminescence of CQDs at 448 nm with 340 nm excitation wavelength was observed by changing the excitation wavelength from 310-380 nm.

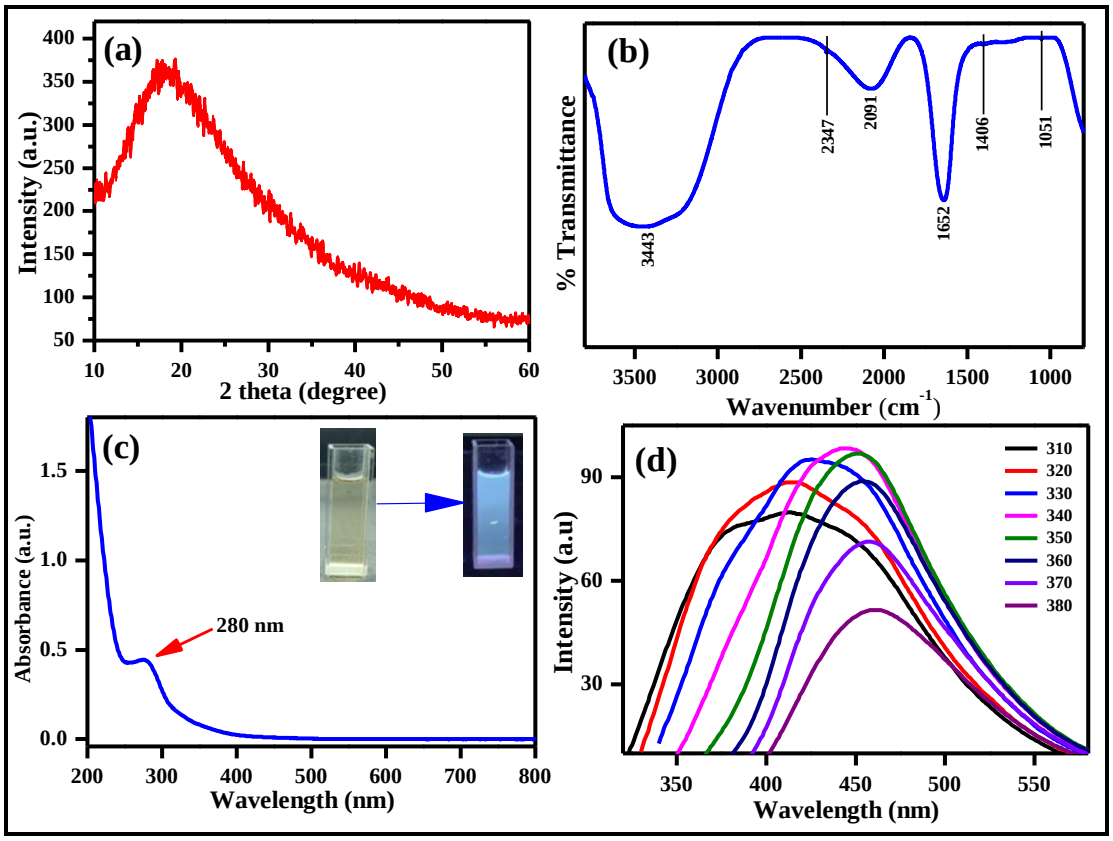

Figure 4.1: (a) XRD, (b) FT-IR, (c) UV-Visible spectra, inset depicts luminance of CQDs in daylight and high wavelength light; (d) fluorescence spectra of CQDs having excitation wavelengths from 310- 380 nm

4.A4 Optical Studies

4.A4.1 Detection of CPX

The (CQDs) were employed for the purpose of detecting concentrations of CPX within the range of 1 to 100 μM, by measuring the fluorescence intensity enhancement. It was

seen that with each addition of CPX concentration, there is an enhancement in fluorescence intensity [Figure 4.2 (a)]. Further, the linear graph was plotted between the CPX concentrations and fluorescence intensity of CQDs, showing consecutive increases in fluorescence intensity of CQDs for CPX concentrations [Figure 4. 2 (b)]. The CQDs show a linear detection of CPX ranging from 1–100 μM, having a detection limit of 6.06 μM that was calculated using the formula of 3*S* /*m* (where, S represents the standard error of the intercept, while m denotes the slope of the linear plot).

4.A4.2 Interference Study

The selectivity of CQD was done against various potential interfering agents for the detection of CPX [Figure 4.2 (c)]. The common antibiotics were taken and added separately to the sensing system. It was observed that no increase in intensity was thereupon adding the various interferents. However, the fluorescence intensity increased upon adding the CPX concentration (50 μM). Thus, the CQDs show good selectivity towards CPX.

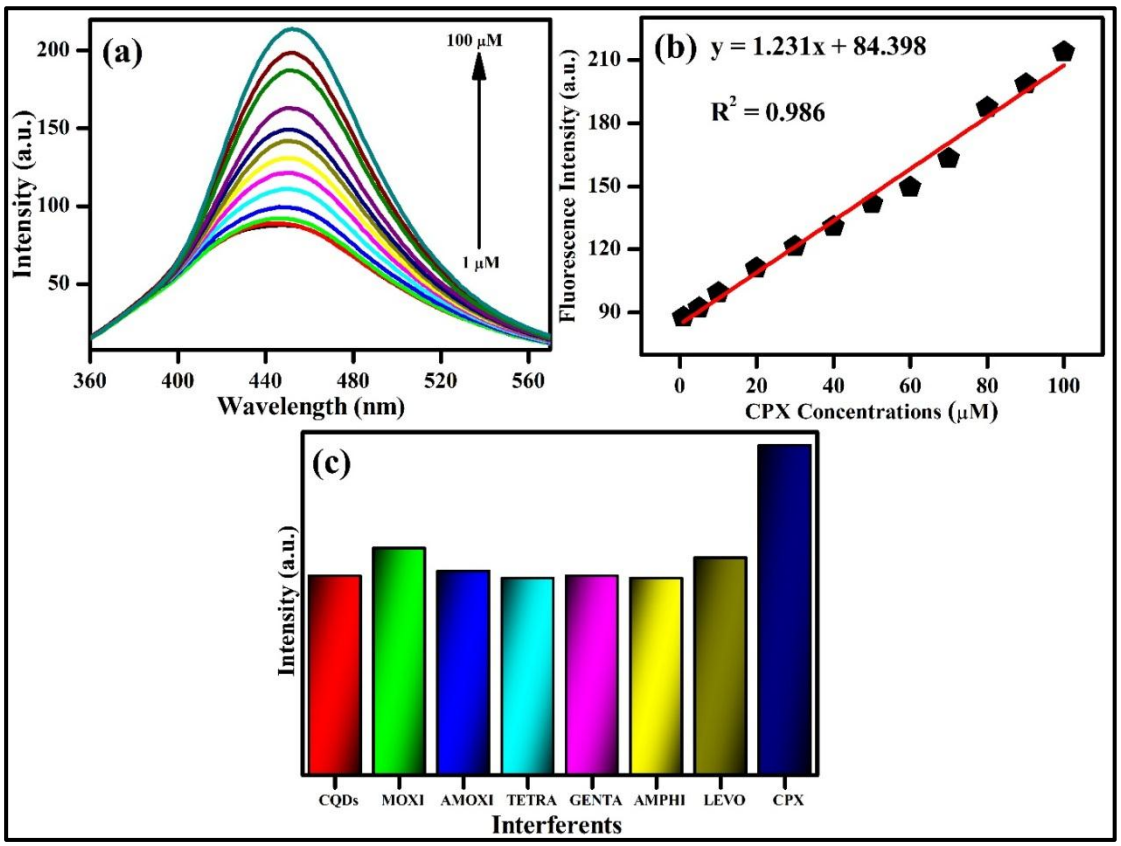

Figure 4.2: (a) The effect of CPX concentrations on the fluorescence intensity of CQDs, (b) Linear plot between CQDs fluorescence intensity and CPX concentrations; and (c) Interferent study of CQDs towards other antibiotics

4.A5 The Sensing Mechanism of CPX Detection using CQDs

The enhancement in fluorescence intensity of CQDs is ascribed to the hydrogen bonding interactions and charge transfer taking place between CQDs and CPX. As depicted from Scheme 4.2, the CQDs consist of carboxyl and hydroxyl groups which give aqueous solubility for combining with CPX through hydrogen bonding. Moreover, the charge transfer also plays a vital role. Due to the accepting nature of the nitrile group of CQDs and the electron-releasing effect of CPX, a connection is created between the two through a conjugated system that might encourage C=C bond polymerization. Thus, the synergetic effect of hydrogen bonding and charge transfer helped in fluorescence intensity enhancement by adding more CPX concentrations[19].

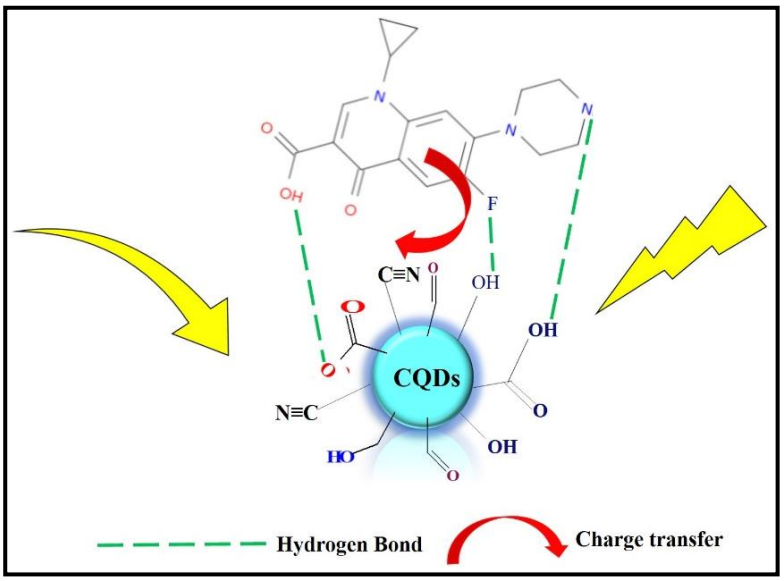

Scheme 4.2: Hypothetical mechanism of CPX detection using CQDs

4.A6 References

[1] Y. Zhao, G. Zhang, Q. Liu, M. Teng, J. Yang, and J. Wang, "Development of a lateral flow colloidal gold immunoassay strip for the rapid detection of enrofloxacin residues," *J. Agric. Food Chem.*, vol. 56, no. 24, pp. 12138–12142, 2008.

[2] M. C. Dodd, A. D. Shah, U. von Gunten, and C.-H. Huang, "Interactions of fluoroquinolone antibacterial agents with aqueous chlorine: reaction kinetics, mechanisms, and transformation pathways," *Environ. Sci. Technol.*, vol. 39, no. 18, pp. 7065–7076, 2005.

[3] G. Carlsson, S. Örn, and D. G. J. Larsson, "Effluent from bulk drug production is toxic to aquatic vertebrates," *Environ. Toxicol. Chem.*, vol. 28, no. 12, pp. 2656–2662, 2009.

[4] L. Chen, Z. Wang, M. Ferreri, J. Su, and B. Han, "Cephalexin residue detection in milk and beef by ELISA and colloidal gold based one-step strip assay," *J. Agric. Food Chem.*, vol. 57, no. 11, pp. 4674–4679, 2009.

[5] G. R. Marchesini, W. Haasnoot, P. Delahaut, H. Gerçek, and M. W. F. Nielen, "Dual biosensor immunoassay-directed identification of fluoroquinolones in chicken muscle by liquid chromatography electrospray time-of-flight mass spectrometry," *Anal. Chim. Acta*, vol. 586, no. 1–2, pp. 259–268, 2007.

[6] A. K. Yadav, T. K. Dhiman, G. Lakshmi, A. N. Berlina, and P. R. Solanki, "A highly sensitive label-free amperometric biosensor for norfloxacin detection based on chitosan-yttria nanocomposite," *Int. J. Biol. Macromol.*, vol. 151, pp. 566–575, 2020.

[7] S. Mostafa, M. El-Sadek, and E. A. Alla, "Spectrophotometric determination of ciprofloxacin, enrofloxacin and pefloxacin through charge transfer complex formation," *J. Pharm. Biomed. Anal.*, vol. 27, no. 1–2, pp. 133–142, 2002.

[8] H. Y. Ji, D. W. Jeong, Y. H. Kim, H.-H. Kim, D.-R. Sohn, and H. S. Lee, "Hydrophilic interaction liquid chromatography–tandem mass spectrometry for the determination of levofloxacin in human plasma," *J. Pharm. Biomed. Anal.*, vol. 41, no. 2, pp. 622–627, 2006.

[9] G. Carlucci, "Analysis of fluoroquinolones in biological fluids by high-performance liquid chromatography," *J. Chromatogr. A*, vol. 812, no. 1–2, pp. 343–367, 1998.

[10] G. G. Snitkoff, D. W. Grabe, R. Holt, and G. R. Bailie, "Development of an Immunoassay for Monitoring the Levels of Ciprofloxacin Patient Samples," *J. Immunoass. Immunochem.*, vol. 19, no. 4, pp. 227–238, 1998.

[11] S. Huang *et al.*, "Dual functional nanocomposites of magnetic MnFe2O4 and fluorescent carbon dots for efficient U (VI) removal," *Chem. Eng. J.*, vol. 368, pp. 941–950, 2019.

[12] N. Chaudhary, P. K. Gupta, S. Eremin, and P. R. Solanki, "One-step green approach to synthesize highly fluorescent carbon quantum dots from banana juice for selective detection of copper ions," *J. Environ. Chem. Eng.*, vol. 8, no. 3, p. 103720, 2020.

[13] S. Sri, R. Kumar, A. K. Panda, and P. R. Solanki, "Highly biocompatible, fluorescence, and zwitterionic carbon dots as a novel approach for bioimaging applications in cancerous cells," *ACS Appl. Mater. Interfaces*, vol. 10, no. 44, pp. 37835–37845, 2018.

[14] J. Yue *et al.*, "Mechanism insights into tunable photoluminescence of carbon dots by hydroxyl radicals," *J. Mater. Sci.*, vol. 54, no. 8, pp. 6140–6150, 2019.

[15] A. Salinas-Castillo *et al.*, "Carbon dots for copper detection with down and upconversion fluorescent properties as excitation sources," *Chem. Commun.*, vol. 49, no. 11, pp. 1103–1105, 2013.

[16] G. Sharma and A. R. Nautiyal, "Cinnamomum tamala: a valuable tree from Himalayas," *Int. J. Med. Aromat. Plants*, vol. 1, no. 1, pp. 1–4, 2011.

[17] V. N. Mehta, S. Jha, and S. K. Kailasa, "One-pot green synthesis of carbon dots by using Saccharum officinarum juice for fluorescent imaging of bacteria (Escherichia coli) and yeast (Saccharomyces cerevisiae) cells," *Mater. Sci. Eng. C*, vol. 38, pp. 20–27, 2014, doi: https://doi.org/10.1016/j.msec.2014.01.038.

[18] J. Xu, T. Lai, Z. Feng, X. Weng, and C. Huang, "Formation of fluorescent carbon nanodots from kitchen wastes and their application for detection of Fe^{3+}," *Luminescence*, vol. 30, no. 4, pp. 420–424, 2015.

[19] J. Hua, Y. Jiao, M. Wang, and Y. Yang, "Determination of norfloxacin or ciprofloxacin by carbon dots fluorescence enhancement using magnetic nanoparticles as adsorbent," *Microchim. Acta*, vol. 185, pp. 1–9, 2018.

Part B: Determination of ciprofloxacin using the Ziziphus mauritania-derived fluorescent carbon dots-based optical sensor

4.B1 Introduction

Over the recent decades, abuse and overuse of antibiotics have become a global problem due to bacterial resistance to antibiotics (ABR), which poses a risk to human health [1][2]. In terms of consumption of antibiotics worldwide, India ranks top, second by China and then by the USA [3]. As a result of an overall rise in patients and the accompanying costs of care, antibiotic resistance in bacteria, which is caused by drug overuse, has become a significant issue in many settings, including hospitals, health centers, and society [4][5]. According to a report published by the Centers for Disease Control and Prevention (CDC), an estimated annual mortality rate of approximately 23,000 individuals in the United States can be attributed to illnesses caused by bacteria that have developed resistance to antibiotics [6]. Recent investigations have shown that the drinking water of India contains huge quantities of antibiotics, exceeding the maximum permitted limits (MRLs). Due to multi-drug resistance illnesses this has had a serious impact on vulnerable populations living close to industrial services in India, where approximately 58,000 neonates die each year [7]. The targeted and timely detection of antibiotics has drawn a lot of interest owing to the rising prevalence and incidence of ABR globally.

Quinolones, for example, fluoroquinolones (FQs), come under the class of antibiotics that are extensively used as human and veterinary medicines for fighting against many Gram(+) and Gram (-)bacteria[8].FQs, which are commonly used in aquatic and veterinary medicine, constitute one of the most significant groups of antibiotics that prevent the synthesis of DNA [9][10]. CIP is the most frequently used antibiotic among FQs that is often utilized for treating animal and human diseases[11]. They are highly engaged in agricultural, medical, and other areas owing to their high-cost efficiency and antimicrobial properties [12][13]. But antibiotics are not completely digested by the body; a portion of their active component is discharged into the environment *via* wastewater [14][15]. The leftover CIP might be transferred to the human body through the food chain and accumulate there in the system. To protect

human health, numerous organizations or governments have established maximum residue limits. If a massive proportion of these residues stay in the body, it can cause a variety of negative responses as well as diseases, including pneumonia, respiratory tract infection, and cancer [16][17]. Because of its potentially hazardous consequences, the identification of CIP in biological and clinical samples is of paramount relevance in terms of human health.

Currently, many approaches have been investigated by scientists for antibiotics determination, such as electrochemical techniques[3][18][19][20], colorimetry[8], capillary based electrophoresis [21], HPLC [22], and so on. However, the lengthy detection times, limited sensitivity, and time-consuming and costly nature of these detection approaches restrict their usefulness and make them difficult to use in real-world scenarios. Therefore, the development of a highly sensitive, affordable, and quick method to detect CIP is essential. Over the techniques mentioned above, fluorescence spectrometry has the benefits of an optical sensor of high sensitivity, easy operation, cheap cost, and quantitative measurement. Fluorescence-based optical sensors have been extensively applied to detect many analytes that include biomolecules[23], proteins, and metal ions[24].

Researchers have recently focused more on using naturally occurring resources, including carbon dots (CDs), as a fluorescence sensing material due to their special qualities, for example, biocompatibility, low toxicity-high resistance to photo-bleaching, high quantum yield, chemical stability, impressive optical properties,ultra-small size, and aqueous solubility[25][26][27][28]. They are widely employed in various fields, such as medication administration, metal ion sensing, biological imaging [29], and biosensors [30], as well as in other domains[31]. However, the preparation of CDs typically entails the employment of chemical agents such as powerful oxidizers or acids, which can pose a risk to human health and pollute the environment. The hydrothermal approach was often employed by researchers since it is an environmentally friendly, facile, one-step procedure with a cheap synthesis cost than other methods[32]. The hydrothermal technique of carbonization at low temperatures with self-generated pressure is a green approach since no pollutant is emitted into the environment. To synthesize fluorescent CDs, several natural products, such as tej patta

leaves[33], orange juice[34], amino acids[35], etc., were employed as precursors. Therefore, it becomes critical to look into environmentally friendly, green, and new precursors for the cost-effective preparation of fluorescent CDs. The use of green plants or ecologically friendly resources in the hunt for innovative precursors for CDs is becoming increasingly appealing. However, CD quantum yield obtained from green resources is usually low[36][37]. In the hunt for achieving high quantum yield, the CDs synthesis from natural precursor i.e., pulp extract of *Ziziphus mauritiana* (ZM)as a source of carbon was explored .ZMpopularly recognized as Indian jujube, or Indian plum is a fruit tree species that belongs to *Rhamnaceae family*. In the Mediterranean and subtropical areas such as Australia, Africa, and Asia, it is a widely distributed as semi-arid tree[38]. The most advantageous economic items are expensive medical leaves and edible fruits that are high in antioxidants [39]. Additionally, there has been limited research done on the CD's sustainability as fluorescent probes for CIP sensing. To combat the toxic effects of chemically synthesised CDs using conventional technologies, which result in serious environmental and health problems during biomedical application, it is imperative to investigate a competent strategy towards the selective and sensitive identification of CIP by employing a chemical-free CDs synthesis as a fluorescent probe [40]. Therefore, in order to establish and develop a dependable methodology for the precise and specific quantification of CIP antibiotics in milk samples, ZM derived carbon dots (CDs) have been employed as a fluorescent probe.

In the present work, fluorescent CDs derived from ZM'spulp extract have been synthesized *via* green synthesis methodology using a one-step hydrothermal treatment which doesn't demand an inorganic salt, oxidizing agent, or surface passivation and thus were used for the optical detection of CIP. The complete characterization of CDs was done and the size and structure of the manufactured CDs was found to be intriguing, exhibiting excitation-dependent fluorescence. Additionally, when exposed to UV light in an aqueous phase, the synthesized CDs showed stable photoluminescence and strong blue fluorescence with a 30% quantum yield, stability with a high increased PL emission, and good water solubility. The fabricated CIP optical sensor was developed using the PL technique. The investigation focused on examining the

impact of different concentrations of CIP on the intensity of CDs PL, as well as the selectivity of CIP in relation to various interfering substances. These CDs exhibit linearity from 10-100 µM for CIP determination. Moreover, it gave blue emissions along with high water solubility. To the best of our current understanding, our research represents the initial documentation of the photoluminescence capabilities and application of a CIP sensor using novel, chemical-free carbon dots derived from ZM biomass.

4.B2 Experimental Methods

4.B2.1 Synthesis of Carbon Dots

The preparation of fluorescent CDs was done using a facile green route through one-step hydrothermal treatment. In a typical experiment, the raw pulp was collected and subjected to ethanol washes thrice, and then 40 g of ZM pulp was weighed and cut into small pieces. The small pieces were then ground and converted into a paste that was diluted by dissolving it in 50 mL of distilled water to make the ZM pulp extract. Subsequently, a volume of 20 mL of the ZM pulp extract was carefully transferred into a stainless steel autoclave reactor equipped with Teflon lining. The reactor was then placed inside a muffle furnace, where a hydrothermal reaction was allowed to occur for a duration of 5 hours at a temperature of 190 °C. Following the reaction, the reactor was left to cool naturally until it reached room temperature. The dark brown solution was obtained, and add 10 mL of distilled water in that solution. This solution was centrifuged for 20 min at 8000 rpm thrice to obtain the dark-colored supernatant liquid[41]. This dark color supernatant contains our water-soluble carbon dots.

Moreover, for removing other impurities, the supernatant was dialyzed *via* the dialysis membrane in 1 L of distilled water for 12 h with 3.5 KDaporosity, in which distilled water was replaced every 30 min. At last, the yellowish-brown liquid was collected carrying the fluorescent CDs using a micropipette and placed in the refrigeratorat4°C for future experiments. Upon exposure to ultraviolet (UV) light, the prepared solution containing CDs exhibited a pronounced and vibrant blue fluorescence. Scheme 4.3 illustrates the preparation of CDs from ZMatalow temperature (190°C), a one-step hydrothermal reaction followed by the detection of CIP, which depicts fluorescence

enhancement. The following describes the reaction mechanism for the CDs synthesis from ZM: The pulp of ZM extract is first hydrolyzed to form glucose which is then dehydrated to produce ethylene, i.e., C=C (the basic unit of graphene structure). The hydrogen atom (H) of the glucose first combines with the adjacent hydroxyl group (-OH) , and dehydration occurs under a hydrothermal environment. Finally, the C atoms form covalent bonds with one another to form CDs[42][43][44][45].

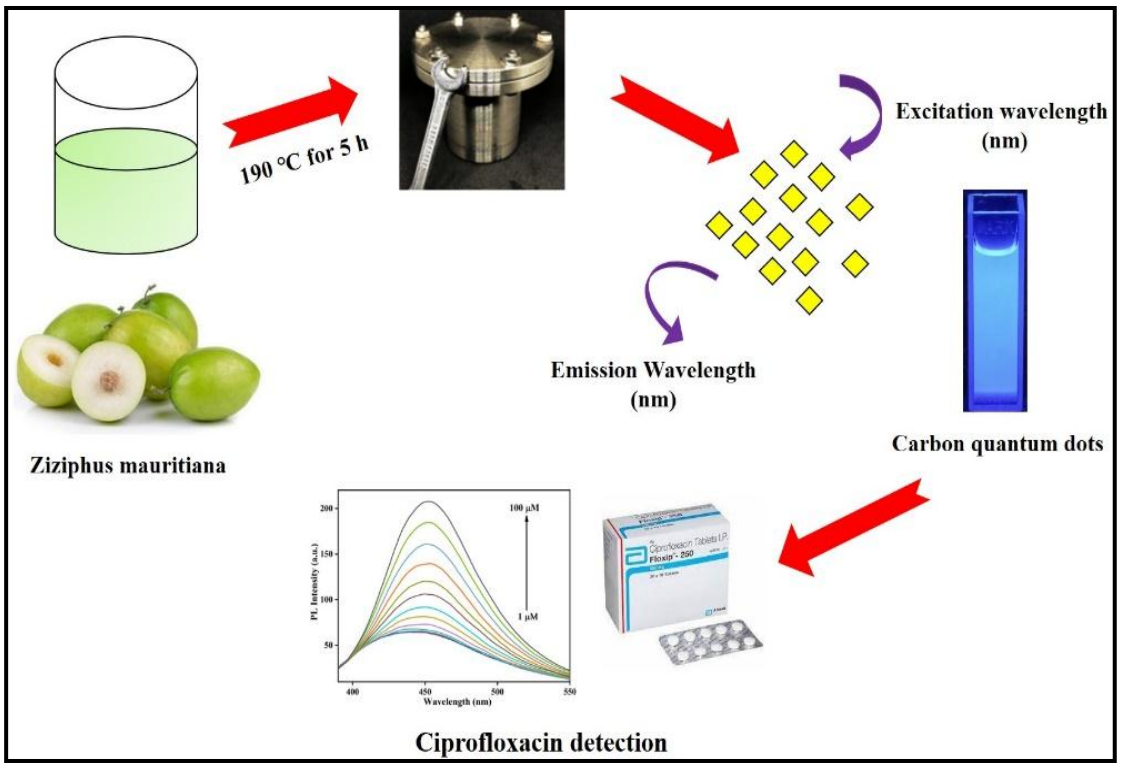

Scheme 4.3: Depicts the preparation of CDs from fruit extract of ZM and its application in CIP detection

4.B2.2 Determination of Fluorescence Quantum Yield

The fluorescence quantum yield [denoted by (Q)] of CDs was estimated at an optimized excitation wavelength of 340 nm employing quinine sulfate(Q= 0.54) in DI as a benchmark. To determine the Q of CDs, the following Eq.1 was utilized[46]:

$$\text{Quantum Yield of CDs} = QR.\frac{ICD}{IR}.\frac{AR}{ACD}.\frac{\eta 2CD}{\eta 2R} \qquad \text{Eq. (1)}$$

In the eq.1 ‘Q’ represents the quantum yield, ‘I’ is used to denotine the intensity of fluorescence spectra, ‘R’ is the reference (Quanine sulfate, 54%) used in the estimation

of QY of CDs, 'A' is the absorbance at a fixed wavelength, and 'η' is the refractive index of the solvent used(DI).

4.B2.3 Preparation of aqueous CIP Dilutions

Different CIP standard dilution concentrations in the range of 1-100μM were made by dissolving CIP in distilled water in a centrifuge tube. During the optical determination, a mixture of 50 μL of each CIP concentration was made with 200μL of stock solution of CDs having 1.5 $mgmL^{-1}$ concentration and shaken well. The fluorescence emission experiment was done with the help of a fluorescence spectrophotometer at a 340 nm excitation wavelength in the 350-600 nm range with both emission and excitation slits of 5 nm size after the reaction has taken place at RT, kept in clear quartz cuvette for 2 min. The measurement of fluorescence intensity (I_0) in the absence of CIP as well as fluorescence intensity (I) of the system after adding CIP, was taken, and the error bars were designed.

4.B2.4 Preparation of CIPin Real Milk Samples

The applicability of this fluorescence sensor was examined in entire milk samples in order to test the feasibility of utilizing CDs to identify CIP in real samples. To investigate the real spiked samples, milk was obtained as a food product and was purchased from a neighboring local store of the JNU campus in New Delhi, India. The pre-treatment of the milk (100 mL) included the addition of 5 mM ethanol (6mL) as well as 20 mM trichloroacetic acid (1mL), which were combined first. The milk was then centrifuged at 10,000 rpm for 15 min at room temperature to get the test sample. Following the pre-treatment of the appeal, the actual sample solution was placed in a 4 ºC environment to be employed. The milk samples were then examined for CIP detection. However, the lack of a change in PL intensity indicates that no CIP was found, which caused the sample to spike. These real samples, particularly milk, were spiked with a range of CIP concentrations (1, 5, 10, 20, 30, 40, 50, 60, 70, 80, 90, and 100 μM), with a 20 μL analyte volume. To conduct the sensing investigation, these real spiked samples were employed in fluorescence emission measurement studies with a fluorescence spectrophotometer.

4.B2.5 Optimization of Experimental Parameters

The experimental settings of the reaction system were optimized to obtain CDs with stronger fluorescence effects. The experimental pH, effect of NaOH, reaction time, and reaction temperature, while maintaining other parameters constant. The pH of the solution was maintained utilizing 0.1 M HCl and NaOH solution employing a rubber-tipped dropper containing 2 mL of CDs solution in a beaker containing. The pH of the solution was estimated utilizing a pH meter for obtaining the various pH of the CD solution. The experimental parameters having the finest fluorescence effect were chosen for preparing CDs for the entire experiments.

4.B3 Results and Discussion

In this work, ZM pulp extracts were used as a source of carbon for preparing multi-functional CDs owing to high bioresource accessibility and rich carbon content. ZM underwent a one-step hydrothermal-assisted synthesis at low temperatures. Due to their simplicity in producing high purity with high yield, hydrothermal-based processes were widely acknowledged as environmentally benign synthesis techniques for making CDs. Because they are inexpensive, simple, and require fewer chemicals than other conventional and unconventional procedures, these techniques have several advantages [47]. In contrast to numerous other techniques, hydrothermal synthesis precipitates the material from the solution directly, retaining the CDs' rate and control over growth, size, morphology, age, and nucleation[15][48][49][50]. The pure CD material was procured after washing, centrifuging, and refining using a membrane dialysis technique. This material showed blue emission when exposed to UV light and was assessed to use as a fluorescent CIP sensor in milk samples. Scheme 4.3 depicts the entire CD synthesis and its CIP sensing application.

4.B3.1 XRD and FTIR Studies

The XRD was performed for the as-synthesized CDs derived from ZM to investigate the phase purity. Figure 4.3(a) shows the XRD graph of the bluish emitting CDs, depicting a broad peak at 25.4^{o}, which specifies the interlayer spacing of the (002) plane characteristic of the graphitic diffraction pattern and amorphous crystalline nature[24]. The interlayer spacing of the prepared CDs (d=0.52 nm) is found to be higher than the interlayer spacing of graphite (d=0.33 nm), suggesting a lower degree of crystallinity in

the CDs. This can be attributed to the presence of a sufficient amount of oxygen-containing groups [51][52][53]. This wide peak also reveals the amorphous nature that developed when oxygen-presenting functional groups were disrupted. The insertion of the defect in the CD's skeleton plane may be the cause of the larger interspacing distance of CDs (0.52 nm) compared to graphite (0.33 nm).

The analysis of the oxygen-holding functional group present in the CD's surface was identified using FTIR [Figure 4.3(b)]. The Fourier Transform Infrared (FTIR) analysis of compact discs (CDs) reveals distinct peaks at 1507 and 3289 cm−1, which are attributed to the stretching of N-H and N-H/O-H groups, respectively. The sharp peak occurred at 2932 $cm^{-1}$is due to the methylene (C-H) or methyl groups that exist owing to the aliphatic hydrocarbons found in the pulp extract of ZM [54][55]. This depicts the existence of amine functional groups present on the surface of CDs[56]. Also, other peaks such as 1020, 1697, 1736, and 2932cm^{-1} are accredited to C-O, C-C, C-O, and C-H stretching vibrations, respectively[57]. The strong peaks at 1388 and 1595cm^{-1} signify the symmetric and asymmetric stretching vibrations, respectively, corresponding to the carboxylate anions. The ample occurrence of epoxide/ether (C-O-C) and hydroxyl (-OH) on CDs surface makes it highly hydrophilic for an aqueoussolution.Thesmall peak located at 1697 cm^{-1}, corresponds to the carbonization processthatinducesformationof C=C bond on the surface of CDs.The existence of oxygen comprising functional groups likeC=O, C-N, and C-O-C on the surface of prepared CQDs may be the cause of the bluish colour emission.

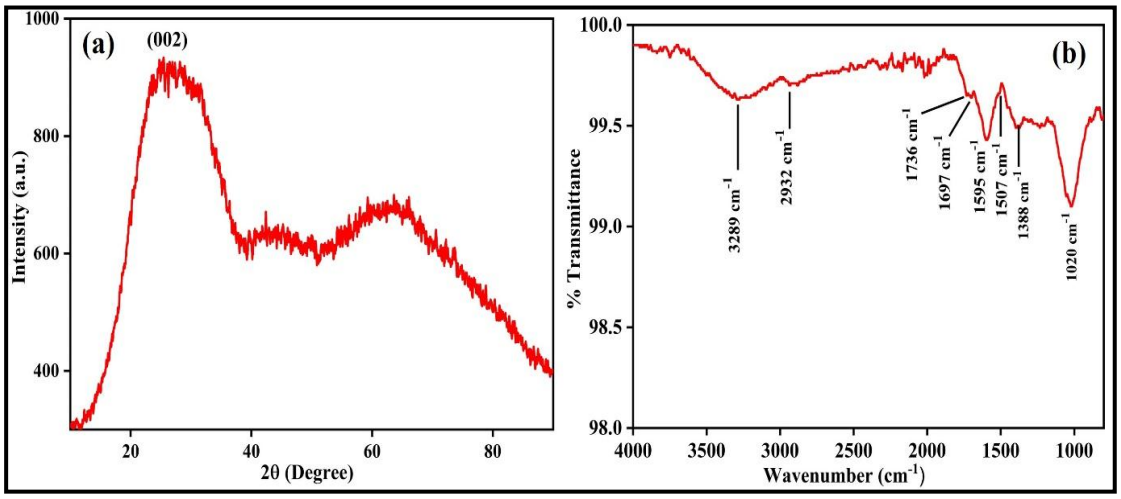

Figure 4.3: (a) XRD of fluorescent CDs, (b) FT-IR of CDs displaying the various functional groups.

4.B3.2 Absorbance, Photoluminescence Properties, and pH Study

To analyze the optical properties of CDs, photoluminescence (PL) transmittance and UV-vis absorption activities were performed utilizing fluorescence and UV–Vis spectroscopy, whose results are depicted in Figure 4.4 (a-c). The dependence of PL intensity of CDs at 340 nm excitation wavelength is depicted in Figure 4.4(a). The relationship between the photoluminescence (PL) of CDs and the excitation wavelength was found to be dependent. The photoluminescence (PL) emission spectra of CDs were observed at various excitation wavelengths between 320 and 400 nm, as depicted in Figure 4.4 (b) [56]. The results indicated a consistent rise in excitation wavelength from 320 to 400 nm, with an increment of 10 nm for each step. It implies that the excitation wavelength-dependent fluorescence properties of CD fluorescent probes exist. Additionally, this figure shows an intense emission peak at 450 nm with 340 nm excitation wavelength. It is ascribed that at 340 nm wavelength, the highest number of CDs are excited. Moreover, the surface characteristic of CDs could also be accountable for excitation-dependent fluorescence performance.

Figure 4.4(c) illustrates the UV-Visible absorption spectra of CDs, revealing the presence of two discernible peaks located approximately at 250 nm and 284 nm. The presence of a minor peak at 250 nm and a prominent peak at 284 nm can be attributed to the n- π^* transition of the carbonyl group (C=O) and the π–π^* transition of the conjugated carbon-carbon (C=C) bond, respectively[58][59][60]. The CDs' functional groups may produce several emissive entrapments between π and π^* states of C=C on their surface, which caused CDs to emit when illuminated at a certain excitation wavelength [61][62]. So, both the effects of size and surface flaws can limit the CDs' fluorescence mechanism. The inset depicts the CDs in daylight to be transparent and give bright blue emissions under UV light. As could be observed from the inset of Figure 4.4(c), the CDs solution in the aqueous suspension daylight was transparent and bright blue under UV lamp irradiation, suggesting that the CDs solution fluorescence has improved PL.

The pH response was performed to see the change in fluorescence intensity of synthesized CDs, as displayed in Figure 4.4(d). For this experiment, various pH ranges

from 2 to 12 were taken to observe the change in fluorescence intensity. There seems to be an increment in fluorescence intensity when the pH ranges from 2 to 7, followed by a reduction in intensity when the pH ranges from 7 to 8. However, when pH increases from 8 to 10, the rise in fluorescence intensity is observed again, and there seems to be a significant fall in fluorescence intensity when the pH shifts to alkaline in nature, i.e., <10. The fluorescence intensity is comparatively stable at around pH=7, i.e., in a neutral atmosphere. Due to the variation in CDs' fluorescence intensity with pH as well as the deprotonation and protonation of a great number of groups on their surface, including carboxyl and amide groups, the results demonstrate that the fluorescence behavior of CDs is suppressed by very alkaline and acidic conditions[63]. Additionally, the existence of numerous charge ions in an environment that is both extremely alkaline and acidic results in the formation of surface effects, which modify the CD's radiative leap efficiency as well as vary the fluorescence emission intensity of CDs in accordance.

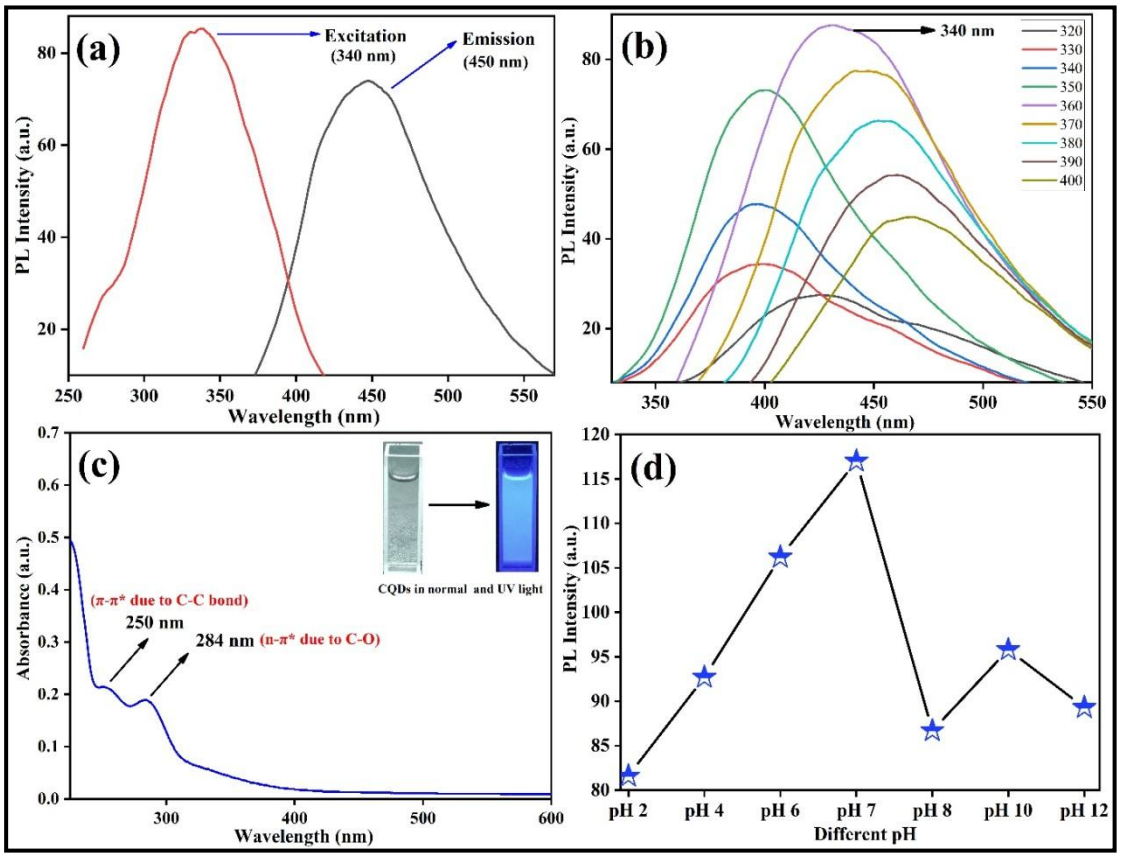

Figure 4.4: (a) PL spectra showing emission and excitation wavelength of CDs,(b) PL spectra of CDs derived from fruit extract of ZM pulp with 320-400 nm excitation wavelengths, (c) UV-Visiblegraphof CDs, inset depicts the fluorescent CDs in daylight as well as UV light; (d) ph response of synthesized CDs with change in fluorescence intensity.

4.B3.3 Energy Dispersive Spectrometer (EDS) Study

Energy Dispersive Spectrometer (EDS) was utilized to determine the amount and type of elements in material micro-region components. The chemical composition of CDs was also analyzed employing EDS. The EDS showed the percentage of nine elements, for example, carbon (40.7wt.%), calcium (0.7wt.%), oxygen (41.8wt.%), nitrogen (1.2wt.%), potassium (6.9wt.%), chlorine (2.8wt.%), sulfur (0.07wt.%), silicon (4.4wt.%), and sodium (1.0wt.%) as depicted in Figure 4.5(a). The nitrogen (N) peak in the EDX depicts the nitrogen-doped CDs in which N atoms are provided by the amino acids present in the pulp extract of ZM. Also, the oxygen (O) element could be ascribed to alkoxy and hydroxy groups present on the CDs' surface. Moreover, Figure 4.5(b)depicts the EDS elemental mapping of CDs derived from ZM. The presence of C, O, Ca, K, S, Si, Cl, Na, and N elements in the CDs fluorescent probes can be observed in EDS elemental mapping images, proving that the doping of N elements was successfully done.

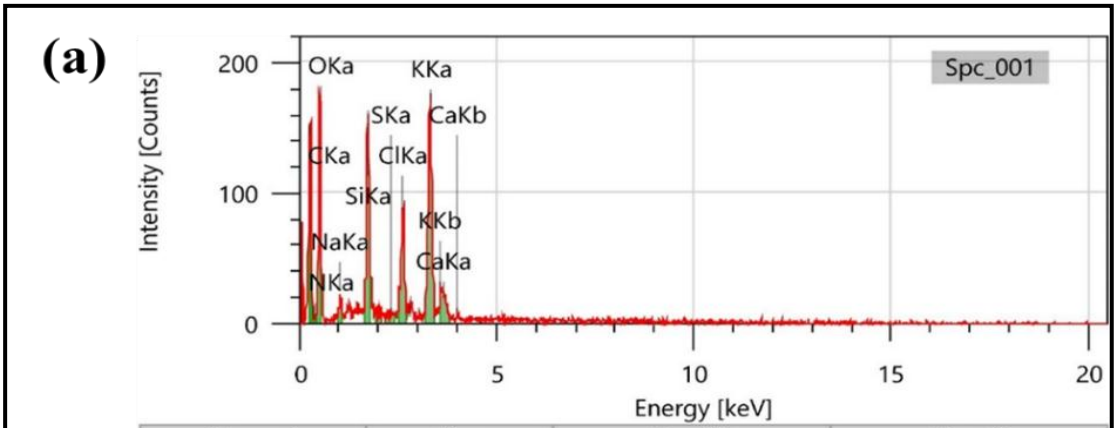

Element	Line	Mass%	Atom%
C	K	40.70±0.68	51.50±0.87
N	K	1.27±0.57	1.37±0.62
O	K	41.87±1.20	39.77±1.14
Na	K	1.03±0.14	0.68±0.09
Si	K	4.45±0.18	2.41±0.10
P	K	nd	nd
S	K	0.07±0.03	0.03±0.02
Cl	K	2.89±0.13	1.24±0.06
K	K	6.99±0.22	2.72±0.09
Ca	K	0.74±0.09	0.28±0.03
Total		100.00	100.00

Figure 4.5: (a) EDX of CDs synthesized from fruit extract of *Ziziphus mauritiana*

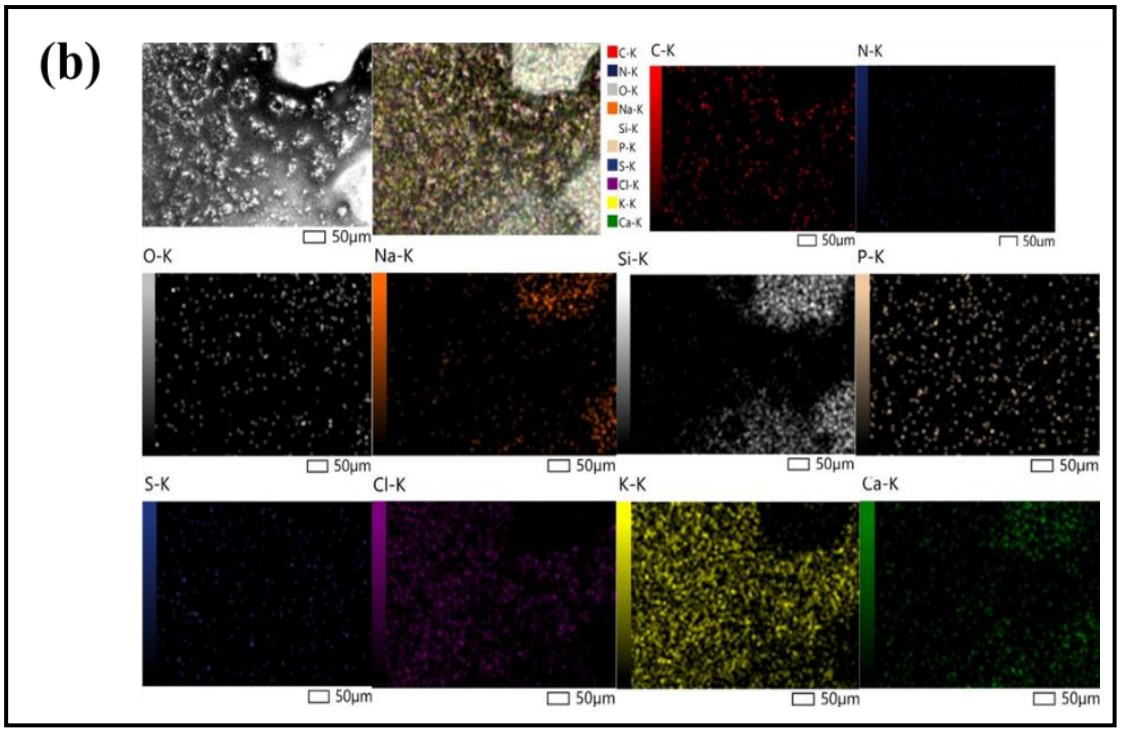

Figure 4.5: (b) EDX mapping of CDs

4.B3.4 Transmission Electron Microscopy (TEM)

TEM was utilized for investigating the size distribution and morphological characteristics of CDs. A distinctive plane angle of a TEM image at various scales is depicted in Figure 4.6(a and b). The CDs that were acquired exhibit a uniform and widespread distribution, characterized by spherical morphology and particle sizes ranging from 0.5 nm to 4.5 nm. The mean size determined for CDs synthesized from ZM was 2.54 nm, as illustrated in the size distribution histogram plot shown in Figure 4.6(c). This finding provides confirmation that compact discs (CDs) exhibit suboptimal crystallization, thereby corroborating the X-ray diffraction (XRD) outcomes.

4.B3.5 Estimation of Quantum Yield (QY)

The QY of CDs derived from the pulp extract of ZM was estimated at an excitation wavelength of 340 nm in distilled water employing quinine sulfate as a reference. It was found that CDs yielded 30% of the quantum yield from the hydrothermal reaction, which is much higher than expected from the other natural precursors of CDs. The possible reason for the high yield could be ascribed to the high pressure as well as

temperature conditions formed during the hydrothermal process providing well-organized carbonization and doping of N, S in pulp extract of CDs, resulting in high QY. Figure 4.6(d) illustrates the quantum yield of earlier reported CDs with the present work CDs[24]made using ZM pulp extract, demonstrating the highest quantum yield of 30%. Moreover, the production yield of CDs was estimated to be 11.1% as 4.47 g of the product was gained from 40 g of ZM pulp. Therefore, the aforementioned approach can be envisaged for the synthesis of CDs on a large scale.

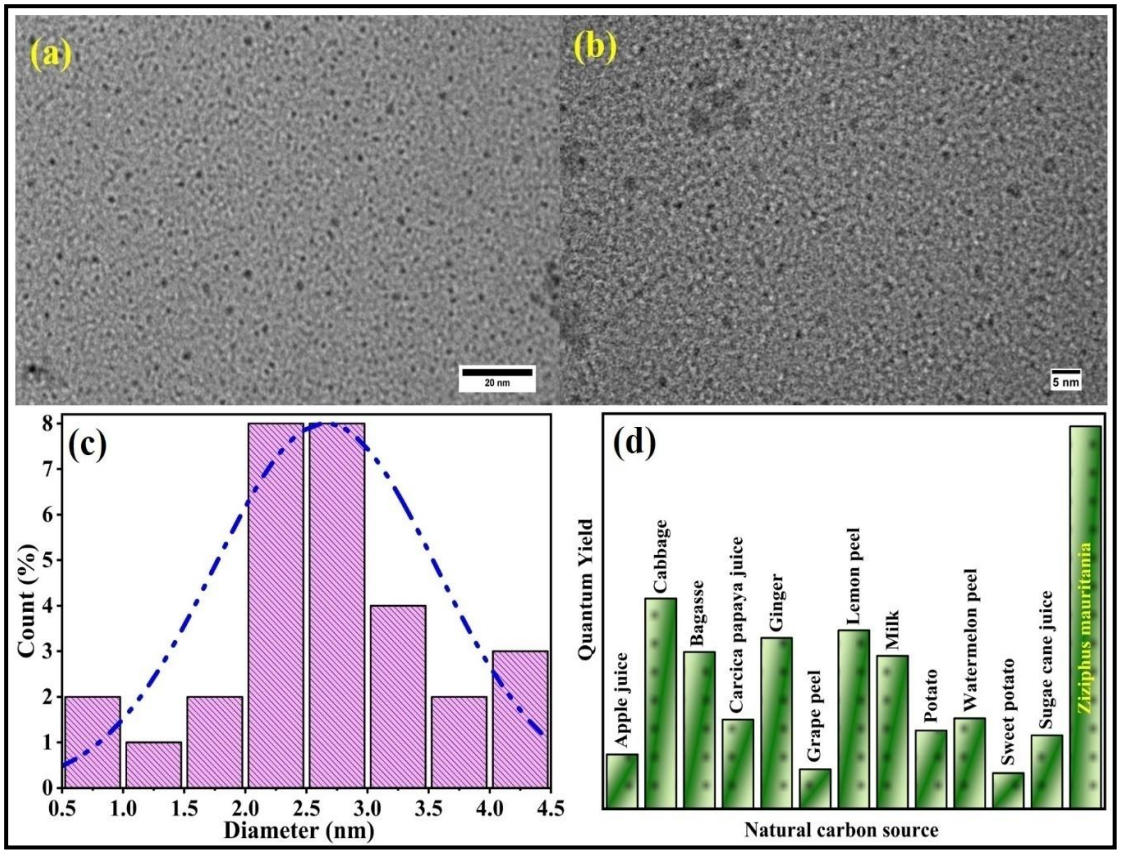

Figure 4.6: (a) and (b) Illustrate TEM images of CDs derived from fruit extract of ZM at lower and higher resolution, respectively, (c) Depicts the size distribution histogram of CDs, (d) Bar diagram showing the highest quantum yield ofCDsderived from ZM pulp extract with others green derived CDs reported in the literature.

4.B3.6 Analysis of Zeta Potential

The homogenously distributed CDs' aqueous solution was taken for zeta potential analysis [Figure 4.7]. The CDs that are majorly rich in amine functional groups (N-H) have a positive zeta potential value (27.67 mV). According to these results, it could be ascribed that positively charged CDs comprising the various functional groups offer an

excellent platform for detecting CIP. As a result, CD interaction with CIP has enhanced the fluorescence intensity of CDs in milk samples.

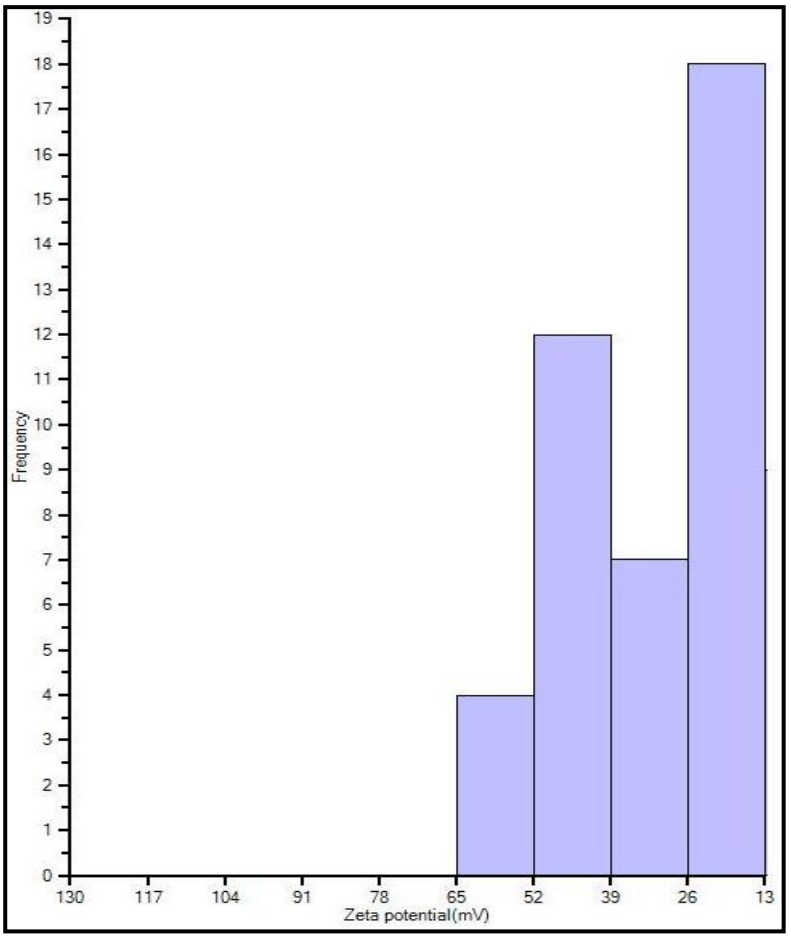

Figure 4.7: Zeta potential of green synthesized CDs derived from ZM fruit extract

4.B4 Optical Detection of CIP using CDs

4.B4.1 Response Study

The CDs obtained from the pulp extract of ZM were employed as a fluorescent probe for fluorescent sensing application. Figure 4.8(a) illustrates the impact of varying concentrations of CIP on the photoluminescence (PL) intensity of CDs. For this experiment, CIP concentrations ranging from 10 to 100 µM were added to the solution, which led to fluorescence intensity enhancement, as seen from the PL spectra at 340 nm excitation wavelength. Figure 4.8(b) represents a relation between the PL intensity of CDs with concentrations of CIP. Good linearity can be seen between CIP concentrations and the PL intensity of CDs ranging from 10–100 µMwitharegression coefficient (R^2) of

0.951 and LOD of 0.56μM. The limit of detection (LOD) was determined using the standard formula of $3\sigma/S$(where σ shows the linear curve slope and S is the standard error of intercept). This confirms that CIP could be determined from the CD's fluorescence enhancement. The sensing parameters of earlier reported analytical techniques for CIP detection are provided in Table 4.1 for comparison with the present work.

Table 4.1: Table showing the sensing parameters of previous analytical techniques reported for the detection of CIP

Analytical technique	Sensing probe	Detection limit	Linear range	Ref.
Fluorescence	AuNPs	12 μM	50−150 μM	[64]
Electrochemical	$BiPO_4$@GOMMIP	390 nm	39−740 μM	[65]
Fluorescence	CdSe quantum dots	4 μmol/L	0- 120 μmol/L	[66]
MIFOFS sensor	MIP	6.86 μM	10 μM-500 μM	[67]
Electrochemical	CZF-CME	2.58 μM	0.909 – 4700 μM	[68]
Electrochemical	NiONPs-GO-CTS: EPH/GCE	6.0 μM	0.040 – 0.97 μM	[69]
Electrochemical	Au/C_3N_4/GN/GCE	4.2×10^{-7} M	0.6–120 μM	[70]
Fluorescence	**CDs**	**0.56μM**	**10-100 μM**	**Present work**

AuNPs: gold nanoparticles, $BiPO_4$:bismuth phosphate, GOMMIP: graphene oxide magnetic nano-sized molecularly imprinted polymer, CdSe: cadmium selenium, CZF-CME: ferrite nanoparticle modified carbon paste electrode, NiONPs: nickel oxide nanoparticles, CTS: EPH/GCE:polysaccharideEpichlorohydrin glassy carbon electrode, Au/C_3N_4/GN: gold nanoparticles/carbon nitride/graphene-modified electrodes.

4.B4.2 Selectivity Analysis

The CDs selectivity was performed utilizing different potential interfering chemicals for CIP determination[Figure 4.8(c)]. For this study, various antibiotics such as gentamycin, ampicillin, amoxicillin, tetracycline, moxifloxacin, levofloxacin, and norfloxacin were added one by one, and their PL intensity was noted. Among all, only CIP exhibited a very intense fluorescence enhancement that displayed that CDs derived from ZMpulp extract have high selectivity towards it, enabling the determination of CIP

against other interfering antibiotics. It indicates clearly that as-produced CDs may be used as fluorescent labels for CIP monitoring in an aqueous solution without encountering any interference from other targets.

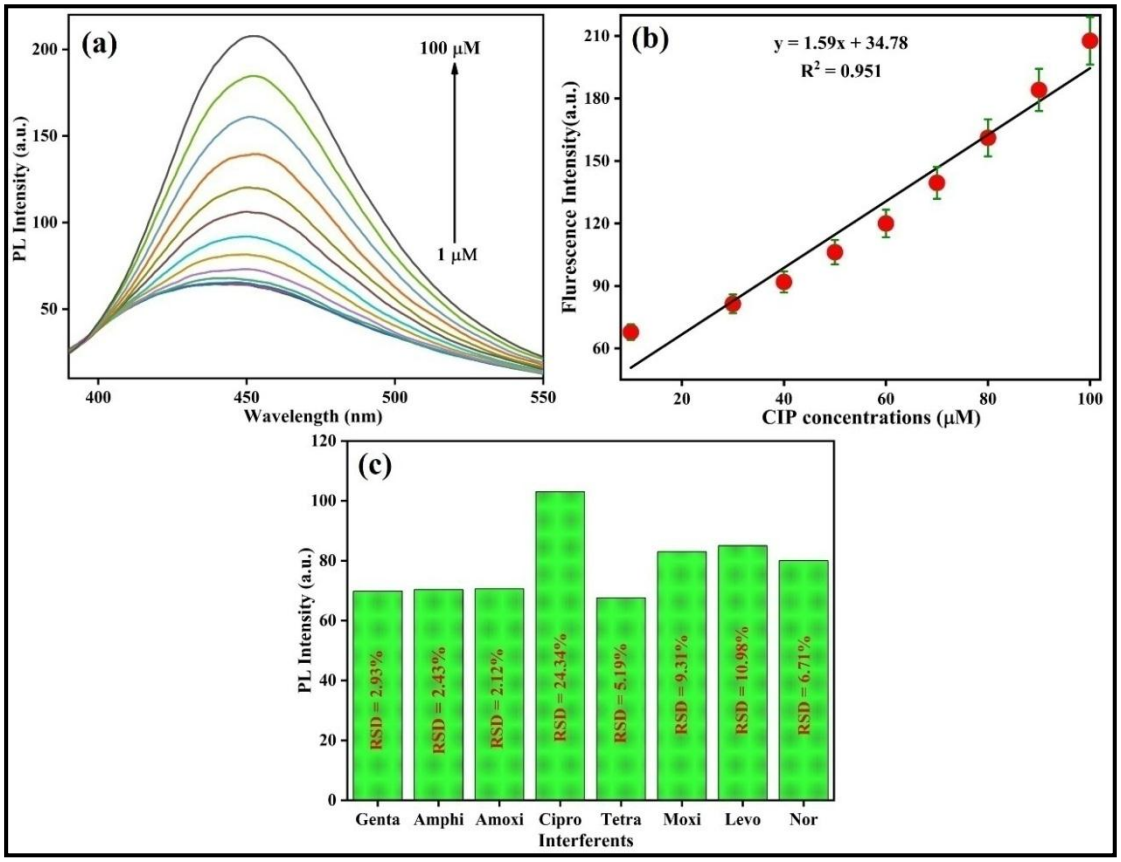

Figure 4.8: (a) The sensing response between the concentrations of CIPand PL intensity of CDs, (b)Calibration curve between concentrations of CIP and CDs PL intensity, and; (c) Selectivity analysis of CDs against other antibiotics

4.B5 Stability Studies and Effect of NaOH on Stability

The change in CD fluorescence was observed for 45 days at 5 days intervals. As shown in Figure 4.9(a), the CDs retain greater than 95% of the fluorescence till the 30th day. Then, a fall in fluorescence was seen, which depicts that the CDs have a good shelf life of 30 days. The obtained CDs were kept at 4 °C until further use. The CD's stability was also investigated at pH 7.0 with various ionic strength concentrations ranging from 0 to 2.0 M NaCl. In Figure 4.9(b), no variation in fluorescence intensity was observed at the inspected ionic strength. These findings show that the obtained CDs are highly tolerant and stable in the increased (ionic) saline solution, enabling a latent probe for sensing and bio-imaging functions at physiological pH in biological systems [71].

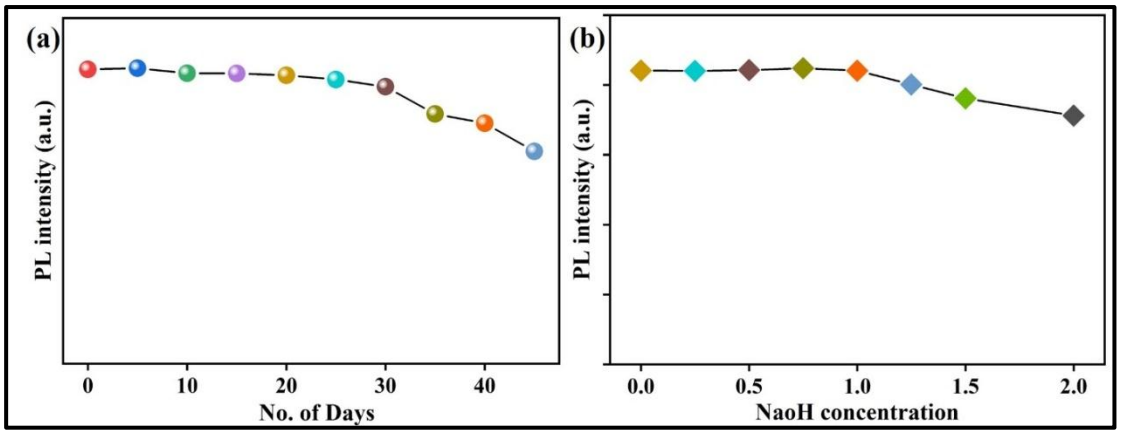

Figure 4.9: (a) Stability of CDs; and (b) Effect of NaOH on the stability of CDs

4.B6 Sensing Mechanism of CDs for Detection of CIP

The CDs derived from the ZMpulp extract could detect CIP for a wide linear detection range. This could be ascribed to the production of a complex formed between the amine group of CDs and the carboxylate group of CIPsas shown in Scheme 4.4. Also, a charge transfer from CDs to CIP can enhance the PL intensity [41]. Moreover, the increased intensity of CDs could also be accredited to the hydrogen bonding interactions, as the CDs comprise hydroxyl and carboxyl groups, as confirmed from FTIR analysis that provides aqueous solubility to bind with CIP *via* hydrogen bonding.

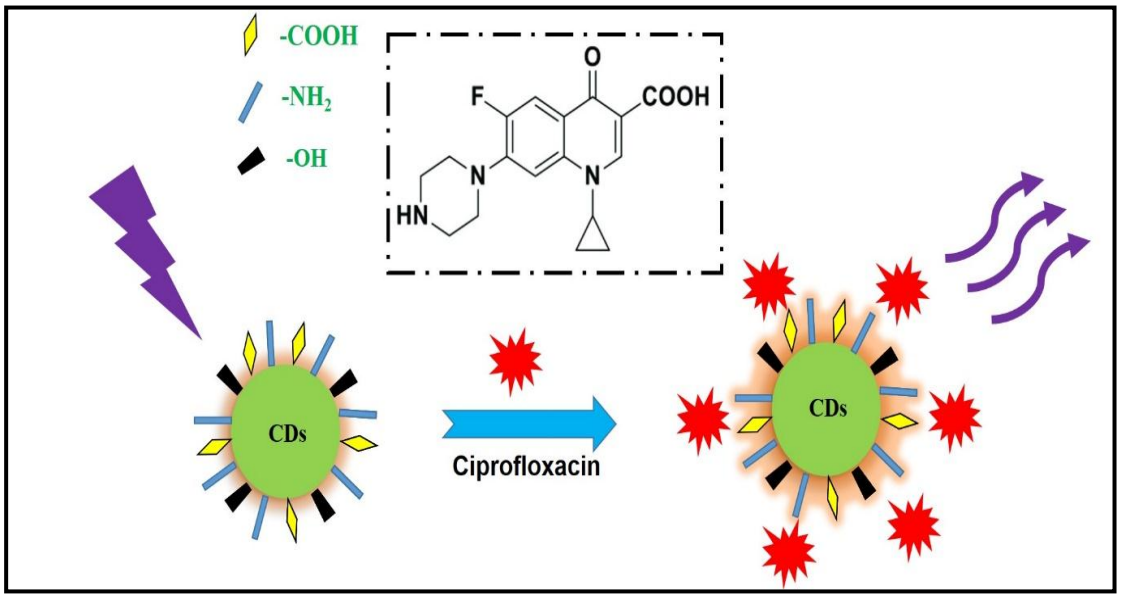

Scheme 4.4: Mechanism of CDs derived from fruit extract of ZM for determination of CIP.

4.B7 Spiked Real Sample Analysis

A milk sample was collected for the purpose of conducting a real sample analysis in order to evaluate the sensor's practical utility. When the milk sample was analyzed using CDs, no detectable presence of CIP was observed. Subsequently, the milk samples were artificially contaminated with varying concentrations of CIP, ranging from 1-100 μM, as per the requirements of optical sensing, showing enhancement in PL intensity as observed from Figure 4.10(a), signifying that the approach is suitable for milk samples. Also, Figure 4.10(b) depicts a bar diagram illustrating the enhanced PL intensity with an increase in concentrations of CIP, as shown by the standard optical response. A calibration plot has been fitted between fluorescence intensity and CIP concentration, as shown in Figure 4.10(c), which exhibited a strong linear relationship (R^2=0.947) in the range of 10-100μM, with a limit ofLODof0.56 μM. Therefore, this method has excellent application having lower detection limits for various real milk samples.

In addition, recovery tests were conducted on CIP in actual samples utilizing the standard addition method to assess the robustness of the CDs fluorescence probes for detecting CIP in milk samples. For the trials, different CIP concentrations (1-100 μM) were administered to treat milk samples. After that, these samples' fluorescence emission intensities were rigorously evaluated. The recoveries and % RSD ranged from 92.7% to 101.50% and 0.48-5.68%, respectively, according to the findings in Table 4.2. The results for this real sample test revealed good recoveries and %RSD, indicating a viable use for CD fluorescent probes in milk sample detection. The methodology employed in this study exhibits a broad linear range and a low detection limit in comparison to various conventional techniques documented in Table 4.2. The suggested approach is practical and feasible and may be used to identify CIP with high sensitivity, accuracy, and rapidness in milk samples.

The excitation, as well as emission crosslinking plots, indicated the maximum intensity for excitation and emission between 460 and 430 nm as well as 400 and 380 nm, respectively, according to the 3D contour spectra [Figure 4.10(d)]. Because CDs have a range of particle sizes and have organic emissive areas on their surfaces, they have changeable emission properties. Additionally, the fluorescence lifetime study gave information on the CDs' emission behavior.

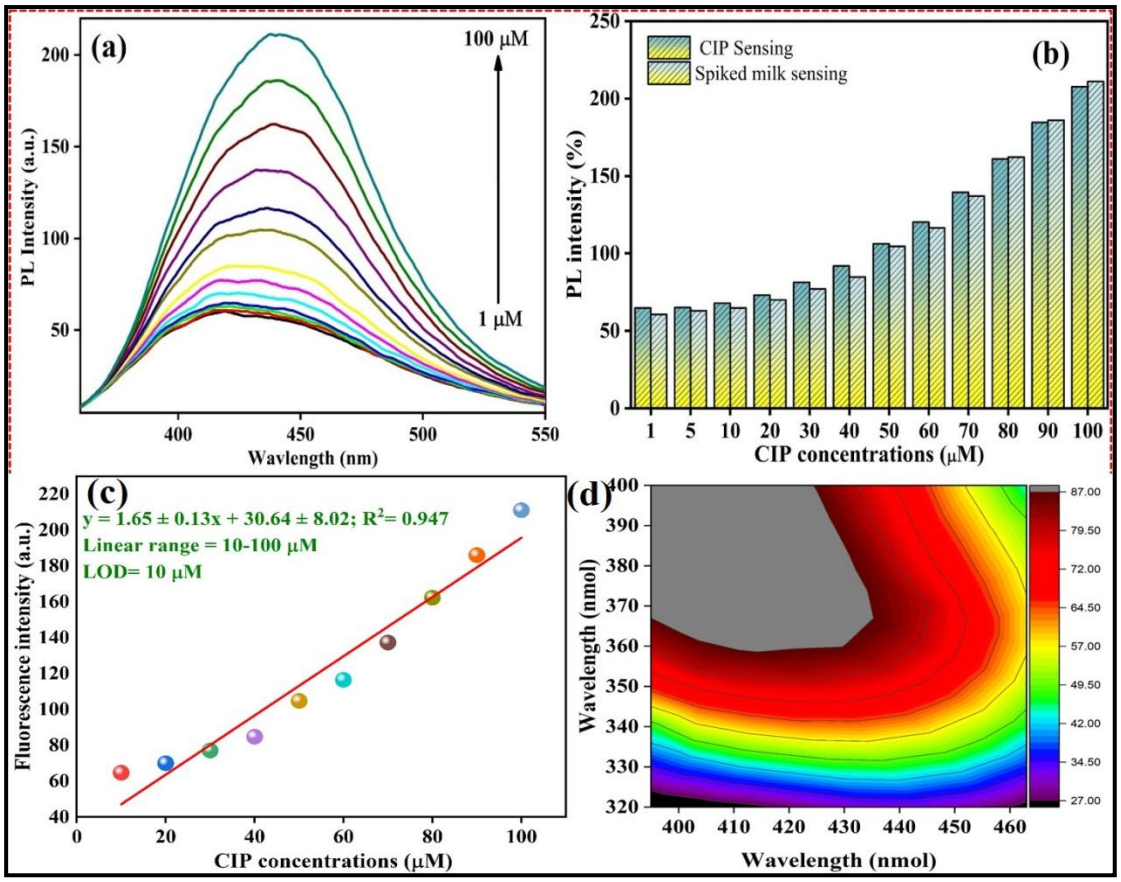

Figure 4.10: (a) Variations in PL intensity with different concentrations of CIP; (b)Bar diagram showing the feasibility of CDsto detect CIP in the milk sample; (c) Calibration plot in real milk samples; and (d) 3D Contour spectrum of CDs showing the relation of fluorescence excitation with emission spectra

Table 4.2: Spiked real sample analysis using green synthesized CDs derived from ZMpulp extract for detection of CIP in the milk sample.

Real sample	Spiked conc. (µM)	PL Intensity during sensing	PL Intensity during spiking of milk with CIP	RSD (%)	Recovery (%)
Milk	1um	64.8	60.6	4.74	93.5
	5	65	63	2.21	96
	10	67.8	64.8	3.20	95.5
	20	73	70	2.97	95.8
	30	81.4	77	3.93	94.5
	40	91.1	84.8	5.68	92.7
	50	106.2	104.6	1.07	98.4
	60	120.2	116.5	2.15	96
	70	139.5	137.1	1.23	98.2
	80	161.1	162.2	0.48	100
	90	184.6	186	0.53	100
	100	207.7	211	1.11	101.5

4.B8 Optimization Conditions for CDs Synthesis

For obtaining the CDs-based fluorescent sensor with high sensitivity and good fluorescence intensity, the different parameters like reaction time and reaction temperature in the action of CDs synthesis were optimized for getting improved fluorescence effect of CDs.CDs were synthesized by altering the reaction temperature, keeping other experimental parameters unchanged constantly. In the temperature range of 120º to 140 ºC, it was observed that there was no discernible alteration in fluorescence intensity, thereby suggesting the absence of CD synthesis. However, it is evident from Figure 4.11 that the fluorescence intensity exhibited an upward trend with increasing reaction temperature, reaching its maximum at 190 ºC, starting from an initial temperature of 140 ºC.

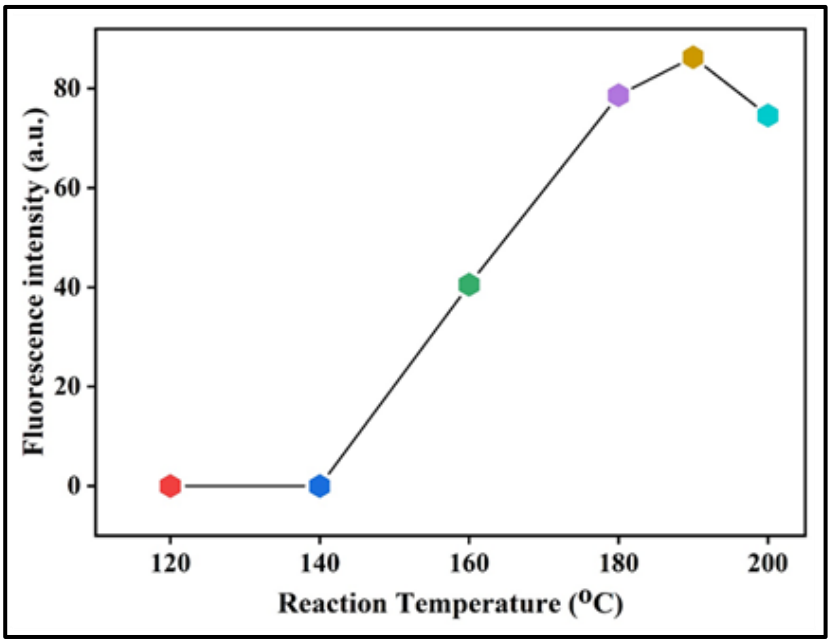

Figure 4.11: Effect of reaction temperature on synthesis of CDs

Upon reaching a temperature of 180 ºC, a decline in fluorescence intensity was observed. Furthermore, variations in reaction temperature resulted in a discernible pattern of initial increase followed by subsequent decrease in the overall fluorescence intensity. The probable mechanism could be owing to the starch dehydration reaction to generate glucose as well as oligosaccharides dehydration at elevated temperatures to form an intermolecular crosslinking. Also, formyl groups in reaction with hydrocarbon undergo hydrothermal conditions and dehydrate to generate CDs after

cyclic condensation reaction[71]. The several CDs were synthesized by varying the reaction time while keeping the other experimental variables constant. As shown in Figure 4.12, the CDs' fluorescence intensity rose as the reaction time increased, with a reaction period of 5 h producing the best fluorescence effect. However, the fluorescence intensity started to decline for reaction times greater than 5 h.

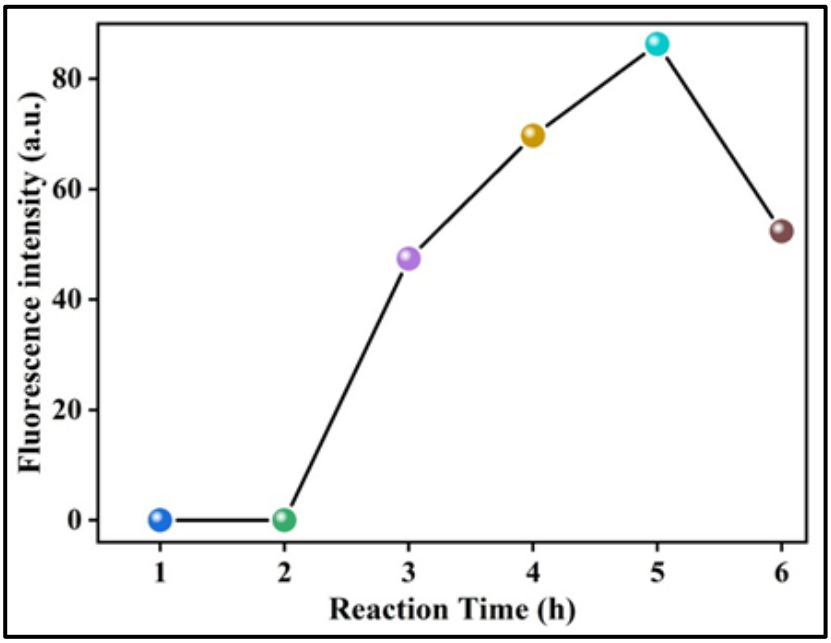

Figure 4.12: Effect of reaction time on the synthesis of CDs

4.B9 References

[1] Pollap A and Kochana J 2019 Electrochemical immunosensors for antibiotic detection *Biosensors***9** 61

[2] Yadav A K, Verma D, Lakshmi G, Eremin S and Solanki P R 2021 Fabrication of label-free and ultrasensitive electrochemical immunosensor based on molybdenum disulfide nanoparticles modified disposable ITO: An analytical platform for antibiotic detection in food samples *Food Chem.***363** 130245

[3] Yadav A K, Dhiman T K, Lakshmi G, Berlina A N and Solanki P R 2020 A highly sensitive label-free amperometric biosensor for norfloxacin detection based on chitosan-yttria nanocomposite *Int. J. Biol. Macromol.***151** 566–75

[4] Wehrli P M, Lindberg E, Angerer T B, Wold A E, Gottfries J and Fletcher J S 2014 Maximising the potential for bacterial phenotyping using time-of-flight secondary ion mass spectrometry with multivariate analysis and Tandem Mass Spectrometry *Surf. interface Anal.***46** 173–6

[5] Newsroom C D C 2014 Untreatable: Report by CDC details today's drug-resistant health threats

[6] Syska J 2013 Frieden wave-function representations via an Einstein-Podolsky-Rosen-Bohm experiment *Phys. Rev. E***88** 32130

[7] Hall W, McDonnell A and O'Neill J 2018 *Superbugs: An arms race against bacteria* (Harvard University Press)

[8] Lavaee P, Danesh N M, Ramezani M, Abnous K and Taghdisi S M 2017 Colorimetric aptamer based assay for the determination of fluoroquinolones by triggering the reduction-catalyzing activity of gold nanoparticles *Microchim. Acta***184** 2039–45

[9] Zhu Y, Li L, Wang Z, Chen Y, Zhao Z, Zhu L, Wu X, Wan Y, He F and Shen J 2008 Development of an immunochromatography strip for the rapid detection of 12 fluoroquinolones in chicken muscle and liver *J. Agric. Food Chem.***56** 5469–74

[10] Higgins P G, Fluit A C and Schmitz F J 2003 Fluoroquinolones: structure and target sites *Curr. Drug Targets***4** 181–90

[11] Picó Y and Andreu V 2007 Fluoroquinolones in soil—risks and challenges *Anal. Bioanal. Chem.***387** 1287–99

[12] Aldred K J, McPherson S A, Turnbough Jr C L, Kerns R J and Osheroff N 2013 Topoisomerase IV-quinolone interactions are mediated through a water-metal ion bridge: mechanistic basis of quinolone resistance *Nucleic Acids Res.***41** 4628–39

[13] Ionescu R E, Jaffrezic-Renault N, Bouffier L, Gondran C, Cosnier S, Pinacho D G, Marco M-P, Sánchez-Baeza F J, Healy T and Martelet C 2007 Impedimetric immunosensor for the specific label free detection of ciprofloxacin antibiotic *Biosens. Bioelectron.***23** 549–55

[14] Borba F H, Schmitz A, Pellenz L, Bueno F, Kasper N, Wenzel B M, Baroni S, Dall'Oglio I C and Modenes A N 2018 Genotoxicity and by-products assessment in degradation and mineralization of Ciprofloxacin by UV/H2O2 process *J. Environ. Chem. Eng.***6** 6979–88

[15] Chaudhary N, Yadav A K, Sharma J G and Solanki P R 2021 Designing and characterization of a highly sensitive and selective biosensing platform for ciprofloxacin detection utilizing lanthanum oxide nanoparticles *J. Environ. Chem. Eng.***9** 106771

[16] Yu W, Zhan S, Shen Z, Zhou Q and Yang D 2017 Efficient removal mechanism for antibiotic resistance genes from aquatic environments by graphene oxide nanosheet *Chem. Eng. J.***313** 836–46

[17] Zhang R, Wang Y and Yu L-P 2014 Specific and ultrasensitive ciprofloxacin detection by responsive photonic crystal sensor *J. Hazard. Mater.***280** 46–54

[18] Yadav A K, Verma D and Solanki P R 2021 Electrophoretically deposited L-cysteine functionalized MoS2@MWCNT nanocomposite platform: a smart approach toward highly sensitive and label-free detection of gentamicin *Mater. Today Chem.***22** 100567

[19] Yadav A K, Verma D, Lakshmi G B V S, Eremin S and Solanki P R 2021 Fabrication of label-free and ultrasensitive electrochemical immunosensor based on molybdenum disulfide nanoparticles modified disposable ITO: An analytical platform for antibiotic detection in food samples *Food Chem.***363**

[20] Hu X, Goud K Y, Kumar V S, Catanante G, Li Z, Zhu Z and Marty J L 2018 Disposable electrochemical aptasensor based on carbon nanotubes-V2O5-chitosan nanocomposite for detection of ciprofloxacin *Sensors Actuators B Chem.***268** 278–86

[21] Montes R H O, Marra M C, Rodrigues M M, Richter E M and Muñoz R A A 2014 Fast determination of ciprofloxacin by batch injection analysis with amperometric detection and capillary electrophoresis with capacitively coupled contactless conductivity detection *Electroanalysis***26** 432–8

[22] Jin T, Wu H, Gao N, Chen X, Lai H, Zheng J and Du L 2016 Extraction of quinolones from milk samples using bentonite/magnetite nanoparticles before determination by high-performance liquid chromatography with fluorimetric detection *J. Sep. Sci.***39** 545–51

[23] Xie H, Lu Y, You R, Qian W and Lin S 2022 Green synthetic nitrogen-doped graphene quantum dot fluorescent probe for the highly sensitive and selective detection of tetracycline in food samples *RSC Adv.***12** 8160–71

[24] Chaudhary N, Gupta P K, Eremin S and Solanki P R 2020 One-step green approach to synthesize highly fluorescent carbon quantum dots from banana juice for selective detection of copper ions *J. Environ. Chem. Eng.***8** 103720

[25] Li Z, Wang Q, Zhou Z, Zhao S, Zhong S, Xu L, Gao Y and Cui X 2021 Green synthesis of carbon quantum dots from corn stalk shell by hydrothermal approach in near-critical water and applications in detecting and bioimaging *Microchem. J.***166** 106250

[26] Nazri N A A, Azeman N H, Luo Y and Bakar A A A 2021 Carbon quantum dots for optical sensor applications: A review *Opt. Laser Technol.***139** 106928

[27] Rajendran K, Rajendran G, Kasthuri J, Kathiravan K and Rajendiran N 2019 Sweet Corn (Zea mays L. var. rugosa) Derived Fluorescent Carbon Quantum Dots for Selective Detection of Hydrogen Sulfide and Bioimaging Applications *ChemistrySelect***4** 13668–76

[28] Supchocksoonthorn P, Thongsai N, Moonmuang H, Kladsomboon S, Jaiyong P and Paoprasert P 2019 Label-free carbon dots from black sesame seeds for real-time detection of ammonia vapor via optical electronic nose and density functional theory calculation *Colloids Surfaces A Physicochem. Eng. Asp.***575** 118–28

[29] Atchudan R, Edison T N J I, Perumal S, Selvam N C S and Lee Y R 2019 Green synthesized multiple fluorescent nitrogen-doped carbon quantum dots as an efficient label-free optical nanoprobe for in vivo live-cell imaging *J. Photochem. Photobiol. A Chem.***372** 99–107

[30] Anh N T N, Chowdhury A D and Doong R 2017 Highly sensitive and selective detection of mercury ions using N, S-codoped graphene quantum dots and its paper strip based sensing application in wastewater *Sensors Actuators B Chem.***252** 1169–78

[31] Zong J, Yang X, Trinchi A, Hardin S, Cole I, Zhu Y, Li C, Muster T and Wei G 2014 Carbon dots as fluorescent probes for "off–on" detection of Cu2+ and l-cysteine in aqueous solution *Biosens. Bioelectron.***51** 330–5

[32] Hua J, Yang J, Zhu Y, Zhao C and Yang Y 2017 Highly fluorescent carbon quantum dots as nanoprobes for sensitive and selective determination of mercury (II) in surface waters *Spectrochim. Acta Part A Mol. Biomol. Spectrosc.***187** 149–55

[33] Chaudhary N, Verma D, Sharma J G and Solanki P R 2022 A novel bioinspired carbon quantum dots based optical sensor for ciprofloxacin detection *Mater. Lett.***308** 131090

[34] Sahu S, Behera B, Maiti T K and Mohapatra S 2012 Simple one-step synthesis of highly luminescent carbon dots from orange juice: application as excellent bio-imaging agents *Chem. Commun.***48** 8835–7

[35] Pei S, Zhang J, Gao M, Wu D, Yang Y and Liu R 2015 A facile hydrothermal approach towards photoluminescent carbon dots from amino acids *J. Colloid Interface Sci.***439** 129–33

[36] Feng X and Zhang Y 2019 A simple and green synthesis of carbon quantum dots from coke for white light-emitting devices *Rsc Adv.***9** 33789–93

[37] Dager A, Uchida T, Maekawa T and Tachibana M 2019 Synthesis and characterization of mono-disperse carbon quantum dots from fennel seeds: photoluminescence analysis using machine learning *Sci. Rep.***9** 1–12

[38] Boudechiche N, Fares M, Ouyahia S, Yazid H, Trari M and Sadaoui Z 2019 Comparative study on removal of two basic dyes in aqueous medium by adsorption using activated carbon from Ziziphus lotus stones *Microchem. J.***146** 1010–8

[39] Rahman A, Tan A L, Harunsani M H, Ahmad N, Hojamberdiev M and Khan M M 2021 Visible light induced antibacterial and antioxidant studies of ZnO and Cu-doped ZnO fabricated using aqueous leaf extract of Ziziphus mauritiana Lam *J. Environ. Chem. Eng.***9** 105481

[40] Ibrahim A A, Umar A, Amine A, Kumar R, Al-Assiri M S, Al-Salami A E and Baskoutas S 2018 Highly sensitive and selective non-enzymatic monosaccharide and disaccharide sugar sensing based on carbon paste electrodes modified with perforated NiO nanosheets *New J. Chem.***42** 964–73

[41] Kim K and Kim J 2018 Synthesis of carbon quantum dots from jujubes for detection of iron (III) ions *J. Nanosci. Nanotechnol.***18** 1320–2

[42] Bayat A and Saievar-Iranizad E 2017 Synthesis of green-photoluminescent single layer graphene quantum dots: Determination of HOMO and LUMO energy states *J. Lumin.***192** 180–3

[43] Li X, Kurasch S, Kaiser U and Antonietti M 2012 Synthesis of monolayer-patched graphene from glucose *Angew. Chemie Int. Ed.***51** 9689–92

[44] Miyazawa T and Funazukuri T 2003 Production of Mono-and Oligo-Saccharides from Hydrothermal Degradation of Polygalacturonic Acid *Hydrothermal Reactions and Techniques* (World Scientific) pp 75–81

[45] Tang L, Ji R, Cao X, Lin J, Jiang H, Li X, Teng K S, Luk C M, Zeng S and Hao J 2012 Deep ultraviolet photoluminescence of water-soluble self-passivated graphene quantum dots *ACS Nano***6** 5102–10

[46] Song Y, Zhu C, Song J, Li H, Du D and Lin Y 2017 Drug-derived bright and color-tunable N-doped carbon dots for cell imaging and sensitive detection of Fe^{3+} in living cells *ACS Appl. Mater. Interfaces***9** 7399–405

[47] Pourabbas B and Jamshidi B 2008 Preparation of MoS_2 nanoparticles by a modified hydrothermal method and the photo-catalytic activity of MoS2/TiO2 hybrids in photo-oxidation of phenol *Chem. Eng. J.***138** 55–62

[48] Verma D, Yadav A K, Mukherjee M Das and Solanki P R 2021 Fabrication of a sensitive electrochemical sensor platform using reduced graphene oxide-molybdenum trioxide nanocomposite for BPA detection: An endocrine disruptor *J. Environ. Chem. Eng.***9** 105504

[49] Chauhan D, Yadav A K and Solanki P R 2021 Carbon cloth-based immunosensor for detection of 25-hydroxy vitamin D 3 *Microchim. Acta***188** 1–11

[50] Verma D, Chauhan D, Mukherjee M Das, Ranjan K R, Yadav A K and Solanki P R 2021 Development of MWCNT decorated with green synthesized AgNps-based electrochemical sensor for highly sensitive detection of BPA *J. Appl. Electrochem.***51** 447–62

[51] Alam AM, Park BY, Ghouri Z K, Park M and Kim HY 2015 Synthesis of carbon quantum dots from cabbage with down-and up-conversion photoluminescence properties: excellent imaging agent for biomedical applications *Green Chem.***17** 3791–7

[52] Peng J, Gao W, Gupta B K, Liu Z, Romero-Aburto R, Ge L, Song L, Alemany L B, Zhan X and Gao G 2012 Graphene quantum dots derived from carbon fibers *Nano Lett.***12** 844–9

[53] Li J, Yun X, Hu Z, Xi L, Li N, Tang H, Lu P and Zhu Y 2019 Three-dimensional nitrogen and phosphorus co-doped carbon quantum dots/reduced graphene oxide composite aerogels with a hierarchical porous structure as superior electrode materials for supercapacitors *J. Mater. Chem. A***7** 26311–25

[54] Sandford S A, Bernstein M P and Materese C K 2013 The infrared spectra of polycyclic aromatic hydrocarbons with excess peripheral H atoms (Hn-PAHs) and their relation to the 3.4 and 6.9 μm PAH emission features *Astrophys. J. Suppl. Ser.***205** 8

[55] Nagy B, Modzeleski V and Murphy M T J 1965 Hydrocarbons in the banana leaf, Musa sapientum *Phytochemistry***4** 945–50

[56] Liang Q, Ma W, Shi Y, Li Z and Yang X 2013 Easy synthesis of highly fluorescent carbon quantum dots from gelatin and their luminescent properties and applications *Carbon N. Y.***60** 421–8

[57] Mehta V N, Jha S and Kailasa S K 2014 One-pot green synthesis of carbon dots by using Saccharum officinarum juice for fluorescent imaging of bacteria (Escherichia coli) and yeast (*Saccharomyces cerevisiae*) cells *Mater. Sci. Eng. C***38** 20–7

[58] Ali H R H, Hassan A I, Hassan Y F and El-Wekil M M 2020 Development of dual function polyamine-functionalized carbon dots derived from one step green synthesis for quantitation of Cu 2+ and S 2− ions in complicated matrices with high selectivity *Anal. Bioanal. Chem.***412** 1353–63

[59] Murugan N, Prakash M, Jayakumar M, Sundaramurthy A and Sundramoorthy A K 2019 Green synthesis of fluorescent carbon quantum dots from Eleusine coracana and their application as a fluorescence 'turn-off'sensor probe for selective detection of Cu2+ *Appl. Surf. Sci.***476** 468–80

[60] Zhou M, Zhou Z, Gong A, Zhang Y and Li Q 2015 Synthesis of highly photoluminescent carbon dots via citric acid and Tris for iron (III) ions sensors and bioimaging *Talanta***143** 107–13

[61] Liu X, Pang J, Xu F and Zhang X 2016 Simple approach to synthesize amino-functionalized carbon dots by carbonization of chitosan *Sci. Rep.***6** 1–8

[62] Tong G, Wang J, Wang R, Guo X, He L, Qiu F, Wang G, Zhu B, Zhu X and Liu T 2015 Amorphous carbon dots with high two-photon fluorescence for cellular imaging passivated by hyperbranched poly (amino amine) *J. Mater. Chem. B***3**700–6

[63] Jia X, Li J and Wang E 2012 One-pot green synthesis of optically pH-sensitive carbon dots with upconversion luminescence *Nanoscale***4** 5572–5

[64] Springer V, Segundo M A, Centurion M E and Avena M 2019 Fully-programmable synthesis of sucrose-mediated gold nanoparticles for detection of ciprofloxacin *Mater. Chem. Phys.***238** 121917

[65] Kumar S, Karfa P, Majhi K C and Madhuri R 2020 Photocatalytic, fluorescent $BiPO_4$@Graphene oxide based magnetic molecularly imprinted polymer for detection, removal and degradation of ciprofloxacin *Mater. Sci. Eng. C***111** 110777

[66] Xia H, Peng M, Li N and Liu L 2020 CdSe quantum dots-sensitized FRET system for ciprofloxacin detection *Chem. Phys. Lett.***740** 137085

[67] Huang QD, Lv CH, Yuan XL, He M, Lai JP and Sun H 2021 A novel fluorescent optical fiber sensor for highly selective detection of antibiotic ciprofloxacin based on replaceable molecularly imprinted nanoparticles composite hydrogel detector *Sensors Actuators B Chem.***328** 129000

[68] Kingsley M P, Kalambate P K and Srivastava A K 2016 Simultaneous determination of ciprofloxacin and paracetamol by adsorptive stripping voltammetry using copper zinc ferrite nanoparticles modified carbon paste electrode *RSC Adv.***6** 15101–11

[69] Santos A M, Wong A, Almeida A A and Fatibello-Filho O 2017 Simultaneous determination of paracetamol and ciprofloxacin in biological fluid samples using a glassy carbon electrode modified with graphene oxide and nickel oxide nanoparticles *Talanta***174** 610–8

[70] Yuan Y, Zhang F, Wang H, Gao L and Wang Z 2018 A sensor based on Au nanoparticles/carbon nitride/graphene composites for the detection of chloramphenicol and ciprofloxacin *ECS J. Solid State Sci. Technol.***7** M201

[71] Li H, Kang Z, Liu Y and Lee ST 2012 Carbon nanodots: synthesis, properties and applications *J. Mater. Chem.***22** 24230–53

Chapter 5

Conclusion and Future Perspective

CHAPTER 5

CONCLUSION AND FUTURE PERSPECTIVE

The present thesis work presents the development of nanomaterial-based biosensors/ sensors for CPX detection. To detect CPX antibiotics, electrochemical biosensors, and optical-based sensors have been developed. Lanthanum oxide nanomaterial-based electrochemical biosensors have been fabricated for CPX detection. Moreover, an optical sensor has also been utilized for CPX detection. The thesis aimed to develop an efficient, reliable, and simple detection tool for CPX at very low concentrations.

5.1 Conclusion of Research Work

5.1.1 Electrochemical Biosensing Platform for CPX Detection

Part-A: ***Designing and characterization of a highly sensitive and selective biosensing platform for ciprofloxacin detection utilizing lanthanum oxide nanoparticles***

This work describes the fabrication of an electrochemical biosensor using lanthanum oxide (La_2O_3) nanomaterials for the detection of CPX antibiotic First time, lanthanum oxide nanomaterial-based immunosensor BSA/anti-CPX/nLa_2O_3/ITO was fabricated for CPX detection. The fabricated immunosensor showed the improved sensitivity of 11.44 μA ng^{-1} mL cm^{-2} and LOD of 1 pM against the CPX concentrations ranging from 1pM to 1 μM. The response of the fabricated immunosensor was also utilized for analyzing spiked milk samples with 0.91-2.89% recovery. Thus, it showed efficient biosensor fabrication for CPX.

Part-B: ***Electrochemical immunosensor based on nanostructured lanthanum oxide substituted reduced graphene oxide interface for ultralow ciprofloxacin detection in spiked milk samples***

This work presents an efficient electrochemical biosensor using lanthanum oxide @ reduced graphene oxide nanocomposite (La_2O_3@rGO) for CPX detection. The crystalline

phase of La_2O_3@rGO was synthesized at room temperature and was characterized using several techniques such as XRD, Raman spectroscopy, FTIR, EDX, and TEM. First-time-lanthanum oxide @ reduced graphene oxide nanocomposite-based immunosensor BSA/anti-CPX/nLa_2O_3@rGO/ITO was fabricated for CPX detection. The immunosensor showed a sensitivity of 6.52µA μg^{-1} mL $cm^{-2}$and LOD of 0.055µgmL^{-1}against concentrations of 10^{-6} –600 µgmL^{-1}.TheBSA/anti-CPX/nLa_2O_3@rGO/ITO immunosensor showed 95.87-102.73% recovery for the spiked milk sample.

5.1.2 Optical Sensing for CPX Detection

Part-A: ***A novel bio-inspired carbon quantum dots-based optical sensor for ciprofloxacin detection***

In this work, a novel bioinspired, fluorescent, simple, cost-effective, water-dissolving CQDs from *C.tamala* leaf extract was synthesized. The green synthesized CQDs show blue fluorescence, along with a good quantum yield of 31%. The quantum dots (CQDs) exhibited a wide linear range spanning from 1 to 100 µM, with a detection limit of 6.06 µM for the detection of CPX. Furthermore, it exhibits good selectivity (fluorescence enhancement) towards CPX as compared to others. Hence, these bioinspired CQDs are promising sensing materials that could be applied for other applications owing to their tunable optical properties, excellent dispensability, and low cytotoxicity.

Part-B: ***Determination of ciprofloxacin using the Ziziphus mauritania-derived fluorescent carbon dots-based optical sensor***

In this work, a chemical-free synthesis method utilizing ZM pulp extract as a carbon-rich precursor was used to synthesize CDs from an efficient and simple method in the aqueous medium. The characterizations of the green fluorescent CDs were confirmed and supported by XRD, FTIR, UV-vis, PL, SEM, and TEM for selective fluorescence detection of CPX. The green synthesized CDs demonstrated remarkable selectivity for CPX determination among the other analytes examined by enhancement in fluorescence intensity along with a high quantum yield of 30%. Also, the CDs have a 0.5 to 4.5 nm diameter range estimated from the TEM study, showing blue fluorescence. As a result, the fluorescent-based optical sensor exhibited wide linearity from 10 to 100 µM

and a LOD of0.57 µM. Further, the sensor was used for practical application in real milk samples for detecting CPX, showing good % recoveries and RSDs in an acceptable range. The developed synthesis procedure of CDs derived from the pulp extract of ZM is highly economically feasible, greener, and convenient and could be utilized for detecting other antibiotics in the future.

Summarize the table of CPX detection from different techniques.

S.N.	Nanomaterial	Detection Method	Analyte	Detection range	Limit of detection/ Sensitivity
1	La_2O_3 nps	Electrochemical Biosensor	Ciprofloxacin	1×10^{-6} –1 µgmL^{-1}	LOD: 1×10^{-6}µg/mL^{-1} Sensitivity:11.4-64 µA µg-1mLcm^{-2}
2	La_2o_3@rGO nps	Electrochemical Biosensor	Ciprofloxacin	1×10^{-6} –600 µgmL^{-1}	LOD: 0.055µgmL^{-1} Sensitivity:6.52µA µg^{-1} mL cm^{-2}
3	CQDs synthesis from *Ziziphus mauritiana*	UV-visible Spectroscopy (Optical sensor)	Ciprofloxacin	10 to 100 µM	LOD: of 0.56 µM
4	CQDs synthesis from *C. tamala*	UV-visible Spectroscopy (Optical sensor)	Ciprofloxacin	1 to 100 µM	LOD: 6.06µM

5.2 Future Outlook

The electrochemical and optical biosensors/sensors mentioned earlier can be employed in the development of a novel sensing platform aimed at the early identification of antibiotics. In the present thesis, the fabricated electrochemical immunosensor could be used as a lab-on-chip device and act as a cost-effective, fast diagnostic, and quick responsive tool. The fabricated biosensor or sensor can be used in the biomedical field for analyzing a variety of analytes.

List of Publications

LIST OF PUBLICATIONS

1. **N Chaudhary**, PK Gupta, S Eremin, PR Solanki, One-step green approach to synthesize highly fluorescent carbon quantum dots from banana juice for selective detection of copper ions, **Journal of Environmental Chemical Engineering**, 2020.

2. **N Chaudhary**, Verma, D., Sharma, J.G.andSolanki, P.R., A novel bioinspired carbon quantum dots based optical sensor for ciprofloxacin detection. **Materials Letters**, 308, p.131090.,2022

3. **N Chaudhary**, AK Yadav, JG Sharma, PR Solanki, Designing and characterization of a highly sensitive and selective biosensing platform for ciprofloxacin detection utilizing lanthanum oxide nanoparticles, **Journal of Environmental Chemical Engineering**, 2021,

4. **N Chaudhary**, Damini VermaAmitK Yadav, Jai Gopal Sharma, Pratima R. Solanki, Rational hydrothermal-assisted green synthesis of blueish emitting carbon dots as an optical sensing platform for antibiotic detection in the milk sample, **IOP Nanotechnology (under review).**

5. SZH Hashmi, TK Dhiman, **N Chaudhary**, AK Singh, JG Sharma, PR Solanki Levofloxacin Detection Using L-Cysteine Capped MgS Quantum Dots via the Photoinduced Electron Transfer Process,**Frontiers in Nanotechnology,** p. 616186.,2021

6. Yadav, A.K., Verma, D., **Chaudhary, N**., Kumar, A.andSolanki, P.R.,2021.AptamerBased Switches: A Futuristic Approach for Helicobacter pylori Detection. **Materials Letters**, p.131239.,2022

7. Verma, D**.**, Yadav, A.K., **Chaudhary, N**., Mukherjee, M.D., Kumar, P., Kumar, A., Solanki, P.R., Recent advances in understanding SARS-CoV-2 infection and updates on potential diagnostic and therapeutics for COVID-19., **Coronavirus**, **Bentham Science Publishers**,2022

8. Mrinal Poddar, GBVS Lakshmi, Mahima Sharma, **Navneet Chaudhary**, Subhasha Nigam, Monika Joshi, Pratima R Solanki., Environmental friendly polyacrylonitrile nanofibre mats encapsulated and coated with green algae mediated Titanium oxide Nanoparticles for efficient oil spill adsorption, **Marine Pollution Bulletin, 2022**

List of Conferences

LIST OF CONFERENCES

1. Poster presentation on " Designing and characterization of a highly sensitive and selective biosensing platform for ciprofloxacin detection utilizing lanthanum oxide nanoparticles" on the 7th Edition of the **International Conference on Nanotechnology for Better Living 2021 (NBL 2021)** jointly organized by NIT Srinagar and IIT Delhi, India from September 7-11,2021.

2. Oral presentation on "Optical Sensor Comprising a Novel Green Synthesized Carbon Quantum Dots for Determination of Ciprofloxacin; at **International Conference on Advances in Biosciences and Biotechnology (ICABB 2022)** organized by the Department of Biotechnology, Jaypee Institute of Information Technology, Noida, Uttar Pradesh, India, from January 20-22, 2022.

3. Poster presentation on "Rational hydrothermal-assisted green synthesis of blueish emitting carbon dots as an optical sensing platform for antibiotic detection in the milk sample" at the **International Workshop on Advanced Material (2023)** organized by Ras Al Khaimah Centre For Advanced Materials, UAE from February 18- 22, 2023.

4. Attend the conference on **National Conference on Nano/Bio-Technology, 2019** organized by the Special Centre for Nanoscience, Jawaharlal Nehru University and National Institute of Immunology, New Delhi from December19-21, 2019

Publication Included in this Thesis

Journal of Environmental Chemical Engineering 9 (2021) 106771

Contents lists available at ScienceDirect

Journal of Environmental Chemical Engineering

journal homepage: www.elsevier.com/locate/jece

Designing and characterization of a highly sensitive and selective biosensing platform for ciprofloxacin detection utilizing lanthanum oxide nanoparticles

Navneet Chaudhary [a,b], Amit K. Yadav [a], Jai Gopal Sharma [b], Pratima R. Solanki [a,*]

[a] Nano-Bio Laboratory, Special Centre for Nanoscience, Jawaharlal Nehru University, New Delhi 110067, India
[b] Department of Biotechnology, Delhi Technological University, New Delhi 110042, India

ARTICLE INFO

Editor: V. Victor

Keywords:
Antibiotics
Differential pulse voltammetry
Electrochemistry
Immunosensor
Lanthanum oxide
Nanoparticles

ABSTRACT

The pervasive presence of antibiotics in food has severe health impacts due to the rise in antibiotic-resistant bacteria. Therefore, the fabrication of a reliable, sensitive, rapid, and selective platform for antibiotics detection is the required for healthcare services. Here, we aim to fabricate an electrochemical immunosensor based on lanthanum oxide nanoparticles (nLa_2O_3 NPs) for sensitive and selective determination of trace amounts of ciprofloxacin (CPX) antibiotic. Briefly, the synthesis of nLa_2O_3NPs was carried out via wet-chemical co-precipitation process and characterized with various techniques using X-ray diffraction, fourier transform infrared spectroscopy, Raman spectroscopy, contact angle, atomic force microscopy, transmission electron microscopy, and electrochemical methods. These nLa_2O_3 NPs were used for enhancing the electrochemical response of the immunosensor. Further, nLa_2O_3 NPs were functionalized by APTES and were deposited electrophoretically on the surface of ITO glass substrate, followed by immobilizing anti-CPX antibodies covalently via EDC-NHS chemistry. Blocking of the non-specific area was done with the help of BSA. The change in electrochemical response studies of the developed immunosensor (BSA/anti-CPX/APTES/nLa_2O_3/ITO) was monitored to detect CPX. Under optimized conditions, studies showed that the developed biosensor had a wide linear detection range of 0.001–0.5 ng/mL and 1–1000 ng/mL, with the sensitivities of 11.44 μA ng^{-1} mL cm^{-2} (R^2 = 0.968), and 7.88 μA ng^{-1} mL cm^{-2} (R^2 = 0.972), respectively and having lower detection limit of 0.001 ng/mL. The developed immunosensor showed good reproducibility, repeatability, sensitivity, and stability that was effectively explored to detect CPX in milk samples.

1. Introduction

Antibiotics are being used widely in veterinary practices to manage livestock and inhibit microbial infections [1,2]. Over-use and possibly fraudulent misuse of these antibiotics as dietary growth promoters necessitate the development of surveillance and monitoring technologies. After China and the USA, India is in third place in the consumption of antibiotics [3]. The over-usage of drugs has led to antibiotic resistance in bacteria, creating challenges for many societies, hospitals, and health centers due to increased patient numbers and costly treatment [4–6]. Quinolones such as fluoroquinolones (FQs) are the most important classes of antibiotics that inhibit DNA synthesis and are widely used in veterinary and aquatic medicine [7,8]. Ciprofloxacin (CPX) [1-cyclopropyl-6-fluoro-1,4-dihydro-4-oxo-7-(1-piperazinyl) 3-quinolone carboxylic acid] that belongs to FQs is a very stable antibiotic that does not go through complete metabolism in the body, and 30–90% of CPX constantly remains [9,10]. The growing public concern of the accumulation of drug residues in the food supply chain and livestock has led to the general administration of this antibiotic. However, CPX residues have been found to jeopardize people's health by influencing mammalian cell replication and adverse drug reactions. There is a strong probability that it reaches the environment through patients'urine samples and wastewater due to inadequate metabolization of CPX in the body, which induces antibiotic resistance [4–6]. In the coming future, the phenomenon of antibiotic resistance will be more complex. The primary stumbling block is failure to detect pathogenic bacteria, resulting in inadequate antibiotic use and a lower survival rate in septic situations. As a result, there is an urgent requirement to closely

* Corresponding author.
E-mail addresses: partima@mail.jnu.ac.in, pratimarsolanki@gmail.com (P.R. Solanki).

https://doi.org/10.1016/j.jece.2021.106771
Received 28 July 2021; Received in revised form 2 November 2021; Accepted 6 November 2021
Available online 12 November 2021

track the use and discharge of these medications in the atmosphere via the human body.

Several techniques for detection of CPX have been used so far, including spectrophotometry [11], liquid chromatography-mass spectrophotometry [12], high pressure liquid chromatography [13], immunoassay [14], chemiluminescence [15], capillary electrophoresis [16] and electrochemical techniques [17,18]. The only disadvantage of these approaches is that they are all time-consuming, costly, complex methods, and they all necessitate advanced automation and the assistance of skilled users.Various efforts have been made to develop simple, rapid, inexpensive, and sensitive sensors for CPX detection electrochemically, as given in Table [1,18–28]. Ganta et al., developed a disposable and cost-effective sensor for rapid detection of CPX in water with a linear range of 13.75–135 μM, the sensitivity of 0.031 μA μM^{-1} with a limit of detection of 0.33 μM [25]. Gayen et al., fabricated an electrochemical sensor for CPX detection using multi-walled carbon nanotube (MWCNTs) and boron-doped diamond electrodes. They got dynamic detection ranges from 0.005 to 0.05 μM and 0.05–10 μM and sensitivities of 41 μA μM^{-1} and 2.1 μA μM^{-1} in natural water and wastewater effluents, respectively [28]. Cinkova et al., designed an electrochemical method based on the boron-doped diamond electrode as a point of care detection (POC) for CPX within a concentration range from 0.74 to 20.0 × 10^{-6} M with a limit of detection (LOD) of 6.0 × 10^{-7} M [29]. Also, Yan et al., developed a simple and reliable molecularly imprinted polymer-based electrochemical sensor to determine CPX hydrochloride (HCl) with a linear range from 1 × 10^{9}-1 × 10^{-3} M with a detection limit of 7.58 × 10^{-11} M [30].

The development of an immobilization matrix for biosensing is an essential step in the biosensor fabrication process. The immobilization matrix is critical for obtaining a long-life and reliable biosensor, i.e., the biosensing element should be fixed on the surface of the electrode and protect the structure of the bioreceptor during the examination to utilize it for tracking the getting electrical signal [31]. For this purpose, rare earth metal oxides have recently attracted researchers' attention because of their zero toxicity and outstanding electro catalytic and electrochemical properties [32]. Among various rare earth metal oxide, nanostructured lanthanum oxide (nLa_2O_3) comes under the category of p-type semiconductors, having unique chemical and physical properties like electrochemical inertia, dielectric constant, high stability, and surface area to volume ratio, environmental friendliness, large band gap (4.3 eV) and chemical co-ordination capability [33]. The electrochemical properties of nLa_2O_3 are primarily due to the transfer of electrons inside the 4f shell. Also, nLa_2O_3 offers more free binding or adsorption sites, resulting in increased bioactive molecule loading (antibodies) with improved biosensing electrode stability make them an effective material for the application of biosensing. The cubic La_2O_3 is stable at low temperature, whereas hexagonal La_2O_3 is more stable at high temperature [34]. These kinds of metal oxides are explored in optical coatings, biomedicine, biosensors, magnetic resonance imaging, magnetic storage, optical devices,catalysts, Li-ion batteries, photoelectrochemical cells, supercapacitors, gas sensors, etc. [35]. Further, nLa_2O_3 is also not much explored as a sensing material for fabrication of biosensor and thus, was selected for electrochemical detection of CPX for the first time.

In this study, nLa_2O_3NPs were synthesized by the co-precipitation method, considered the facile and quickest NPs synthesis process. These nLa_2O_3 NPs have significant physio-electrochemical properties, resulting in developing a highly efficient electrochemical biosensor for detection of CPX having excellent sensitivity, repeatability, stability, and selectivity. To the best of our knowledge, this is the first work on developing an electrochemical-based immunosensor for detecting CPX using nLa_2O_3 NPs. Indium tin oxide (ITO) coated glass electrodes modified with nLa_2O_3 NPs have been used as the biofunctional substrate with monoclonal antibodies against the CPX (anti-CPX), which was applied for sensitive detection of target CPX from milk samples. As a result of their outstanding properties, like better surface adhesion, wide electrochemical working area, good electrical conductivity, improved optical visibility, low cost, and robust physical and electrochemical features of ITO materials have attracted a lot of attention in recent years [36], several experiments using ITO materials as the working electrode have been conducted to develop optical and electrochemical sensors [32,33,37]. The developed immunosensor has shown outstanding biosensing parameters in two broad linear ranges from 0.001 to 0.5 ng/mL and 1–1000 ng/mL with two superior sensitivities of 11.44 μA ng^{-1} mL cm^{-2} (R^2 = 0.968), and 7.88 μA ng^{-1} mL cm^{-2} (R^2 = 0.972), respectively with the LOD of 0.001 ng/mL. Practical application of the developed CPX biosensor was also examined in the real milk sample. Consequently, this innovative immunosensor is appropriate for the amperometric detection of CPX in milk samples.

2. Experimental section

2.1. Material and methods

Sodium hydroxide (NaOH) (98%), ethanol, hydrogen peroxide (H_2O_2), acetone, and potassium hydroxide (KOH), were bought from fisher scientific, India. Lanthanum nitrate tetrahydrate (99.99%) ($LaN-O_3.4H_2O$), bovine serum albumin (BSA), acetonitrile (ACN), (3-aminopropyl) trimethoxysilane (APTES), and 1-(3-(dimethylamino)-propyl)−3-ethylcarbodiimide hydrochloride (EDC), was obtained from Sigma Aldrich. Urea, sodium hydroxide (NaOH), sodium diphosphatedihydrate [$Na_2HPO_4.2H_2O$], sodium monophosphate anhydrous [NaH_2PO_4], potassium ferrocyanide ($K_4[Fe(CN)_6].3H_2O$), potassium ferricyanide ($K_3[Fe(CN)_6]$), uric acid, and ciprofloxacin antigen (CPX), were acquired from SRL Limited. N-hydroxysulfosuccinimide (NHS) [$C_4H_5NO_3$] was obtained from SpectroChem. The indium tin oxide (ITO) glass substrate was procured from Balzers, UK (having sheet resistance 25 Ω $sq.^{-1}$ and 90% transmittance). $Na_2HPO_4.2H_2O$ and NaH_2PO_4 were utilized to make the fresh phosphate buffer solution (PBS) of 0.2 M in deionized water (DI) with pH 7.0 and stored in the refrigerator for further use. The monoclonal antibodies specific for ciprofloxacin (anti-CPX) were acquired from MyBioSource, USA.All the chemicals were used as such and of analytical grade.

2.2. Instrumentation

The crystalline nature and phase structure of nLa_2O_3 NPs were explored with the help of an X-ray diffractometer (XRD) [Rigaku Miniflex 600 diffractometer (Japan), Cu-Kα radiation having monochromatic beam of X-ray at λ = 1.54 Å]. The information has been accessed at room temperature (RT) with a step size of 5° (2θ) and carried out in the 2θ range from 10° to 80° that was examined by EVA software. The APTES modified La_2O_3NPs, and its further immobilization with anti-CPX and BSA on ITO electrode was confirmed through Fourier transform infrared spectroscopy (FT-IR, Perkin Elmer, US). Its structural and morphological studies were conducted via high-resolution transmission electron microscopy (HR-TEM, JEM-2200 FS, Jeol, Japan). For the TEM sample preparation, nLa_2O_3 NPs were dispersed in ethanol and sonicated for 3 h that was drop-casted on a carbon-coated copper grid and dried overnight. Raman active bands for nLa_2O_3NPs were confirmed by Raman spectroscopy [EnSpectr R532 (US)]. To get the topographical data of the electrodes, atomic force microscopy (AFM) study has been was carried out [WITEC system].

The hydrophobic/hydrophilic behavioral change in ITO, APTES/nLa_2O_3/ITO, anti-CPX/APTES/nLa_2O_3/ITO, and BSA/anti-CPX/APTES/nLa_2O_3/ITO immunoelectrode were conducted using the contact angle (CA) on SURFTENS universal instrument (OEG GmbH Germany). All measurements of electrochemistry, such as differential pulse voltammetry (DPV), frequency response analysis (FRA), and cyclic voltammetry (CV), were performed utilizing an Autolab Galvanostat/Potentiostat electrochemical analyzer (EcoChemie, The Netherlands) which is connected to a computer having software NOVA (version 1.10). The whole

experiments of electrochemistry were done using a three-electrode system in 0.2 M PBS of pH 7.0 having 5 mM $[Fe(CN)_6]^{3-/4-}$ as the redox coupler where platinum acted as counter, Ag/AgCl as a reference, and BSA/anti-CPX/APTES/nLa_2O_3/ITO as a working electrode.

2.3. Synthesis and functionalization of lanthanum oxide nanoparticles (La_2O_3 NPs)

Nanostructured La_2O_3NPs were synthesized via the wet chemical co-precipitation method. For this, 0.1 M solution of $La(NO_3).4H_2O$ and 0.3 M NaOH solution were made in distilled water (DI). The addition of NaOH to the solution of $La(NO_3).4H_2O$ was done drop-wise till the pH of the solution became 14. It was observed that a white-colored precipitate was formed at the end of the reaction that was filtered, washed with DI, and ethanol using centrifugation for 20 min at 6000 rpm to neutralize the pH and remove the impurities. Finally, the resultant precipitate was dried at 80 °C dried in an oven for 12 h to obtain $La(OH)_3$NPs. Then, with the help of mortar-pestle, crushing of the product was carried out to get the fine powder of $La(OH)_3$ NPs. Further, the sample was calcined for 2 h at 800 °C for converting $La(OH)_3$NPs to nanostructured lanthanum oxide (nLa_2O_3NPs). The biochemical reaction for the synthesis of nLa_2O_3 NPs was given in Scheme 1(a).

Moreover, the functionalization of nLa_2O_3NPs was achieved using (3-aminopropyl) trimethoxysilane (APTES). For this, 100 mg of nLa_2O_3 NPs was dissolved in 40 mL of isopropanol at the constant stirring of 250 rpm at 60 ℃. When a highly dispersed solution of nLa_2O_3NPs was obtained, 200 μL of APTES (98%) was added to this solution and stirred at 300 rpm for 48 h under constant stirring at room temperature. Finally, washing the APTES/nLa_2O_3 NPs was done with DI to eliminate the unbound APTES, followed by drying and storing the sample in a dry place [38–40].

2.4. Deposition of functionalized nLa_2O_3 NPs via electrophoretic on ITO electrode (APTES/nLa_2O_3/ITO)

A similar size, i.e., 1.5 × 0.5 cm of ITO coated glass substrates, was taken, and hydrolyzation was carried out in the solution mixture of H_2O: NH_4OH: H_2O_2 having 5:1:1 ratio for 1 h at 80 ℃ followed by washing with DI and ethanol and dried in an oven at 60℃. The smooth films of nLa_2O_3NPs were made on ITO coated glass surface via EPD technique as this method provides reproducible and uniforms films. Before deposition, a stock colloidal solution of nLa_2O_3NPs (5 mg/mL) in ACN and isopropyl alcohol (1:1) was prepared, followed by ultra-sonication. Here, platinum wire and ITO were used as a reference and working electrode, respectively, placed 1 cm apart in the glass cell. The surface area of the APTES/nLa_2O_3NPs/ITO electrodes was also optimized and determined as 0.25 cm^2. Next, 4 mL of ACN was taken in a cell carrying a two-electrode system along with 200 μL of stock APTES/nLa_2O_3 NPs solution and 20 μL of magnesium ions [0.1 M] were added. After optimizing the parameters, the EPD of APTES/La_2O_3 NPs was achieved at 80 V for 2 min on ITO coated glass surface. The fabricated electrode was then washed with Mili-Q water followed by drying at 25 °C overnight, further used for FTIR, contact angle, and electrochemical studies such as DPV and CV.

2.5. Fabrication of biosensing platform (BSA/anti-CPX/APTES/nLa_2O_3 NPs/ITO)

To fabricate the immunoelectrode, an anti-CPX (50 μg/mL) solution was freshly made in PBS of pH 7.0. Next, the anti-CPX solution was

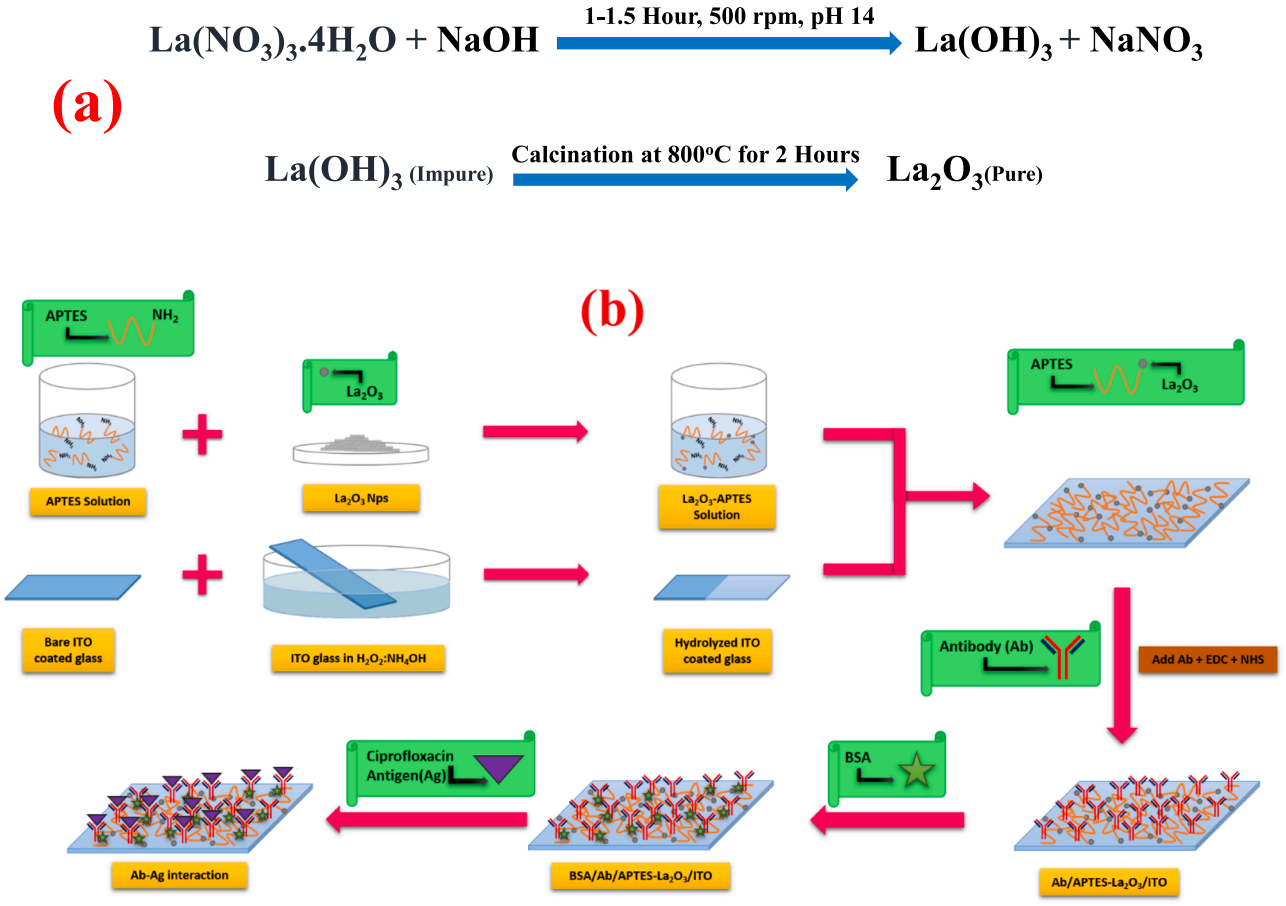

Scheme 1. (a). Synthesis process of nLa_2O_3 nanoparticles. (b).The fabrication process of BSA/anti-CPX/ATPES/nLa_2O_3/ITO immunoelectrode for CPX detection.

mixed with EDC activator (0.4 M) and NHS coupling agent (0.2 M) in a ratio of 2:1:1 and stored at 4 °C for 1 h. Subsequently, 30 μL of this solution was drop casted on the APTES/nLa_2O_3Nps/ITO electrode to form a uniform layer. This electrode was further retained for 6 h in a humid chamber at room temperature, after which washing was done with PBS for removing the unbound anti-CPX particles. To prevent the leaching-out of antibodies from the electrode surface, the carboxylic group (–COOH) present upon the Fc fragment of anti-CPX antibodies was involved in covalent bond formation with the amine group (-NH_2) of APTES silane molecules. EDC activated -COOH groups of anti-CPX, resulting in the generation of unstable O-acylisourea ester, which upon further reaction with the NHS was converted to an amine-reactive NHS ester (a stable intermediate product). The anti-CPX activation by NHS promotes the connection of –NH_2 groups of silane molecules (APTES), resulting in amide bond formation. Furthermore, 10 μL of BSA (2%) was utilized as a blocking agent to cover non-specific areas on the surface of the anti-CPX/APTES/nLa_2O_3/ITO electrode by keeping it at 25°C in a humid chamber for 4 h. Finally, BSA/anti-CPX/APTES/nLa_2O_3Nps/ITO immunoelectrode was washed using PBS buffer and kept at 25 °C when not in use. A step-wise fabrication process of the BSA/anti-CPX/APTES/nLa_2O_3Nps/ITO immunoelectrode was shown in Scheme 1(b).

3. Results and discussions

3.1. XRD analysis

Fig. 1 showed the X-ray diffraction (XRD) pattern of the synthesized product nLa_2O_3 after calcination at 800 °C that confirmed the crystalline structure and phase purity of nLa_2O_3NPs. The XRD spectrum analysis was conducted in a 2θ angle range from 20° to 80° at room temperature. The peaks observed at 2θ = 25.7°, 28.8°, 29.6°, 39.2°, 45.7°, 51.8°, 53.4°, 55.0°, 55.5°, 60.0°, 61.9°, 66.6°, 71.8°, 73.2°, 74.9° and 78.8° correspond tohexagonal planes of nLa_2O_3as (100), (002), (011), (012), (110), (103), (200), (112), (201), (004), (202), (014), (023), (210), (121) and (114), respectively. These data show good co-relation with JCPDS card no.83-1344 for the hexagonal phase of nLa_2O_3. The sharp, strong, and well-defined peaks prove the high crystallinity of nLa_2O_3NPs [41,42]. After optimizing the calcination temperature (400 °C, 600 °C and 800 °C), best results were seen at 800 °C, showing increment in peaks intensity along with reduction in FWHM as compared to the lower calcined temperature. Hence, XRD characterization confirms the formation of the hexagonal phase of nLa_2O_3,and no additional impurity peakswere obtained in its XRD.

The crystallite size (D) of as-synthesized nLa_2O_3NPs was estimated using the Scherrer formula and was obtained as 30.9 nm that relates to 2θ = 29.6 (grain), as given below:

$$D = K\lambda/\beta \cos\theta \quad (1)$$

where β shows the full width at half maximum (FWHM) of the diffraction peak, θ shows the Bragg's diffraction angle, λ depicts the wavelength of the target Cu-Kα (1.540 Å), and K depicts the dimensionless shape factor (0.9).

3.2. Raman analysis

Raman spectroscopy is a useful tool to observe phonon vibration modes of chemical bonds, especially in crystalline sample. This method is well-known for detecting the existence of secondary phases. This characterization technique is quite sensitive to microcrystals and could detect various defects in elaborated layers. Fig. 2 shows the Raman active modes of nLa_2O_3 NPs at 190 cm^{-1}, 404 cm^{-1}, 452 cm^{-1}, and 557 cm^{-1}. Out of these peaks, 196 cm^{-1} is associated with hexagonal structure [43] while peaks at 404 and 452 cm^{-1} are associated with to La–O stretching vibration and Eg^1 mode [44,45]. However, due to the non-polarization effect in nLa_2O_3 NPs, some of the peaks are absent. Further, the XRD analysis also agree with this finding.

3.3. High-resolution transmission electron microscopy study

The morphology, shape, and size of as-synthesized nLa_2O_3 NPs were investigated via TEM [Fig. 3 (A-D)]. The TEM image of nLa_2O_3 NPs at lower and higher magnification revealed that nLa_2O_3 NPs have irregular shape that are highly agglomerated as shown in Fig. 3 (A and B). This is due to high surface energy and smaller sizes of nLa_2O_3 NPs, they have a general tendency to clump together. Fig. 3 (C and D) notably showed high-resolution TEM image (HR-TEM) and selected area electron diffraction (SAED) patterns of nLa_2O_3 NPs, respectively. The value of D-spacing is calculated to be 5.39 Å, which relates to the (011) plane of the hexagonal nLa_2O_3 NPs. Moreover, the highly crystalline nature of nLa_2O_3 NPs was confirmed by the SAED ring pattern, which are well indexed to (011), (012), (110), (103), and (112) planes of hexagonal nLa_2O_3 NPs (JCPDS NO. – 83-1344). As it is a known fact that polycrystalline materials show a ring pattern whereas single crystal materials show a spotty diffraction pattern in SAED [46]. Thus, the rings obtained are well defined which indicates the high crystallinity of nLa_2O_3 NPs that show polycrystalline nature. Further, these results are also found to be in good agreement with the XRD data.

3.4. Fourier transform-infrared spectroscopy study

Fig. 4 [A] shows the FTIR spectra of the nLa_2O_3 NPs calcined at 800 °C in the wavenumber range (4000–400 cm^{-1}). The existence of O–H stretching, consistent with absorbed moisture on the sample surface, is confirmed by the strong bands found at 3574 cm^{-1}, 3557 cm^{-1}, and 3453 cm^{-1}[41]. The asymmetric and symmetric stretching of -COO functional groups were responsible for the peaks at 1638 and 1329 cm^{-1} and the sharp bands at 1487 and 1428 cm^{-1} [42]. The intense bands at

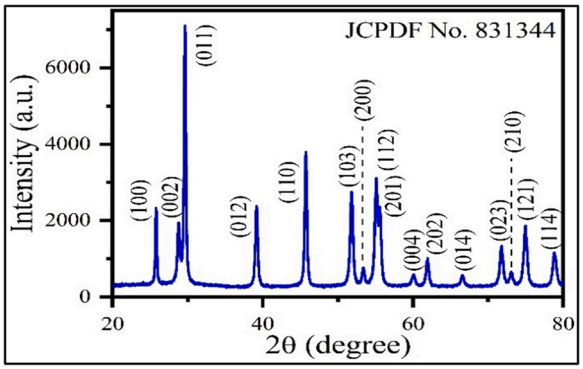

Fig. 1. XRD spectra of nLa_2O_3 NPs.

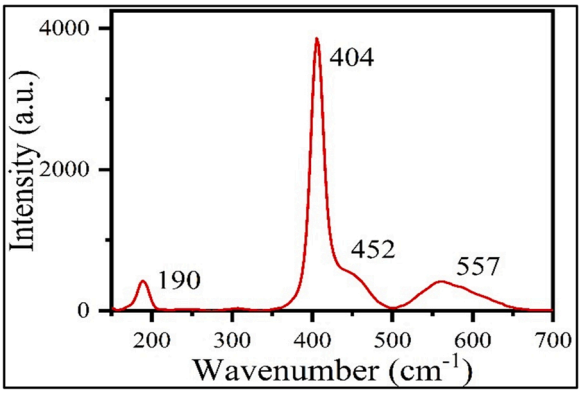

Fig. 2. Raman spectra of La_2O_3 NPs.

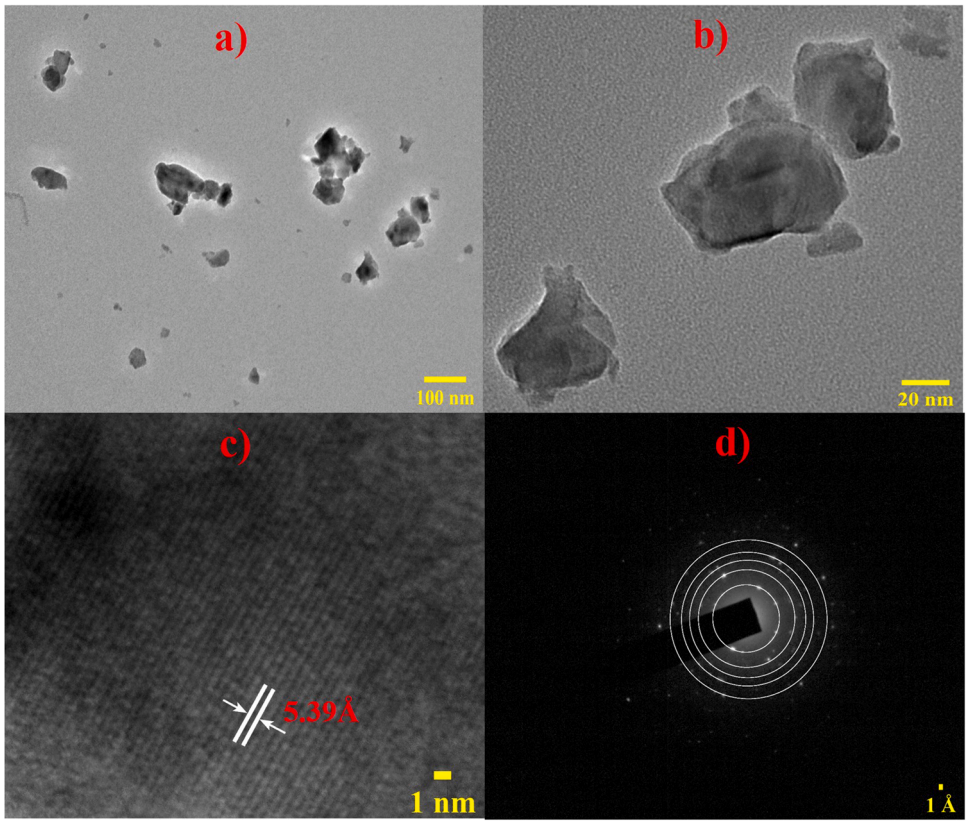

Fig. 3. (A and B) TEM image. (C) HR-TEM image, and (D) SAED pattern of nLa_2O_3 NPs.

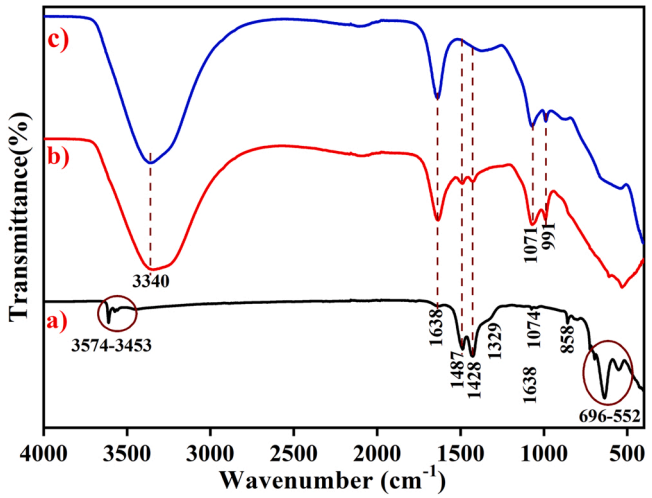

Fig. 4. FTIR spectra of (A) APTES/nLa_2O_3/ITO; (B) anti-CPX/nLa_2O_3/ITO; and (C) BSA/anti-CPX/nLa_2O_3/ITO immunoelectrode.

858 cm^{-1} are connected to C–O bending vibrations, while another band at 1074 cm^{-1} is linked to C–O stretching vibrations. The large bands at 696 and 636 cm^{-1} are caused by La–O stretching, while the small bands at 552 cm^{-1} are caused by La–O bending vibrations. As a result, the inclusion of these La–O stretching and bending vibration bands supports nLa_2O_3 phases in NPs samples [47]. The -OH and -NH stretching vibrations of water molecules are also represented by the peak present at 3340 cm^{-1} in Fig. 4 [B]. The –C═O stretching and amide II peak formed between the -COOH group of the anti-CPX and $-NH_2$ present on the APTES/nLa_2O_3/ITO were seen at 1071 and 991 cm^{-1}, supporting the antibodies attachment on the functionalized nano-hybrid [40]. As shown in Fig. 4 [C], the peak at 1487 and 1428 cm^{-1} disappeared, and peak intensities of 1071 and 991 cm^{-1} got shrunk, which confirmed the blocking of immunoelectrode with BSA molecules.

3.5. Contact angle

The wettability and hydrophilicity of the electrode's surface were strongly influenced by its chemistry. The wettability calculation is necessary as the operative charges stay on the surface ofthe electrode. For this, the water contact angle (CA) of ITO, nLa_2O_3/ITO, anti-CPX/nLa_2O_3/ITO, and BSA/anti-CPX/nLa_2O_3/ITO immunoelectrode are calculated in a static state [Fig. 5]. Using a syringe, a drop of water was kept on each electrode surface, and a measurement of the contact angle at the electrode surface's interface was done. The ITO touch angle was estimated at 73.4°, showing that it is hydrophobic [Fig. 5 (A)]. The CA of the nLa_2O_3/ITO electrode was 25.6° [Fig. 5(b)], indicating more hydrophilic than ITO. The enhanced hydrophilic activity of the nLa_2O_3/ITO electrode creates ideal conditions for monoclonal anti-CPX adsorption. The interface angle value was decreased to 0° after immobilization of bioactive molecules such as anti-CPX and BSA on nLa_2O_3/ITO electrode [Fig. 5 (C and D)], indicating a significant rise in hydrophilic properties of anti-CPX/nLa_2O_3/ITO; and BSA/anti-CPX/nLa_2O_3/ITO immunoelectrode sowing to the covalent association between anti-CPX and nLa_2O_3/ITO electrode [38,48].

3.6. Atomic force microscopy studies

AFM studies result showed the smooth surface and granular topography with dense composite smoothly spread on the ITO surface. The average roughness value of nLa_2O_3 was found as - 4.98×10^{-9} nm. Fig. S1 (Supplementary Fig. 1) (b) displayed AFM images of anti-CPX/nLa_2O_3/ITO electrode that showed globular structures due to the covalent attachment of anti-CPX with enhancement in average roughness

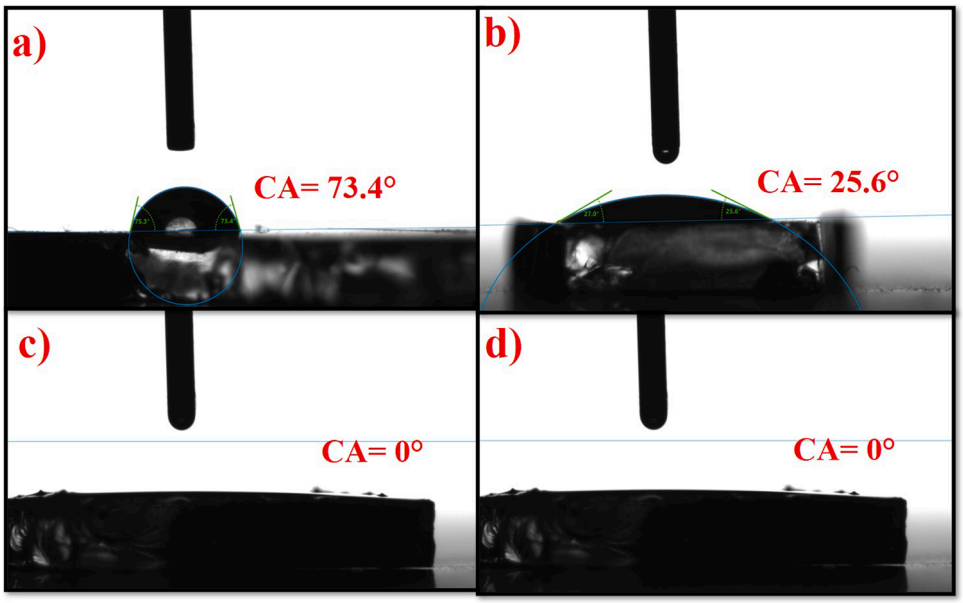

Fig. 5. Contact angle of (A) ITO; (B) APTES/nLa_2O_3/ITO; (C) anti-CPX/nLa_2O_3/ITO; and (D) BSA/anti-CPX/nLa_2O_3/ITO immunoelectrode.

value of -4.60×10^{-9} nm. The detailed explanation has been given in the supplementary file.

3.7. Electrochemical studies

3.7.1. Optimization studies

Optimizing the different experimental conditions is vital for constructing a reproducible, repeatable, and sensitive biosensor. Effect of pH, the concentration of anti-CPX and BSA molecules, and interaction period between anti-CPX and CPX were examined before the characterization to obtain the optimal experimental conditions.The detailed explanation about optimization study of the concentration of anti-CPX and BSA molecules has been given in the Supplementary information in Fig. S2 (a and b).

3.7.2. pH study

Structural conformations of biomolecules are dependent on the pH of the buffer, which affect the antibody-antigen interaction. Thus, the pH effect has been evaluated before electrochemical studies. The pH study has been done using DPV technique at 50 m Vs^{-1} scan rate and using 5 mV step potential at 0.5 ms interval in the potential range of −0.4–0.8 V in PBS of different pH (6.0–8.0) having Ferro-Ferri to investigate the electro-kinetics of anti-CPX present on the designed immunoelectrode. At pH 7.0, maximum peak current was observed for BSA/anti-CPX/ATPES/nLa_2O_3/ITO immunoelectrode [Fig. 6(a)], as the biomolecules show powerful activity at pH 7.0 i.e., in their pure form

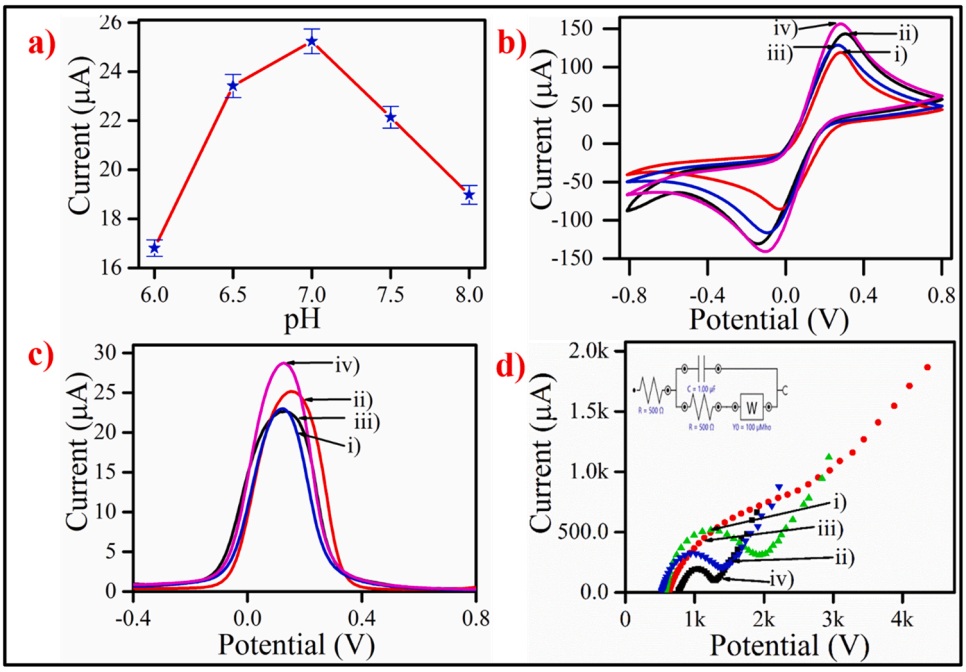

Fig. 6. (a) Effect of pH concentration on BSA/anti-CPX/APTES/nLa_2O_3/ITO immunoelectrode; (b) CV, (c) DPV, and (d) FRA of (i) ITO; (ii) nLa_2O_3/ITO, (iii) anti-CPX/APTES/nLa_2O_3/ITO, and (iv) BSA/anti-CPX/APTES/nLa_2O_3/ITO immunoelectrode.

while at basic or acidic pH, the polypeptides of antibodies are deactivated due to excessive OH^- or H^+ ions [49]. Based on the results, all the further electrochemical studies were carried out at pH 7.0. The voltammetric curve (DPV) of the pH study has been depicted in Fig. S3 (a).

3.7.3. Electrode study

Moreover, the steps included in the synthesis of the BSA/anti-CPX/ATPES/nLa_2O_3/ITO immunoelectrode over the surface of bare ITO were electrochemically inspected by using DPV plots of the ITO (curve i), APTES/nLa_2O_3/ITO (curve ii), anti-CPX/ATPES/nLa_2O_3/ITO (curveiii) and BSA/anti-CPX/ATPES/nLa_2O_3/ITO (curve iv) immunoelectrode as illustrated in Fig. 6(c). The DPV curves were employed at 50 mVs^{-1} scan rate and employing a 5 mV step potential at 0.5 ms interval in the − 0.4–0.8 V potential range. The DPV plots of all the electrodes displayed symmetry, with bare ITO exhibiting the lowest peak current among all the electrodes (i.e., curve i; 22.67 μA). Among the modified electrodes, the deposition of APTES/nLa_2O_3 on the ITO electrode enhanced this current to 25.15 μA because of the rise in the transfer of electrons between the APTES/nLa_2O_3/ITO electrode and medium (curve ii). A significant decrease was seen after immobilizing the anti-CPX monoclonal antibodies, i.e., anti-CPX/APTES/nLa_2O_3/ITO immunoelectrode (curve iii; 22.98 μA), which might be due to the bulky size and insulating nature of anti-CPX where Ferro-Ferri species were captured into macrostructure of antibodies [50]. Furthermore, the blocking of non-specific areas at anti-CPX/APTES/nLa_2O_3/ITO immunoelectrode surface was carried out by immobilization of BSA, which resulted in an apparent rise in peak current of BSA/anti-CPX/APTES/nLa_2O_3/ITO immunoelectrode (curve iv; 28.71 μA). This is due to the metal oxide associated with the zwitterionic nature of BSA and thus alters isoelectric point at the interface of the electrolyte and electrode, which can lead to an increase in the current [51,52]. The connection between BSA and metal ions can also help establish an electron transfer route between electrolyte-rich electrons and electrodes, increasing current [48]. The same conclusion is given by CV studies, as shown in Fig. 6(b).

Moreover, the electrochemical impedance spectroscopic analysis of ITO, APTES/nLa_2O_3/ITO, anti-CPX/APTES/nLa_2O_3/ITO, and BSA/anti-CPX/APTES/nLa_2O_3/ITO immunoelectrode have been processed in PBS (pH 7.0) solution containing $[Fe(CN)_6]^{3-/4-}$ in the frequency range of 100 kHz to 10 Hz [Fig. 6(d)]. Various characteristics comprising heterogeneous electron transfer rate constant (K_{ct}) and charge transfer resistance (R_{ct}), were calculated for different electrodes as given in Table S1, determined by dielectric features of the electrolyte and electrode surface, details of which are provided in the Supplementary file.

3.7.4. Scan rate studies

Cyclic voltammetry (CV) techniques were used to explore the responses of nLa_2O_3/ITO electrode and BSA/anti-CPX/ATPES/nLa_2O_3/ITO immunoelectrode at the interface of electrolyte and surface of the electrode with varying scan rate from 10 to 100 mV/s. The obtained results and detailed information are displayed in Fig. S4 (a) and (b). Also, the standard heterogeneous electron transfer rate constant (K_s), the surface concentration of redox probe of the electrode (I*), effective electroactive surface area (A_e), and kinetic interface factor or diffusion constant (D) for ATPES/nLa_2O_3/ITO electrode and BSA/anti-CPX/ATPES/ nLa_2O_3/ITO immunoelectrode were estimated to study the movement of electrons. A detailed explanation has been given in the supplementary file in the section of scan rate. The obtained interface kinetic parameters are summarized in Table S2.

3.7.5. Electrochemical response study

Initially, the duration needed to stabilize the current response of the synthesized BSA/anti-CPX/ATPES/nLa_2O_3/ITO immunoelectrode towards CPX (10 ng/mL) was adjusted, and achieved results are summarized in Fig. 7(a). Results exhibited erratic behavior till 12 min followed by constant value suggesting that optimal time needed for complete attachment of CPX molecule to anti-CPX is 12 min and was selected as the ideal incubation time for further experiments.

The DPV response was applied to examine the variation in the

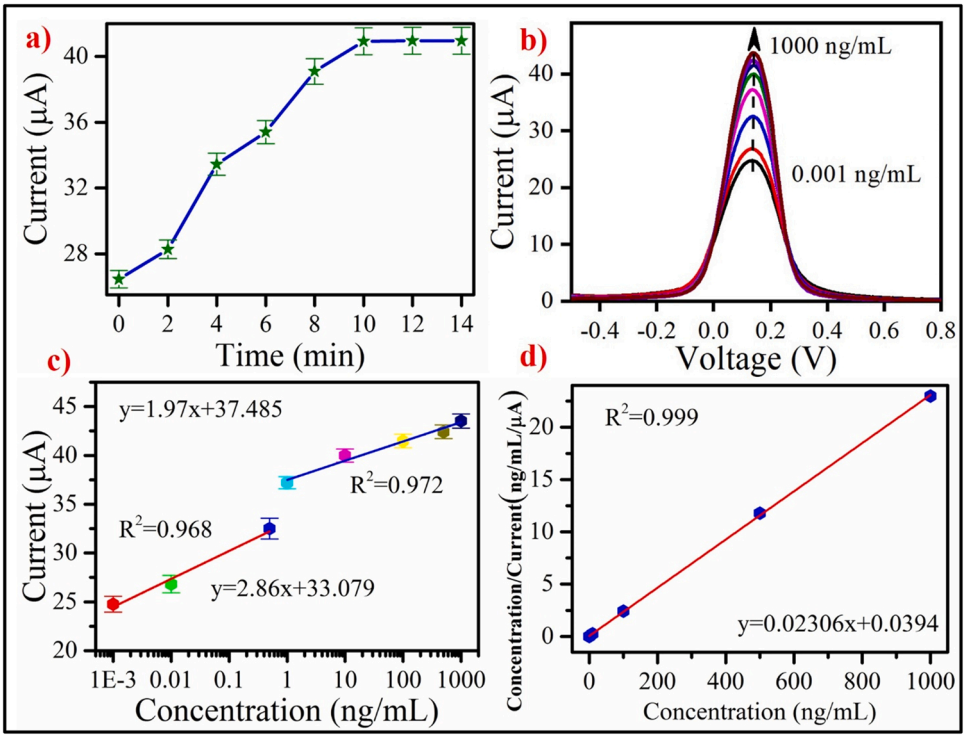

Fig. 7. (a) Incubation study; (b) DPV response studies of BSA/anti-CPX/ATPES/nLa_2O_3/ITO immunoelectrode with different CPX concentrations in 0.2 M PBS (pH 7.0) containing $[Fe(CN)_6]^{3-/4-}$; (c) Calibration curve of BSA/anti-CPX/ATPES/nLa_2O_3/ITO immunoelectrode between peak current and concentration of CPX; and (d) Hanes-wolf Graph plot for BSA/anti-CPX/ATPES/nLa_2O_3/ITO immunoelectrode.

electrochemical response of BSA/anti-CPX/ATPES/nLa_2O_3/ITO immunoelectrode with increasing concentration of CPX from 0.001 ng/mL to 1000 ng/mL, recorded in the − 0.2 V to + 0.6 V potential range with 12 min as incubation time. The current response was increased linearly with the addition of each CPX concentration as illustrated in [Fig. 7(b)] within the concentration range 0.001 ng/mL to 1000 ng/mL due to interaction that occurred between CPX molecules and anti-CPX on the electrode surface and became constant after 1 μM. On the addition of CPX concentration, there is a rise in the peak current mainly due to the CPX and anti-CPX complex formation over the BSA/anti-CPX/ATPES/nLa_2O_3/ITO immunoelectrode surface, further resulting in the development of an electron transfer accelerating layer at the surface of biosensor [53]. The development of an electron transfer accelerating layer on the surface of the BSA/anti-CPX/APTES/nLa_2O_3/ITO immunoelectrode by the interaction between the CPX and anti-CPX might explain the increase in anodic peak current with regard to increasing CPX concentration. The positively charged immune-complex attracted the negatively charged redox probe $[Fe(CN)_6]^{3-/4-}$, enhancing the redox reaction at the electrode surface and resulting in an increase in current when CPX is added.

Linear calibration curves were observed at two distinct concentration ranges, as depicted in Fig. 7(c). Two distinct linear behavior were obtained, one in the range of 0.001–0.5 ng/mL (slope = 2.86 μA ng/mL, $R^2 = 0.968$), and another in 1–1000 ng/mL (slope = 1.97μA ng/mL, $R^2 = 0.972$). The initial sharp rise in current value could be credited to prompt interaction between CPX and anti-CPX on BSA/anti-CPX/ATPES/nLa_2O_3/ITO immunoelectrode surface. A slower increase of peak current is due to a decrease in the concentration of freely available anti-CPX on the surface of the electrode with Ag-CPX. The Eq. (2) and (3) obtained from linear plots between peak current and CPX concentration are:

$$IP = \left(\left(2.86 \quad \mu A \quad ng^{-1} \quad\right) * log(conc. \quad of \quad CPX\left(\frac{ng}{mL}\right)\right)] + 33.07; R^2 = 0.968. \tag{2}$$

$$IP = \left(\left(1.97 \quad \mu A \quad ng^{-1} \quad\right) * log(conc. \quad of \quad CPX\left(\frac{ng}{mL}\right)\right)] + 37.48; R^2 = 0.972. \tag{3}$$

The sensitivity of BSA/anti-CPX/ATPES/nLa_2O_3/ITO immunoelectrode was assessed from calibration curve' slope/surface area of electrode i.e., 0.25 cm^2, as 11.44 μA ng^{-1} mL cm^{-2} ($R^2 = 0.968$) and 7.88 μA ng^{-1} mL cm^{-2} ($R^2 = 0.972$) of the linear plots [54]. Further, formula 3σ/k has been used to calculate the lower detection limit of the immunoelectrode, where'k' denotes the slope of linear calibration and 'σ' denotes the standard deviation of the intercept. The obtained lower detection limit of BSA/anti-CPX/ATPES/nLa_2O_3/ITO immunoelectrode is 0.001 ng/mL. The obtained linear range of BSA/anti-CPX/ATPES/n-La_2O_3/ITO immunoelectrode is from 0.001 ng/mL to 1000 ng/mL. From obtained results, it could be inferred that the immunoelectrode exhibited high sensitivity, wide linear range, low detection limit, and faster response time for CPX. The results were also compared with earlier published research articles in Table 1. Moreover, the reproducibility and repeatability of sensing studies were evaluated three times.

Compared to previous studies (Table 1), the optimized BSA/anti-CPX/APTES/nLa_2O_3/ITO immunosensor had a higher sensitivity, lower LOD, and a broader detection range than other sensors. This was due to the modified antibodies, which expanded the amount of reactive functional groups on the ITO electrode, resulting in more effective CPX binding. Furthermore, the procedure was soft, causing no harm to the electrode surface, which was beneficial for responsive CPX identification. Based on our literature survey, it can be stated that this study delivers the first reporton the fabrication of electrochemical immunosensor for CPX detection based on nLa_2O_3 NPs in 12 min at low concentration (0.001 ng/mL) with high sensitivity (11.44 μA ng^{-1} mL cm^{-2}).

Fig. 7(d) displays the Hanes-wolf plot [(CPX concentration) v/s (CPX conc/ΔI)] of BSA/anti-CPX/ATPES/nLa_2O_3/ITO immunoelectrode. The curve's linearity represents affinity towards immune-complex formation in terms of the dissociation constant (K_d). The K_d value is estimated by dividing the intercept of the linear curve by the slope. The obtained lower K_d value of immunoelectrode (1.7 ng/mL) demonstrates a stronger binding affinity towards CPX.

3.7.6. Control, interference, spiked, reproducibility, repeatability and stability studies

Furthermore, a controlled experiment was carried out to validate that CPX- anti-CPX interaction is the sole reason behind electrochemical responses displayed by BSA/anti-CPX/ATPES/nLa_2O_3/ITO immunoelectrode upon exposure to CPX [Fig. 8(a)]. For this, the ATPES/nLa_2O_3/ITO electrode response was recorded at varying CPX concentrations. Even at higher concentrations, no substantial variation was observed in electrode responses. Thus, these results can verify the importance of CPX- anti-CPX interactions towards the response of immunosensors. Moreover, from obtained results, it could be stated that the surface of the ATPES/nLa_2O_3/ITO electrode is inert towards the CPX molecule. The voltammetric curve (DPV) of the control study has been given in the Fig. S3 (b).

Specificity plays an essential role in the examination of the sensing performance of a biosensor. To evaluate specificity, changes in the

Table 1
Comparison of BSA/anti-CPX/ATPES/nLa_2O_3/ITO biosensor to previously reported bio-sensor for CPX detection.

Sensor/Biosensor	Technique	Sensitivity	LOD (μM)	Linear Range (μM)	Sample	Ref.
$MgFe_2O_4$-MWCNT/GCE	CV		0.01 μM	0.1−1000	tablet, plasma, and urine	[18]
PAR/EGR/GCE	DPV	–	0.01 μM	0.04–10 and 10–120	pharmaceutical preparation and biological media	[19]
P-β-CD-L-arg/CPE	DPV	–	0.05 μM	0.05–100	pharmaceutical formulations and human serum	[20]
DNA biosensor	DPV	–	9 μM	40–80	–	[21]
NiONPs-GO-CTS: EPH/GCE	SWV	9.87 μA/ μM	6.0×10^{-3} μM	0.040–0.97	urine, serum	[22]
MWCNT/GCE	CA	–	6 μM	40–1000	urine and serum	[23]
CZF/CPE	ASV	0.657 μA/μM	2.58×10^{-3} μM	$0.909–4.70 \times 10^3$	urine, serum, pharmaceutical preparations	[24]
SPE	CA	0.031 μA/μM	0.33 μM	13.75–135	DI water	[25]
TiO_2/PB/AuNPs/CMK-3/Nafion/GE	CV	15.93 μA/ μM	1.08×10^{-1} μM	1–10	environmental water	[26]
NP-GCE	DPV	–	0.008 μM	0.25–100	groundwater and tap water	[27]
Porous-Nafion-MWCNT/BDD	DPV	41 ± 5.2 μA/μM and 2.1 ± 0.22 μA/μM	0.005 μM	0.005−0.05, 0.05−10	natural waters and wastewater effluents.	[28]
BSA/anti-CPX/ APTES/ nLa_2O_3/ITO	DPV	11.44 μA/ ng and 7.88 μA/ ng	0.001 ng/mL	0.001–0.5 ng/mL and 1–1000 ng/mL	Milk	This work

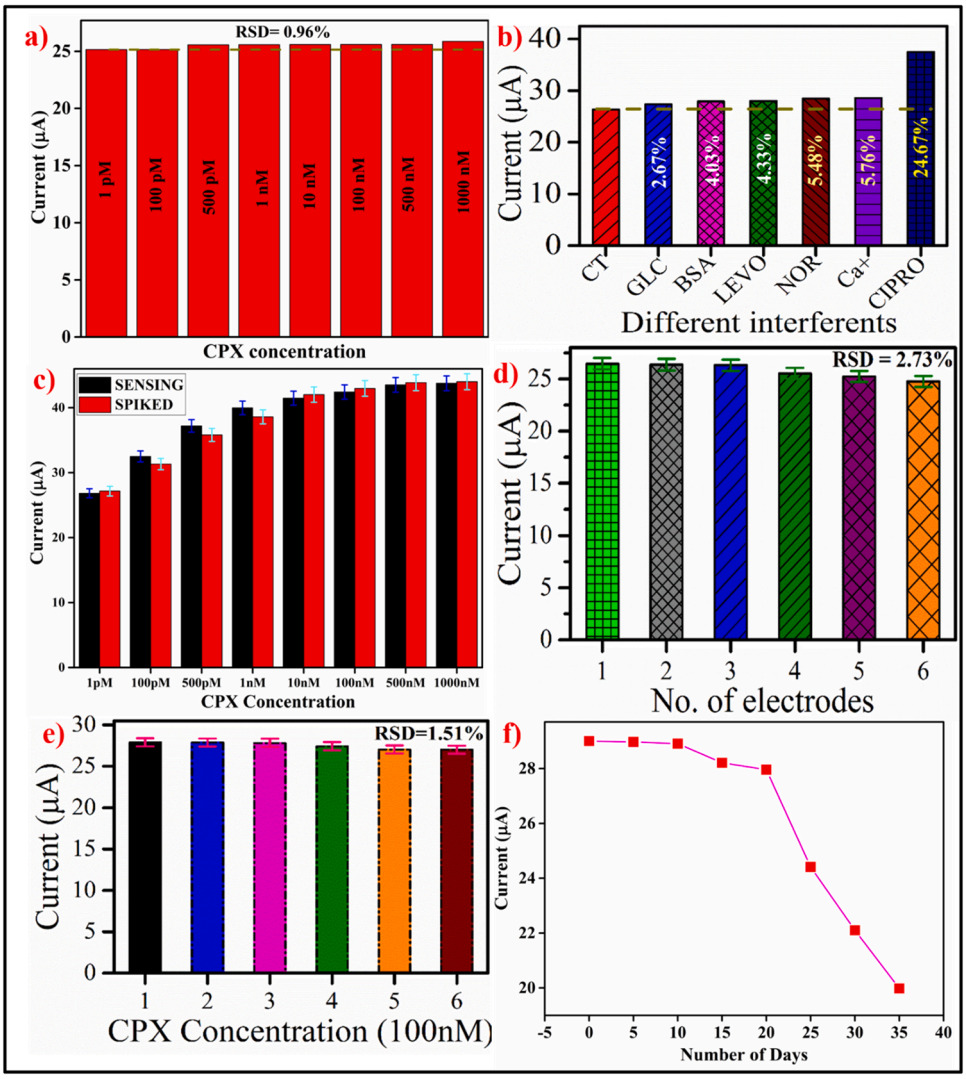

Fig. 8. (a) Control study; (b) Interferent study; (c) Spiked sample study in milk; (d) Reproducibility study; (e) Repeatability study; and (f) Stability study.

electrochemical responses of the designed BSA/anti-CPX /ATPES/nLa_2O_3/ITO immunoelectrode were investigated by DPV studies in the presence of interfering agents [Fig. 8(b)]. Initially, the biosensor response was obtained in the presence of CPX (10 ng/mL) that showed increased current value due to CPX and anti-CPX interaction. Further, different interferents (generally present in milk) were added sequentially, including BSA [100 μM], Glucose [100 μM], Norfloxacin [5 mM], Levofloxacin [5 mM], and Calcium ions (Ca^{2+}) [0.015 g/100 mL]. Negligible changes (0–1%) were noticed in the peak response after the addition of various interferents. Therefore, it can be concluded that the designed BSA/anti-CPX/ATPES/nLa_2O_3/ITO immunoelectrode is not affected by the presence of different interferents, and it isa great candidate to detect CPX for practical usage.

Further, the practicability of developed BSA/anti-CPX/ATPES/nLa_2O_3/ITO immunoelectrode in the real sample was evaluated using a prepared spiked milk sample. CPX recovery percentage and the obtained RSD from spiked milk samples (summarized in Table 2) are 95.9 – 101.3% and 0.91–2.89%, respectively, illustrated in Fig. 8(c). The estimated values are better, validating the sensor's accuracy and its reliability for applicability in real milk samples.

Repeatability and reproducibility results are vital parameters in immunosensor fabrication. To examine the reproducibility of the fabricated biosensor, six immunoelectrodes were developed in the same set of conditions and studied using the DPV. The obtained RSD value for reproducibility was 2.73% ofthe BSA/anti-CPX/ATPES/nLa_2O_3/ITO immunoelectrode, as illustrated in Fig. 8(d). The reproducibility of immunoelectrode was within a reasonable range. The repeatability of the BSA/anti-CPX/ATPES/nLa_2O_3/ITO immunoelectrode was monitored by studying DPV response at the particular concentration (100 ng/mL) of CPX [Fig. 8(e)]. RSD for consecutive measurements (6 times) was found at 1.51%. The repeatability experiment of BSA/anti-CPX/ATPES/nLa_2O_3/ITO immunoelectrode was satisfactory.

Table 2
Recovery of CPX from milk samples using BSA/anti-CPX/ATPES/nLa_2O_3/ITO immunoelectrode.

CPX Added to the milk sample	DPV peak current for CPX (μA)	DPV peak current of spiked-sample (μA)	Relative Standard Deviation (%)	Recovery (%)
1 pM	26.824	27.163	0.89	101.263
100 pM	32.501	31.324	2.69	96.378
500 pM	37.200	35.810	2.69	96.263
1 nM	39.978	38.601	2.45	96.588
10 nM	41.473	42.013	0.91	101.302
100 nM	42.419	42.968	0.91	101.294
500 nM	43.518	43.863	2.74	96.196
1 μM	43.762	44.011	2.89	95.998

The shelf-life of BSA/anti-CPX/ATPES/nLa_2O_3/ITO immunoelectrode was determined for 40 days at an interval of 5 days via the DPV technique. Fig. 8(f) shows that the immunoelectrode retains 90% of the peak current till the 20^{th} day. Afterward, a rapid decrease in current was observed, suggesting that the immunosensor has good stability up to 20 days. The fabricated BSA/anti-CPX/ATPES/nLa_2O_3/ITO biosensor was kept in the refrigerator when not in utilization.

As nanomaterials have a large surface area so they could be used for loading a large number of bio-recognition molecules like enzymes, antibodies, DNA etc. for amplifying the electrochemical response. Thus, it is important to synthesize nanomaterials having good biocompatibility and electrochemical properties using a simple and cost-effective technique. Keeping this in our mind, in the present study, we have synthesized nLa_2O_3 NPs using a facile, easy, economical and rapid technique called co-precipitation method without using any harsh conditions (temperature, pressure etc.). This method was adopted as to obtain water soluble nanoparticles directly with much higher yields. Further, this method offers several advantages like control over shape, morphology, and properties of the prepared nanomaterials [19]. The as-synthesized nLa_2O_3 NPs have shown significant physio-electrochemical properties, resulting in developing a highly efficient electrochemical biosensor for detection of CPX having excellent sensitivity, repeatability, stability, and selectivity. Moreover, we believe that the fabricated biosensing platform could be used for detecting other various antibiotics or other analytes by substituting the specific bio-recognition molecules against target analyte. However, the key challenges for developing the biosensor using nLa_2O_3 NPs was the sensitivity as the antibiotics are found to be highly diluted in milk samples. Therefore, we need to improve the sensitivity of the biosensor by utilizing other nanomaterials (graphene, carbon nanotubes, etc.) in combination to the existing one.

4. Conclusions

Herein, an innovative BSA/anti-CPX/ATPES/nLa_2O_3/ITO immunoelectrode has been effectively designed to fabricate CPX immunosensor. nLa_2O_3NPs have been fabricated by employing the co-precipitation method. The obtained nLa_2O_3 NPs were thoroughly validated using multiple characterization techniques such as XRD, FTIR, AFM, Raman, and TEM. The ATPES/nLa_2O_3/ITO thin films were synthesized via ATPES/nLa_2O_3 colloidal solution on the surface of the ITO electrode and further utilized to immobilize anti-CPX via EDC-NHS mixture. The contact angle measurements study was used for evaluating the surface wettability of designed electrodes. Additionally, the oxidation/reduction characteristics of BSA/anti-CPX/ATPES/nLa_2O_3/ITO immunoelectrode were assessed using the CV. Moreover, the DPV technique was used to record responses of BSA/anti-CPX/ATPES/nLa_2O_3/ITO immunoelectrode at distinct CPX concentrations (0.001 ng/mL-1000 ng/mL). The results have shown a remarkable linearity range from 0.001 ng/mL to 1000 ng/mL CPX concentration, high sensitivity 11.44 μA $ng^{-1}mLcm^{-2}$, and lower LOD of 0.001 ng/mL compared to earlier reported sensors. The developed immunoelectrode was very specific against CPX. Furthermore, efforts were made to explore such a bio-sensing platform to analyze real milk samples. Therefore, the designed immunosensor introduced an alternative way to develop highly biocompatible, sensitive, and rapid biochip and biosensors devices.

CRediT authorship contribution statement

P.R.S. and J.G.S designed and conceptualized the research work. They also reviewed and finalized the manuscript. N.C. and A.K.Y. have conducted the experiments and data analysis. N.C. and A.K.Y. wrote the manuscript. All authors reviewed the manuscript.

Declaration of Competing Interest

The authors declare that they have no known competing financial interests or personal relationships that could have appeared to influence the work reported in this paper.

Acknowledgment

The authors thank AIRF, JNU for their characterization facilities. PRS thanks the Government of India for financial supports for this work through Department of Biotechnology (DBT), Indo-Russia Project (DBT/IC-2/Indo-Russia/2017–19/02), and Department of Science and Technology (DST); BDTD, India, Government of India. Navneet Chaudhary thanks the Indian Council of Medical Research (ICMR), India, for his fellowship. Amit K. Yadav thanks the Ministry of Education, Govt. of India for the Prime Minister Research Fellowship for the financial assistants.

Appendix A. Supporting information

Supplementary data associated with this article can be found in the online version at doi:10.1016/j.jece.2021.106771.

References

[1] R.M. Kalunke, G. Grasso, R. D'Ovidio, R. Dragone, C. Frazzoli, Detection of ciprofloxacin residues in cow milk: a novel and rapid optical β-galactosidase-based screening assay, Microchem. J. 136 (2018) 128–132.
[2] A. Yadav, D. Verma, P. Solanki, Electrophoretically deposited L-cysteine functionalized MoS_2@ MWCNT nanocomposite platform: a smart approach toward highly sensitive and label-free detection of gentamicin, Mater. Today Chem. 22 (2021), 100567.
[3] R. Laxminarayan, R.R. Chaudhury, Antibiotic resistance in India: drivers and opportunities for action, PLOS Med. 13 (2016), e1001974.
[4] F. Toldrá, M. Reig, Methods for rapid detection of chemical and veterinary drug residues in animal foods, Trends Food Sci. Technol. 17 (2006) 482–489.
[5] L. Chen, Z. Wang, M. Ferreri, J. Su, B. Han, Cephalexin residue detection in milk and beef by ELISA and colloidal gold based one-step strip assay, J. Agric. Food Chem. 57 (2009) 4674–4679.
[6] G.R. Marchesini, W. Haasnoot, P. Delahaut, H. Gerçek, M.W. Nielen, Dual biosensor immunoassay-directed identification of fluoroquinolones in chicken muscle by liquid chromatography electrospray time-of-flight mass spectrometry, Anal. Chim. Acta 586 (2007) 259–268.
[7] Y. Zhu, L. Li, Z. Wang, Y. Chen, Z. Zhao, L. Zhu, X. Wu, Y. Wan, F. He, J. Shen, Development of an immunochromatography strip for the rapid detection of 12 fluoroquinolones in chicken muscle and liver, J. Agric. Food Chem. 56 (2008) 5469–5474.
[8] P. Higgins, A. Fluit, F. Schmitz, Fluoroquinolones: structure and target sites, Curr. Drug Targets 4 (2003) 181–190.
[9] M.C. Dodd, A.D. Shah, U. von Gunten, C.-H. Huang, Interactions of fluoroquinolone antibacterial agents with aqueous chlorine: reaction kinetics, mechanisms, and transformation pathways, Environ. Sci. Technol. 39 (2005) 7065–7076.
[10] G. Carlsson, S. Örn, D.J. Larsson, Effluent from bulk drug production is toxic to aquatic vertebrates, Environ. Toxicol. Chem. 28 (2009) 2656–2662.
[11] S. Mostafa, M. El-Sadek, E.A. Alla, Spectrophotometric determination of ciprofloxacin, enrofloxacin and pefloxacin through charge transfer complex formation, J. Pharm. Biomed. Anal. 27 (2002) 133–142.
[12] H.Y. Ji, D.W. Jeong, Y.H. Kim, H.H. Kim, D.-R. Sohn, H.S. Lee, Hydrophilic interaction liquid chromatography–tandem mass spectrometry for the determination of levofloxacin in human plasma, J. Pharm. Biomed. Anal. 41 (2006) 622–627.
[13] G. Carlucci, Analysis of fluoroquinolones in biological fluids by high-performance liquid chromatography, J. Chromatogr. A 812 (1998) 343–367.
[14] G.G. Snitkoff, D.W. Grabe, R. Holt, G.R. Bailie, Development of an Immunoassay for Monitoring the Levels of Ciprofloxacin Patient Samples, J. Immunoass. Immunochem. 19 (1998) 227–238.
[15] H.W. Sun, L.Q. Li, X.Y. Chen, Flow-injection enhanced chemiluminescence method for determination of ciprofloxacin in pharmaceutical preparations and biological fluids, Anal. Bioanal. Chem. 384 (2006) 1314–1319.
[16] R.H. Montes, M.C. Marra, M.M. Rodrigues, E.M. Richter, R.A. Muñoz, Fast determination of ciprofloxacin by batch injection analysis with amperometric detection and capillary electrophoresis with capacitively coupled contactless conductivity detection, Electroanalysis 26 (2014) 432–438.
[17] A. Radi, M. El Ries, S. Kandil, Electrochemical study of the interaction of levofloxacin with DNA, Anal. Chim. Acta 495 (2003) 61–67.
[18] A.A. Ensafi, A.R. Allafchian, R. Mohammadzadeh, Characterization of MgFe2O4 nanoparticles as a novel electrochemical sensor: application for the voltammetric determination of ciprofloxacin, Anal. Sci. 28 (2012) 705–710.

[19] X. Zhang, Y. Wei, Y. Ding, Electrocatalytic oxidation and voltammetric determination of ciprofloxacin employing poly (alizarin red)/graphene composite film in the presence of ascorbic acid, uric acid and dopamine, Anal. Chim. Acta 835 (2014) 29–36.
[20] F. Zhang, S. Gu, Y. Ding, Z. Zhang, L. Li, A novel sensor based on electropolymerization of β-cyclodextrin and l-arginine on carbon paste electrode for determination of fluoroquinolones, Anal. Chim. Acta 770 (2013) 53–61.
[21] H. Nawaz, S. Rauf, K. Akhtar, A.M. Khalid, Electrochemical DNA biosensor for the study of ciprofloxacin–DNA interaction, Anal. Biochem. 354 (2006) 28–34.
[22] A.M. Santos, A. Wong, A.A. Almeida, O. Fatibello-Filho, Simultaneous determination of paracetamol and ciprofloxacin in biological fluid samples using a glassy carbon electrode modified with graphene oxide and nickel oxide nanoparticles, Talanta 174 (2017) 610–618.
[23] L. Fotouhi, M. Alahyari, Electrochemical behavior and analytical application of ciprofloxacin using a multi-walled nanotube composite film-glassy carbon electrode, Colloids Surf. B: Biointerfaces 81 (2010) 110–114.
[24] M.P. Kingsley, P.K. Kalambate, A.K. Srivastava, Simultaneous determination of ciprofloxacin and paracetamol by adsorptive stripping voltammetry using copper zinc ferrite nanoparticles modified carbon paste electrode, RSC Adv. 6 (2016) 15101–15111.
[25] D. Ganta, N. Trevino, W. Montes, Disposable chronoamperometric sensor for detecting ciprofloxacin, Eng. Res. Express 1 (2019), 015031.
[26] A. Pollap, K. Baran, N. Kuszewska, J. Kochana, Electrochemical sensing of ciprofloxacin and paracetamol in environmental water using titanium sol based sensor, J. Electroanal. Chem. 878 (2020), 114574.
[27] T. Chen, Y. Liu, J. Lu, J. Xing, J. Li, T. Liu, Q. Xue, Highly efficient detection of ciprofloxacin in water using a nitrogen-doped carbon electrode fabricated through plasma modification, New J. Chem. 43 (2019) 15169–15176.
[28] P. Gayen, B.P. Chaplin, Selective electrochemical detection of ciprofloxacin with a porous nafion/multiwalled carbon nanotube composite film electrode, ACS Appl. Mater. Interfaces 8 (2016) 1615–1626.
[29] K. Cinková, D. Andrejcakova, L. Svorc, Electrochemical method for point-of-care determination of ciprofloxacin using boron-doped diamond electrode, Acta Chim. Slov. 9 (2016) 146–151.
[30] C. Yan, J. Li, T. Meng, X. Liu, R. Zhang, Y. Chen, G. Wang, Selective recognition of ciprofloxacin hydrochloride based on molecular imprinted sensor via electrochemical copolymerization of pyrrole and o-phenylenediamine, Int. J. Electrochem. Sci. 11 (2016) 6466–6476.
[31] S. Soylemez, Y.A. Udum, M. Kesik, C.G. Hızlıateş, Y. Ergun, L. Toppare, Electrochemical and optical properties of a conducting polymer and its use in a novel biosensor for the detection of cholesterol, Sens. Actuators B: Chem. 212 (2015) 425–433.
[32] P.-p Wang, B. Bai, S. Hu, J. Zhuang, X. Wang, Family of multifunctional layered-lanthanum crystalline nanowires with hierarchical pores: hydrothermal synthesis and applications, J. Am. Chem. Soc. 131 (2009) 16953–16960.
[33] M.R. Sovizi, S. Mirzakhani, A chemiresistor sensor modified with lanthanum oxide nanoparticles as a highly sensitive and selective sensor for dimethylamine at room temperature, New J. Chem. 44 (2020) 4927–4934.
[34] A. Weidenkaff, R. Robert, M. Aguirre, L. Bocher, T. Lippert, S. Canulescu, Development of thermoelectric oxides for renewable energy conversion technologies, Renew. Energy 33 (2008) 342–347.
[35] H. Kabir, S.H. Nandyala, M.M. Rahman, M.A. Kabir, Z. Pikramenou, M. Laver, A. Stamboulis, Polyethylene glycol assisted facile sol-gel synthesis of lanthanum oxide nanoparticles: Structural characterizations and photoluminescence studies, Ceram. Int. 45 (2019) 424–431.
[36] H. Tang, W. Zhang, P. Geng, Q. Wang, L. Jin, Z. Wu, M. Lou, A new amperometric method for rapid detection of Escherichia coli density using a self-assembled monolayer-based bienzyme biosensor, Anal. Chim. Acta 562 (2006) 190–196.
[37] S. Tiwari, P.K. Gupta, Y. Bagbi, T. Sarkar, P.R. Solanki, L-cysteine capped lanthanum hydroxide nanostructures for non-invasive detection of oral cancer biomarker, Biosens. Bioelectron. 89 (2017) 1042–1052.
[38] A.K. Yadav, D. Verma, G. Lakshmi, S. Eremin, P.R. Solanki, Fabrication of label-free and ultrasensitive electrochemical immunosensor based on molybdenum disulfide nanoparticles modified disposable ITO: an analytical platform for antibiotic detection in food samples, Food Chem. 363 (2021), 130245.
[39] C. Chaudhary, S. Kumar, R. Chandra, Monophasic molybdenum selenide-reduced graphene oxide nanocomposite sheets based immunosensing platform for ultrasensitive serotonin detection, Microchem. J. 159 (2020), 105344.
[40] S. Kumar, J.G. Sharma, S. Maji, B.D. Malhotra, Nanostructured zirconia decorated reduced graphene oxide based efficient biosensing platform for non-invasive oral cancer detection, Biosens. Bioelectron. 78 (2016) 497–504.
[41] X. Wang, M. Wang, H. Song, B. Ding, A simple sol–gel technique for preparing lanthanum oxide nanopowders, Mater. Lett. 60 (2006) 2261–2265.
[42] M. Salavati-Niasari, G. Hosseinzadeh, F. Davar, Synthesis of lanthanum carbonate nanoparticles via sonochemical method for preparation of lanthanum hydroxide and lanthanum oxide nanoparticles, J. Alloy. Compd. 509 (2011) 134–140.
[43] A. Orera, G. Larraz, M. Sanjuán, Spectroscopic study of the competition between dehydration and carbonation effects in La_2O_3-based materials, J. Eur. Ceram. Soc. 33 (2013) 2103–2110.
[44] J. Denning, S. Ross, The vibrational spectra and structures of rare earth oxides in the a modification, J. Phys. C: Solid State Phys. 5 (1972) 1123–1133.
[45] J. Cui, G.A. Hope, Raman and Fluorescence Spectroscopy of CeO_2, Er_2O_3, Nd_2O_3, Tm_2O_3, Yb_2O_3, La_2O_3, and Tb_4O_7, J. Spectrosc. 2015 (2015) 1–8.
[46] R.B. Borade, S.E. Shirsath, G. Vats, A.S. Gaikwad, S.M. Patange, S. Kadam, R. Kadam, A. Kadam, Polycrystalline to preferred-(100) single crystal texture phase transformation of yttrium iron garnet nanoparticles, Nanoscale Adv. 1 (2019) 403–413.
[47] Q. Zhou, H. Zhang, F. Chang, H. Li, H. Pan, W. Xue, D.Y. Hu, S. Yang, Nano La_2O_3 as a heterogeneous catalyst for biodiesel synthesis by transesterification of Jatropha curcas L. oil, J. Ind. Eng. Chem. 31 (2015) 385–392.
[48] A.K. Yadav, T.K. Dhiman, G. Lakshmi, A.N. Berlina, P.R. Solanki, A highly sensitive label-free amperometric biosensor for norfloxacin detection based on chitosan-yttria nanocomposite, Int. J. Biol. Macromol. 151 (2020) 566–575.
[49] D. Chauhan, A.K. Yadav, P.R. Solanki, Carbon cloth-based immunosensor for detection of 25-hydroxy vitamin D_3, Microchim. Acta 188 (2021) 1–11.
[50] M. Garg, M. Chatterjee, A.L. Sharma, S. Singh, Label-free approach for electrochemical ferritin sensing using biosurfactant stabilized tungsten disulfide quantum dots, Biosens. Bioelectron. 151 (2020), 111979.
[51] A.V. Singh, B.M. Bandgar, M. Kasture, B. Prasad, M. Sastry, Synthesis of gold, silver and their alloy nanoparticles using bovine serum albumin as foaming and stabilizing agent, J. Mater. Chem. 15 (2005) 5115–5121.
[52] A. Singh, R. Patil, M. Kasture, W. Gade, B. Prasad, Synthesis of Ag–Pt alloy nanoparticles in aqueous bovine serum albumin foam and their cytocompatibility against human gingival fibroblasts, Colloids Surf. B: Biointerfaces 69 (2009) 239–245.
[53] S. Kumar, S. Kumar, S. Augustine, B.D. Malhotra, Protein functionalized nanostructured zirconia based electrochemical immunosensor for cardiac troponin I detection, J. Mater. Res. 32 (2017) 2966–2972.
[54] G. Lakshmi, A.K. Yadav, N. Mehlawat, R. Jalandra, P.R. Solanki, A. Kumar, Gut microbiota derived trimethylamine N-oxide (TMAO) detection through molecularly imprinted polymer based sensor, Sci. Rep. 11 (2021) 1–14.

Materials Letters 308 (2022) 131090

Contents lists available at ScienceDirect

Materials Letters

journal homepage: www.elsevier.com/locate/matlet

A novel bioinspired carbon quantum dots based optical sensor for ciprofloxacin detection

Navneet Chaudhary [a,b], Damini Verma [a], Jai Gopal Sharma [b], Pratima R. Solanki [a,*]

[a] Nano-Bio Laboratory, Special Centre for Nanoscience, Jawaharlal Nehru University, India
[b] Department of Biotechnology, Delhi Technological University, India

ARTICLE INFO

Keywords:
Carbon quantum dots
Ciprofloxacin
Fluorescent
Green synthesis
Quantum yield

ABSTRACT

Green route has been a centre of attraction for synthesizing carbon quantum dots from natural sources owing to its outstanding optical properties. In the current work, a novel bioinspired and fluorescent carbon quantum dots were prepared from *Cinnamomum tamala (tejpata)* leaves extract utilizing a simple one-step hydrothermal method for the first time. The current method delivers a high quantum yield of 31% having 340 nm excitation wavelength for detection of ciprofloxacin. The developed fluorescent sensor showed ciprofloxacin detection in the linear range of 1 to 100 μM, with a detection limit of 6.06 μM.

1. Introduction

Fluoroquinolones are the class of antibiotics extensively used for fighting against numerous Gram positive and Gram negative microorganisms as human and veterinary medicines [1]. Among them, ciprofloxacin (CPX) [1-cyclopropyl-6-fluoro-1,4- dihydro-4-oxo-7-(1-piperazinyl) 3-quinolone carboxylic acid] is the most explored antibiotic known for its stability that does not go complete metabolism and 30–90% residue stays in the body [2,3]. The growing public concern of the accumulation of drug residues in the food supply chain and livestock has led to the general administration of this antibiotic. However, CPX residues have been found to jeopardize people's health by influencing mammalian cell replication and adverse drug reactions. There is a strong probability that it reaches the environment through patients' urine samples and wastewater due to inadequate metabolization of CPX in the body, which induces antibiotic resistance [4,5]. In the coming future, the phenomenon of antibiotic resistance will be more complex. Failure to detect pathogenic bacteria is the primary stumbling block, resulting in inadequate antibiotic use and a lower survival rate in septic situations [6]. Therefore, detection of antibiotics residues is a serious issue and need of the hour. Numerous techniques are employed for detecting CPX remains, such as spectrophotometry [7], liquid chromatography-mass spectrophotometry [8], high pressure liquid chromatography [9], and immunoassay [10], etc.

But due to several disadvantages associated with it, they are not suitable for onsite food safety and environmental monitoring. On the other hand, the fluorometric detection technique has emerged as an alternate way for detecting CPX in real samples due to their rapid response, cost-efficiency, less interferences, selectivity, and high sensitivity [11,12]. The fluorescent carbon quantum dots (CQDs) are attractive and smart members of the carbon family. They have gained attention owing to their high biocompatibility, rich functional groups, less toxicity, excellent water solubility, easy, rapid synthesis process, etc. [13,14]. The green synthesis of CQDs from natural carbon precursors has gained significance as it is economical, environment-friendly, repeatable, and straightforward than chemical synthesis. The ample availability of carbon from natural sources is another reason for achieving attention to synthesize green CQDs [15]. Out of the various spices, *Cinnamomum tamala* (*C. tamala*) was chosen as a natural precursor to synthesize green CQDs prepared *via* hydrothermal process. *C. tamala,* recognized as *tejpata,* belongs to the family Lauraceae whose *tejpata* oil is used as a medicine for treating cardiac disorders, diuretic, anti-flatulent, and carminative [16].

In the present work, we have reported novel bioinspired, fluorescent CQDs derived from *C. tamala* leaves extract *via* a one-step, simple hydrothermal approach. The CQDs were characterized using different techniques and gave good quantum yield (QY). The CQDs show excellent solubility in water with blue emission and specific determination of CPX in the range from 1 to 100 μM.

* Corresponding author.
E-mail addresses: partima@mail.jnu.ac.in, pratimarsolanki@gmail.com (P.R. Solanki).

https://doi.org/10.1016/j.matlet.2021.131090
Received 4 September 2021; Received in revised form 30 September 2021; Accepted 12 October 2021
Available online 16 October 2021

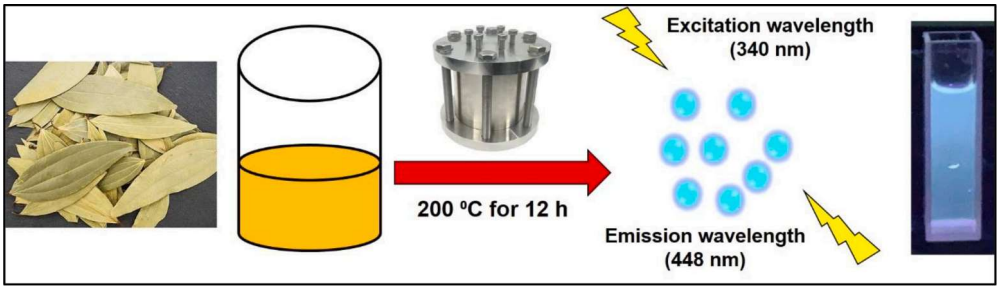

Scheme 1. Green synthesis of CQDs from *C. tamala* leaves extract.

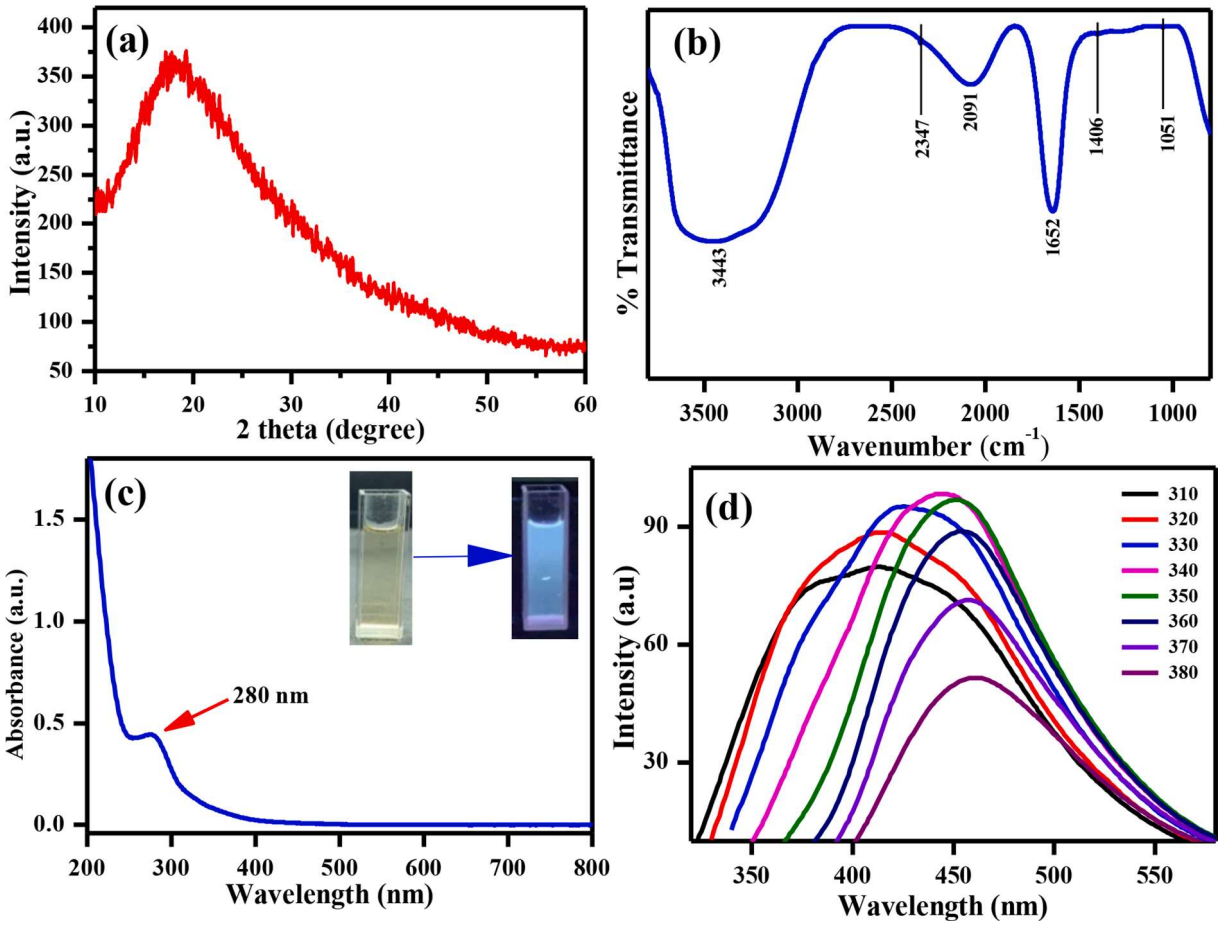

Fig. 1. (a) XRD, (b) FT-IR, (c) UV–Visible spectra, inset depicts luminance of CQDs in daylight and high wavelength light; (d) fluorescence spectra of CQDs having excitation wavelengths from 310 to 380 nm.

2. Experiments

2.1. Reagents and instruments

C. tamala (tejpata) was bought from the local market. CPX and other antibiotics were procured from SRL. CQDs' functional group and crystallite structure were analyzed using Fourier transformation infrared spectroscopy (FTIR), Perkin Elmer, and X-ray Diffractometer (Miniflex, Rigaku). The fluorescence spectrum of CQDs was conducted on fluorescence spectrophotometer, Shimadzu; model rf 5301 pc.

2.2. Synthesis of CQDs

The CQDs were synthesized from *C. tamala via* a simple, one-step hydrothermal approach. For this, leaves extract was prepared by boiling the chopped leaves in 100 mL distilled water (DI) for 1 h. Then 40 mL of leaves extract was sonicated for 30 min and shifted to Teflon vessel. The hydrothermal pot carrying Teflon vessel was kept in the muffle furnace for 12 h at 200 °C. The obtained brownish-yellow solution was centrifuged for removing the bigger particles. Also, the filtrate after centrifugation was dialyzed in 1 L DI through dialysis membrane having 3.5 KDa for 6 h whose water was changed in every 30 min. Finally, the acquired fluorescent, green CQDs were kept at 4 °C for further use. Scheme 1 shows the synthesis of CQDs from *C. tamala* leaves extract.

3. Results and discussion

The QY of CQDs was found in an aqueous medium at 340 nm excitation wavelength using quinine sulfate as a reference. It was observed

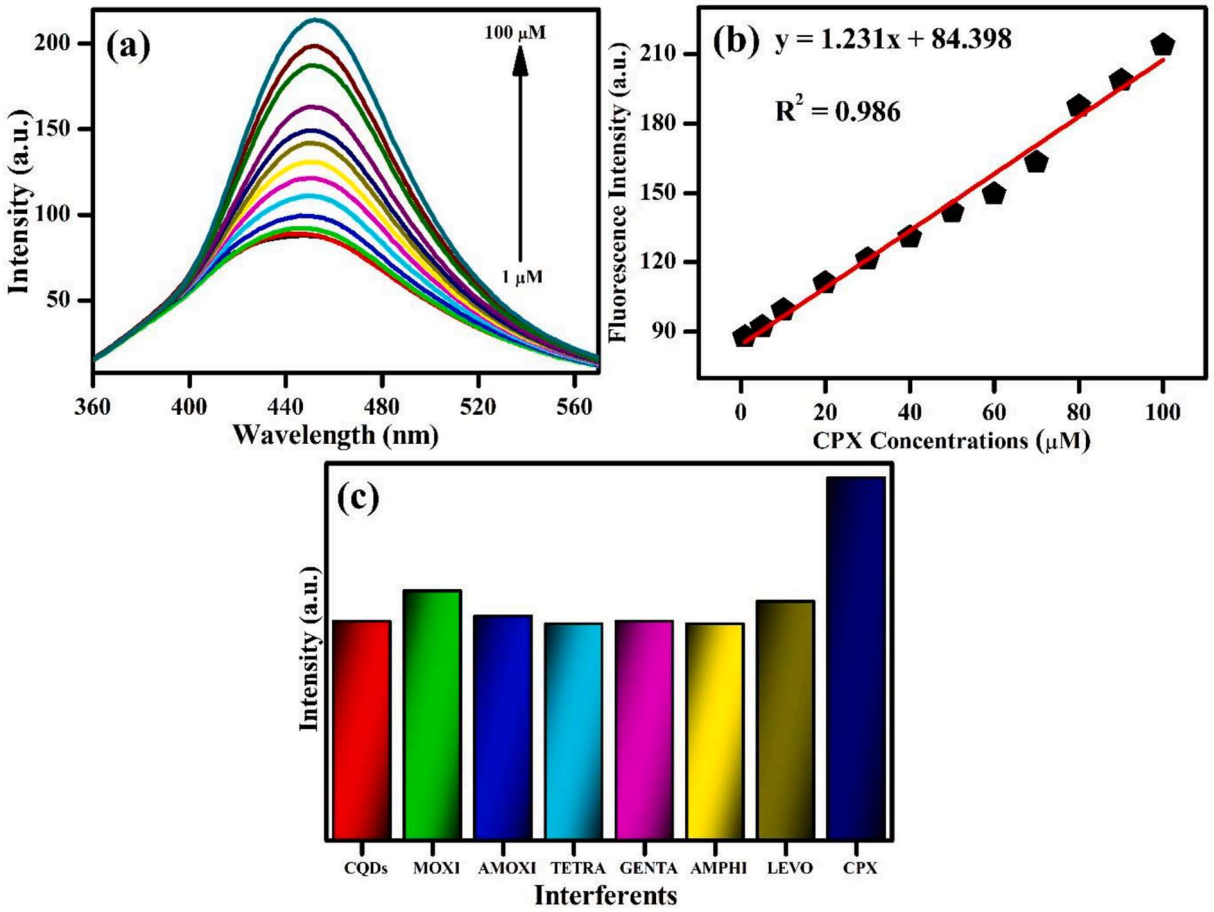

Fig. 2. (a) The effect of CPX concentrations on the fluorescence intensity of CQDs, (b) Linear plot between CQDs fluorescence intensity and CPX concentrations; and (c) Interferent study of CQDs towards other antibiotics.

that hydrothermal synthesis of CQDs from *C. tamala* yielded 31 % of QY that was highest compared to other naturally derived CQDs [17,18]. This could be due to the high temperature and pressure conditions generated during the hydrothermal reaction owing to the well-organized carbonization of leaves extract.

The crystallinity of CQDs was examined through XRD. Fig. 1 (a) depicts the XRD pattern of CQDs whose broad peak is located at 17.1°, which corresponds to the (0 0 2) plane of graphitic material.

The functional group analysis of CQDs was done using FTIR. Fig. 1(b) depicts broad peaks at 3443 and 2091 cm^{-1} corresponding to O—H/N—H stretching vibrations of hydrogen bond and —C≡C— stretch, respectively. Also, the occurrence of a prominent peak at 1652 cm^{-1} corresponds to the C═O stretch bond, while weak peaks at 2347,1406, and 1051 cm^{-1} are ascribed to C≡N, C—N, and C—O stretching vibrations, respectively.

The UV–Visible spectra of CQDs depict an absorption peak at 280 nm that corresponds to the π–π* transition of the conjugated C═C group [Fig. 1 (c)]. Also, in Fig. 1 (d), a strong luminescence of CQDs at 448 nm with 340 nm excitation wavelength was observed by changing the excitation wavelength from 310 to 380 nm.

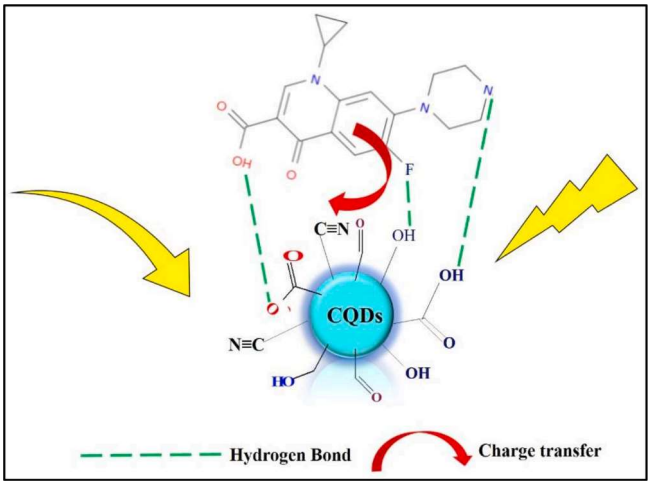

Scheme 2. Hypothetical mechanism of CPX detection using CQDs.

3.1. Detection of CPX

The CQDs were utilized to detect CPX concentrations ranging from 1 to 100 µM as a function of fluorescence intensity (enhancement). It was seen that with each addition of CPX concentration, there is an enhancement in florescence intensity [Fig. 2 (a)]. Further, the linear graph was plotted between the CPX concentrations and fluorescence intensity of CQDs, showing the consecutive increase in fluorescence intensity of CQDs for CPX concentrations [Fig. 2 (b)]. The CQDs show a linear detection of CPX ranging from 1 to 100 µM, having a detection limit of 6.06 µM that was calculated using the formula of 3*S* /*m* (where *S* depicts the standard error of intercept, and *m* is the slope of the linear plot).

3.2. Interferent study

The selectivity of CQDs was done against various potential interfering agents for the detection of CPX [Fig. 2 (c)]. The common antibiotics were taken and added separately to the sensing system. It was observed that no increase in intensity was there on adding the various interferents; however, the fluorescence intensity increases on adding the CPX concentration (50 μM). Thus, the CQDs show good selectivity towards CPX.

3.3. Sensing mechanism of CPX detection using CQDs

The enhancement in fluorescence intensity of CQDs is ascribed to the hydrogen-bonding interactions and charge transfer taking place between CQDs and CPX. As depicted from Scheme 2, the CQDs consist of carboxyl and hydroxyl groups, giving aqueous solubility for combining to CPX through hydrogen bonding. Moreover, charge transfer also plays a vital role. Due to the accepting nature of the nitrile group of CQDs and the electron releasing effect of CPX, a connection is created between the two through a conjugated system that might encourage C═C bonds polymerization. Thus, the synergetic result of hydrogen bonding and charge transfer helped increase the fluorescence intensity by adding more CPX concentrations [19].

4. Conclusion

In this paper, we have reported a novel bioinspired, fluorescent, simple, cost-effective, water dissolving CQDs synthesized from *C. tamala'* leaves extract. The green synthesized CQDs show blue fluorescence, along with a good quantum yield of 31%. These CQDs showed a broad linear range from 1 to 100 μM, with a detection limit of 6.06 μM for CPX detection. Furthermore, it exhibits good selectivity (fluorescence enhancement) towards CPX as compared to others. Hence, these bioinspired CQDs are promising sensing materials that could be applied for other applications owing to their tunable optical properties, excellent dispensability, and low cytotoxicity.

Declaration of Competing Interest

The authors declare that they have no known competing financial interests or personal relationships that could have appeared to influence the work reported in this paper.

Acknowledgment

This work is financially supported by the Government of India, Department of Biotechnology, India; Indo-Russia project (DBT/IC-2/IndoRussia/2017-19/02). Navneet Chaudhary is grateful to the Indian Council of Medical Research (ICMR), India, for providing the fellowship.

References

[1] Y. Zhu, L. Li, Z. Wang, Y. Chen, Z. Zhao, L. Zhu, X. Wu, Y. Wan, F. He, J. Shen, J. Agric. Food. Chem. 56 (2008) 5469.
[2] M.C. Dodd, A.D. Shah, U. von Gunten, C.H. Huang, Environ. Sci. Technol. 39 (2005) 7065.
[3] G. Carlsson, S. Örn, D.J. Larsson, Environ. Toxicol. Chem. 28 (2009) 2656.
[4] L. Chen, Z. Wang, M. Ferreri, J. Su, B. Han, J. Agric. Food. Chem. 57 (2009) 4674.
[5] G.R. Marchesini, W. Haasnoot, P. Delahaut, H. Gerçek, M.W. Nielen, Anal. Chim. Acta 586 (2007) 259.
[6] A.K. Yadav, T.K. Dhiman, G. Lakshmi, A.N. Berlina, P.R. Solanki, Int. J. Biol. Macromol. 151 (2020) 566.
[7] S. Mostafa, M. El Sadek, E.A. Alla, J. Pharm. Biomed. Anal. 27 (2002) 133.
[8] H.Y. Ji, D.W. Jeong, Y.H. Kim, H.H. Kim, D.R. Sohn, H.S. Lee, J. Pharm. Biomed. Anal. 41 (2006) 622.
[9] G. Carlucci, J. Chromatogr. A 812 (1998) 343.
[10] G.G. Snitkoff, D.W. Grabe, R. Holt, G.R. Bailie, J. Immunoassay Immunochem. 19 (1998) 227.
[11] S. Huang, S. Jiang, H. Pang, T. Wen, A.M. Asiri, K.A. Alamry, A. Alsaedi, X. Wang, S. Wang, Chem. Eng. J. 368 (2019) 941.
[12] N. Chaudhary, P.K. Gupta, S. Eremin, P.R. Solanki, J. Environ. Chem. Eng. 8 (2020), 103720.
[13] S. Sri, R. Kumar, A.K. Panda, P.R. Solanki, ACS Appl. Mater. Interfaces 10 (2018) 37835.
[14] J. Yue, K. Zhang, H. Yu, L. Yu, T. Hou, X. Chen, H. Ge, T. Hayat, A. Alsaedi, S. Wang, J. Mater. Sci. 54 (2019) 6140.
[15] A. Salinas-Castillo, M. Ariza-Avidad, C. Pritz, M. Camprubí-Robles, B. Fernández, M.J. Ruedas-Rama, A. Megia-Fernández, A. Lapresta-Fernández, F. Santoyo-Gonzalez, A. Schrott-Fischer, Chem. Commun. 49 (2013) 1103.
[16] G. Sharma, A. Nautiyal, Int. J. Med. Aromatic Plants 1 (2011) 1.
[17] V.N. Mehta, S. Jha, S.K. Kailasa, Mater. Sci. Eng., C 38 (2014) 20.
[18] J. Xu, T. Lai, Z. Feng, X. Weng, C. Huang, Luminescence 30 (2015) 420.
[19] J. Hua, Y. Jiao, M. Wang, Y. Yang, Microchim. Acta 185 (2018) 1.

National Institute of Technology Srinagar
Department of Physics

7th edition of Hybrid

International Conference on

"Nanotechnology for Better Living"

NBL-2021

From 7-11 September, 2021

Certificate of Participation

This is to certify that Prof./Dr./Mr./Miss. NAVNEET CHAUDHARY *from* DEPTT. OF BIOTECHNOLOGY, DELHI TECHNOLOGICAL UNIV. *has attended/ participated and presented a scientific paper entitled,"* DESIGNING AND CHARACTERIZATION OF A ....LANTHANUM OXIDE NANOPARTICLES" *in the NBL-2021 Convention Organized by National Institute of Technology Srinagar.*

Jointly organized by NIT Srinagar and NRF, IIT Delhi in association with Prestigious Universities

Issued today on : 11th of September 2021

Asmaz Shah

Dr. M A Shah

Convener/ HOD Physics

NBL-2021

Prof. Rakesh Sehgal

Patron/ Director NIT Srinagar

In association with:

सत्यमेव जयते
Goverment Of India

BT/ICABB-22/069

International Conference on Advances in Biosciences and Biotechnology (ICABB-2022)

Organized by:

Department of Biotechnology, Jaypee Institute of Information Technology, Noida, Uttar Pradesh, India

Certificate of Presentation

Certified that ***Mr. Navneet Chaudhary*** *from* ***Delhi Technological University*** *participated in the* ***International Conference on Advances in Biosciences and Biotechnology*** *on "Innovation in Life Sciences and Computational Biology" held at Jaypee Institute of Information Technology, Noida from January 20-22, 2022.* ***He*** *presented a paper as Oral presentation titled* ***"Optical Sensor Comprising a Novel Green Syntheized Carbon Quantum Dots for Determination of Ciprofloxacin"****.*

PROF. PAMMI GAUBA
Chairperson

PROF. RACHANA
Convener

DR. SHAZIA HAIDER
Convener

RAK CAM

Certificate of Participation

Mr. Navneet Chaudhary

for presenting your scientific paper entitled *"Ziziphus Mauritania derived green fluorescent carbon quantum dots for optical determination of ciprofloxacin"* at

The International Workshop on Advanced Materials
19 -21 February 2023
Ras Al Khaimah, United Arab Emirates

AK. Cheetham

Anthony K. Cheetham, Kt FRS
Research Professor, MRL, UC Santa Barbara
Distinguished Visiting Professor, NUS, Singapore
Goldsmiths' Professor Emeritus, University of Cambridge